# Seismic tomography of an amagmatic ultra-slow spreading ridge

Mohamadhasan Mohamadian Sarvandani

**THÈSE DE DOCTORAT DE SORBONNE UNIVERSITÉ**

Opérée au sein de :

**ISTeP - UMR 7193 Institut des Sciences de la Terre de Paris**

**Ecole Doctorale** Géosciences Ressources Naturelles et Environnement (ED 398)

**Spécialité de doctorat :** Géophysique - Science des Données

**Mohamadhasan MOHAMADIAN SARVANDANI**

Soutenue publiquement en décembre 2022

# Seismic tomography of an amagmatic ultra-slow spreading ridge

Devant le jury composé de :

| | |
|---|---|
| **Frauke KLINGELHOEFER**<br>Chercheure, Ifremer | **Rapporteur.e** |
| **Piero POLI**<br>Prof, Università degli Studi di Padova | **Rapporteur** |
| **Matthias DELESCLUSE**<br>Maître de Conférences, ENS | **Rapporteur** |
| **Loic LABROUSSE**<br>Prof, ISTEP, Sorbonne Université | **Examinateur** |
| **Sylvie LEROY**<br>Directrice de recherche CNRS, Sorbonne Université | **Directrice de thèse** |
| **Lapo BOSCHI**<br>Prof, Università degli Studi di Padova | **Co-Directeur de thèse** |
| **Mathilde CANNAT**<br>Directrice de recherche CNRS, IPGP | **Invitée** (le cas échant) |

# Contents

# List of Figures

# List of Tables

## Abstract

Ultra-slow spreading ridges are a new category of spreading ridges characterized by quasi-amagmatic crustal accretion, exposing considerable amounts of mantle-derived peridotites on the seafloor. Investigating the contributions of tectonic, magmatic, and other involved processes is necessary to gain a comprehensive conceptual model of ultra-slow spreading ridges. Imaging the crustal and upper mantle structures can help us to understand the past and current geological activities in the ultra-slow spreading ridges. The aim of the project is to understand the oceanic crust formed in an ultra-slow spreading ridge called the Southwest Indian Ridge with a low melt supply. Our research project is based on the processing and modeling of the active and passive seismic data in the easternmost part of Southwest Indian Ridge. The data acquisition took place in 2014 during the SISMOSMOOTH cruise. We analyzed vertical component recordings from 43 ocean-bottom seismometers in our passive seismic approach and the hydrophone components of 16 ocean-bottom seismometers in the active seismic approach. Ambient-noise interferometry and full-waveform inversion (FWI) of refraction data were used to image the internal structures of the lithosphere. In the modeling of ambient-noise interferometry, we find an average crustal thickness of 7 km with a shallow layer of low shear velocities. Moreover, we infer that the uppermost 2 km are highly porous and may be strongly serpentinized. The average shear wave velocity between the base of the crust and the maximum depth of our model (15 km) was less than the global reference value of 4.5 km/s and was explained by the younger age of the seafloor in our area. Our two-dimensional P-wave velocity model obtained from FWI suggests considerable variations in the upper lithospheric compositions along the axis-parallel profile. A transition is expected at a distance of $\sim$65-95 km along the profile from the predominantly volcanic domain in the western zone to variable serpentinized peridotite in the eastern zone. Dike injections are predicted in this area. A westward increase in melt supply is proposed in the seafloor accretion mode. The serpentinization and P-wave velocity model suggests that the Moho is a gradual transition from hydrated to unaltered peridotite.

## Le résumé

Les dorsales ultra-lentes quasi-amagmatiques constituent une nouvelle catégorie de dorsales océaniques caractérisées par une accrétion crustale, exposant sur le fond marin des quantités considérables de péridotites provenant du manteau. L'étude de la contribution des processus tectoniques, magmatiques et d'autres processus impliqués est nécessaire pour obtenir un modèle conceptuel complet des dorsales océaniques à accrétion ultra-lente. L'imagerie des structures de la croûte et du manteau supérieur peut nous aider à comprendre les activités géologiques passées et actuelles sur les dorsales à accrétion océanique ultra-lente. L'objectif du projet est de comprendre la croûte océanique formée dans une dorsale à accrétion ultra-lente appelée ride sud-ouest indienne, à faible apport de magma. Notre projet de recherche est basé sur le traitement et la modélisation de données sismiques actives et passives dans la partie la plus orientale de la dorsale Sud-Ouest Indienne. L'acquisition des données géophysiques a eu lieu en 2014 lors de la campagne SISMOSMOOTH, à bord du N/O Marion-Dufresne. Nous avons analysé les enregistrements des composantes verticales de 43 sismomètres fond de mer (OBS) dans notre approche sismique passive et les composantes hydrophones de 16 sismomètres fond de mer pour l'approche sismique active. L'interférométrie de bruit ambiant et l'inversion de forme d'onde complète (FWI) des données de réfraction ont été utilisées pour imager les structures internes de la croûte et de la lithosphère. Grâce à la modélisation de l'interférométrie de bruit ambiant, on trouve une épaisseur moyenne de croûte de 7 km avec une couche peu profonde de faibles vitesses de cisaillement. De plus, nous en déduisons que les 2 km supérieurs sont très poreux et peuvent être fortement serpentinisés. La vitesse moyenne des ondes de cisaillement entre la base de la croûte et la profondeur maximale de notre modèle (15 km) est inférieure à la valeur de référence globale de 4.5 km/s et peut s'expliquer par le jeune âge des fonds marins de notre zone. Notre modèle bi-dimensionnel de vitesse des ondes P obtenu à partir de notre analyse FWI suggère des variations considérables de composition dans la partie supérieure le long du profil parallèle à l'axe. Notre étude propose un domaine de transition entre un domaine à prédominance volcanique et un non magmatique, entre $\sim$65 à 95 km de distance sur le profil. Des injections magmatiques dans des dikes sont proposées dans le domaine oriental non volcanique. Une augmentation vers l'ouest de l'apport de matériel magmatique est confirmée pour le mode d'accrétion océanique. Le modèle de vitesse des ondes P associé aux variations de serpentinisation suggère que le Moho est une transition graduelle d'une péridotite hydratée vers une péridotite non altérée.

## Acknowledgment

I would like to acknowledge the Flotte océanographique française and an NSERC Ship Time grants that funded the SISMOSMOOTH cruise, and CNRS-INSU Tellus and ANR Rift2Ridge NT09-48546 for providing support for the cruise. I would like to appreciate ANR Ridge Factory 18-CE01-0002-01 and Sorbonne Universite for giving the grant for this thesis.

I would like to express my deepest gratitude to my supervisors. It would have been next to impossible to write this thesis without my supervisors, research director Sylvie Leroy, Prof. Lapo Boschi, and Prof. Mathilde Cannat. They continuously provided encouragement and were always enthusiastic to support and guide me in all the time of my academic research and daily life. Their immense knowledge, plentiful experience, and skillful advice enriched this thesis significantly.

I would also like to express my deep appreciation to Dr. Emanuel Kästle, who has consistently assisted me with the processing and modeling of ambient noise data. I will never ever forget his moral and professional character. I would like to extend my special thanks to Dr. Sylvie Wolf. Her assistance with the ISTEP cluster is greatly appreciated. Many thanks to Dr. Hanchao Jiang, Dr. Milena Marjanovic and Dr. Ekeabino Momoh for discussing and responding to my questions.

I would like to announce my sincere appreciation to the ISTEP research team, authorities, and administrative staff who graciously supplied the best facilities, and kindly answered all of my questions.

I am deeply grateful to all members of the jury for agreeing to review the manuscript, sharing their wealth of scientific experiences, and participating in the defense of this thesis. I am most grateful.

I would like to thank my lab mates, and colleagues for their help, and the cherished time spent together. Some special words of gratitude go to my friends who have always been a major source of fun and encouragement when things would get a bit discouraging. Thanks guys for always being supportive and kind to me.

And the last but not least, I am very thankful to my family, for their endless and selfless efforts and support throughout my life. My warm and heartfelt thanks go to my parents whose constant love keeps me motivated and confident.

# Chapter 1

# Introduction and the objectives


## Summary

The subject matter investigated in this thesis is discussed in this chapter. We start introducing mid-ocean ridges and we explain why ultra-slow spreading ridges are interesting. The discussion of ultra-slow spreading ridges is narrowed to the Southwest Indian Ridge. The chapter brings to attention the main objectives of the work and the outlines of the thesis.


## 1.1 Different plates

Plate tectonics is the theory that characterizes the distribution of geological phenomena on a global scale. it refers to the movement of the earth's lithosphere and the resulting geological events such as mountain building, seismicity, volcanism, and continental drift. According to the theory of plate tectonics, Earth's rigid outermost layer, or lithosphere (crust plus upper mantle) overlies a plastic (moldable) layer called the asthenosphere. The lithosphere is broken into seven major continental-sized and ocean-sized plates: African, Antarctic, Eurasian, Indo-Australian, North American, Pacific, and South American. There are also some minor plus micro plates. The plates of the lithosphere move relative to each other at different rates (Kay et al., 1970; Dewey and Bird, 1970; Cawood et al., 2006; Palin and Santosh, 2021).

The movement of plates can be convergent, divergent, or transform. At divergent boundaries, the separation between plates may occur either on the continental lithosphere or on the oceanic lithosphere. Rift valleys will be produced as long as the plates are taken apart on the continental lithosphere. As the rift valleys widen, the separation of plates is achieved and a new oceanic lithosphere is created. The mid-ocean ridges will be formed as a result of the formation of the oceanic crust. The details of mid-ocean ridges, and in particular the Indian mid-ocean ridge, which is the focus of this research, will be studied in the next sections.

### 1.1.1 Divergent boundary: different types of mid-ocean ridges and their features

The difference between the spreading rates, volcanic activity, structural behaviors (tectonic stretching), and morphology has categorized the mid-ocean ridges. Mid-ocean ridges are classified into 4 divisions based on their spreading rates (DeMets et al., 1994; Schmid, 2017): 1. Fast (> 8 cm/yr) 2. Intermediate (5-8 cm/yr) 3. Slow (< 5 cm/yr) 4. Ultra-slow (< 2cm/yr). Fast-spreading ridges are hotter and a significant amount of magma breaks the sea floor through volcanic eruptions. Slow-spreading ridges act like cold chocolate and they crack when the sea floor stretches enough. Therefore, in fast-spreading ridges, the morphology is mainly affected by volcanic activity, while in slow-spreading ridges, tectonic stretching is dominant (Snow and Edmonds, 2007). The difference between the morphology of fast and slow-spreading ridges is shown in Figure 1.1. As we see, the slow-spreading ridges are characterized by axial rift valleys and more rough topography, while the fast-spreading ridges have axial highs and smooth topography. Intermediate spreading ridges can have axial highs, axial rift valleys, and transitional morphology. In spite of dissimilarities between slow, fast, and intermediate spreading ridges, they share certain characteristics: 1) similar crustal thickness and composition. 2) The involvement of dominant transform faults in spreading (Püthe and Gerya, 2014). The comparable characteristics of mid-ocean ridges were explained by the

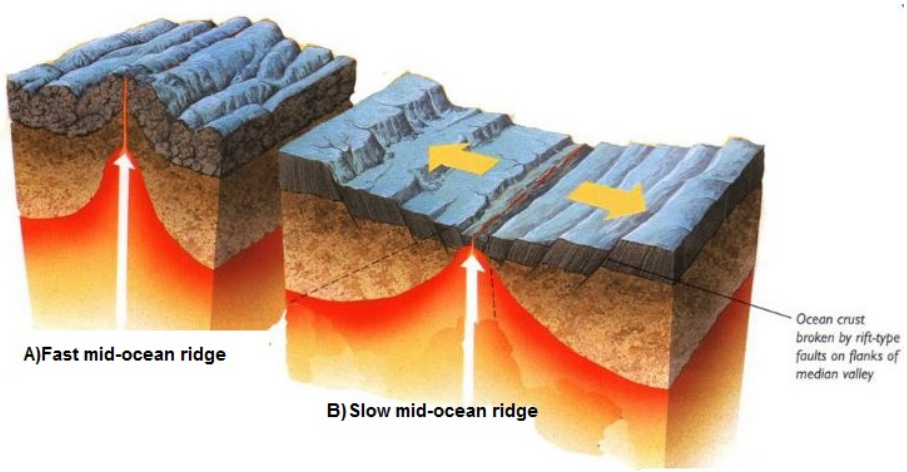


Figure 1.1: Morphology of fast and slow mid-ocean ridges (Slideplayer, 2019). Mid-ocean ridges are classified into four divisions based on their spreading rates (Schmid, 2017): 1. fast (> 8 cm/yr) 2. Intermediate (5-8 cm/yr) 3. slow (< 5 cm/yr) 4. ultra-slow (< 2cm/yr)

traditional Penrose model and similar ideas (MASON, 1985). The robustness of these traditional models came into question for the following reasons:

1. According to the Penrose model, a 6 km layer of basaltic rocks and gabbro was proposed to cover the upper mantle peridotite. However, widespread exposure of serpentinized mantle-derived peridotite was found on the sea floor of slow and ultra-slow spreading ridges such as the Mid-Atlantic ridge and Southwest Indian Ridge (SWIR) (Aumento and Loubat, 1971; Dick, 1989; Engel and Fisher, 1975). Additionally, the old-fashioned model didn't have any display of how water penetrated into the mantle and created serpentinized peridotite

(Snow and Edmonds, 2007).

2. The crustal thickness of mid-ocean ridges is commonly considered as a direct measure of the amount of produced melt (Schmid, 2017). Another violation of the Penrose model was recognized when the thickness of the oceanic crust of ultra-slow spreading ridges was studied through seismic data. However, in most of the mid-ocean ridges, the thickness is nearly constant at around 6 km, in ultra-slow spreading ridges, we observe thinner and variable oceanic crust (Conley and Dunn, 2011).

3. Seafloor sampling and seismic tomography studies in parts of the slow-spreading Mid-Atlantic Ridge, especially at the end of spreading segments and the ultra-slow-spreading Southwest Indian Ridge indicate that the magmatic crustal model may not adequately describe the observations in these domains, especially when the melt supply is relatively low. As early as the 1980s and early 1990s, the possibility of a crust forming when the magma supply is moderate began to receive intense attention. Various crustal models were proposed and were refined and are still being refined as new data becomes available. However, the 'smooth seafloor' model from Cannat et al. (2006) is supported by mantle-derived rocks outcrop over areas up to 82 km across the axis and >20 km along the axis. The smooth seafloor is not found in faster spreading ridges and is shaped in the form of broad ridges with a rounded smooth tomography (Cannat et al., 2006; Sauter and Cannat, 2010).

4. In contrast to the Penrose model, a significant level of volcanism was discovered in the ultra-slow Gakkel ridge, which means that the temperature is not depending solely on the spreading rate (Sohn et al., 2008; Edwards et al., 2001).

## 1.2 Objectives

The aspects of ultra-slow spreading ridges (especially in SWIR and Gakkel ridges) show the necessity of new research to describe the processes involved in the ultra-slow spreading ridges (Dick et al., 2003). The aim of our project is to contribute to this case by focusing on SWIR. To gain a more comprehensive conceptual model of slow-spreading ridges, we will try to investigate the contributions of tectonic and magmatic processes and image the crustal structures in SWIR. In parallel, we will have this opportunity to study active processes which can affect mantle exhumation. Imaging the crustal structure is necessary to understand past and ongoing geological processes and provides an important base for mantle tomographic studies.

As a consequence of the low melt supply, the creation of the seafloor was explained by successive, flipping polarity, detachment faults that form north and south of spreading ridge in the SWIR (Cannat et al., 2006, 2019; Sauter et al., 2013). According to recent studies, these detachment fault systems, have been proposed to explain the emplacement of ultramafic rocks. However, the geometry of detachment faults has been studied by numerical modeling (Buck, 1988; Lavier

et al., 1999; Schouten et al., 2010), paleomagnetic studies of core samples (Garcés and Gee, 2007) and seismic reflection data (Momoh, 2018; Momoh et al., 2017, 2020), the geometry of the detachment fault system at depth is not well known yet. In a recent seismic reflection study of the area, the limitation of streamer length (4.5 km) restricted us to less information about the deep parts (Momoh, 2018). Imaging the velocity structure of the footwall of this detachment fault system is critical to discover the damaged zone of the system. To investigate deep parts of the fault, we will apply the full waveform inversion (FWI) of refraction seismic data and ambient noise tomography. However, imaging methods such as full waveform inversion and tomography of reflection and refraction data have been widely used in mid-ocean ridges (Purdy and Detrick, 1986; Arnulf et al., 2012; Kandilarov et al., 2008; Operto et al., 2006; Lizarralde et al., 2004), this is the first time that full waveform inversion of refraction data and passive seismic tomography of ambient noise data are being tried in our study area. More importantly, it is quite new to do passive seismic tomography of ambient noise data in mid-ocean ridges, mostly due to the limited availability of ocean bottom seismometers and high levels of local noise. We also investigate the robustness of the ambient noise method in a marine exploration setting. The obtained subsurface S-wave velocity model will be compared to previous studies and interpreted in the context of the regional tectonic evolution. Taking the advantage of more complete information of data in FWI, we also attempt to improve the results of recent travel time tomography obtained in (Momoh, 2018) and (Corbalán et al., 2021). We aim to have a P-wave velocity model of FWI with better resolution than current models and an S-wave velocity model of ambient noise interferometry. The detailed velocity model could be utilized to produce a more robust pre-stack depth migration of selected seismic lines (Canales et al., 2017).

Another importance of our study is to construct a more accurate crustal thickness by the seismic method where the crust modeled from gravity is probably invalid (Cannat et al., 2008, 2006). A number of studies applied passive seismic interferometry to reconstruct the crust with increasing resolution, confirming the interest of our selected method (Zulfakriza et al., 2014; Saygin and Kennett, 2012; Kao et al., 2013; Lin et al., 2008). Recent travel time tomography of P-wave has revealed the crustal thickness (4-5 Km) with variable velocity from 3.5 to 7.3 Km/s (Momoh et al., 2017), which will be looked into more thoroughly in our research.

The spatial distribution and intensity of serpentinization in the crust of slow-spreading ridges are another interest of our study. The samples from dredges, submersibles, and drilling holes were collected from the uppermost part of the detachment fault system and they could not easily be the best representative of the deepest parts (Cannat et al., 1995; Rouméjon and Cannat, 2014). Increasing the degree of serpentinization from 0 % to 100 % leads to a decrease in seismic velocities and density (Miller and Christensen, 1997). Therefore, our seismic approach can provide information about the degree of serpentinization at deeper parts of the detachment fault system.

The ratio of P and S wave velocities provides an additional constraint on the lithology (Kandilarov et al., 2008) and is sensitive to the presence of fluids (Hamada,

2004). The final P-wave velocity model of FWI and S-wave velocity model of ambient noise interferometry will be included in a general model of SWIR.

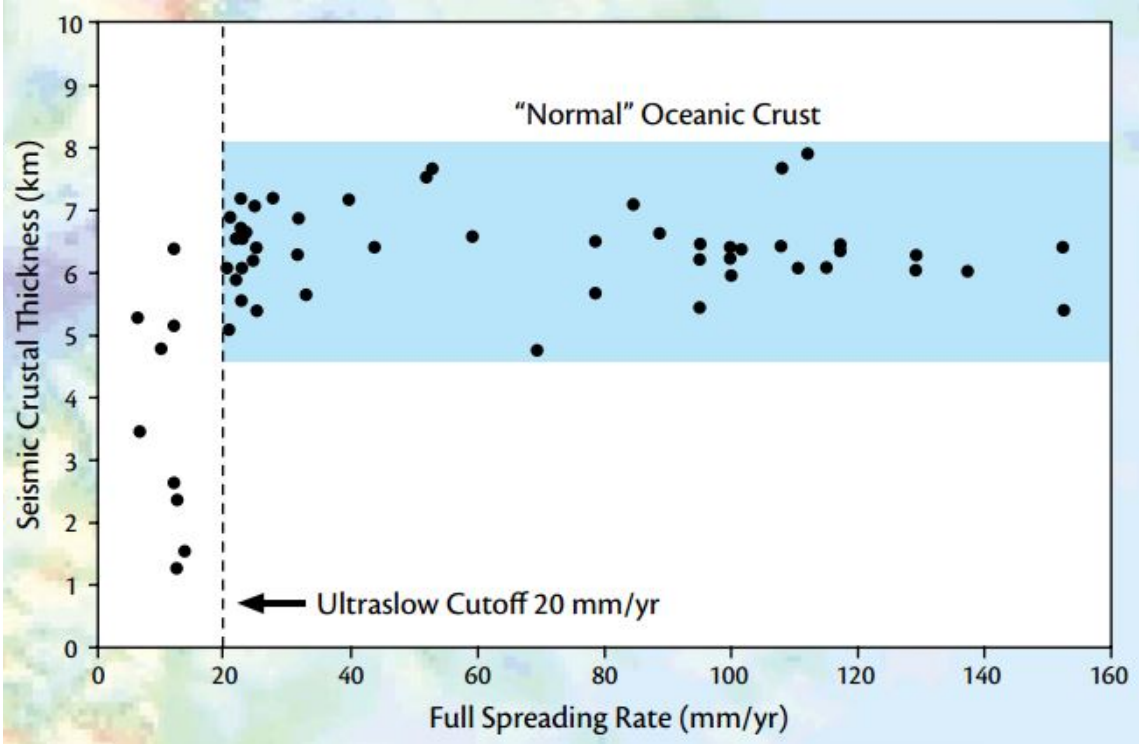


Figure 1.2: crustal thickness obtained by seismic studies, as a function of full spreading rate (Snow and Edmonds, 2007).

# Chapter 2

# Seismic method: acquisition, processing, and imaging


## Summary

This chapter starts with the initial concepts of the marine seismic method, such as body waves, surface waves, passive source, active source, and OBS in Appendix B. A brief description of marine seismic data acquisition and data display is discussed. We focus on some necessary theoretical notions for the processing and imaging of passive and active seismic data.


## 2.1 Acquisition of Marine seismic data

Acquisition of marine seismic data in terms of receiver type is divided into two main methods, which are called multi-channel seismic data (abbreviated as MCS for reflection) and ocean bottom seismometer (wide-angle seismic). Both of these methods can be utilized to gain active seismic data, but only the OBS acquisition is recruited for recording passive seismic data. In 2D seismic surveys, the sources and receivers are located on the same profile (Mari, 2021). The main differences between marine reflection seismology and refraction seismology will be explained in the following.

The characteristics of reflection seismology (multi-channel seismic) in the marine acquisition are defined as follows:

1. The distance between the source and receiver is small in comparison with the depth of the target.

2. The receivers for this method are groups of hydrophones (channels) that are placed on streamers.

3. Depending on the characteristics of the seismic source, the vertical and horizontal resolution of the reflection method is at a better level than the refraction method.

The features of refraction seismology are described as:

1. It is known as wide-angle refraction because the distance between source and receiver must be large to detect deeper structures (Dondurur, 2018). In addition to refraction, we can also have a reflection.

2. The receivers of this method are three component geophones and one hydrophone at the bottom of the ocean. The receivers can also be sonobuoys on the sea surface.

3. It has a relatively low structural resolution.

We can see in Figure 2.1 how to collect the data in marine seismic by MCS and OBS acquisition. In this study, we work on OBS data, and our focus is not on MCS data. You can find in the appendix A.5 more details about the seismic surveys.

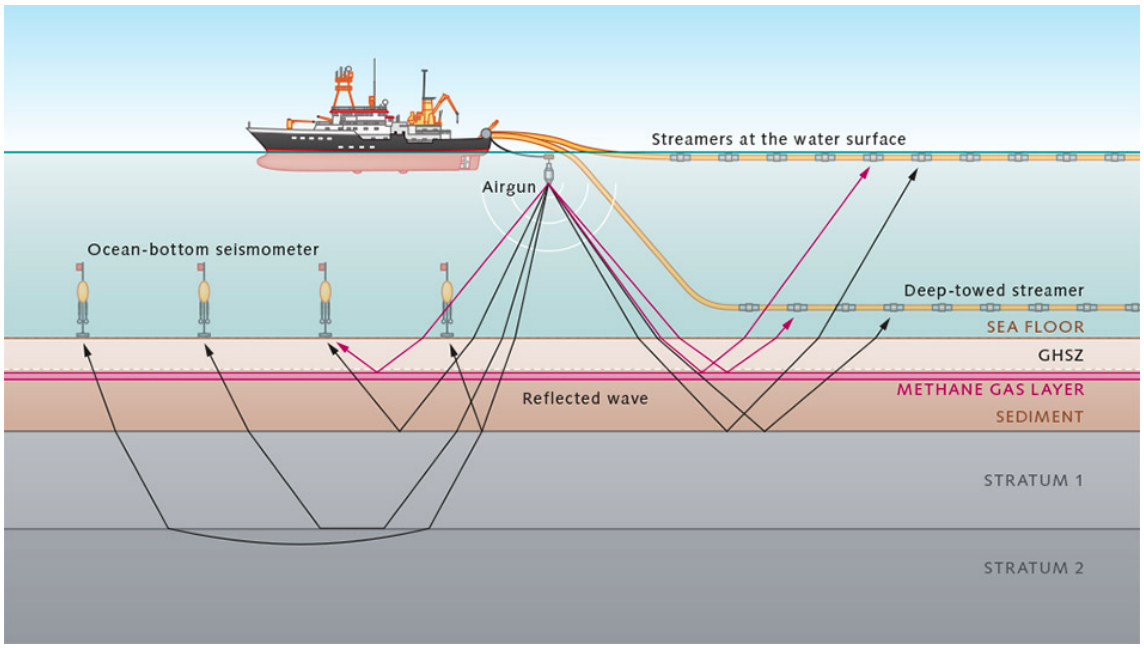


Figure 2.1: Marine seismic acquisition for MCS and OBS methods. MCS records reflection data and OBS measures refraction and reflection data (Bücker et al., 2014).

## 2.2 Display of active and passive seismic data

### 2.2.1 Convolution and seismic trace

The concept of convolution in seismic is utilized to explain how the seismic traces (seismograms) are created. According to this concept, a recorded seismic trace $s(t)$ is defined as follows (Yilmaz, 2001; Mousa and Al-Shuhail, 2011):

$$s(t) = w(t) * e(t) + \gamma(t) \tag{2.1}$$

where $w(t)$ is the generated source's wavelet, $e(t)$ is the Earth's impulse response and $\gamma(t)$ is random noise. We have shown in Figure 2.2 how the convolution model can produce a seismic trace.

### 2.2.2 Receiver gather and seismogram

In active seismic surveys, a seismic record is usually a set of seismic traces displayed in a shot gather or receiver gather. The horizontal axis (X) and vertical axis (T) of gathers are defined based on the distance between the source and receivers (offset)

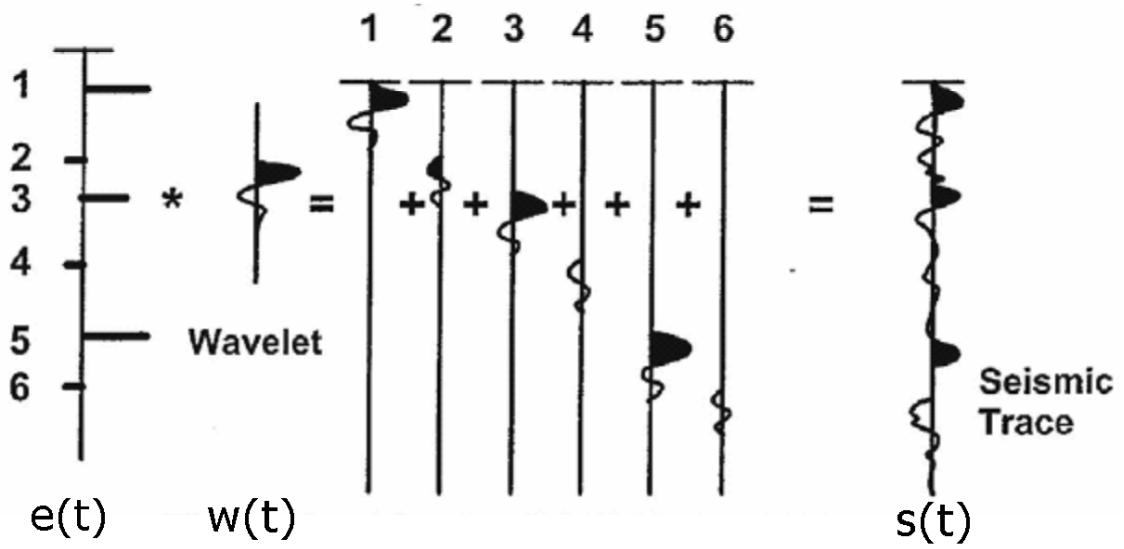


Figure 2.2: Convolution seismic trace model. $w(t)$ is the generated source's wavelet, $e(t)$ is the Earth's impulse response and $\gamma(t)$ is random noise. A seismic wavelet source is convoluted with the impulse response of the Earth to create a recorded trace (GEOS, 2006).

and the arrival time of waves (in minutes or seconds), respectively. The horizontal and vertical axes can also be shown by the number of recorded traces and sampled data, respectively. Body waves and surface waves can be distinguished by their T-X curves in a seismic record (seismogram). The ray-path of body waves in a medium for one shot (yellow star) and an array of receivers have been imaged in Figure 2.3a. T-X curves associated with different body waves are displayed in a shot gather (Figure 2.3b). A similar display can be shown by the receiver gather. Different types of body waves in a shot gather are explained as follows (Zhou, 2016):

* Direct waves (green arrows): they travel directly from source to receiver without undergoing seismic reflection or refraction from the medium's layers.

* Wide angle refraction or diving waves or turning waves (green dash arrows): This type of wave dives into a higher velocity zone so as to arrive at the receiver in a shorter time than a direct wave. They leave nearly a straight move-out. When body waves strike an interface at the critical angle, the refracted wave is created. This only occurs when the wave is transmitted from a lower velocity layer to a higher velocity layer (Mari, 2021). The wave propagating in parallel with the interface acts as a secondary source and produces waves toward the receivers.

* Reflected waves (blue, red, and purple arrows): When a wave strikes at interfaces, part of its energy is reflected back to the surface. This reflection creates significant hyperbolic shapes in the seismogram. Blue, red, and purple arrows present the reflected waves at the depths of 1.5, 3, and 5 km.

* Wide angle reflection waves (dashed red and dashed purple arrows): Another form of reflection is that if the angle of the strike is greater than the critical angle, all the energy of the wave will be reflected. This reflection is known as a wide-angle reflection (Sheriff and Geldart, 1995; Mari, 2021).

* Diffracted wave (yellow arrows): that is the radial scattering of a wave into the new wavefronts after a wave strikes a sharp edge, a discontinuity, or an unconformity

in the rock. They appear as hyperbolic-like shapes in the seismogram.

* Multiples (Cyan arrows): These are the waves that have been reflected multiple times between the surface and interface or only between the interfaces.

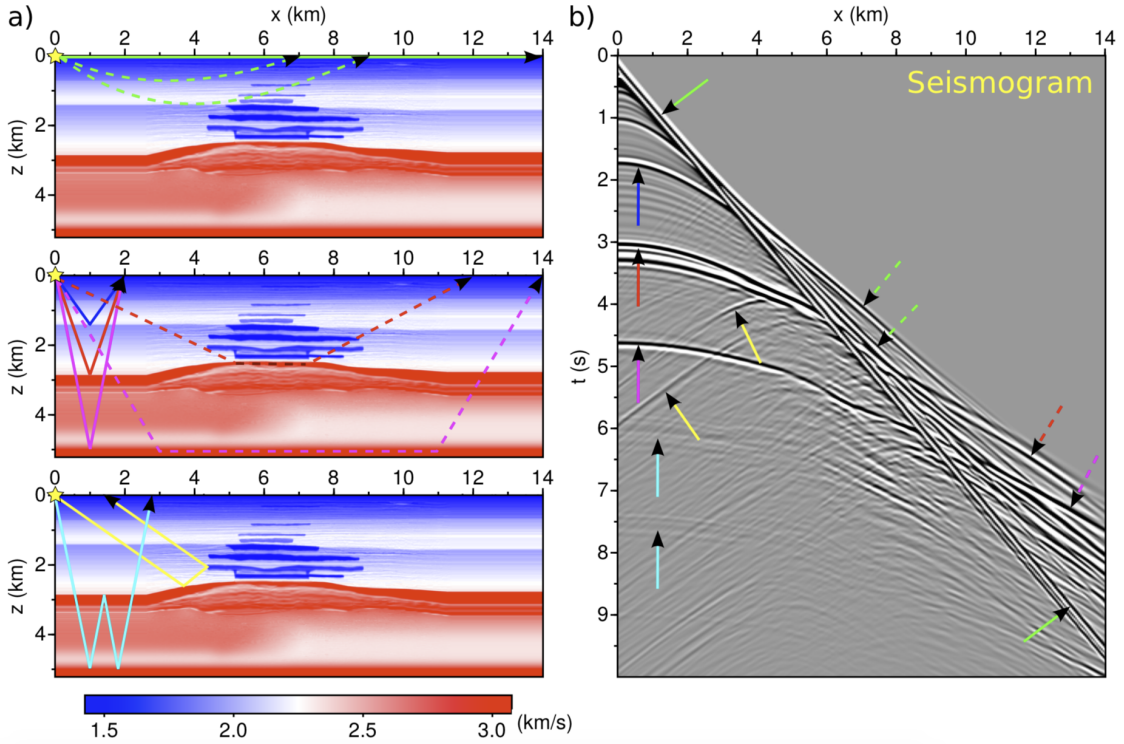


Figure 2.3: Display of the active seismic record. A) Velocity model. B) Shot gather or seismogram. The yellow star presents the location of the shot. The colored arrows denoted the different types of P-waves in the seismogram and their associated ray-paths. These arrows are explained in the text (Zhou, 2016).

In passive seismic, the display of the data is a single seismogram that shows the ground motions over some days, months, or years. In the data, the horizontal axis shows the time and the vertical axis shows the magnitude of amplitude. What we record in the horizontal and vertical components of geophones is like Figure 2.4B.

## 2.3 Velocity of P-wave, velocity of S-wave and elastic modules

The occurrence of passive seismic sources such as earthquakes or active sources like explosions produces stress (including compression, tension, and shearing) within the Earth. The consequence of this stress is the change in the volume and/or shape of the internal materials, which is known as strain. In elastic earth, the variations between stress and strain are defined by 21 modules. In this case, the medium is anisotropic, and the properties of the material may change with direction. However, in reality, while anisotropy exists, it has been proven that the properties of the earth's interior are, within a reasonable approximation, the same in all directions, i.e., in the first approximation, the earth can be treated as approximately isotropic. The relationship between stress and strain in an elastic isotropic earth is determined by only two $\lambda$ and $\mu$ modules, known as the Lamé parameter and shear modulus, respectively. The velocity of P and S waves can be written in relation to the Lamé

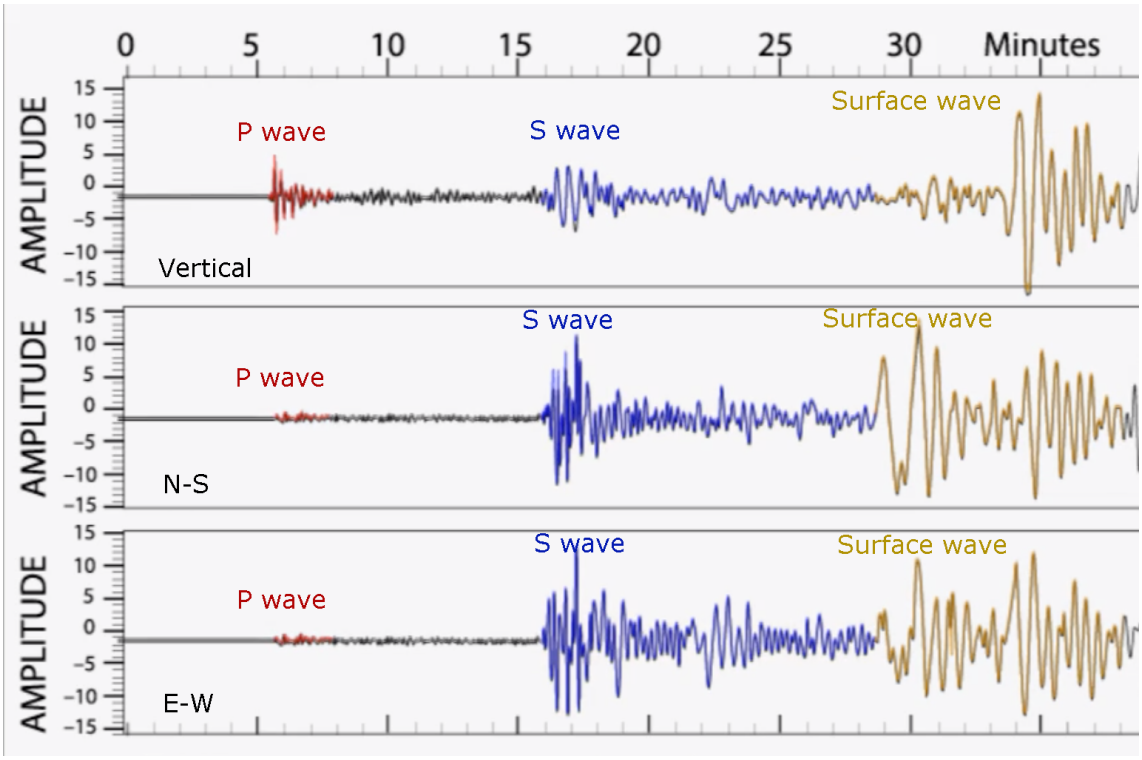


Figure 2.4: Passive seismic data is recorded by vertical, N-S, and E-W geophones. P-waves mostly affect the vertical component of the geophone. The motion produced by S-wave is more energetic in the horizontal components of geophones (E-w and N-S). Surface waves can be detected and distinguished in the horizontal and vertical components of geophones (IRIS, 2021). The display is with some exaggeration: for example, there can be other signals than "S waves" in the blue. If there are S waves, it's not the direct S waves during all that time.

parameter and shear modulus by defining the wave propagation equation in terms of density ($\rho$), strain (displacement), and stress tensor and solving this equation in a homogeneous medium as follows (Bormann et al., 2012):

$$Vp = \sqrt{\frac{\lambda + 2\mu}{\rho}} \tag{2.2}$$

$$Vs = \sqrt{\frac{\mu}{\rho}} \tag{2.3}$$

There are some main parameters that can affect seismic velocities:

1. Composition of rocks: In principle, the Vp and Vs of igneous, metamorphic, anhydrite, and carbonate rocks are higher than the velocities of soils and sedimentary rocks. In fact, the resistance of the rocks against the stress affects the elastic modulus and increases the velocity (Geosci, 2017). Vp of some materials has been shown in Figure 2.5.

2. Porosity: It is defined as a fraction of the volume of empty spaces in rocks over the total volume of rocks (including solid and empty space) (see Figure A.6). This empty space can be filled with fluids such as water, oil, and gas. When the porosity is higher, the seismic velocity decreases (Salah et al., 2018).

3. Pore fluids and saturations: The empty spaces in the rocks can be filled with oil and air, known as pore fluids. The velocity of the P-wave in water and oil is larger

| Material | $V_P$ (m/s) |
|---|---|
| Air | 330 |
| Water | 1450–1530 |
| Petroleum | 1300–1400 |
| Loess | 300–600 |
| Soil | 100–500 |
| Snow | 350–3000 |
| Solid glacier ice* | 3000–4000 |
| Sand (loose) | 200–2000 |
| Sand (dry, loose) | 200–1000 |
| Sand (water saturated, loose) | 1500–2000 |
| Glacial moraine | 1500–2700 |
| Sand and gravel (near surface) | 400–2300 |
| Sand and gravel (at 2 km depth) | 3000–3500 |
| Clay | 1000–2500 |
| Estuarine muds/clay | 300–1800 |
| Floodplain alluvium | 1800–2200 |
| Permafrost (Quaternary sediments) | 1500–4900 |
| Sandstone | 1400–4500 |
| Limestone (soft) | 1700–4200 |
| Limestone (hard) | 2800–7000 |
| Dolomites | 2500–6500 |
| Anhydrite | 3500–5500 |
| Rock salt | 4000–5500 |
| Gypsum | 2000–3500 |
| Shales | 2000–4100 |
| Granites | 4600–6200 |
| Basalts | 5500–6500 |
| Gabbro | 6400–7000 |
| Peridotite | 7800–8400 |
| Serpentinite | 5500–6500 |
| Gneiss | 3500–7600 |
| Marbles | 3780–7000 |
| Sulphide ores | 3950–6700 |
| Pulverised fuel ash | 600–1000 |
| Made ground (rubble etc.) | 160–600 |
| Landfill refuse | 400–750 |
| Concrete | 3000–3500 |
| Disturbed soil | 180–335 |
| Clay landfill cap (compacted) | 355–380 |

Figure 2.5: A) P-wave velocity for different materials (Kohnen, 1974).

than in the air, and the saturation can increase the Vp of the material (Kahraman, 2019; Hamada, 2004).

## 2.4 Dispersion curve of surface waves

The penetration depth of surface waves is comparable to the skin effect of electromagnetic waves. Surface waves with longer periods or shorter frequencies sense shallower layers, and surface waves with shorter periods or longer frequencies penetrate into shallower layers of the Earth. This feature led to the frequency dependency of their horizontal propagation velocity. The display of the velocity of a surface wave versus period or frequency is called a dispersion curve. Dispersion curves may vary in terms of group or phase velocity, Rayleigh and Love waves, the medium, and the mode of surface waves (Bormann et al., 2012). Group velocity is defined as the velocity of wave packets while phase velocity is based on the velocity of individual peaks (see Figure 2.6). Using the harmonic wave parameters, group wave

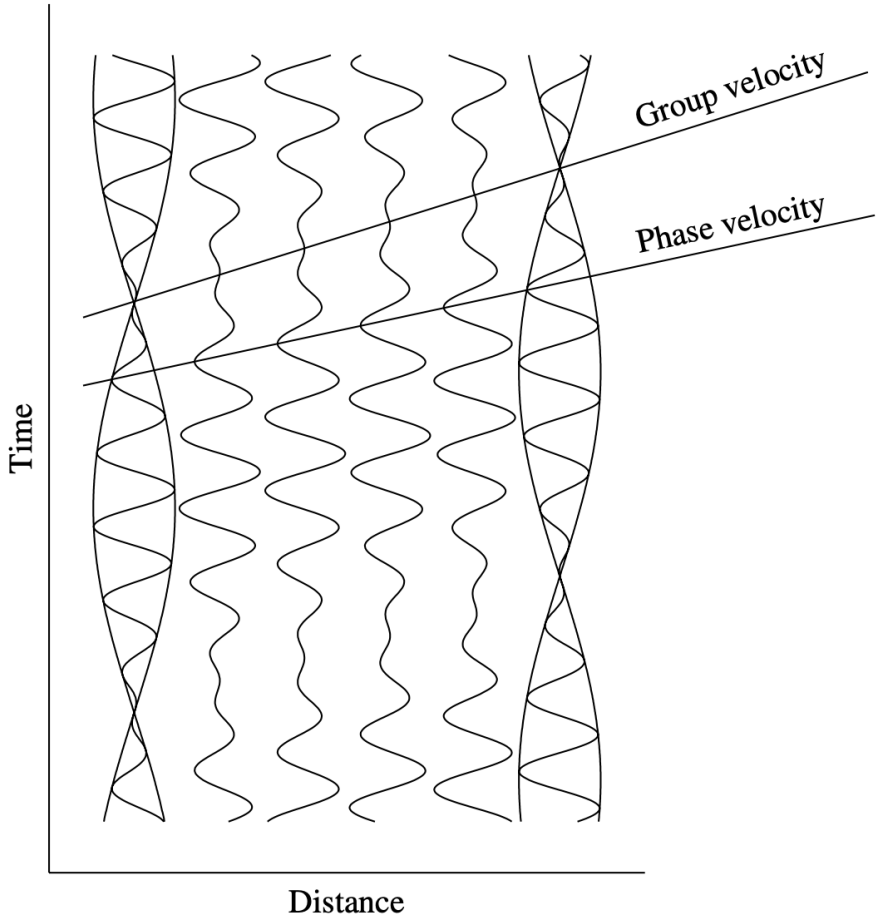


Figure 2.6: The group velocity is defined in terms of the velocity of the wave packets. The phase velocity is identified as the velocity of the individual peaks (Konter, 2021).

velocity (U) may be written in terms of phase velocity (c) as follows (Konter, 2021):

$$U = \frac{d\omega}{dk} = c + k\frac{dc}{dk} = c(1 - k\frac{dc}{d\omega})^{-1} \tag{2.4}$$

Where $\omega$ is frequency and k is wave number. The phase velocity of both Love and Rayleigh waves normally decreases with frequency; thus, $dc/d\omega$ is negative. Therefore, in principle, the phase velocity is supposed to be larger than group

velocity. It can be seen in Figure 2.7 which presents Love and Rayleigh dispersion curves calculated from the PREM (Preliminary Reference Earth Model). More than one phase velocity can be attributed to a given frequency of surface waves because these waves can travel at different velocities at any relevant frequency. The lowest velocity for the frequency range is known as the fundamental mode velocity. All velocities that are higher than the fundamental mode or first mode velocities are called higher modes (Xia et al., 2003). The differences in crustal thickness and composition between oceanic and continental areas result in various related average group-velocity dispersion curves (Figure 2.8). They are particularly significant for Rayleigh waves.

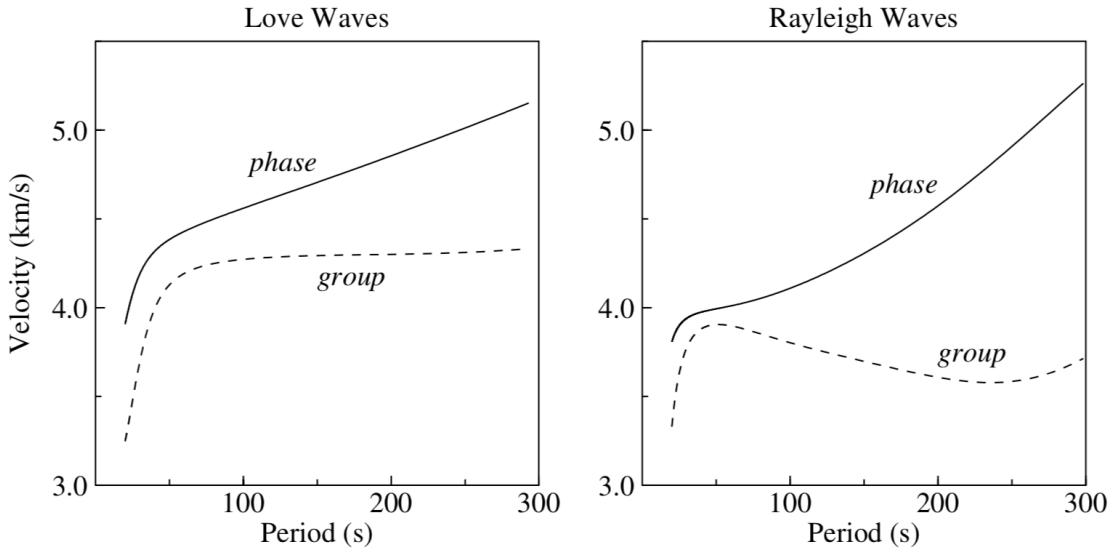


Figure 2.7: Dispersion curves related to the fundamental mode of Rayleigh and Love waves are calculated from the PREM (Preliminary Reference Earth Model) (Konter, 2021).

## 2.5 Passive seismic interferometry (ambient noise method)

The passive seismic method is classified into three main branches: 1. based on the use of local earthquakes as a source 2. A source based on distant earthquakes. 3. Based on the source of the ambient noise. The frequency of ambient noise sources used in most regional-scale tomography is 0.03 to 1 Hz. At higher frequencies, the dominant source of noise is attributed to human activity (Mordret et al., 2013). The start of interferometry is steamed from Claerbout (1968) and Rickett and Claerbout (1999), where they showed the reflected response of ambient noise sources in the horizontally layered medium and 3D Earth, respectively. The first detailed evidence of a theory can be attributed to Lobkis and Weaver (2001). Until 2003, scientists didn't know how to extract useful information from ambient noise. That's why most of the research was relevant to removing the ambient noise to enhance the resolution of coherent signals (Nicolson et al., 2012). Theoretical derivations became complete in (Derode et al., 2003; Snieder, 2004; Wapenaar, 2004). These days, the usage of passive seismic interferometry has been applied in four main areas, which are

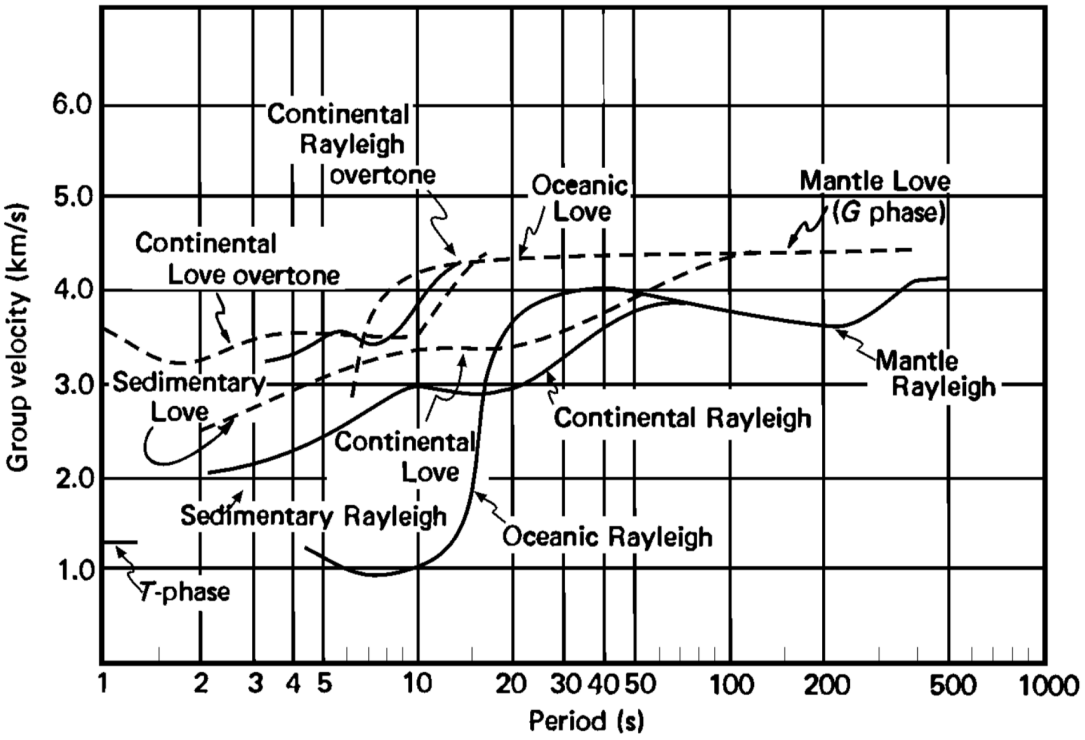


Figure 2.8: Group-velocity dispersion curves versus period for Love and Rayleigh waves (fundamental mode and higher mode (overtone)) (Bormann et al., 2012).

imaging, monitoring, determination of quality factor, and suppression of surface waves (Draganov and Ruigrok, 2014). The successful applications on solid Earth were started by Campillo and Paul (2003) and Shapiro and Campillo (2004) using ambient seismic noise and earthquakes. It should be noted, however, the passive data include P-wave and S-wave from body waves and Rayleigh wave and love waves from surface waves, surface waves dominate in the ambient noise data (Kästle et al., 2016; Friedrich et al., 1998).

In comparison with active seismic methods and passive seismic methods with earthquake sources, the advantages of ambient noise interferometry are explained as follows:

1. There are some conditions where the acquisition of passive methods can be more successful and useful in comparison with active measurement. These are as follows (Hanssen, 2011): A. Where the explosive sources are forbidden, such as urban areas (Wathelet, 2005). B. Where we have limited access to vibro-trucks, streamers, and proper geophone lines for reasons such as protected jungles, mountainous regions, shallow depths of water, and glaciers. C. Where we have the weakness of active methods like imaging of sub-salts. D. Passive methods could be one of the solutions to preventing the plausible negative effects of active methods such as physical, auditory, and behaviorally-mediated damages on marine mammals like whales, dolphins, seals, and turtles (Gordon et al., 2003).

2. Surface waves in the period range from 5 s to 30 s cannot be detected by the teleseismic method, and the teleseismic method is more successful for mantle imaging. The observation of the ambient seismic noise method can provide

complementary information to the teleseismic method in this period range, which means the ambient noise method is more suitable for crustal and lithosphere imaging (Molinari et al., 2015; Boschi and Weemstra, 2015).

3. This method produces an S-wave velocity model where the active method cannot be easily implemented (Hanssen, 2011).

4. Ambient noise is always available while the occurrence of earthquakes is too rare. For this reason, ambient noise interferometry is sometimes more suitable for monitoring and investigating changes in structures such as faults (Gouedard et al., 2008).

Passive seismic interferometry has been widely utilized to image the crust and upper mantle in continental areas (Lin et al., 2007; Moschetti et al., 2007; Zheng et al., 2008; Yang et al., 2007). Nevertheless, there are few cases in oceanic regions, mainly because of the limited availability of seismic networks on the ocean bottom and the short duration of a vessel's deployment (Stewart, 2006; Harmon et al., 2007; Yao et al., 2011). Nevertheless, the industrial applications of passive seismic in oceanic regions are getting more popular (de Ridder, 2011; Bussat and Kugler, 2011; Mordret et al., 2013).

## 2.6 Passive seismic processing

### 2.6.1 Cross-correlation

The term "passive seismic interferometry" is defined as producing the new seismic responses of passive sources by cross-correlating the recorded passive data at different receiver locations. In fact, we need to do cross-correlation to estimate the empirical Green's function, which is considered a recorded seismogram at the location of one of the receivers due to an impulsive source at the location of another receiver. Because of the role of this empirical green function, the passive interferometry method is sometimes called Green's function retrieval (Wapenaar et al., 2010). In contrast to passive seismic interferometry, we have active seismic interferometry, which involves the summation of correlations over different source locations in addition to the receivers' cross-correlations (Schuster, 2001; Bakulin and Calvert, 2004). Shapiro and Campillo (2004) emerged as the first pioneers who represented the reconstruction of Green's function between seismometers distributed over the United States from the cross-correlation of long-recorded seismic noise data. The dispersion curves extracted from ambient noise were similar to those reconstructed from earthquakes.

Let us clarify the basics of cross-correlation using a simple example. We illustrate the cross-correlation by 1D analysis of direct waves, which directly arrive from source to receivers without any reflection. We consider an impulsive unit source and two receivers along the x-axis and the direction of propagation is rightward. The impulse source and receivers are located at $x_s$, $x_a$, and $x_b$, respectively, and with $t$ as the initial time of propagation, the recorded times at the receivers are $t_a$ and $t_b$ (Figure 2.9a). With regard to the assumptions, the responses of receivers to

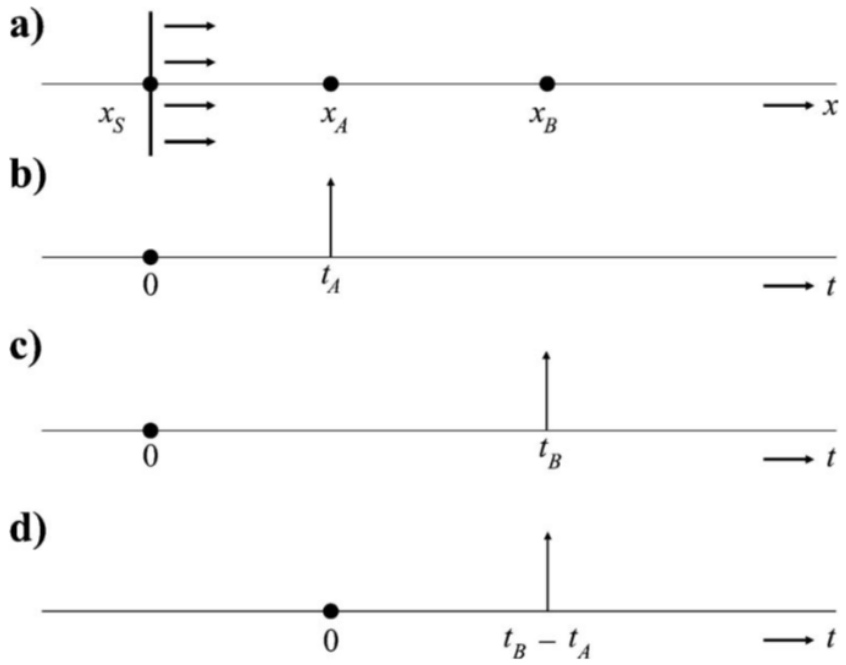


Figure 2.9: cross-correlation once the source is impulse unit. a) The location of the source and receivers. b) Recorded time at receiver $x_a$. c) Recorded time at receiver $x_b$. d) cross-correlation of responses of $x_a$ and $x_b$ (Wapenaar et al., 2010).

the source are denoted by Green's function as follows:

$$G(x_a, x_s, t) = \delta(t - t_a) \tag{2.5}$$

$$G(x_b, x_s, t) = \delta(t - t_b) \tag{2.6}$$

The delta denotes Dirac delta. The cross-correlation of responses at receivers $x_a$ and $x_b$ is defined as follows:

$$G(x_b, x_s, t) * G(x_a, x_s, -t) = \delta(t - (t_b - t_a)) = G(x_b, x_a, t) \tag{2.7}$$

This equation shows that the cross-correlation is equal to a new Green's function (right side of the equation), which is interpreted as the receiver $x_b$ recording the response of the source $x_a$.

Now suppose the source is a wavelet ($s(t)$) (see Figure 2.10). The response of receivers to the wavelet source is defined as below:

$$u(x_b, x_s, t) = G(x_b, x_s, t)s(t) \tag{2.8}$$

The cross-correlation of responses at the location of receivers results in:

$$u(x_b, x_s, t) * u(x_a, x_s, -t) * s(t) * s(-t) = G(x_b, x_a, t) * S_s(t) \tag{2.9}$$

where $S_s(t)$ is the wavelet's auto-correlation. Therefore, when we have a source function, the cross-correlation is equal to the green function between receivers, convolved with the auto-correlation of the wavelet.

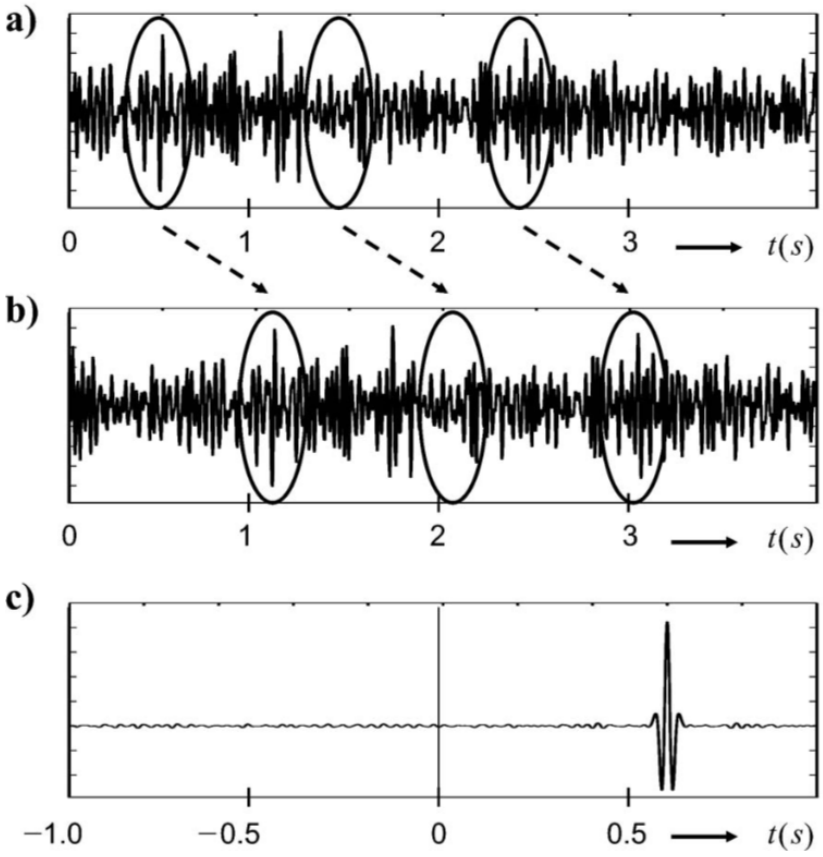


Figure 2.10: Cross-correlation once the source is a wavelet. a) The response observed at $x_a$ receiver. b) The response observed at $x_b$ receiver. c) correlation of $x_a$ and $x_b$ responses (Wapenaar et al., 2010).

### 2.6.2 Phase velocity determination

The comparison between the empirical Green's function and the theoretical Green's function is analyzed in different ways with the final purpose of obtaining information about the subsurface between two receivers (Boschi et al., 2012). Most scientists either extract group velocity from the peak of the surface waves (Shapiro et al., 2005; Stehly et al., 2006, 2009) or measure phase velocity in dispersion curves or on maps (Lin et al., 2008; Ekström et al., 2009). Fewer scientists preferred to utilize full waveform for analysis of passive seismic data (Tromp et al., 2010). However, both phase and group velocity have been used to get S-wave velocity models (e.g., (Molinari et al., 2015), but phase velocity is the preferable method for modeling because of the following advantages (Kästle et al., 2016):

- Obtaining the group velocity from the peak of the envelope in a surface wave is less precise than measurements of phase velocity.
- Phase velocity is more useful for imaging deeper structures (Boschi et al., 2012).
- Phase velocity is less contaminated by interfering phases since measurements are done in wider time windows (Molinari et al., 2015).

Several methods for measuring phase velocity have been proposed, including the

image transformation technique in the time domain (Yao et al., 2006), the method based on the time delay between stations in the time domain (Bensen et al., 2007), Frequency-wave number (F-K) method (Lacoss et al., 1969; Capon, 1969), multiple filter analysis (Herrmann, 2013), Bessel function matching with the usage of zero-crossing in the frequency domain (Ekström et al., 2009; Ekström, 2014; Aki, 1957), zero-crossing with regard to attenuation (Prieto et al., 2009), zero crossing with vertical-vertical (ZZ) and vertical-radial (ZR) components (Haney et al., 2012), Waveform fitting of Aki formula in the frequency domain (Menke and Jin, 2015). We use the Bessel function matching with the usage of zero-crossing introduced in (Kästle et al., 2016). Before cross-correlation, the signals are filtered in the proper frequency range, which can decrease the sampling rate and speed up the processing. For cross-correlating, the signal is cut into overlapping time windows (e.g., 30 minutes) with an overlapping range of 1 to 99 percent. More complete explanations of the effects of overlapping time windows can be found in (Seats et al., 2012). A cosine tapper is applied at both ends of the signal. Moreover, spectral whitening is implemented to equalize the amplitudes and down-weight the effects of earthquake signals. However, it is notable that the removal of the earthquake signal has negligible effects on the phase velocity determinations (Kästle et al., 2016).

The theoretical Green's function is estimated by cross-correlating the vertical displacement of one station pair given in equation (7.144) of Aki and Richards (2002), which is a multiplication with conjugate complex, with assumptions that the ambient noise is dominated by fundamental mode, the amplitude is normalized according to Snieder (2004) and we have a large number of sources. After some simplifications, the theoretical Green's function (theoretical cross-correlation) in the frequency domain and in terms of the Bessel function is defined as follows (Ekström et al., 2009):

$$C(\omega) \approx (A(\omega))^2 J_0(\frac{\omega\Delta}{c(\omega)}) \tag{2.10}$$

where $\omega$ is frequency, phase velocity is indicated by c. and amplitude is shown by A. $J_0$ is Bessel function which is variant with the inter-station distance $\Delta$, frequency and phase velocity. The empirical Green's function is determined by the cross-correlation of ambient noise data between station pairs. The real part of equation 2.10 is supposed to be equal to the real part of cross-correlation. The importance of equation 2.10 is that by having the real part of the cross-correlation of recorded ambient noise and the distance between station pairs, we will be able to estimate the phase velocity. This real part often generates the additional zero-crossings in the cross-correlation spectrum and, consequently, velocity jumps in phase velocity measurement (see Figure 2.11A in frequency 0.038 Hz). For this reason, a smoothing filter was recruited to overcome this problem (red curve in Figure2.11A). The zero crossing of this smooth curve is identified and compared with the Bessel function. With regard to the proposed method in (Ekström et al., 2009), whenever the cross-correlation is zero (or we have zero-crossing), for every discrete frequency, we can derive all the possible phase velocities. The final goal is to choose the most realistic dispersion curve by picking the right phase velocity

(red curve in Figure 2.11B). The least ambiguity is discovered at the low-frequency end, where only a few probable phase velocities take place in a realistic range (Kästle et al., 2016). In order to choose the most likely value, we can be guided by a reference model (yellow curve in Figure2.11A). This reference model can be estimated from previous studies or by the average dispersion curve of a couple of station pairs in the region.

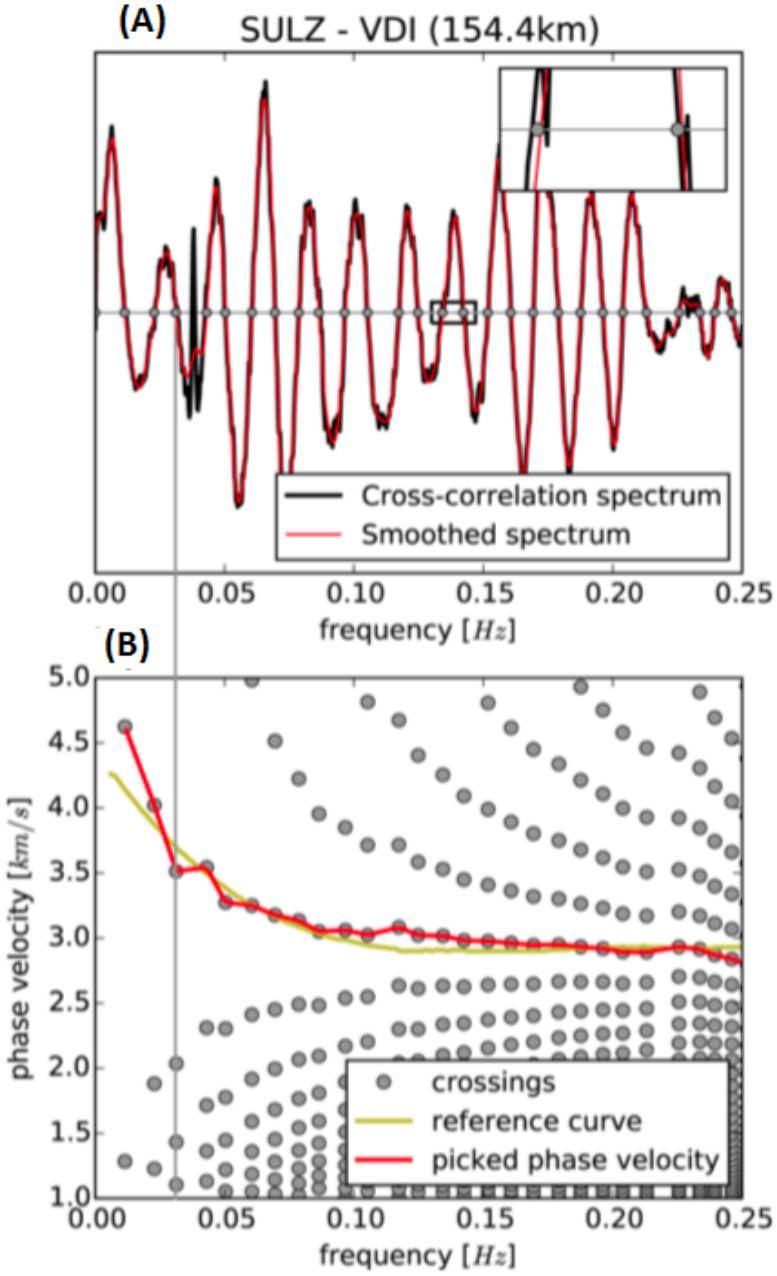


Figure 2.11: A) Processing of ambient noise Cross-correlation. In the real part of Cross-correlation, the original spectrum is black, and smoothed version is red. A clear peak is seen at 0.038 Hz, which is not related to the rest of the spectrum and is ignored by smoothing. B) Phase velocities from the zero crossing spectrum, are shown in gray circles, and the picked phase velocity has been shown in red. The reference curve in yellow usually helps to pick the right curve (Kästle et al., 2016).

## 2.7 Passive seismic tomography

The dispersion curve of surface waves can be used to obtain the Vs versus depth through an inversion (Wathelet, 2005; Herrmann, 1994). The derivation of Vs model used to be solved by linearized approaches of inversion (Nolet, 1981; Tarantola, 1987). However, the strong non-linearity in the inversion of the dispersion curve has proposed the usage of non-linear inversion methods such as the grid spacing methods, gradient methods, Newton's methods, Monte Carlo methods, simulated annealing methods, and neighborhood algorithms (Menke, 2018; Wathelet, 2005). Our dispersion curve inversion is based on the conditional neighborhood algorithm. Its objective is to sample all the regions of the parameter space.

As in other Monte Carlo methods, we have to pre-define a range of priors for the pseudo-random sampling approach. The range of statistical speculation and the role of prior information in this method are discussed in articles such as (Scales and Tenorio, 2001) and (Mosegaard and Tarantola, 1995). The parameter space of this approach is limited to a volume defined by the parameter prior ranges. All the generated models take place in this defined volume (Wathelet, 2005). Compared to other Monte Carlo approaches, the conditional neighborhood algorithm is more self-adaptive when searching through the parameter space. The search starts with a pre-defined number ($n_{s0}$) of models distributed with a uniform probability in parameter space. The misfit function ($L_2$ norm) is calculated for every model and the $n_r$ models with the lowest misfits are selected for the next iterations. This is iterated $n_t$ times, and at each iteration the selected lowest-misfit models are decomposed into $n_s/n_r$ new models. The data misfit is given in relative units, normalized by the input data. In the conditional neighborhood algorithm, the dependency between parameters is taken into account at the beginning of the inversion by using a variable transformation (Wathelet, 2005).

The model is parameterized in terms of thickness, shear wave velocity (Vs), compressional wave velocity (Vp), and density ($\rho$) for each layer. Among them, Vs has the most important role and $\rho$ exercises the least influence on the dispersion curve. The Poisson's ratio, links Vs and Vp, according to the value of Poisson's ratio for geological materials (Wathelet, 2005). Vp and Vs are free parameters of the inversion. The Poisson's ratio is not a free parameter, but if a solution is generated with Vp and Vs such that the value of the Poisson's ratio is outside of the allowed range, that solution is discarded. An example of inversion for S-wave velocity can be found in Figure 2.12.

## 2.8 Processing of active seismic data

Active seismic data can be corrupted by noise originating from different types of sources. This noise can be categorized into two main groups (Yilmaz, 2001): coherent noise and random noise (incoherent noise). If the noise is distinguished from the signal by one of its characteristics, such as amplitude, frequency band or velocity, then it is easier to attenuate the noise while preserving the signal (Dondurur, 2018).

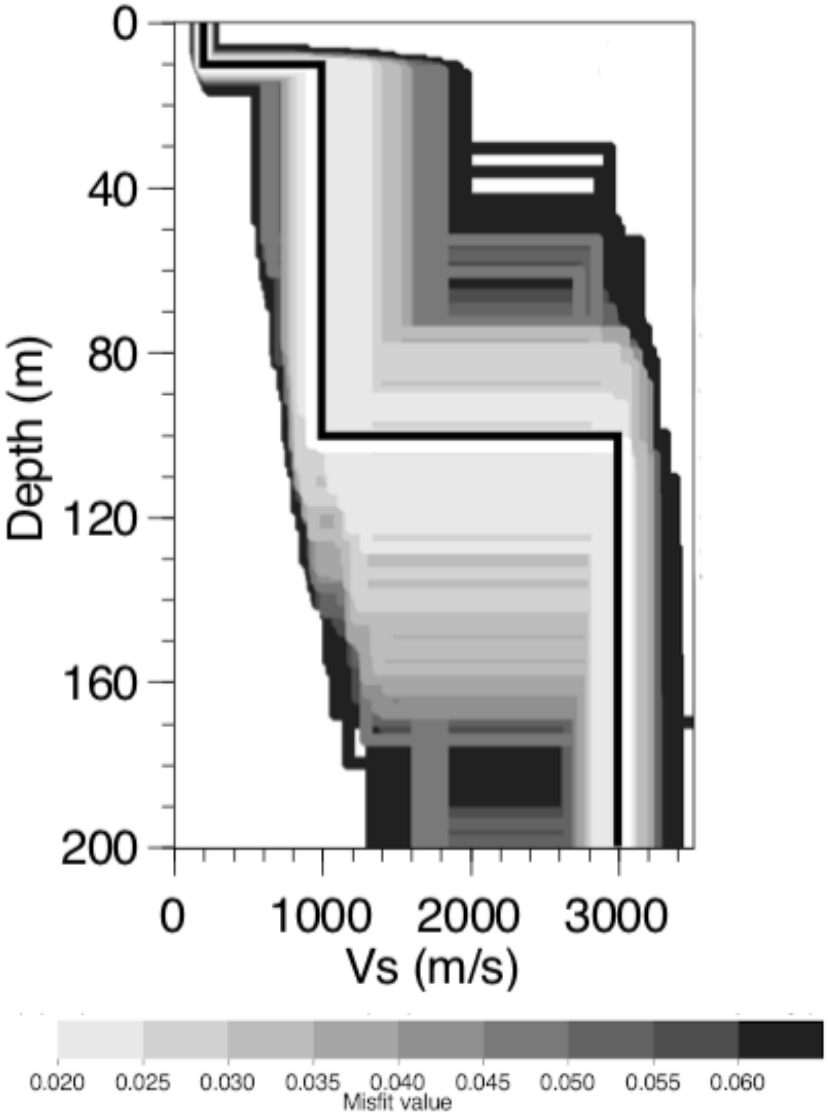


Figure 2.12: Synthetic example of inversion result for S-wave velocity. The black line is the theoretical velocity model (Wathelet, 2005).

Disturbances without phase coherency between consecutive traces of seismic data are considered random noise. Such disturbances are usually not related to the seismic source. Instruments, near-surface scatterers, rain, and wind can be sources of random noise. Coherent noise is the disturbance that is produced by a seismic source. Coherent noise appears with a consistent phase between adjacent traces. Examples of coherent noises are multiples, surface waves like ground roll, airwaves, and coherent scattered waves (Mousa and Al-Shuhail, 2011). Seismic data processing, in principle, cannot remove all noises interfered with in the seismic signal. Therefore, the objective of processing is to increase the signal-to-noise ratio (SNR) by using adapted approaches.

### 2.8.1 Frequency filtering of noise

The swell noise is the most dominant disturbance in the marine seismic data. It mainly originates from weather conditions that generate wind–driven longitudinal sea surface waves. Swell noise is a type of incoherent noise that interferes in the amplitude spectrum's low-frequency band (Dondurur, 2018). Marine seismic data can also be contaminated by high-frequency noise produced from electrical cables or heavy machines (Asghar, 2011). To mitigate the effects of noise on the signal, a frequency filter is designed and applied to the data (Yilmaz, 2001). The application of frequency filtering requires the conversion of data from the time domain into the frequency domain (amplitude as a function of frequency). This conversion is implemented by using a Fourier transform. The frequency filtering is based on the multiplication of converted data into the designed filter. The conventional filters in the data processing are low-pass filter, high-pass filter, band-pass filter, and band stop filter (Figure 2.13). A low-pass preserves low frequencies. A high-pass filter retains high frequencies. The band pass and band stop contain and suppress the frequencies within a defined range of frequency, respectively (Sheriff and Geldart, 1995; Asghar, 2011). The band-pass filter is by far the most common filter used.

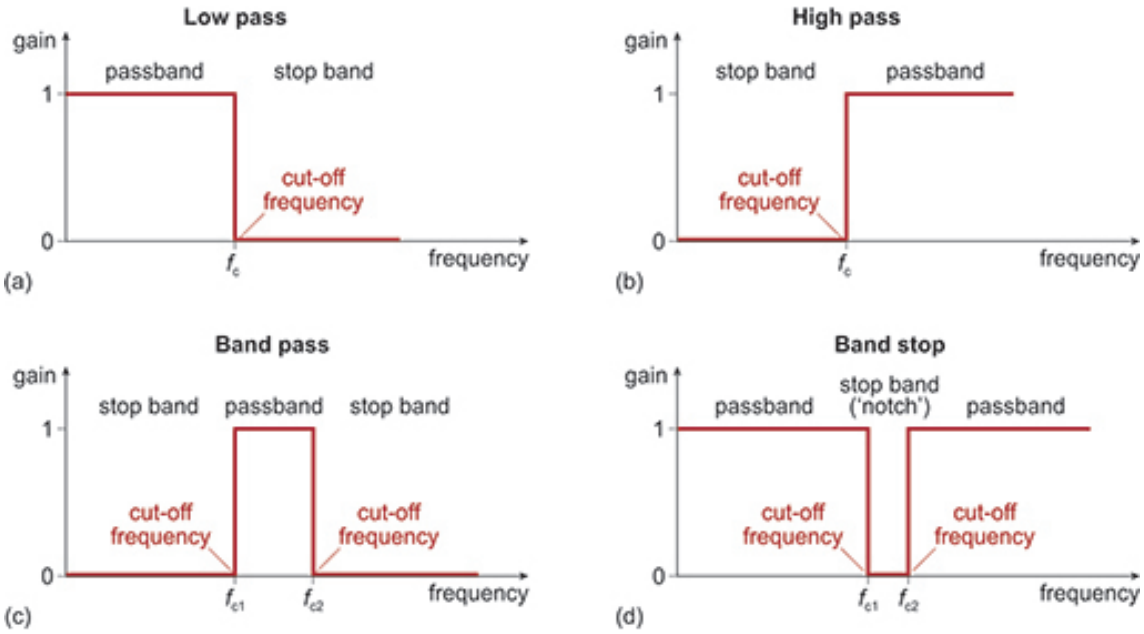


Figure 2.13: Four typical filters. (a) Low-pass(b) High-pass (c) band-pass(d) band-stop (Allan Jones and Picton, 2020).

In general, it is better to use a smooth version of a band-pass filter to avoid the undesired ringing in the signal in the time domain (known as the Gibbs effect). This effect is easily produced with Ormsby filters by determining unrealistic steep slopes taken from four corner frequencies (like Figure 2.13c). Band-pass filters increase the overall gain of each seismic shot gather and consequently the SNR ratio. An example of band-pass filtering has been shown in the frequency domain in Figure 2.14. We can see the effects of band-pass filtering on the raw seismic data in Figure 2.15.

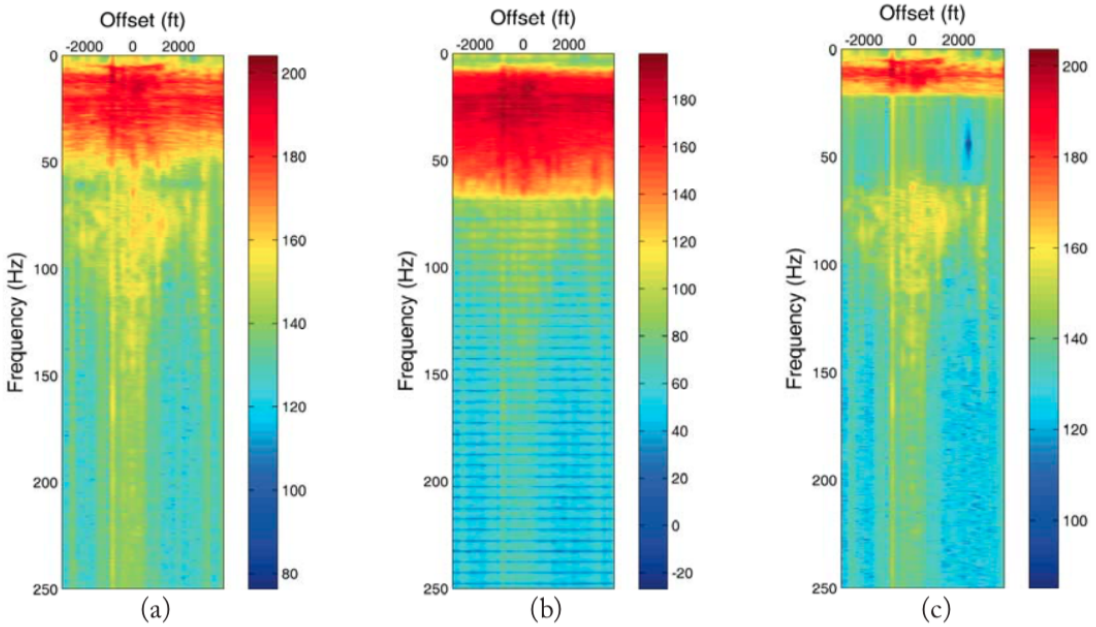


Figure 2.14: Amplitude spectrum of seismic data in the frequency domain (F-X magnitude spectra). (a) Before band-pass filtering. (b) After band-pass filtering (c) the difference between raw data and filtered data (Mousa and Al-Shuhail, 2011).

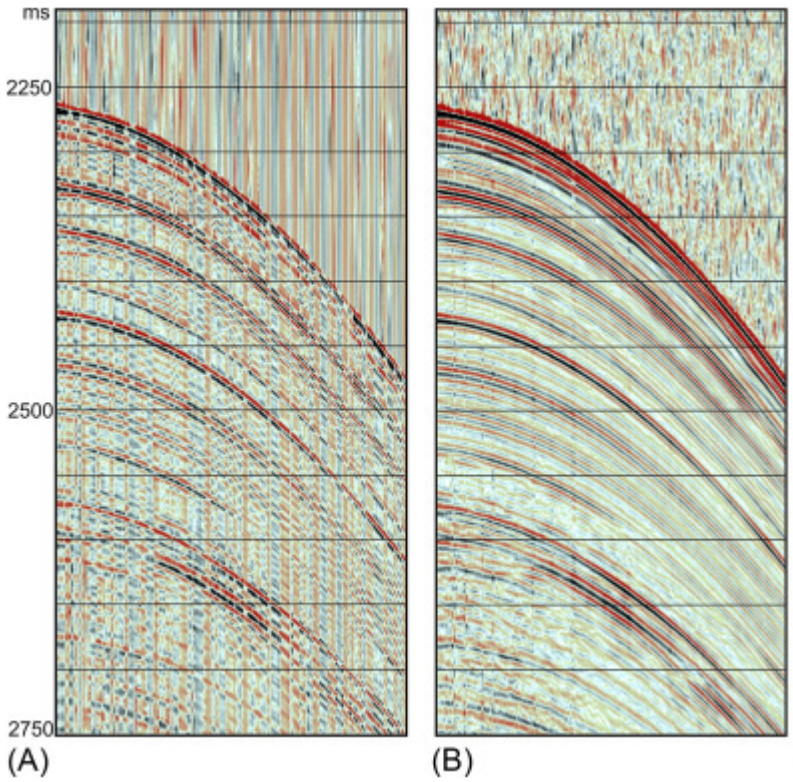


Figure 2.15: Seismic data in the time domain. (A) Before band-pass filtering. (B) After band-pass filtering (Dondurur, 2018).

## 2.9 Active seismic imaging by full waveform Inversion

The full waveform inversion (FWI) is a technique in which the computed shot gather attempts to reproduce the observed shot gather in order to gain an optimal model (here, the P-wave velocity model). However, while the concept seems to be easy, the practical application of the FWI is a hard procedure. We may encounter some difficulties as follows (Bishop et al., 1985; Billette and Brandsberg-Dahl, 2005; Operto et al., 2013; Chauris, 2021):

- The process is non-linear.
- Having a proper initial model is important.
- The quality and accuracy of the final inverted model are really dependent on the low-frequency range of observed data.
- Lack of data in the frequency range or limited data due to the acquisition causes an aliasing problem.
- Wave equation inaccuracies in generating synthetic seismographs due to approximations, in theory, such as grid dispersion in finite difference schemes, a simplified earth model such as a 1-D model or 2-D for a 3-D structure, and ignoring anisotropy or attenuation.

The first configuration and formalism of FWI were created by Tarantola and his group (Tarantola, 1984; Mora et al., 1987). The new perspective for the applicability of FWI to MCS data was proposed by (Sirgue and Pratt, 2004). Their strategy was to begin the inversion at low frequencies and gradually refine the modes of higher frequencies. At first, the concentration of FWI was on the 1D velocity model. Nevertheless, the advancement of computer facilities and progress in data acquisition has extended the application of FWI to 2D models (Operto et al., 2006; Arnulf et al., 2011), and recently to 3D models (Plessix et al., 2013; Raknes et al., 2015). FWI has experienced the development from acoustic medium to elastic and visco-elastic mediums, including the context of anisotropy and attenuation parameters (Chauris, 2021).

### 2.9.1 Theory of FWI

The objective of FWI is to find a velocity model that minimizes the least-squared difference between observed data and calculated (synthetic) data. The least-squares misfit function is defined as follows (Chauris, 2021):

$$J(m) = \frac{1}{2} \left\| d_{cal}(m) - d_{obs} \right\|^2 \tag{2.11}$$

where m is the model and it is a function of spatial coordinates. $d_{obs}$ is the observed data. The calculated data set, $d_{cal}$, denotes the solution of the wave equation and is a function of the model. The general form of the wave equation is as follows:

$$L(m) d_{cal}(s, r, t) = \delta(s - r)\Omega(t) \tag{2.12}$$

where $L$ represents the wave equation operator, $\Omega$(t) represents the seismic source, and $\delta$ represents the Dirac distribution. There are three important parameters to evaluate the quality of the obtained models: 1. Choosing a model of the elastic parameters of the medium of propagation 2. Selection of seismic source 3. Forward model resolution (Louboutin et al., 2018). In general, two strategies can be used to determine the models in FWI. The first strategy is global search methods such as Monte Carlo and genetic algorithms (Sajeva et al., 2016). These approaches would be advantageous if the model space's unknown parameters were small, but in reality, the model space is discretized along the axes (x, y, and z) with millions of unknown parameters. Moreover, the CPU cost of this strategy is quite expensive (Raknes et al., 2015). The second strategy, which is more practical, is local search methods (Shipp and Singh, 2002). This approach determines the model iteratively through the calculation of the gradient of the misfit function (Tarantola, 1987; Plessix, 2006). The starting model of this strategy is usually determined based on a standard tomography model. The gradient of the misfit function is defined as the derivative of the misfit function with regard to the model parameters (Chauris, 2021). The iterative procedure of this approach is as follows:

$$m_{n+1} = m_n - \alpha \frac{\partial J}{\partial m} \tag{2.13}$$

where the number of iterations is n, the gradient of the misfit function is $\frac{\partial J}{\partial m}$, and $\alpha$ represents a positive scalar length step. $\alpha$ is assessed at each iteration like the method of (Pica et al., 1990). In parallel with the objective of FWI, the gradient of the misfit function indicates the direction that the misfit function is minimized (Shipp and Singh, 2002).

The gradient for each source location can be calculated in three steps: 1. Solving wave equation 2.12 to obtain shot gathers for every source ($d_{cal}$). 2. calculating $\lambda$ = $d_{cal}$ - $d_{obs}$ for every source, which is the backward residual (in time) between $d_{cal}$ and $d_{obs}$. 3. The gradient is derived from the cross-correlation of $\lambda$ and $d_{cal}$ with the sum of all times (Shipp and Singh, 2002).

FWI can be performed either in the time domain or in the frequency domain (Virieux and Operto, 2009; Raknes and Arntsen, 2017). As long as we include the full range of frequencies, both domains lead to the same results. As a result, the misfit function for both domains will be the same (Chauris, 2021):

$$J(m) = \frac{1}{2} \left\| d_{cal}(m)[t] - d_{obs}[t] \right\|^2 = \frac{1}{2} \left\| d_{cal}(m)[\omega] - d_{obs}[\omega] \right\|^2 \tag{2.14}$$

where t and $\omega$ represent time and frequency domains, respectively. However, the computational cost of the frequency domain is lower, the selection of frequency range is the drawback of this domain (Shoja et al., 2018). Therefore, the inclusion of more complete data in the time domain could bring more robust results (Freudenreich and Singh, 2000). Moreover, temporal windowing, which proved to be an important step in the inversion of real data, is more difficult in the frequency domain.

### 2.9.2 Forward modeling

In order to obtain the calculated data, we have to solve the wave equation introduced in 2.12. Depending on our interest, the wave equation operator can be different. For example, if we are going to consider the attenuation factor, the wave equation should be written with visco-acoustic or visco-elastic terms. The elasticity should be considered as long as surface wave analysis is of interest (Chauris, 2021).

2D wave equation for elastic and isotropic medium (x horizontal and z vertical axis) in terms of velocity ($v_x$, $v_z$) and components of stress tensor ($\tau_{xx}$, $\tau_{xz}$, $\tau_{zx}$, $\tau_{zz}$) is written as follows (Levander, 1988):

$$\begin{aligned} \rho\frac{\partial^2 v_x}{\partial t^2} &= \frac{\partial \tau_{xx}}{\partial x} + \frac{\partial \tau_{xz}}{\partial z} \\ \rho\frac{\partial^2 v_z}{\partial t^2} &= \frac{\partial \tau_{zx}}{\partial x} + \frac{\partial \tau_{zz}}{\partial z} \end{aligned} \tag{2.15}$$

The components of the stress tensor for the mentioned medium are written:

$$\begin{aligned} \tau_{xx} &= (\lambda + 2\mu)\frac{\partial v_x}{\partial x} + \lambda\frac{\partial v_z}{\partial z} \\ \tau_{zx} &= \mu(\frac{\partial v_x}{\partial z} + \frac{\partial v_z}{\partial x}) \\ \tau_{zz} &= (\lambda + 2\mu)\frac{\partial v_z}{\partial z} + \lambda\frac{\partial v_x}{\partial x} \end{aligned} \tag{2.16}$$

where $\lambda$ and $\mu$ are Lame parameters. To have a better comprehension of the stress tensor, look at figure A.4. The equations 2.15 and 2.16 are first-order coupled equations for particle motion, stress, and velocity.

Different numerical methods have been introduced to find the solutions of differential equations:

1. Volumetric methods such as finite-difference approaches (Virieux, 1986; Levander, 1988), finite-element methods (Marfurt, 1984; Min et al., 2003), finite-volume (Brossier et al., 2008) and pseudo-spectral methods (Danecek and Seriani, 2008).

2. Boundary discretization methods such as boundary integral methods (Kennett, 1983), discrete wave-number methods (Bouchon et al., 1989) and generalized screen methods (Wu, 2003).

3. Generalized ray methods (Popov, 1982; Chapman et al., 1985; Klem-Musatov et al., 1985).

Solving the coupled set of equations 2.15 and 2.16 is performed by the finite-difference method with discretization on a grid. Our preferred method was introduced in (Levander, 1988) based on a staggered grid with a scheme of second order in time and fourth order in space. The finite difference is one of the most efficient and flexible numerical methods which is used in solving wave equation (Cao and Greenhalgh, 1992). Alterman and Karal Jr (1968) and Boore (1972) were the first pioneers of the finite-difference method and the accuracy and capability of the

method were developed by Madariaga (1976) and Levander (1988). The coupled set of equations includes spatial and temporal derivatives. The calculation of the spatial derivatives and temporal derivatives of the first mentioned equation is obtained on the grid as follows:

$$D_t^+ v_x(m,n,l-1/2) = 1/\rho(m,n)[D_x^- \tau_{xx}(m+1/2,n,l) + D_z^- \tau_{xz}(m,n+1/2,l)] \tag{2.17}$$

where $D_x^+$ and $D_x^-$ are forward and reverse finite-difference operators in the space domain. $D_t^+$ is a forward operator in the time domain. The density and vertical velocity are specified in (n, m) on the grid. We can have a similar approach for other equations. The location of density and horizontal velocity is (m+1/2, n+1/2). The normal stresses and Lame parameters are defined at the location (m+1/2, n). Shear stress and $\mu$ are at (m, n+1/2). Vertical and horizontal velocities are on the time levels l-1/2 and l+1/2. Stress components are defined on the time levels l and l+1 (Levander, 1988).

In the finite-difference method, the time and space increment on the grid cannot be random, and the increment should satisfy the dispersion and stability conditions. If we define the space increment along the x and z axis by $\Delta x$ and $\Delta z$ and we define the time increment by $\Delta t$, the dispersion and stability conditions are written as follows, respectively (Levander, 1988; Chauris, 2021):

$$\Delta x = \Delta z \leq \frac{1}{5}\frac{v_{min}}{f_{max}} \tag{2.18}$$

$$\Delta t \leq 0.606\frac{\Delta x = \Delta z}{v_{max}} \tag{2.19}$$

The space increment $\Delta x$ or $\Delta z$ in the stability equation dispersion condition should be 5 times smaller than the minimum wavelength, defined by the minimum expected velocity and maximum frequency. Five grid points per wavelength is a good improvement in comparison with the schemes of Virieux (1984) and Kelly et al. (1976). As long as the dispersion condition is not met in finite difference, the dispersion can be seen on the signal. Notice that for a larger value of maximum frequency, the grid increment must be smaller, and, consequently, more storage and a stronger CPU will be needed. The stability equation 2.19 is a function of maximum velocity. Not satisfying this condition can lead to unprofitable information (Chauris, 2021).

The other two significant conditions in finite-difference modeling of wave propagation are the free-surface condition and the boundary condition. The free-surface condition must be satisfied at the top of the model space. This condition is applied at the surface (z = 0) with zero vertical stress, which means that $\tau_{zz}$and $\tau_{zx}$in the equation 2.16 are both zero (Lan and Zhang, 2011). However, different methods have been presented to deal with zero vertical stress equations. Our approach is based on a Levander (1988). A boundary condition is applied to prevent spurious reflections from the boundaries on the modeled data. To mitigate this problem, we followed the approach proposed by Martin and Komatitsch (2009).

# Chapter 3

# Geological and geophysical backgrounds of Study area


## Summary

In this chapter, we present the geological features and geophysical studies of SWIR. Detachment fault systems are explained because of their main role in the low melt supply of the region. The context is continued with serpentinized peridotite on the seafloor ascribed to exhumation in the footwall of the detachment faults. We also provide some information about the role of the seismic method in determining serpentinization and melt supply.


## 3.1 Crustal accretion models in ultra-slow spreading ridges

The plate separation at the slow-spreading ridges can be accommodated by two contrasting mechanisms of accretion. If the melt supply is enough, the magmatic spreading is dominant and produces a thick igneous crust. Plate divergence in the center of most slow and ultra-slow spreading ridges is a result of the volcanic injection and moderate offset faults (see Figure 3.1A). Therefore, more volcanic rocks might be seen on the seafloor of axial domains (Smith and Cann, 1999). In contrast, at segment ends and segments with poor melt supply, the plate separation is mainly accommodated through detachment fault systems (see Figure 3.1B). The detachment fault systems were proposed to explain the presence of ultramafic rocks in the ultra-slow spreading ridges. They bring mantle-derived ultramafic rocks on the seafloor through the axial lithosphere (Cannat, 1993).

The mechanism or mode of spreading has a large effect on the lithology of the crust and upper mantle, the chemical interaction between the ocean and the solid earth, as well as the biology of the seafloor (Cannat et al., 2019). Seismic studies of Vp and Vs velocities in most mid-ocean ridges (including slow ridges with rich melt supply) suggested that the oceanic crust is composed of mafic rocks located on the underlying upper mantle peridotite. In this case, the Moho is a petrological boundary (Carlson, 2001). In more detail, at the Penrose conference, the layer model of the ocean lithosphere was proposed based on seismic studies and seafloor dredging. According to the Penrose model, layer 1 of the oceanic crust

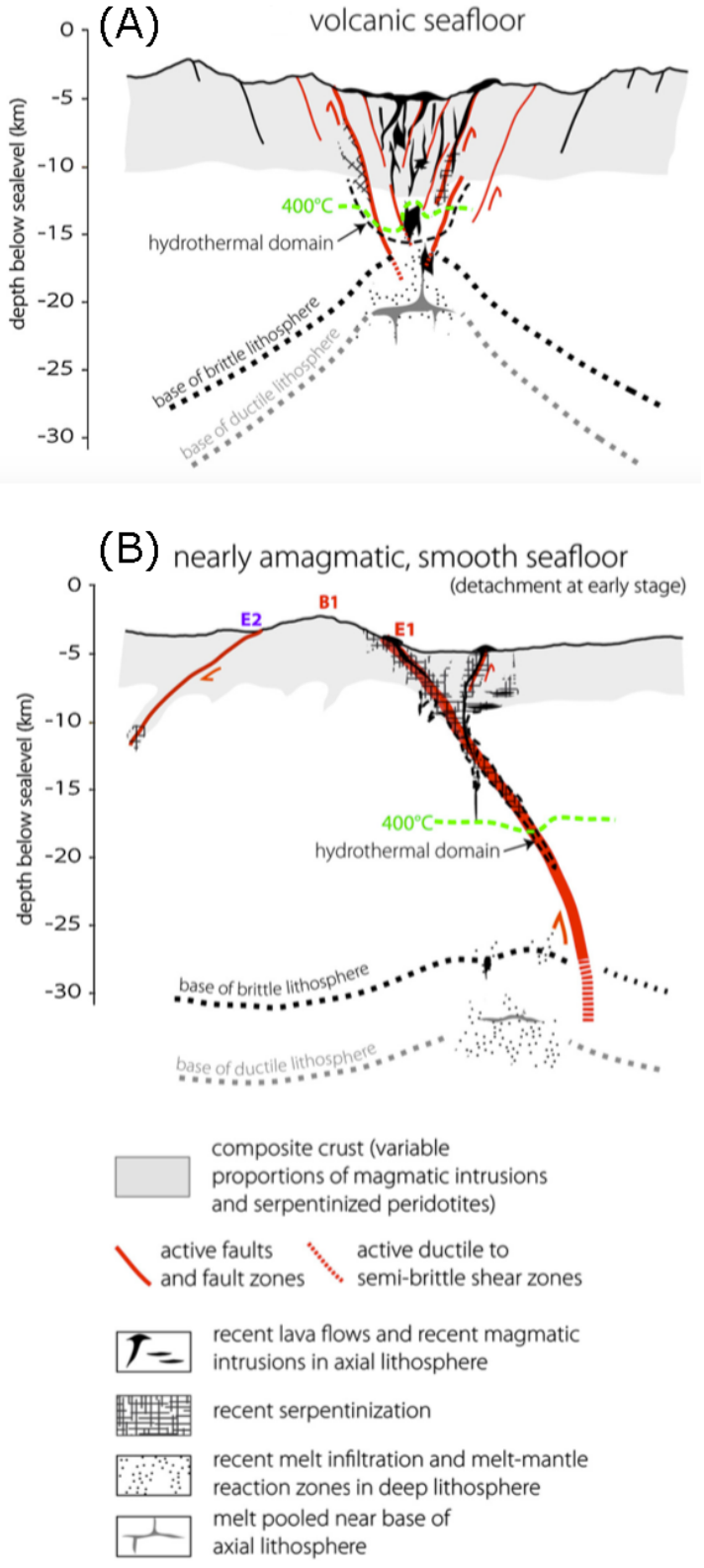


Figure 3.1: Spreading modes at slow and ultra-slow spreading ridges: A) Magmatic spreading mode. A combination of magma injection and several moderate normal offset normal faults accommodate the plate divergence and the seafloor exposes magmatic rocks. B) detachment-dominated spreading mode. The detachments fault system brings mantle-derived ultramafic rocks up through the axial lithosphere and creates smooth seafloor. B and E are the breakaway and emergence of fault system (Cannat et al., 2019).

is sediment. Layer 2 of the oceanic crust includes basalt, either intruded as dikes or extruded on the seafloor as pillow-lava. Layer 3 consists of basalt and gabbro, and layer 4 is the upper mantle, consisting of peridotite. Layer 4 separates from layer 3 through a seismically defined Moho at a depth of around 6 km beneath the seafloor (Mével, 2003) (see Figure 3.2left). The crust formed at ultra-slow spreading ridges with poor melt supply does not follow the proposed model of Penrose and a heterogeneous structure is specified (Cannat et al., 1995). In ultra-slow spreading ridges, the abundance of partially serpentinized peridotites in the oceanic crust is more compatible with the introduced model by Dietz (1963); Hess et al. (1962); Hess (1965). In this model, the oceanic crust is composed of partially serpentinized peridotites with gabbros inclusions and is separated from the upper mantle by peridotites (see Figure 3.2right). So, the Moho is supposed to be a phase transition between the crust and the upper mantle.

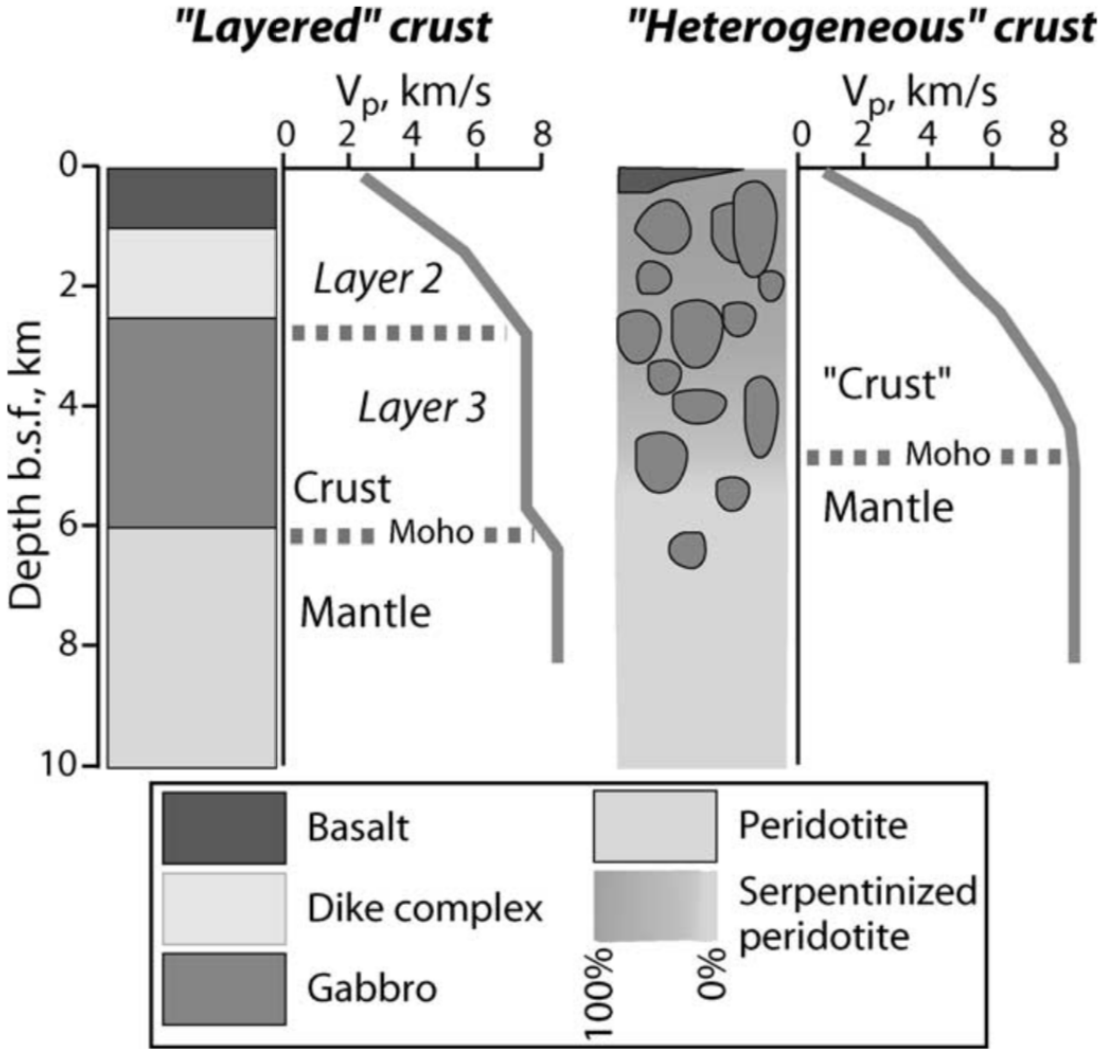


Figure 3.2: Left: Geological Penrose layered model and seismic P-wave velocity model proposed for the oceanic crust and upper mantle of mid-ocean ridges with richer melt supply. Right: a geological heterogeneous model and a seismic P-wave velocity model are proposed for the oceanic crust and upper mantle at slow and ultra-slow mid-ocean ridges with low melt supply (Mével, 2003).

## 3.2 Detachment fault systems and oceanic core complexes

The initial conceptual models of detachment faults with the role of exhumation were introduced in Dick et al. (1981); Brown and Karson (1988); Karson (1990). Among the indicated faults in Figure 3.3 detachment faults are considered in the normal group. In the detachment fault system, uplifted footwalls in slow-spreading ridges are known as oceanic core complexes or Magamullions. Detachment faults or normal faults with large offsets initiate at steep dips. After a while, the footwall of the faults rotates over a hing to be flat in response to a flexural failure and then they create oceanic core complexes (Lavier et al., 1999; Pressling et al., 2012). We show schematically in Figure 3.4 how normal faults with large offsets form oceanic core complexes and exhume the lower crust and upper mantle at the ridge. However, in this figure, we are showing that oceanic core complexes form when a zero rate of magma is injected into the lithosphere (pure amagmatic process). Recent geological, geophysical, numerical, and modeling studies suggest that detachment faulting can occur when 30–70 percent of plate divergence is due to moderate melt supply (magmatic process) (Cannat et al., 1995; Dick et al., 2008; Buck et al., 2005; Tucholke et al., 2008; Cannat et al., 2019). Oceanic core complexes are so significant because they contribute up to 60 percent of the new seafloor at intermediate to slow-spreading ridges (Smith et al., 2006, 2008; Olive et al., 2010). Figure 3.5 shows the global distribution of the exhumed footwall of detachment fault systems (oceanic core complexes) in slow and ultra-slow spreading ridges.

To comprehend the relative contributions of melt supply and faulting in the detachment fault systems, one could use the M factor introduced by Buck et al. (2005). This factor is defined as the proportion between melt supply through dike intrusion and plate separation. For M = 0, melt supply accounts for none of the plate separations, and for M = 1, melt supply accommodates all of the plate spreading. It was shown by numerical modeling of slow-spreading ridges that when M = 0.95 (Buck et al., 2005) and in general, M > 0.5 (Tucholke et al., 2008), a symmetric axial valley with nearly symmetric inward-dipping small-offset faults is observed (see Figure 3.6A). These small-offset faults thickened with the distance from the ridge axis and finally break on the opposite side. This break creates symmetric abyssal hills in the mid-ocean ridge (see Figure B.1). Under the condition M = 0.5, two large offset faults (20-30 km) on one side and a bunch of small-offset faults were modeled on the other side of the spreading axis. Almost all the magmatic accretion takes place on the side with a series of small-offset faults. The modeled structures with M = 0.5 are like the observed oceanic core complexes in over 20 ridge-transform intersections on slow-spreading ridges (Buck et al., 2005; Momoh et al., 2017). As M is reduced by less than 0.5, the hanging wall of large-offset faults moves toward the outside of the axial domain. This characteristic tends to induce the initiation of new faults and flip the polarity (you can see Figure 3.4 and Figure B.2 defined in (Platt et al., 2015)).

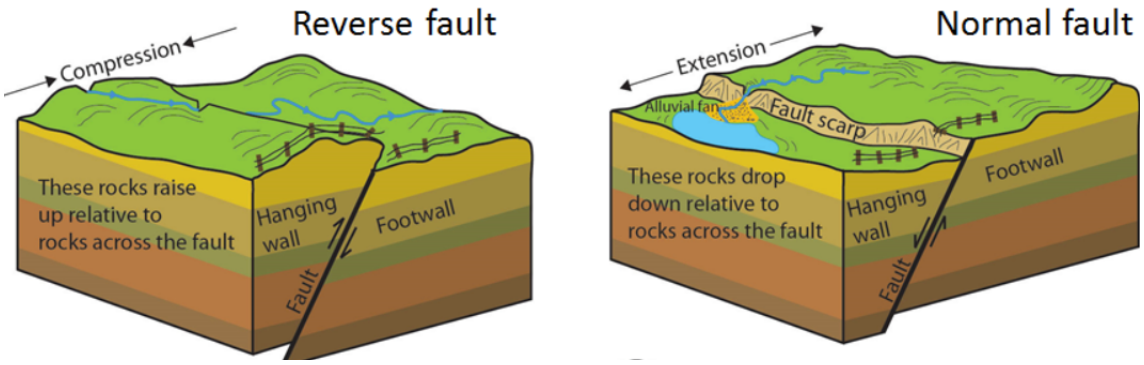


Figure 3.3: Fault types: 1. normal, 2. reverse, and 3. transverse. The detachment fault system is a normal fault (Earle, 2019). To have a better understanding of the detachment fault system, the main components of normal faults have been reported as follows: A) Fault plane: it is a surface that has two parts of the fault moving on it. B) Footwall and hanging wall: two sides of faults are the hanging wall and the footwall. In normal faults, the footwall is on the upper side and the hanging wall is on the lower side. C) Fault scarp: it is a small offset of the ground surface where one side of the fault has moved vertically.

## 3.3 Ultramafic rocks of crust in slow-spreading ridges

Mafic rocks and a significant amount of ultramafic rocks are present in slow and ultra-slow spreading ridges. First, let's look at the basic concepts of igneous rocks to understand the difference between mafic and ultramafic rocks. Chemical analysis proved that igneous rocks have abundant silicate oxides. Igneous rocks are differentiated based on this characteristic, and in terms of increasing the order of silica content, they are classified into four groups: ultramafic, mafic, intermediate, and felsic (Britannica, 2020). Felsic rocks are igneous rocks that contain more than 66 percent silica. Intermediate rocks have a silica content of 52–66 weight percent. They are called mafic with 45–52 weight percent silica, and those with less than 42 weight percent silica are ultra-mafic (Rakovan, 2009). The two most common mafic rocks are gabbro and basalt, and the most common ultra-mafic rock is peridotite, which includes mostly the silicate minerals olivine and pyroxene.

## 3.4 Serpentinization in slow-spreading ridges

The serpentinization reaction in the crust of slow-spreading ridges occurs when the upper mantle peridotite interacts with seawater at temperatures under ∼450°C (Albers et al., 2021). This reaction forms serpentinite. The main and initial consequence of the hydration of the mantle is serpentinization. The volume of consumed water is often utilized as an approximation to determine the degree of serpentinization (Mével, 2003).

The knowledge of the spatial distribution and intensity of serpentinization in the crust of slow-spreading ridges has been of great interest for the following reasons:

- The consequences of serpentinization on the environment and geodynamics are significant (Rouméjon and Cannat, 2014).
- It changes the rheology of the oceanic lithosphere (Reinen et al., 1994).

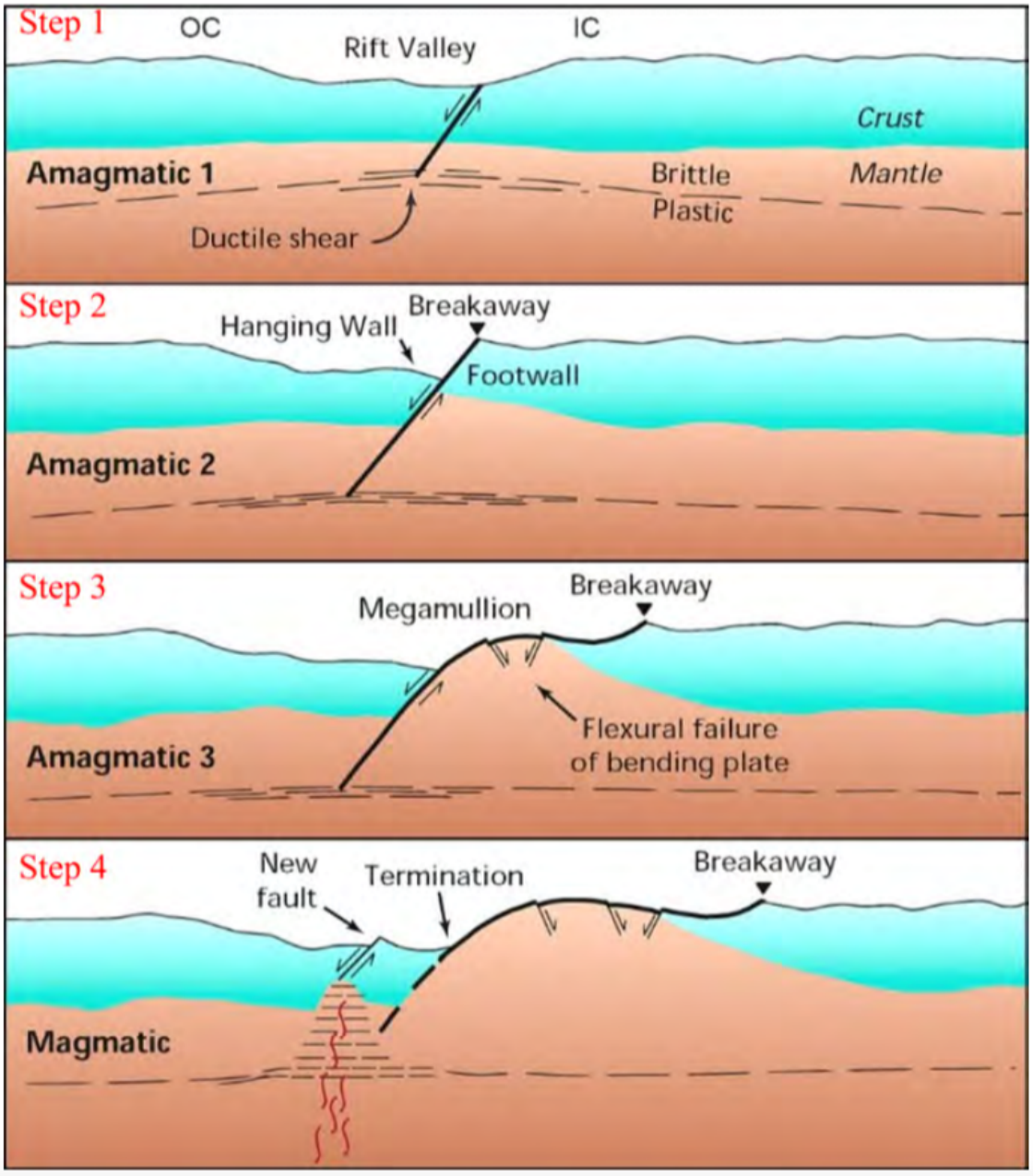


Figure 3.4: Detachment fault system. 1. Normal fault roots into Brittle-ductile transition zone, which is the strongest part of the crust. 2. The footwall of the fault is coming up due to the slip on the fault. 3. The slip continues until the plate is bent, which causes minor faults on the footwall and consequently leads to the oceanic core complex (Megamullion). 4. The magmatic process heats up the lithosphere and makes melt sills, leading to the abandonment of the detachment fault (Tucholke et al., 1998).

- The consumption of a large amount of water in serpentinization reactions creates methane anomalies in the water column and releases large amounts of serpentinization-related fluids at slow spreading mid-ocean ridges (Charlou and Donval, 1993; Charlou et al., 1998).
- Serpentinization contributes to the hydrothermal fluxes at and near slow-spreading ridges. The heat produced by the serpentinization mechanism may partly fuel low-temperature hydrothermal circulations (Kelley et al., 2001; Früh-Green et al., 2003).

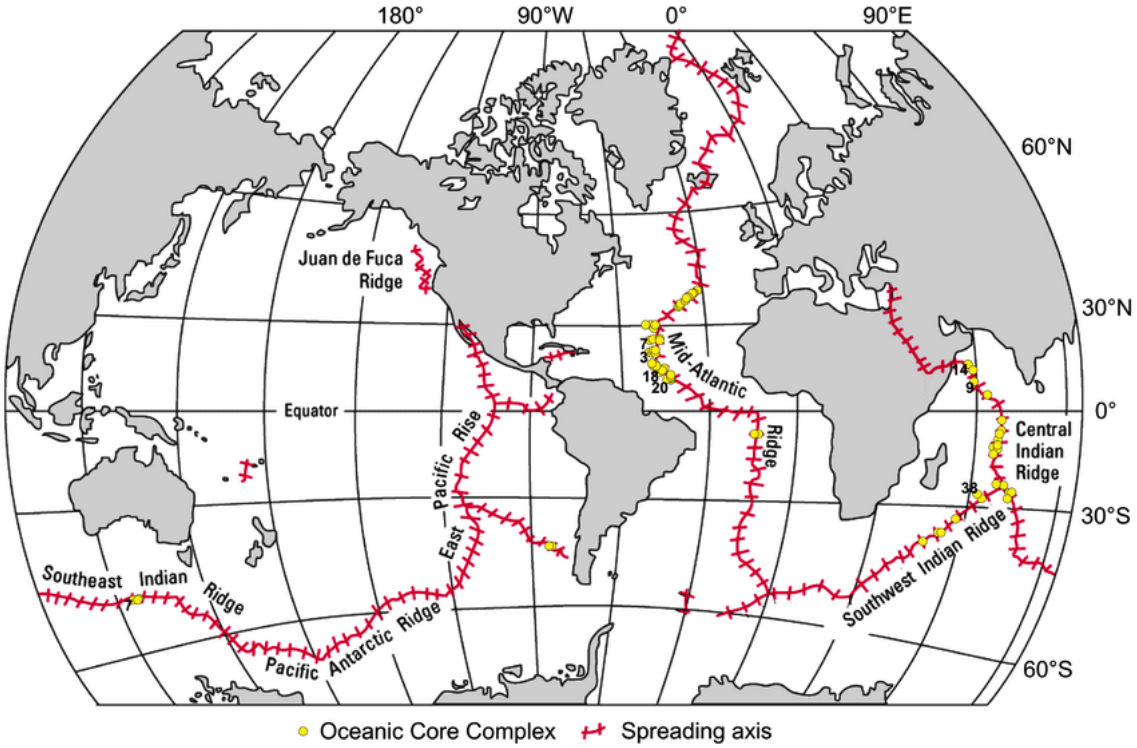


Figure 3.5: The global distribution of oceanic core complexes in slow and ultra-slow spreading ridges when the spreading rate is less than 25 mm/year. (Ciazela et al., 2015).

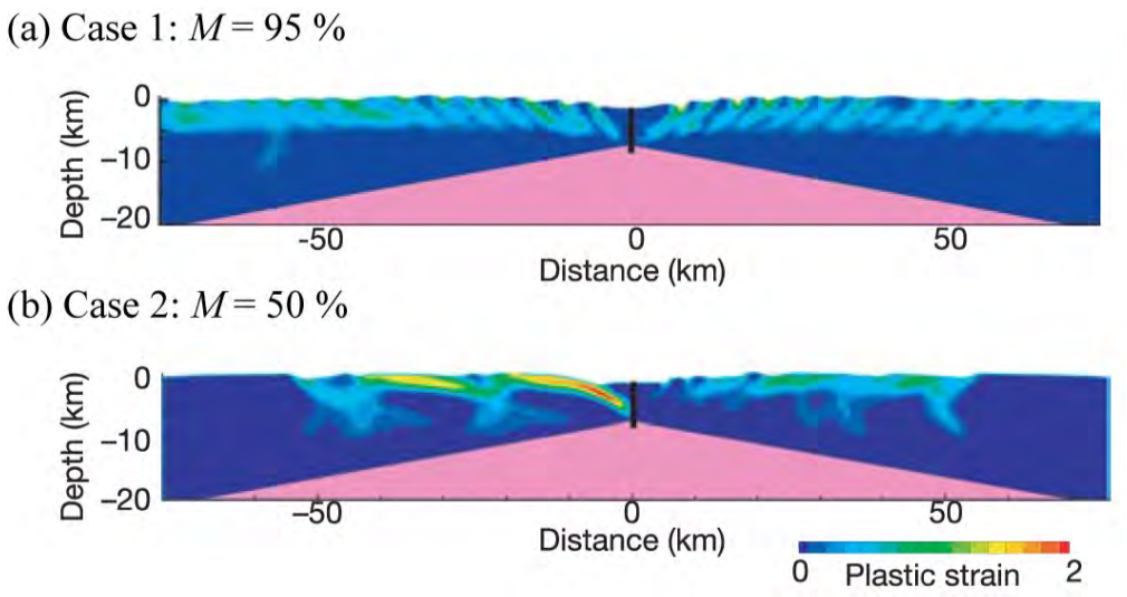


Figure 3.6: Numerical modeling shows the contribution of faulting and melts supply in a detachment fault system. A) M = 0.95, melt supply is abundant, and symmetric small offset faults can be seen on both sides of the ridge axis. (B) M = 0.5, an equal proportion of melt supply and faulting. Large offset faults form on one side, resulting in asymmetric spreading. Modified from (Tucholke et al., 1998).

- The volume of methane and hydrogen resulting from serpentinization reactions can affect the quantity of produced biomass at mid-ocean ridges (Cannat et al., 2010).

- The ecosystems and specific conditions of serpentine-hosted hydrothermal vents may be similar to those that existed on the early Earth and led to the emergence of life. (Shock and Holland, 2004) .
- Serpentinization at slow-spreading ridges can help us to understand similar processes at the ocean-continental margin transition (Whitmarsh et al., 2001; Cannat et al., 2010).

In general, there are two ways to get information about the intensity and spatial distribution of serpentinization. The first approach is to study samples of serpentinized peridotites at slow-spreading mid-ocean ridges. The limitation of this approach is that the collected samples from dredges, submersibles, and drilling holes indicate the uppermost part of the detachment fault system and one of the deepest holes drilled studied so far was 200 m (Cannat et al., 1995) (see Figure 3.7). Therefore, this approach can not easily be the best representative of the deepest parts of the detachment fault system (Rouméjon and Cannat, 2014). Another approach is geophysical information such as seismic velocities and gravity data. As the degree of serpentinization increases from 0 % to 100 %, seismic velocities and density decrease (Miller and Christensen, 1997) (see Figure 3.7). Therefore, geophysical methodologies can provide information about the degree of serpentinization at deeper parts of the detachment fault system. Conversion of seismic velocity to the degree of serpentinization is defined by a linear relationship for partially serpentinized peridotite described in Carlson and Miller (2003).

## 3.5 Study area: The Southwest Indian Ridge

The Southwest Indian Ridge (SWIR) is an ultra-slow spreading ridge that separates Africa and Antarctica (Figure 3.8A). The extension of SWIR is from Bouvert triple junction (BTJ) in the southern Atlantic Ocean to the Rodrigues triple junction (RTJ) in the Indian Ocean (see Figure 3.8B). The spreading rate of this axis is about 14 mm/year, which changes slightly along the ridge axis (Sauter and Cannat, 2010). From 0° E to 9° E and between 25°E and 60° E of the ridge axis, there are significant fracture zones, but between 9°E and 25°E, and also east of 60°E, long stretches of the ridge axis with few fracture zones are observed.

Ridge obliquity is supposed to have an effect on melt supply. When obliquity of the ridge versus spreading direction increases, mantle up-welling must be slower (Sauter and Cannat, 2010; Montési and Behn, 2007; Dick, 1989). Cannat et al. (2008) suggested that, although this effect is important and considerable, it is not enough to make near-amagmatic spreading in the most oblique regions. Generally, SWIR can be divided into some subsections based on changes in obliquity in the ridge axis:

* From 10° (Shaka Transform fault) to 16°, the supersegment is highly oblique (51°) with poor basalt compositions and a dominant peridotite sea floor except for two anomalous regions of the Joseph Mayont Seamount and the Narrowgate segment (see Figure 3.8B). This feature of oblique supersegment indicates the crust with a mean depth of 4 km (Bach et al., 2002; Standish et al., 2008).

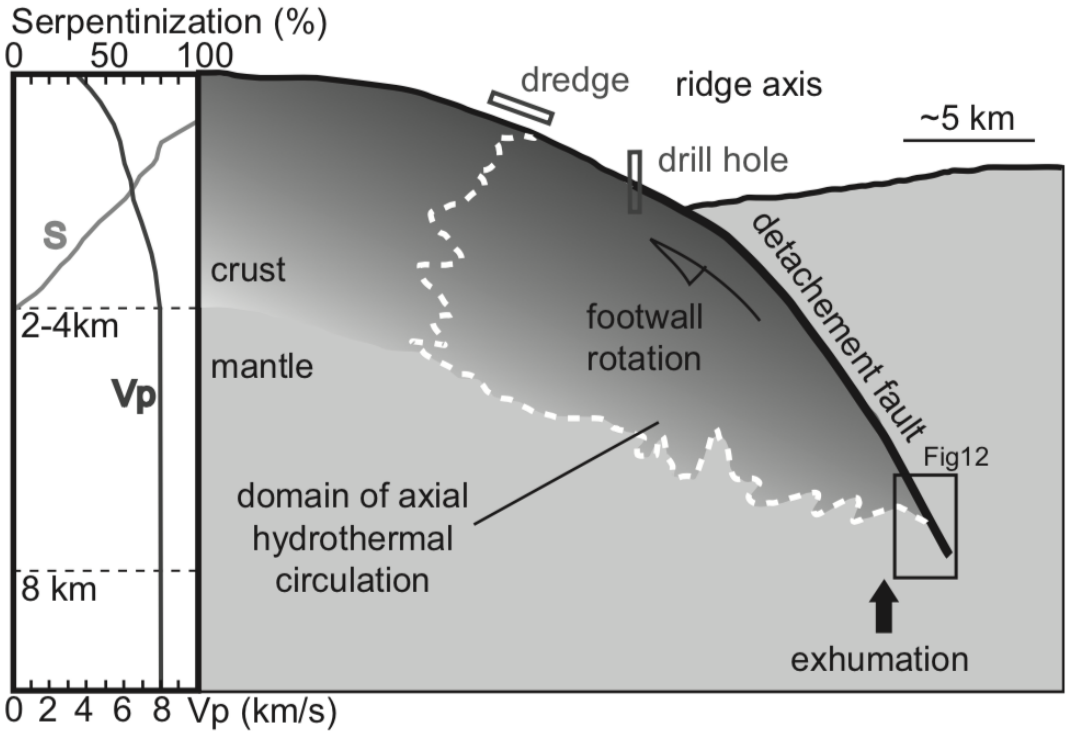


Figure 3.7: Sketch of serpentinization of mantle-derived peridotite and detachment fault system (Rouméjon and Cannat, 2014; Cannat et al., 2010). The detachment fault brings the peridotite into the domain of axial hydrothermal circulation, which results in serpentinization. On the left, we see how the degree of serpentinization changes with the variation of the seismic velocity model. An available sampling of serpentinized peridotites is limited to shallow parts of the crust through the collected (oblique rectangle in the figure) samples from dredges, submersibles, and drilling holes (vertical rectangle in the figure).

* Between 16° and 25°, the supersegment is orthogonal, which is nearly perpendicular to the spreading direction. In the orthogonal supersegment, the seafloor rocks are predominantly basaltic, and the generation of the seafloor has a magmatic nature (Grindlay et al., 1998; Dick et al., 2003).
* From 25°30'to 52°20', SWIR is divided by the subsections: Du Toit (DT transform fault), Andrew Bain Transfrom fault (TF), Marion TF (Ma), Prince Edward TF (PE), Eric Sympson (Es), Discovery TF, Indomed TF (In) and Gallieni TF. The subsections between Prince Edward, Discovery, Indomed, and Gallieni are slightly oblique (25°) (Georgen et al., 2001).
* Between 52°20' (Gallieni Tf) and 64°, the ridge section is oblique (> 30° or oblique supersegment) with Atlantis II, Novara, and Melville TFs.
* From Melville (Me) to Rodriguez triple junction (RTJ), the ridge axis is slightly oblique and becomes more oblique toward RTJ. In this area, the axial valley reaches a mean depth of 4730 meters, which is the deepest part of the ridge (Mendel et al., 1997; Sauter and Cannat, 2010), (Sauter and Cannat, 2010).

Our study area is located in the easternmost part of SWIR, which is centered at 64°35'E of longitude and 28°S of latitude (The blue rectangle in Figure 3.8B) and represents a melt poor member of the global ridge system with few and short-lived

magma centers. This easternmost portion of SWIR presents the widest non-volcanic (smooth) seafloor so far (Corbalán et al., 2021). The first comprehensive off-axis data set in the easternmost part of the SWIR was collected in 2003 by bathymetric, magnetic, and gravimetric methods, covering an area of up to 250 km away from the ridge axis on both sides (Cannat et al., 2006). It was found that 37% of the surveyed seafloor showed only a little or no evidence of volcanic activity. This non-volcanic seafloor is termed "smooth seafloor" because of its rounded topography. It has no equivalent in the faster-spreading ridges (Cannat et al., 2006). Four percent of the mapped region was identified as corrugated OCCs (Tucholke et al., 1998) and the remaining 59 % was found to be the result of volcanic activity (Sauter and Cannat, 2010). The melt supply appears to be focused beneath the volcanic centers. This focus has been explained by melt originating near the base of the lithosphere and rapid extraction via dikes (Momoh et al., 2017; Smith et al., 2006; Cannat et al., 2003; Sauter et al., 2004; Standish et al., 2008). Off-axis studies showed higher values of magnetic anomaly over volcanic seafloor areas and lower magnetization over smooth seafloor or non-volcanic regions. This weakly induced magnetization in non-volcanic areas of the seafloor is supposed to be produced by serpentinized peridotites (Sauter et al., 2008; Sauter and Cannat, 2010). A similar separation can be seen from maps of residual mantle Bouguer gravity anomaly where lower values (negative) were found for the volcanic seafloor and higher values (positive) for deep sections or non-volcanic regions (Standish et al., 2008; Cannat et al., 2003). The scarcity of the melt supply is also predicted as a result of the large axial depth and high mean basalt sodium content (Cannat et al., 2008; Seyler et al., 2003). Moreover, east of the focused area at 66°, the P-wave model of seismic refraction delineated a 4.2km average crustal thickness, which is thinner than typical oceanic crust (6-7km) (Momoh et al., 2017; Minshull et al., 2006; White et al., 1992). A 3D seismic reflection study by Momoh et al. (2017) at 64°30’ was another evidence of low melt supply through a proposed crustal thickness of 4-5 km composed of highly serpentinized peridotite.

As a consequence of the low melt supply, the formation of the seafloor was explained by successive, flipping polarity, detachment faults that formed north and south of the spreading ridge (Cannat et al., 2006, 2019; Sauter et al., 2013). The considerable quantity of outcrops of the serpentinized peridotite on the seafloor is ascribed to exhumation in the footwall of the detachment faults in the amagmatic and smooth terrains of the SWIR known as non-corrugated Oceanic Core Complexes (OCC) (Momoh et al., 2020). The dredging of the non-corrugated OCCs exhibited 90% serpentinized peridotites with a minor contribution of gabbros (Sauter et al., 2013). Corbalán et al. (2021) estimated the serpentinization depth extent on a ridge-perpendicular profile ranging from 2 to 5 km and on a ridge-parallel profile ranging from 2.5 to 4 km. Active and abandoned detachment faults have been imaged and observed by side-scan sonar (Sauter et al., 2013), seismic reflection data (Momoh et al., 2017) and wide-angle OBS profiles (Corbalán et al., 2021) in the study area. In the following the seismic studies in the region, conducted during SISMOSMOOTH cruise (Leroy and Cannat, 2014), will be presented in more detail.

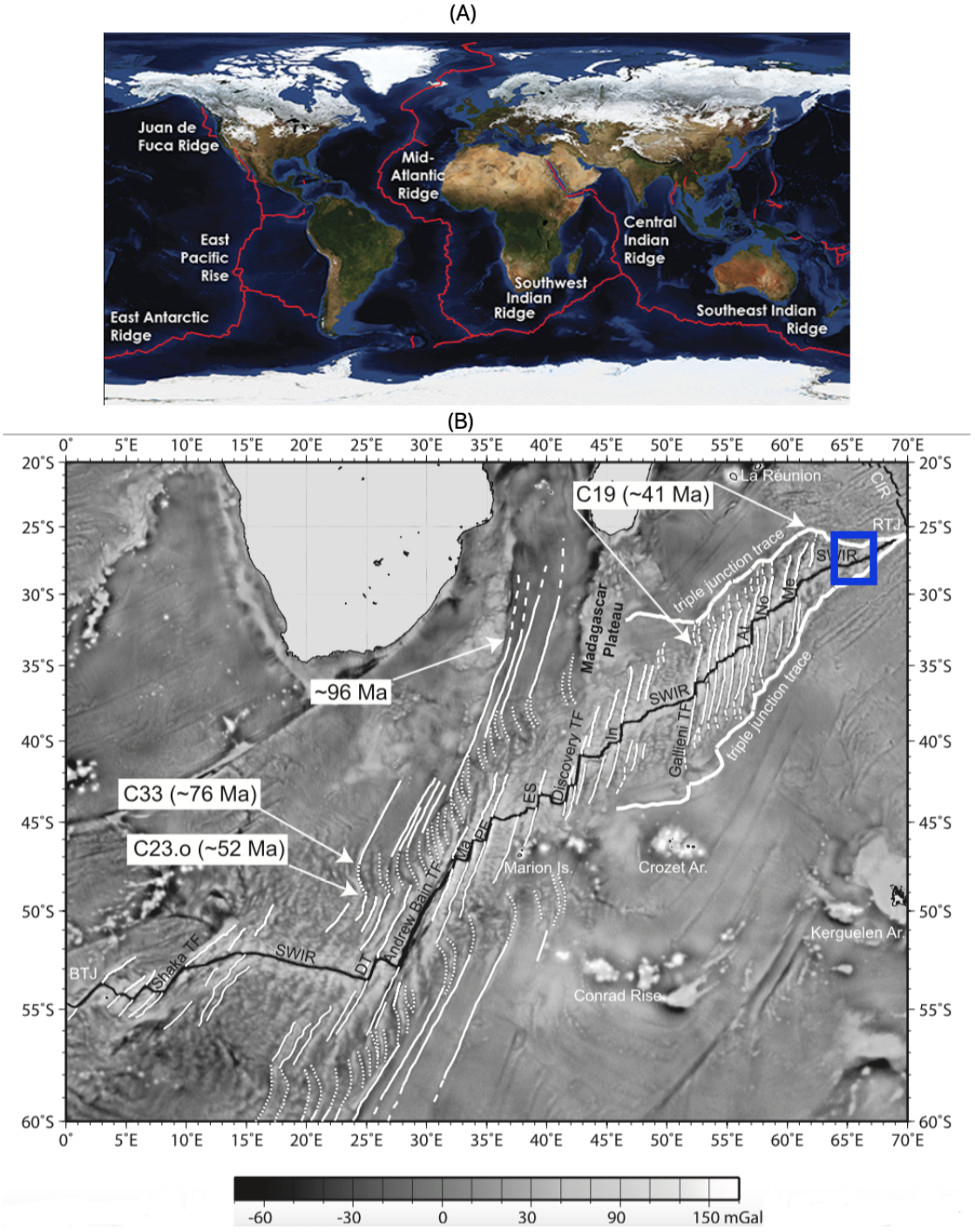


Figure 3.8: A) The location of the SWIR on the map (Rosen, 2015). B) Free-air gravity anomalies over SWIR. The blue rectangle marks the study area of SISMOSMOOTH cruise. The thin black line shows the SWIR axis. Thin white lines indicate the fracture zones. C19, C23.o, and C33 are indicative of magnetic anomalies. The variation in transform fault orientation corresponds to the variation in spreading direction along the ridge axis (Chu and Gordon, 1999; Sauter and Cannat, 2010). The extension of SWIR is from Bouvert triple junction (BTJ) in the southern Atlantic Ocean to the Rodrigues triple junction (RTJ) in the Indian Ocean. Abbreviations of transform faults: DT, Du Toit TF; Ma, Marion TF; PE, Prince Edward TF; ES, Eric Simpson TF; In, Indomed TF; At, Atlantis II TF; no, Novara TF; Me, Melville TF

## 3.6 Seismic studies

Momoh et al. (2017) analyzed 18 multi-channel seismic data lines in a rectangle

19 km long and 1.8 wide along the ridge axis (Figure 3.9). They interpreted these profiles based on the 3D Kirchhoff post-stack time migration and its depth conversion (see Figure 3.10 and Figure 3.11). South-dipping reflectors were identified as the most prevalent events in the northern parts of the profiles and under the emergence of the axial detachment fault (in purple in Figure 3.10). Two distinct packages of south-dipping reflectors were identified. They were separated from each other horizontally and vertically. The upper package was extended up to 2 km below the seafloor. The lower package was traced up to 5 km below the seafloor. The north-dipping reflectors were interpreted in the central and southern parts of the profiles, mostly under the axial valley (in green in Figure 3.10). Their depth was followed up to 4 km below the seafloor. The third and fourth categories of reflectors in the region were shallow and deep sub-horizontal reflectors. The shallow sub-horizontal reflectors were ubiquitous between the north-dipping reflectors and the south-dipping reflectors. They were mostly observed up to 1 km below the seafloor. The shallow sub-horizontal reflectors were located between the deepest portions of the south-dipping reflectors and the deepest portions of the north-dipping reflectors. They were up to 5 km below the seafloor.

Momoh et al. (2017) also obtained a 2D P-wave velocity model from travel time tomography of 10 OBS stations (see Figure 3.9)b and Figure 3.12). With regard to the maximum P-wave velocity of olivine-rich gabbros, the presence of crustal-type rocks was predicted in the upper 4 to 5 km. Moreover, two 1D velocity models were extracted to estimate the percentage of serpentinization (blue and red triangles are the locations of these two OBS in Figure 3.12). According to the empirical relationship between velocity and serpentinization (Miller and Christensen, 1997), the percentage of serpentinization could be 100% in the upper 1 km and decrease up to 16% at the base of the predicted crust. A geological sketch was proposed based on the information from the 3D Kirchhoff post-stack time migration and 2D P-wave velocity models (see Figure 3.13). The green dashed lines are the north-dipping reflectors and were introduced as the hanging wall of the active detachment fault system. The south dipping reflectors were imaged with dashed purple lines beneath the emergence of the active detachment fault and were interpreted as the footwall of the active detachment fault system. The fault plane, which is considered the limit between the hanging wall and the footwall, is shown by the continuous purple line. The horizontal distance (2-2.7 km) between the fault plane and the weaker south dipping reflectors in the footwall was recognized as the damage zone. The shallow sub-horizontal reflectors (Cyan dash lines) were explained by isolated sill-shaped bodies of magmatic rocks that likely cool and crystallize rapidly into the host ultramafic host (Cannat, 1993). The deeper sub-horizontal reflectors (orange dash lines) could be the transition from serpentinized peridotite to the fresh mantle.

Longer 2D reflectivity profiles obtained by time migration were studied by Momoh et al. (2020). The groups of reflectors were identified in across-axis profiles and their crossing along-axis profiles. They considered the surface extent of the detachment fault systems to range from the younger or active detachment fault systems (D1) to the oldest one in the region (D7). Across-axis profiles were indicated by SMOO2, SMOO3, SMOO4, SMOO5 and SMOO33, and along-axis

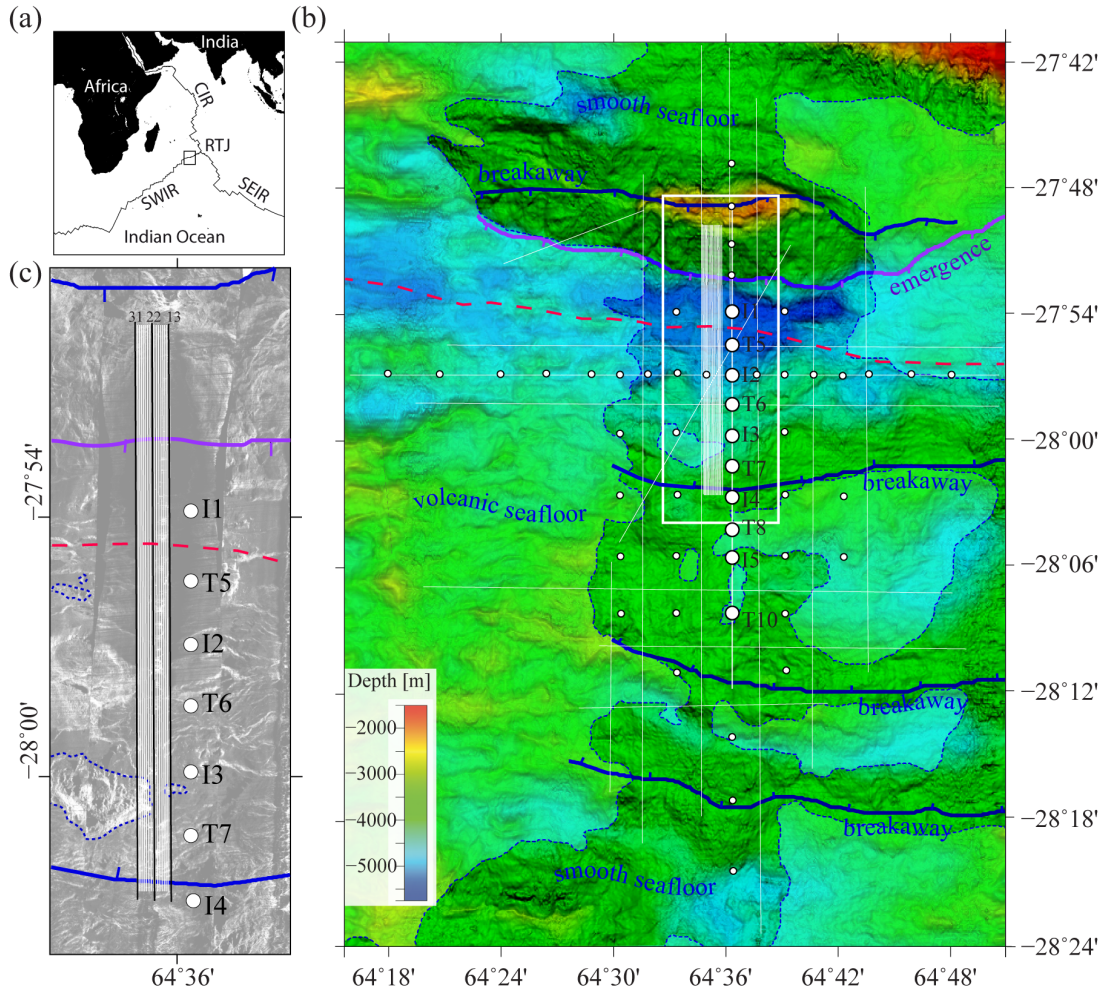


Figure 3.9: a) The location of the area in the SWIR's easternmost region. b)A bathymetric map of the area. The white rectangle presents another reflectivity study (Sauter et al., 2013). The thin white lines in this rectangle are the 18 MCS lines. c) Location of the MCS lines with numbers ranging from 13 to 31 across the ridge axis on the acoustic back-scatter image. OBS stations are shown with white circles. The traces of the breakaway of inactive detachment fault systems are shown with blue lines in the southern part. The breakaway and emergence of an active axial detachment fault are mapped in the northern part of the axial valley in blue and purple, respectively. The thick red line represents the ridge axis (Momoh et al., 2017; Sauter et al., 2013)

profiles were labeled by SMOO8 and SMOO10 (see Figure 3.15). Similar to (Momoh et al., 2017), south-dipping reflectors were located near the emergence of the active detachment fault system (E1) (purple color in Figure 3.16A to Figure 3.16D). North dipping reflectors were observed near the axis between 6 and 14 km south of the mentioned emergence (E1) (green color in Figure 3.16A to Figure 3.16C). Two packages of north-dipping reflectors were seen between 6.8 and 9.6 km north of E1 on profile SMOO33 (green color in Figure 3.16C). Sub-horizontal reflectors near the axis occur between north-dipping reflectors and south-dipping reflectors up to 2.5 s below the seafloor on profiles SMOO2 and SMOO33 (cyan color in Figure 3.16A and Figure 3.16C). Apparent dipping reflectors were detected between 35 and 38 km distance from E1 on SMOO2 (Figure 3.16a), between 19 and 43 km distance from E1 on SMOO3 (Figure 3.16b), between 27 and 42 km

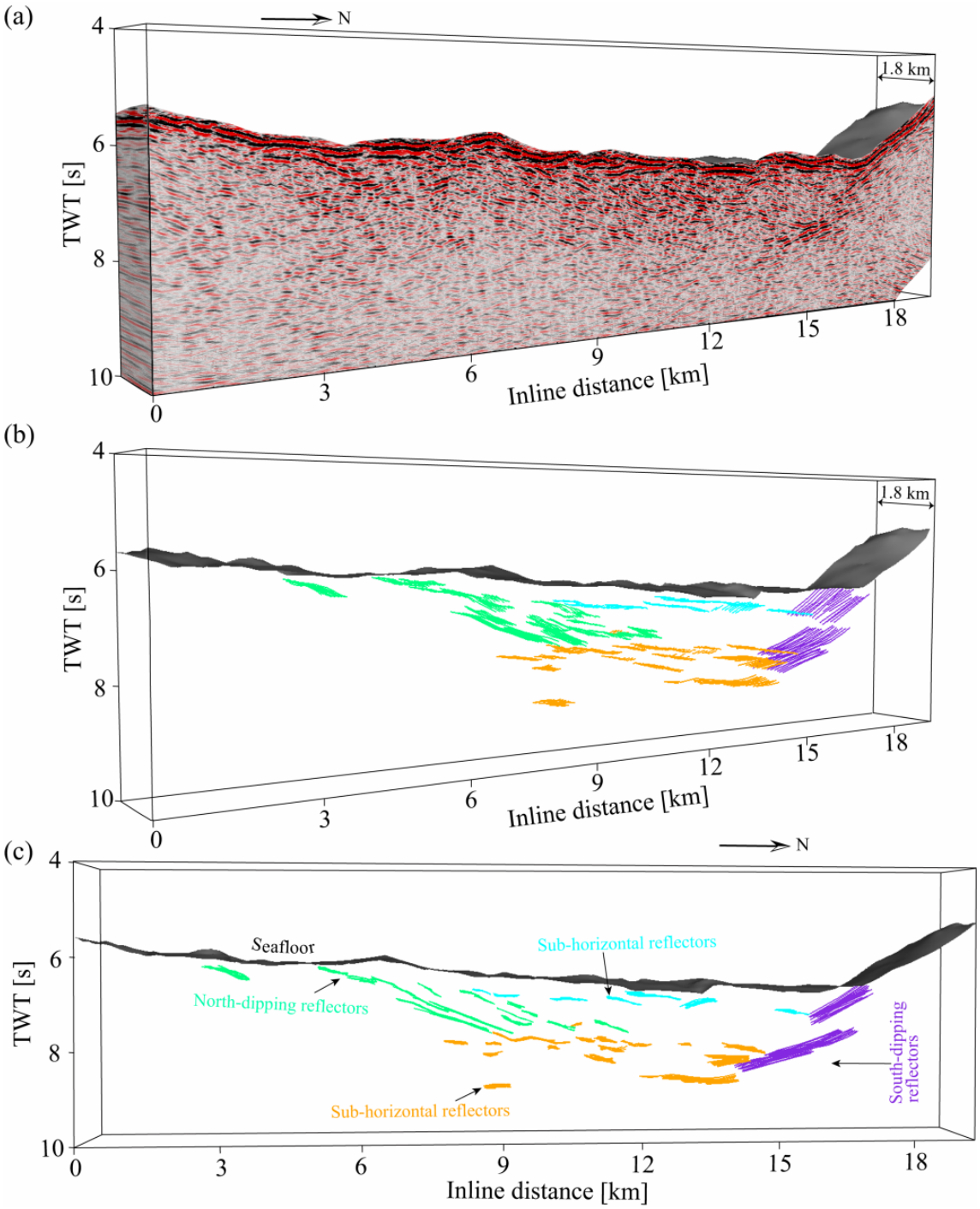


Figure 3.10: a) Perspective of 3D Kirchhoff post-stack time migration of 18 MCS profiles with profile number 13 on the forefront. The view is from the SSE. b) Perspective of interpreted reflectors from migration seismic section. The view is from the SSE. c) The same as b, but the view is from the east. Reflectors are explained in the text (Momoh et al., 2017).

distance on SMOO33 (Figure 3.16c) and between 6 to 10 km from E1 on SMOO5 (Figure 3.16D).

On along-axis profiles SMOO8 and SMOO10, packages of disjointed sub-horizontal reflectors were found. These sub-horizontal reflectors were ubiquitous beneath smooth and volcanic seafloor (Figure 3.17a and Figure 3.17b). The deepest package of sub-horizontal reflectors was observed along the profile SMOO8

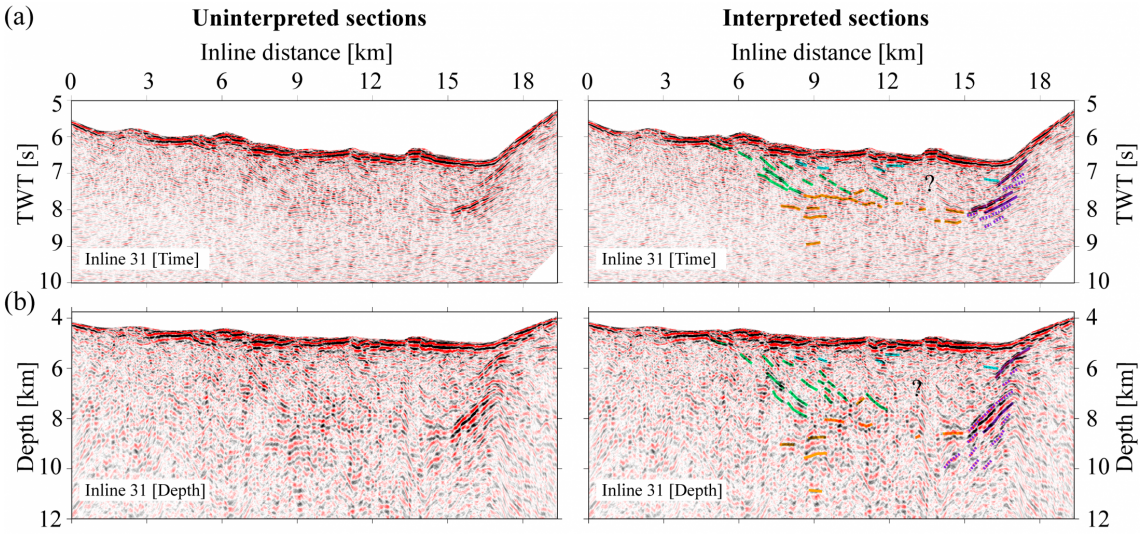


Figure 3.11: a-left) Time migrated section of profile 31. b-left) Depth migrated section of profile 31. a-right) Time migrated section of profile 31 with interpretation. b-right) Depth migrated section of profile 31 with interpretation. (Momoh et al., 2017).

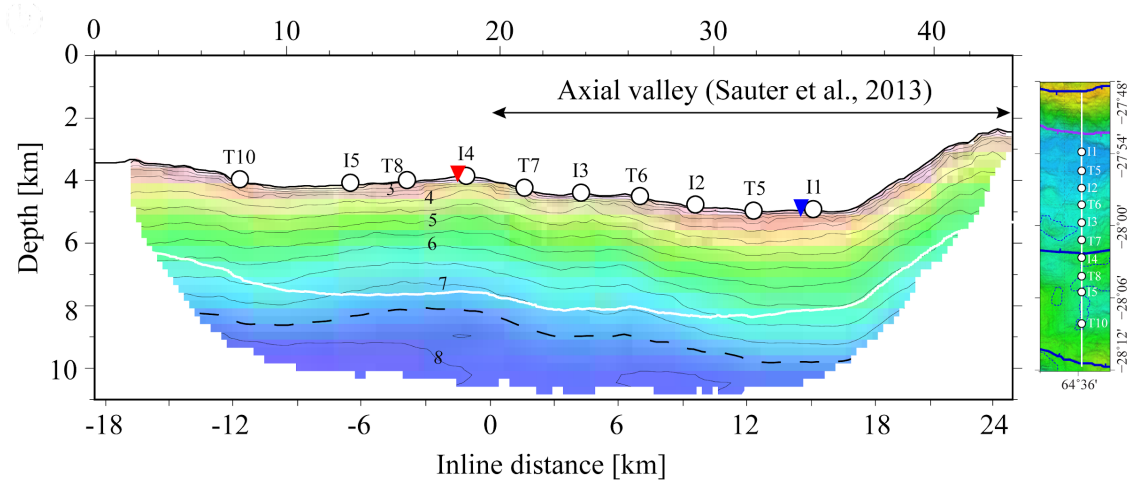


Figure 3.12: 2D P-wave velocity model obtained from first arrival travel time tomography. The white circles indicate the locations of OBSs. The blue and red triangles are the two OBS that are used for serpentinization estimation. The black dashed line corresponds to peridotite with 16 % serpentinization and the white line indicates the base of the crust obtained from constant density gravity (Cannat et al., 2006; Momoh et al., 2017).

between 34.13 and 43.93 km and between 8.74 s and 9.77 s (Figure 3.17b).

Profile SMOO33, which was a combination of three adjacent profiles, was chosen to discuss the origin of different packages of reflectors and interpret their possible structure and/or composition (see Figure 3.18). Magmatic injections, in addition to tectonic damage and serpentinization, were introduced as the possible mechanisms for the formation of the reflectors associated with D1. The preferred interpretation for these reflectors was that they originate from the fractures of the damage zone and may act as a pathway for serpentinizing the magma and fluids. The north-dipping reflectors in the footwall of D1 could be attributed to the fractures generated from bending during tectonic uplift. When the footwall bends during the tectonic uplift, it can be indicative of accommodation faults and accommodate internal deformations.

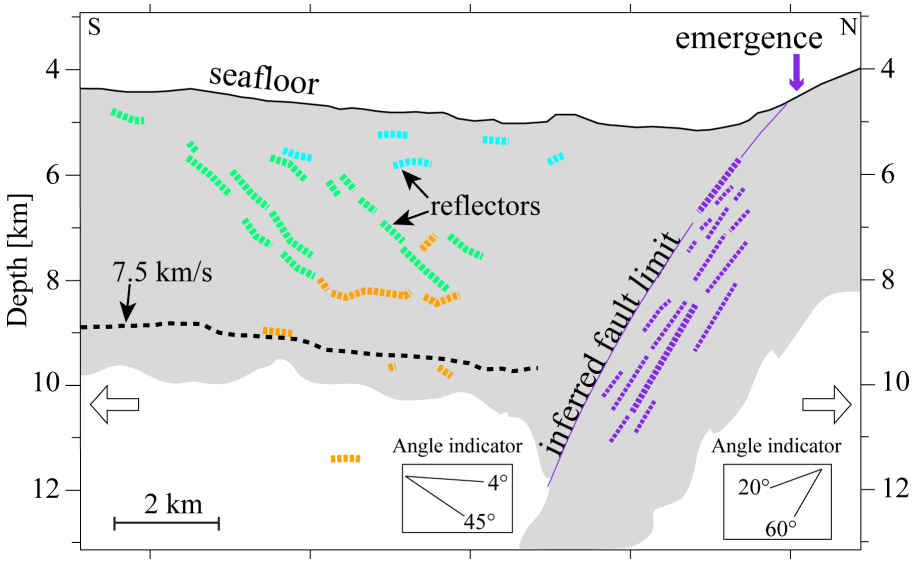


Figure 3.13: Geological sketch obtained from 2D P-wave velocity and 3D Kirchhoff post-stack time migration. The green dashed lines are the north-dipping reflectors introduced as the hanging wall of the detachment fault. The south dipping reflectors are shown by dashed purple lines. Thinner dashed purple lines indicate weaker amplitude reflectors. The shallow sub-horizontal reflectors are indicated by cyan dash lines. We can see the deeper sub-horizontal reflectors by the orange dashed lines. The pale gray represents the serpentinized crustal layer (Momoh et al., 2017).

Moreover, it can serve as a magmatic plumbing system (Momoh et al., 2020). In the northern part of the profile, the sub-horizontal reflectors could be explained by the extent of damage in the footwall of D1, or the boundary between the serpentinized peridotite of D2 and intrusive magmatic sills.

North-dipping reflectors in the hanging wall of active detachment fault were interpreted as recent conjugate faults which may work as magmatic conduits onto the seafloor. It was also proposed that the tectonic damage zone of the previous detachment fault system (D2), which is now in the hanging wall of the active detachment fault, was the cause of the faulting. The sub-horizontal reflectors in the hanging wall could be explained by one or a combination of the following suggestions: 1. magmatic sill boundaries in the ultramafic basement 2. between ultramafic basements that are highly serpentinized and those that are only partially serpentinized 3. a damaged zone filled with magma inherited from D2 (Momoh et al., 2020).

Away from the axial valley, beneath the emergence E3, a package of south-dipping reflectors can be observed which project to volcanic patches on the seafloor. Two hypotheses were proposed to explain these reflectors: 1. They are associated with the damage zone of D3. 2. They might be the traces of magmatic channels feeding the volcanic patches. The reflectors between E3 and E5 were interpreted as a magma-infiltrated damage zone, created either during the D3 detachment fault cycle or the D4 detachment fault cycle (Momoh et al., 2020).

Corbalán et al. (2021) constrained the velocity structures along-axis and across-axis from two orthogonal wide-angle OBS profiles. Around 75 % of the uppermost lithosphere in their investigated area was estimated to be highly fractured and fully serpentinized peridotite at the top. There was no distinct Moho observed in their

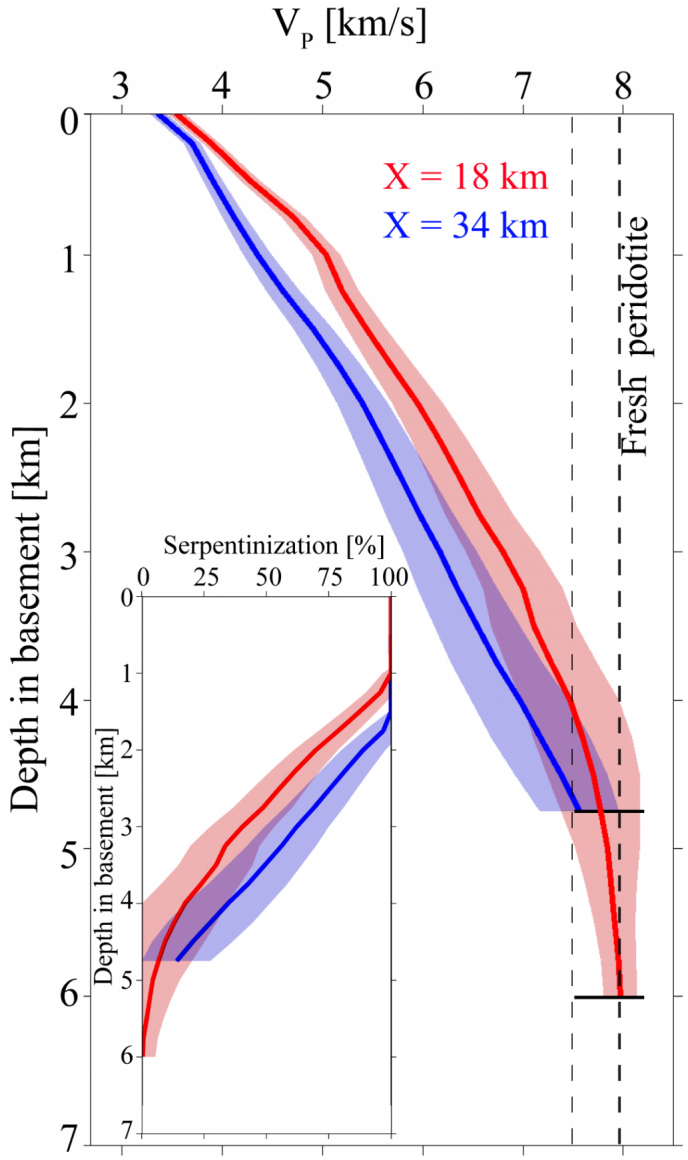


Figure 3.14: 1D P-wave velocity model extracted at model distances of 18 and 31 km. Estimated serpentinization versus depth can be seen on the left part of the figure. The dashed lines correspond to 7.5 and 8 km/s velocities (Momoh et al., 2017).

analysis. One active and five abandoned detachment faults were recognized on the across-axis profile. The sharpest lateral velocity change and the highest vertical gradient were observed on the active axial detachment fault. The comparison between the 1D velocity models of orthogonal profiles at their crossing point proposed 5 % ridge-parallel fast-axis anisotropy at a depth of nearly 0.5 to 2.2 km and 5 % reversed polarity ridge-normal fast-axis anisotropy at depths greater than 2.2 km. They were attributed to the preferential distribution of cracks across the ridge-axis and lattice-preference orientation of olivine minerals in the less serpentinized peridotite, respectively. A westward increase in the melt supply and, consequently, seafloor accretion was suggested by the analysis of the axis-parallel profile.

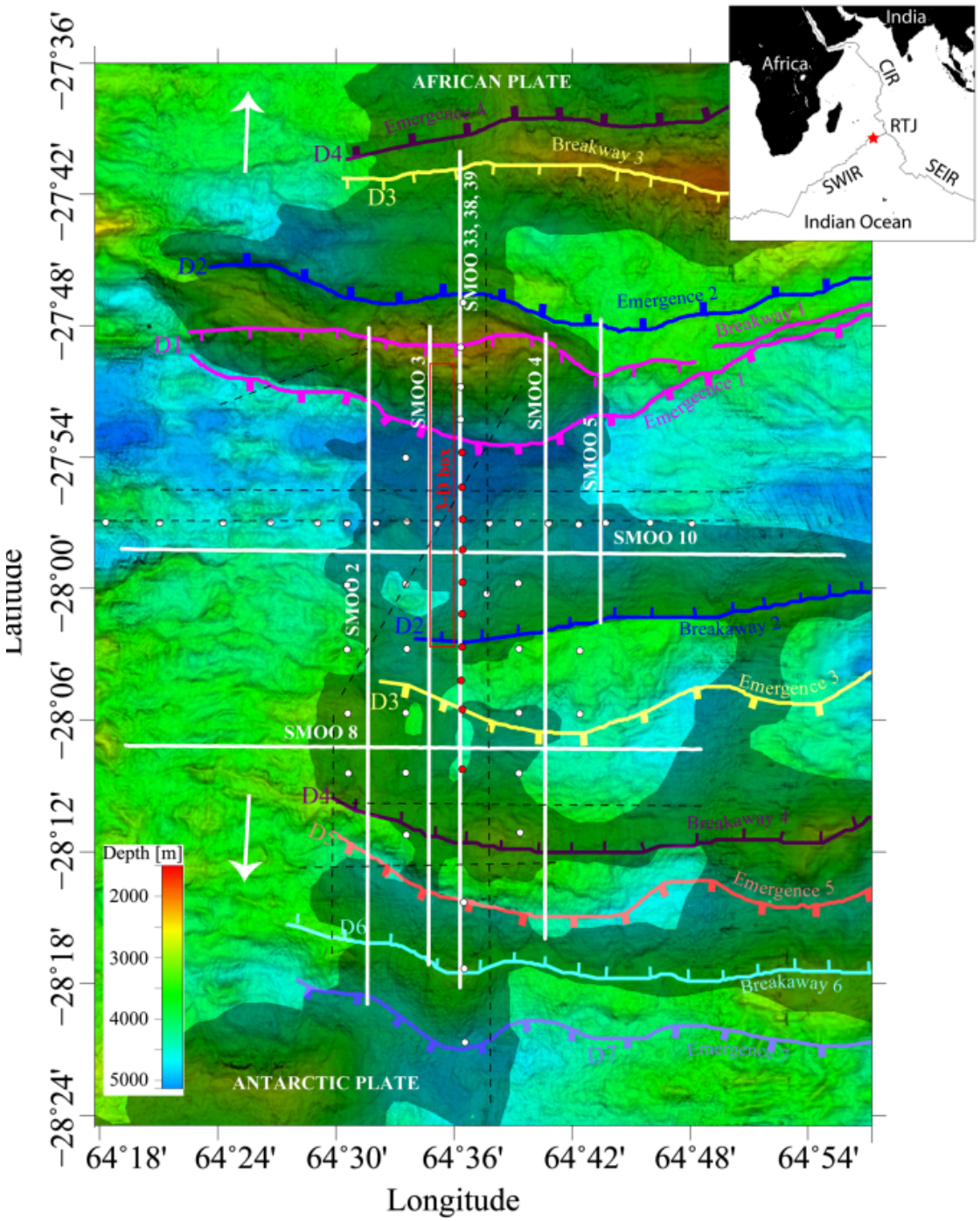


Figure 3.15: Location of the area from SISMOSMOOTH cruise in the easternmost part of SWIR. The region's bathymetric map. The traces of the emergence and breakaway of detachment fault systems with increasing age are labeled with D1, D2, D3,..., D7. 2D reflectivity profiles are shown with white lines. OBS stations are shown with white circles. The darkened region is an indicator of smooth seafloor or ultramafic rocks, and the rest is volcanic seafloor (Momoh et al., 2020).

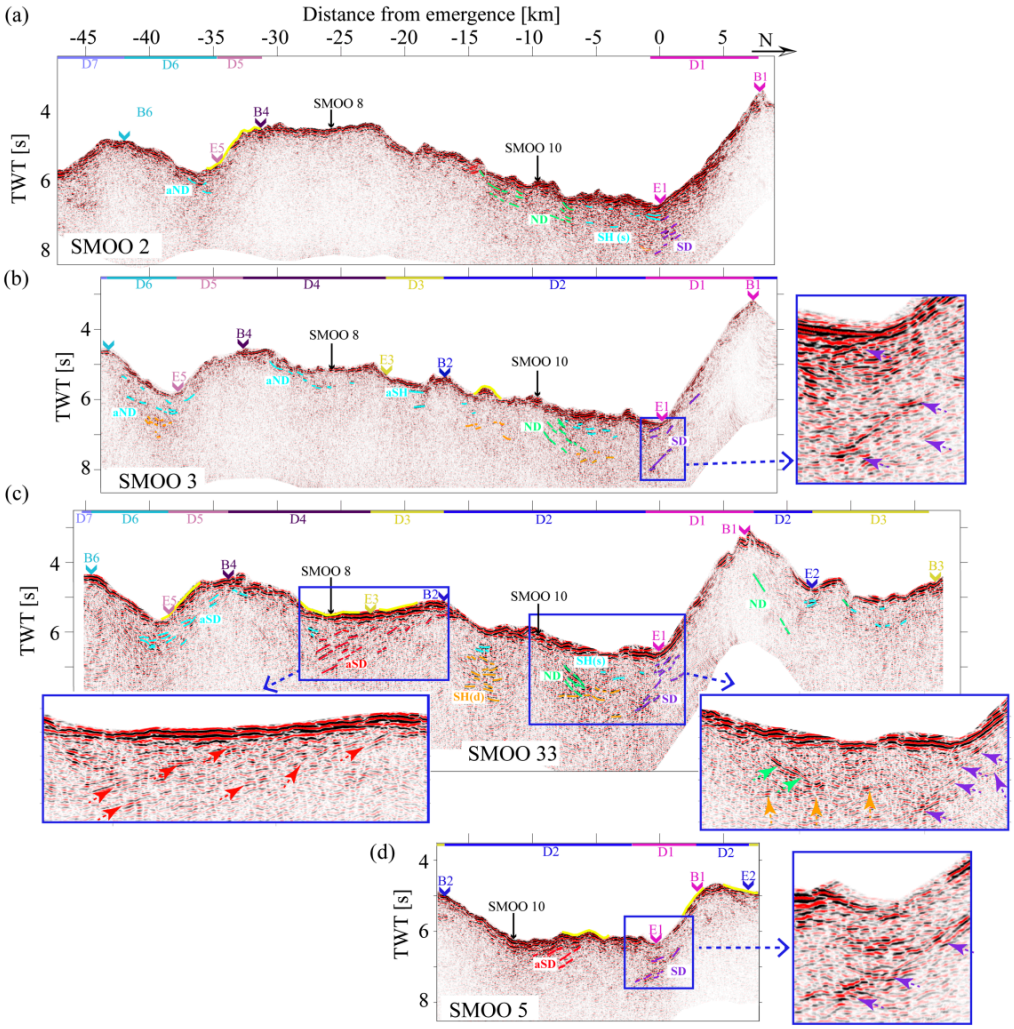


Figure 3.16: Interpretation of across-axis profiles a) SMOO2 b) SMOO3 c) SMOO33 d) SMOO5. The acronyms B and E indicate the breakaway and emergence of detachment fault systems. Colorful lines at the top of each figure and on the horizontal axis represent the extent of the detachment fault system interpreted from seismic data and bathymetry. The yellow lines on the seafloor are indicative of volcanic patches (Cannat et al., 2019). SD = south-dipping reflectors, ND = north-dipping reflectors, SH(s) = subhorizontal reflectors (shallow), aSH = apparent subhorizontal reflectors, aSD = apparent south-dipping reflectors, and aND = apparent north-dipping reflectors. The close-up shows the prevalent reflectors with more details (Momoh et al., 2020).

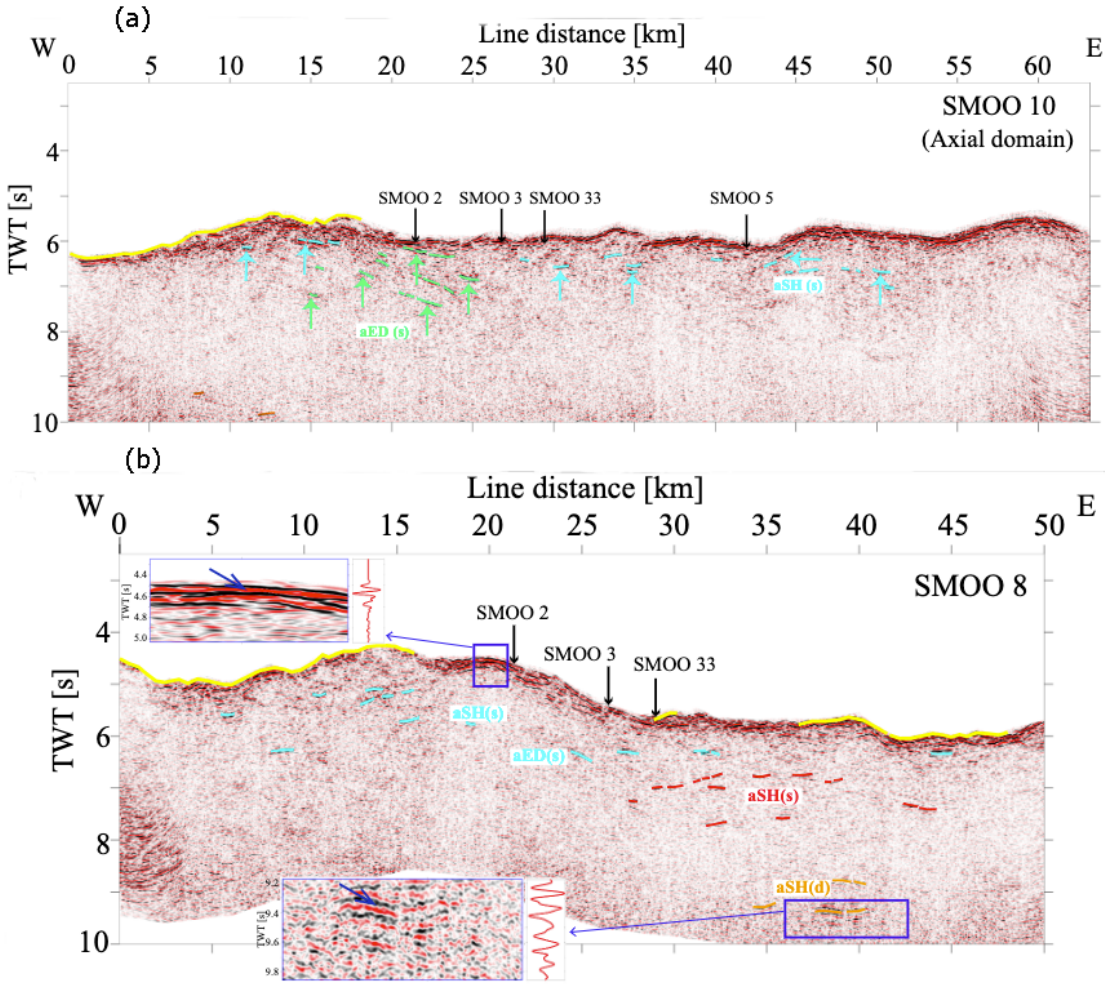


Figure 3.17: Interpretation of along-axis profiles a) SMOO8 b) SMOO10. The close-up shows the prevalent reflectors with more details. aSH(s) = apparent sub-horizontal reflectors shallow, aSH(d) = apparent sub-horizontal reflectors deep, aED(s) = apparent east-dipping reflectors (shallow) (Momoh et al., 2020).

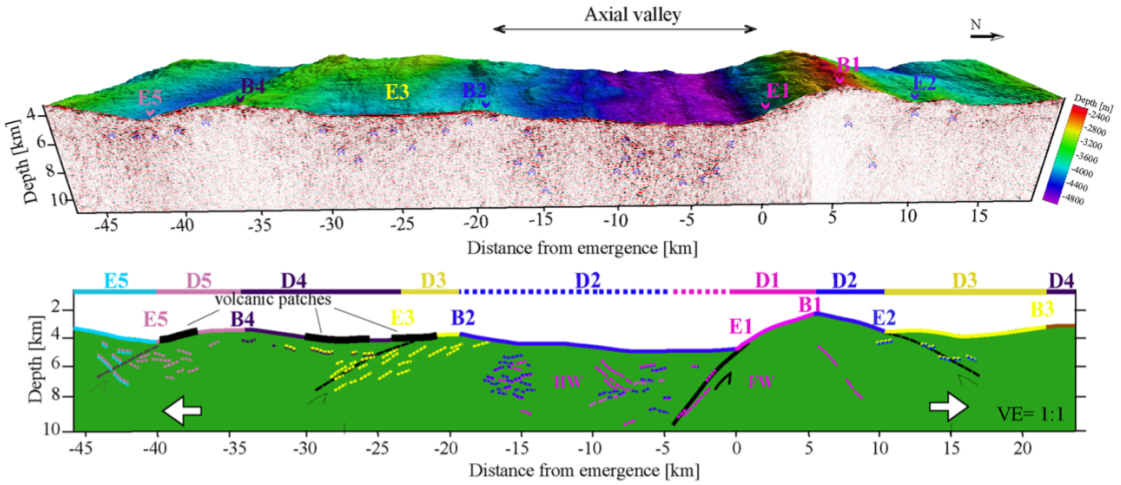


Figure 3.18: The upper part shows the depth-converted section of the combined lines (SMOO33) with the bathymetry overlain. The acronyms B and E indicate the breakaway and emergence of detachment fault systems D. The most visible reflectors are shown with arrows. The lower part shows the interpreted reflectors. Colorful lines at the top of each figure and on the horizontal axis represent the extent of the detachment fault system interpreted from seismic data and bathymetry. Thick black lines at the top of the seafloor are indicative of volcanic patches. The black lines in the model represent the active detachment fault system, and the dashed black lines indicate the inactive detachment fault system (Momoh et al., 2020).

# Chapter 4

# Data acquisition and pre-processing


## Summary

This chapter is a brief description of data acquisition during the SISMOSMOOTH cruise (Leroy and Cannat, 2014). Preparation, pre-processing, and conversion of passive and active data in required formats will be reported in the following.


## 4.1 Pre-processing of passive seismic data

The smooth seafloor was discovered during the SWIR 61-64 cruise of R/V Marion Dufresne in 2003. A more detailed geophysical-geological survey of smooth seafloor was conducted by the SMOOTHSEAFLOOR R/V Marion Dufrense cruise in 2010. The easternmost of SWIR is well documented in terms of gravity, magnetic and seismic data. However, the seismic experiment was restricted to volcanic areas. The selected region for the seismic experiment of the SISMOSMOOTH cruise includes the Smooth seafloor area. The data acquisition took place between 25 September and 30 October 2014 during the SISMOSMOOTH cruise (Leroy and Cannat, 2014; Leroy et al., 2015). The passive seismic data used in this study were acquired by 43 Ocean Bottom Seismometers (OBS), each having three components geophones and one hydrophone. To analyze the ambient-noise signals, we used only the vertical component of the geophones (Yao et al., 2011; Bohlen et al., 2004). As the instruments were from three different countries, we have labeled the stations Canadian (C), Taiwanese (T), and French (F) (Figure 4.2 and Figure 4.1). Of the 43 OBS stations used in this study, 29 were Canadian, 7 Taiwanese, and 7 French. The sampling rate was 250 Hz. The spacing between the OBS stations was 2.1–5 km, and their depth ranged between 3.9 and 5.01 km. The raw records have been split into their components and corrected for clock drift and relocation errors. The OBS data is recorded continuously on the seafloor at a sampling rate of 250 Hz. The deployment time and retrieval time of these stations have been shown in table 4.1.

What we received for passive seismic interferometry was raw data. The conversion of raw data to SAC format is a necessary step in passive seismic interferometry. This stage of the work was very time-consuming. Because the data were from different instruments, and every instrument had its own software or code working

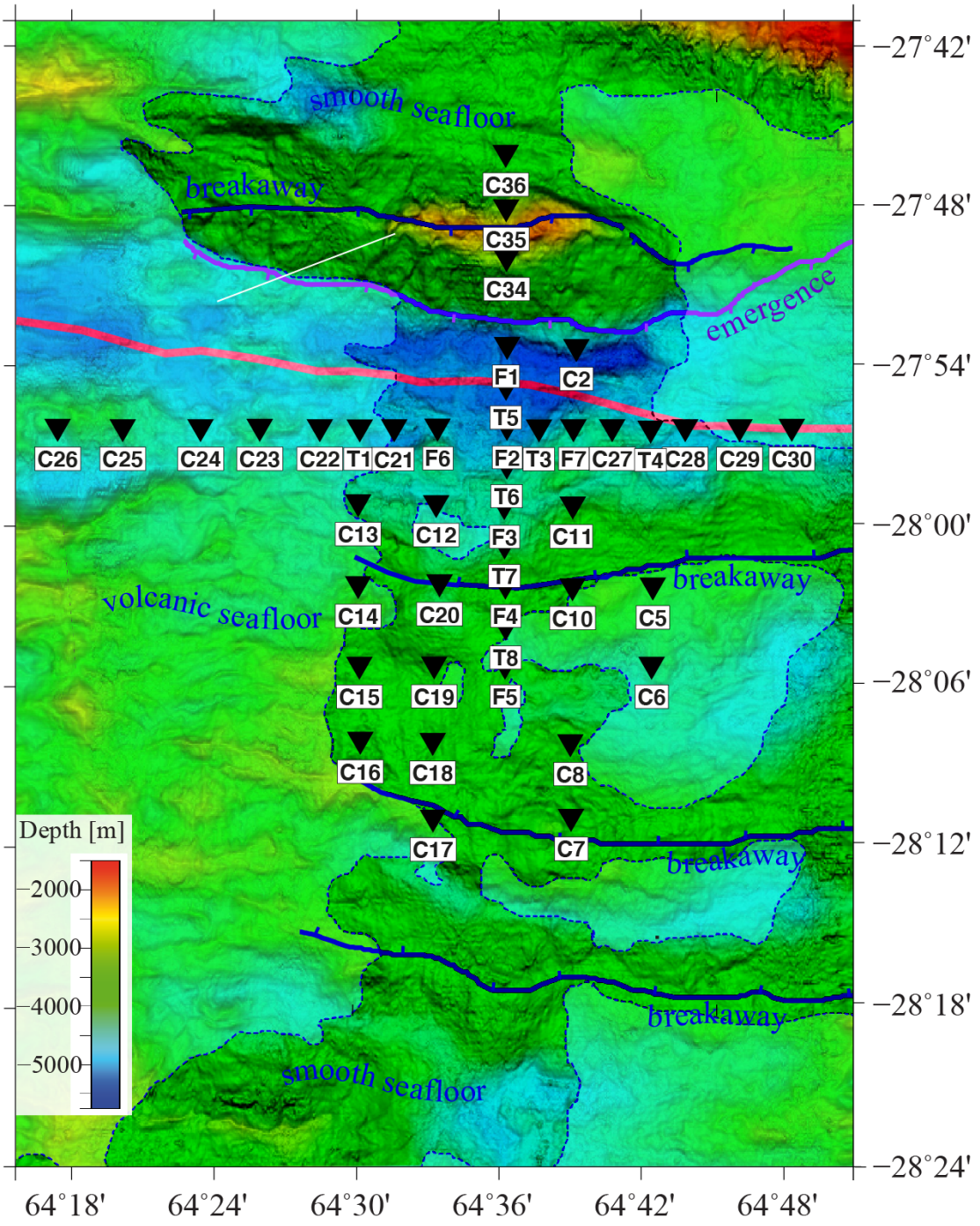


Figure 4.1: Bathymetry map of the study area. The locations of ocean bottom seismometers are shown by reverse triangles. The final stations used for inversion are indicated in black, and the removed stations based on data analysis are shown in gray. The darkened region is an indicator of smooth seafloor or ultramafic rocks, and the rest is volcanic seafloor. Most of the stations have been placed on smooth seafloors. The thick red line is the axis, and the purple line indicates the emergence of the axial detachment fault system. The breakaway of the active fault is located at the top of the northern axial valley and suggested breakaways of inactive faults are seen in the southern Antarctic plate.

in different operating systems. In the next section, we will explain how we obtained the SAC file for each of the three types of OBS instruments. After conversion, every

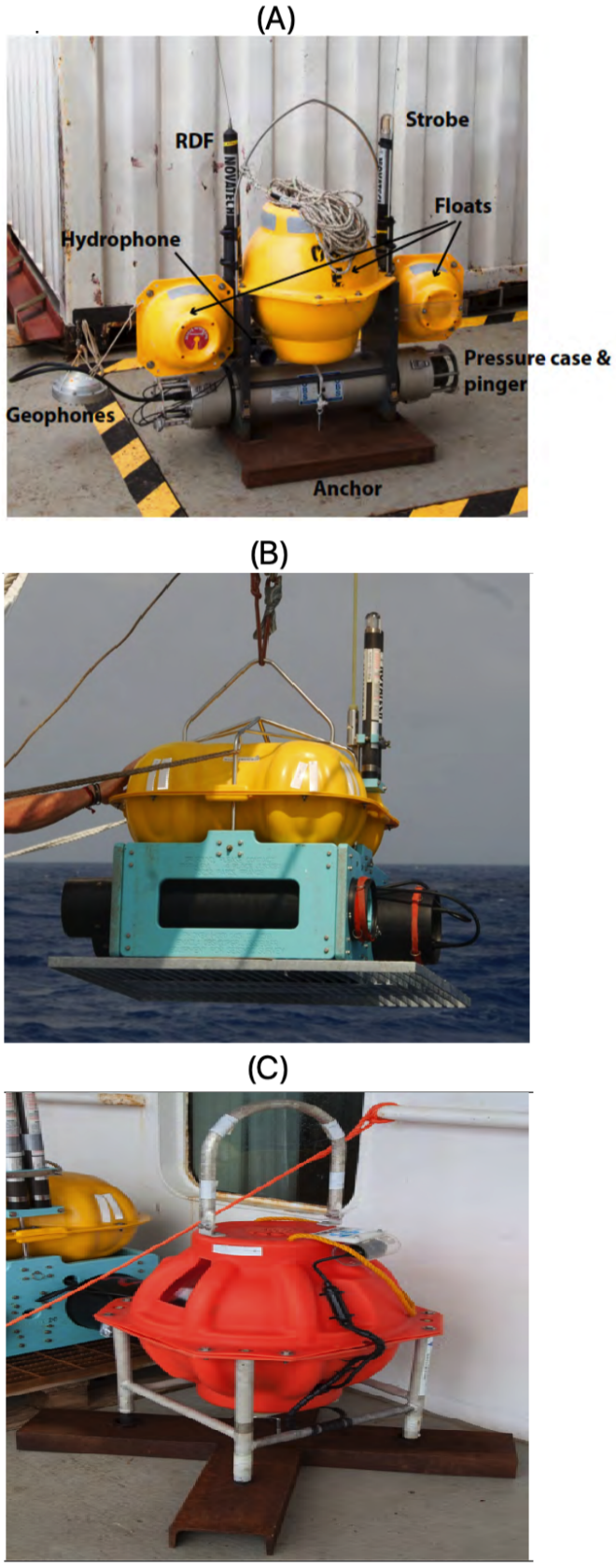


Figure 4.2: A) Canadian OBS instrument B) French OBS instrument C) Taiwanese (MicrOBS)

SAC file is related to one station of OBS, one channel (hydrophone, x, y, and z components of geophone), and a specific period of time (e.g., 1 month). No-shot periods of data are considered passive data. The channel numbers were attributed to different components of OBS in our data set. To ensure using the required component in the next phases, we have indicated the channel numbers and their corresponding OBS instruments in the tables 4.2, 4.3 and 4.4. OBSs may usually experience clock drifts detected after retrieval by a time difference between internal clocks and the GPS clock (Naranjo et al., 2021). The drift of the internal clock of the OBS and moving the OBS on the sea floor during their descent to the seafloor demanded the necessity of the clock drift and relocation corrections. The relocation of data was done by information from table 4.1.

### 4.1.1 French instrument

We converted raw data to SAC format by using $runL2C - SAC.m$ program provided by IPGP in the MATLAB environment. First, we relocated our data in this program and then by giving the information, the clock drift was applied by formula as follows:

clock drift = (end of instrument time - end of GPS time)/(end of GPS time - Time zero)

The produced SAC files for the whole time of acquisition and three French OBS are shown in Figure 4.3.

### 4.1.2 Taiwanese instrument

As the instruments are MicrOBs, MCC-Process 2.10 software from IFREMER was used to obtain SAC data. Figure 4.5 depicts the interface of this program. First, we obtained the SAC file, including the whole information of every station. Then, we relocated our data using SAC software (Goldstein and Snoke, 2005; Goldstein et al., 2003). Clock drift was corrected in MCC-Process 2.10 software. To get smaller sampling intervals, we have written a code in Python. We selected 3 stations as examples to show the processed SAC data for the vertical component of OBSs and the whole time of acquisition in Figure 4.4.

### 4.1.3 Canadian instrument

To get the SAC data of each OBS, we have taken different steps for Canadian instruments. First, we converted raw data into SEG-Y format using Dobs2sgy software. Then, we made the trace table for every minute of one station. Because of the weakness of this software in writing the proper header , we converted SEG-Y format into Ascii format in the Seismic Unix environment (Cohen and Stockwell, 2003). We obtained the SAC file, including the whole time of acquisition, from this Asciil file using Sac software. Then we fixed the problem of headers with the scripts of SAC software. We relocated and applied clock drift in this step. The display of 3 OBSs for the whole time of acquisition is indicated in Figure 4.6.

| STATIONS | DEPLOYMENT | RETRIEVAL | LATITUDE | LONGITUDE |
|---|---|---|---|---|
| C2 | 28/09/2014 | 14/10/2014 | -27.8978 | 64.65360 |
| C5 | 28/09/2014 | 15/10/2014 | -28.0432 | 64.70610 |
| C6 | 28/09/2014 | 15/10/2014 | -28.0914 | 64.70530 |
| C7 | 28/09/2014 | 15/10/2014 | -28.1840 | 64.65000 |
| C8 | 28/09/2014 | 15/10/2014 | -28.1386 | 64.64950 |
| C10 | 28/09/2014 | 15/10/2014 | -28.0436 | 64.6510 |
| C11 | 28/09/2014 | 15/10/2014 | -27.9939 | 64.6512 |
| C12 | 28/09/2014 | 13/10/2014 | -27.9930 | 64.5574 |
| C13 | 28/09/2014 | 13/10/2014 | -27.9924 | 64.5038 |
| C14 | 28/09/2014 | 13/10/2014 | -28.0423 | 64.5038 |
| C15 | 28/09/2014 | 13/10/2014 | -28.0914 | 64.5046 |
| C16 | 28/09/2014 | 14/10/2014 | -28.1371 | 64.5053 |
| C17 | 28/09/2014 | 14/10/2014 | -28.1844 | 64.5552 |
| C18 | 28/09/2014 | 14/10/2014 | -28.1378 | 64.5550 |
| C19 | 28/09/2014 | 13/10/2014 | -28.0913 | 64.5560 |
| C20 | 28/09/2014 | 13/10/2014 | -28.0412 | 64.5597 |
| C21 | 14/10/2014 | 25/10/2014 | -27.9467 | 64.5286 |
| C22 | 14/10/2014 | 23/10/2014 | -27.9466 | 64.4775 |
| C23 | 14/10/2014 | 23/10/2014 | -27.9465 | 64.4363 |
| C24 | 14/10/2014 | 23/10/2014 | -27.9466 | 64.3956 |
| C25 | 14/10/2014 | 23/10/2014 | -27.9466 | 64.3422 |
| C26 | 14/10/2014 | 23/10/2014 | -27.9465 | 64.2975 |
| C27 | 15/10/2014 | 26/10/2014 | -27.9466 | 64.6782 |
| C28 | 15/10/2014 | 26/10/2014 | -27.9466 | 64.7284 |
| C29 | 15/10/2014 | 24/10/2014 | -27.9466 | 64.7656 |
| C30 | 15/10/2014 | 27/10/2014 | -27.9465 | 64.8015 |
| C34 | 15/10/2014 | 25/10/2014 | -27.8430 | 64.6057 |
| C35 | 15/10/2014 | 25/10/2014 | -27.8125 | 64.6054 |
| C36 | 15/10/2014 | 25/10/2014 | -27.7793 | 64.6051 |
| F1 | 28/09/2014 | 24/10/2014 | -27.8965 | 64.60610 |
| F2 | 28/09/2014 | 20/10/2014 | -27.9459 | 64.60600 |
| F3 | 28/09/2014 | 20/10/2014 | -27.9942 | 64.60410 |
| F4 | 28/09/2014 | 20/10/2014 | -28.0426 | 64.60490 |
| F5 | 28/09/2014 | 20/10/2014 | -28.0914 | 64.60460 |
| F6 | 28/09/2014 | 20/10/2014 | -27.9463 | 64.55830 |
| F7 | 28/09/2014 | 24/10/2014 | -27.9467 | 64.65160 |
| T1 | 27/09/2014 | 25/10/2014 | -27.9468 | 64.50490 |
| T3 | 28/09/2014 | 20/10/2014 | -27.9468 | 64.62800 |
| T4 | 28/09/2014 | 24/10/2014 | -27.9475 | 64.70460 |
| T5 | 28/09/2014 | 24/10/2014 | -27.9215 | 64.60530 |
| T6 | 28/09/2014 | 20/10/2014 | -27.9694 | 64.60590 |
| T7 | 28/09/2014 | 21/10/2014 | -28.0181 | 64.60430 |
| T8 | 28/09/2014 | 21/10/2014 | -28.0677 | 64.60510 |

Table 4.1: The columns from left to right are station names, date of deployment, date of retrieval, the latitude of stations in terms of degrees, and the longitude of stations. This information was used for relocation.

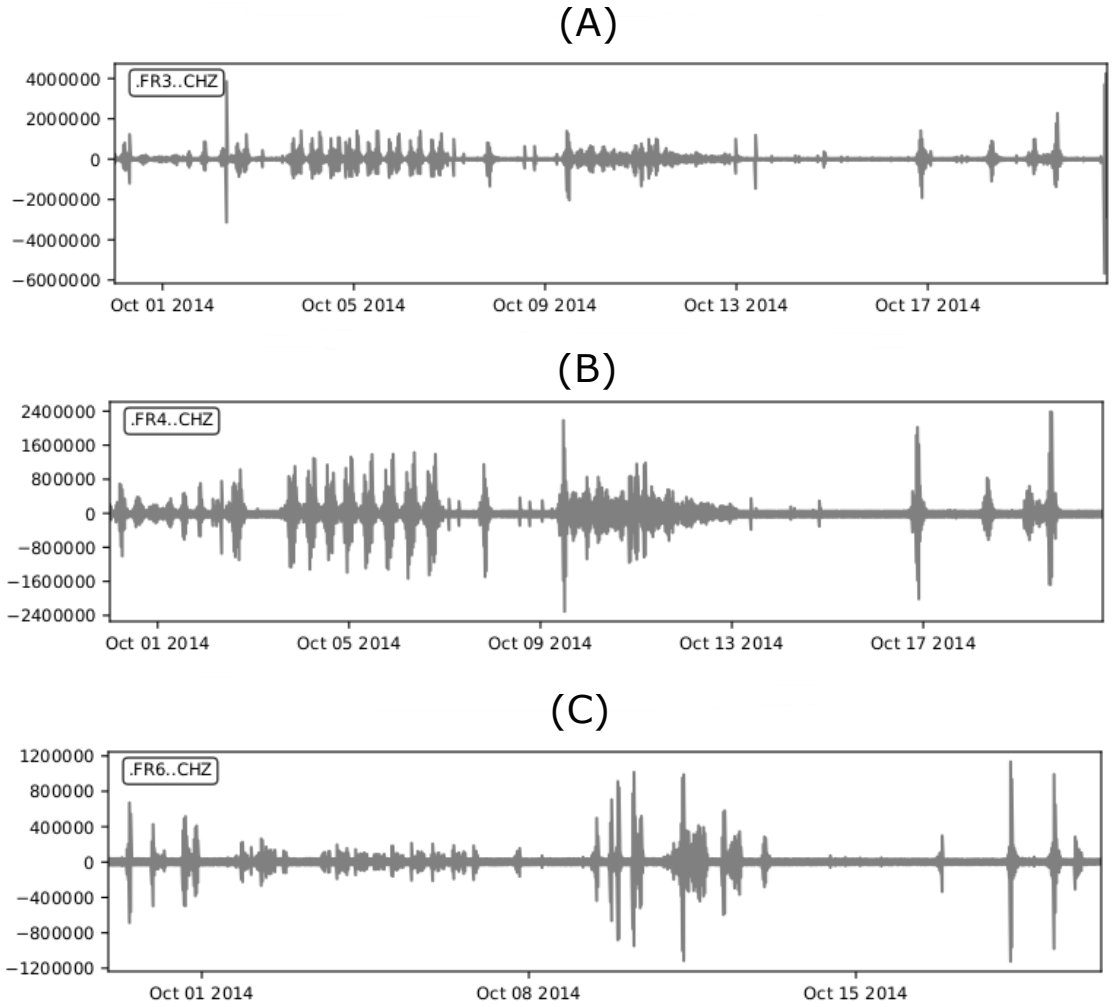


Figure 4.3: Display of SAC data from three French OBS stations for the whole time of acquisition. From top to bottom, the station numbers are F3, F4, and F6. The component of OBS is vertical.

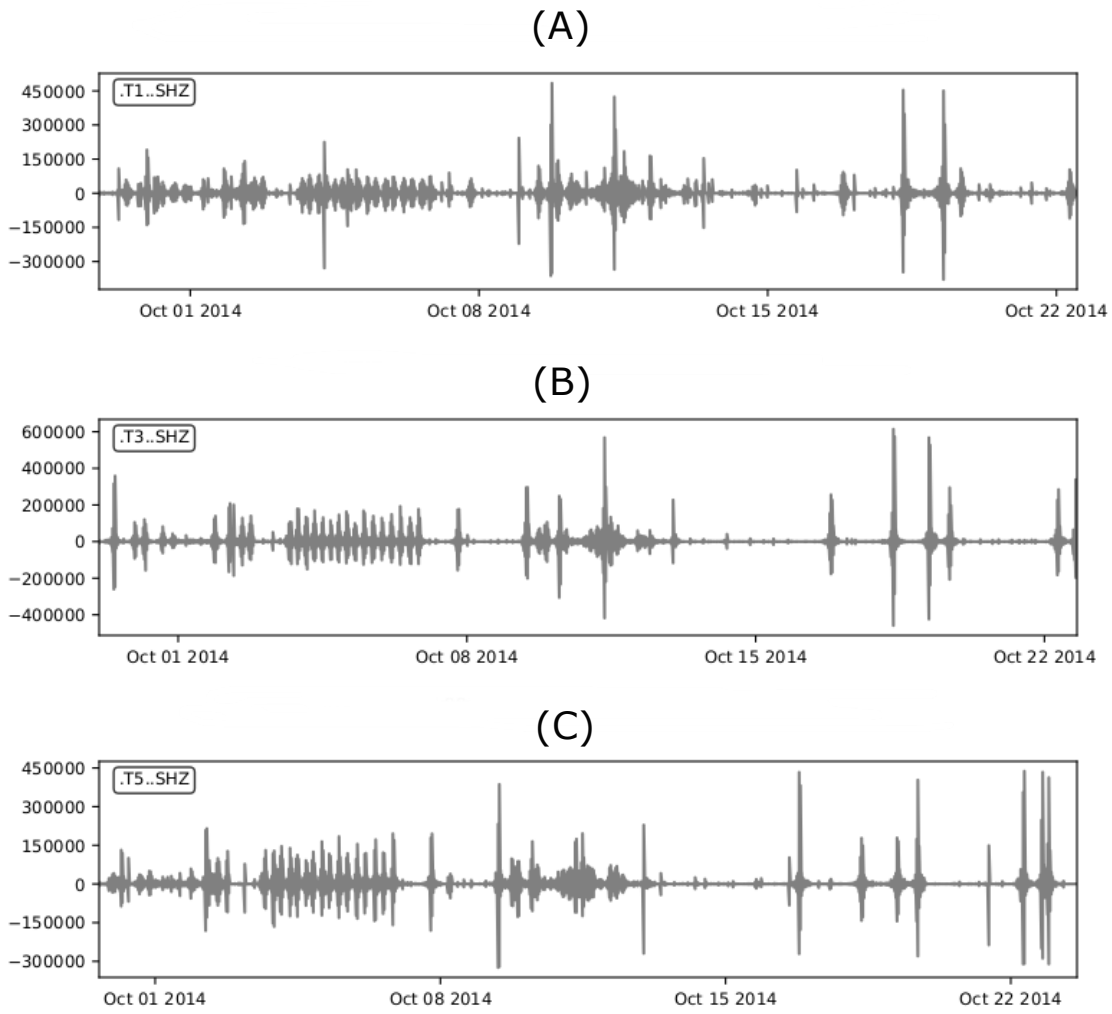


Figure 4.4: Display of SAC data from three Taiwanese stations for the whole time of acquisition. From top to bottom, the station numbers are T1, T3, and T5. The component of OBS is vertical.

| Number of channels | type of French receiver |
|---|---|
| 1 | Hydrophone |
| 2 | Horizontal |
| 3 | Horizontal |
| 4 | Vertical |

Table 4.2: The number of channels shows the type of receiver in a French OBS instrument.

| Number of channels | Type of Taiwanese receiver |
|---|---|
| 1 | Hydrophone |
| 2 | Vertical |
| 3 | Horizontal |
| 4 | Horizontal |

Table 4.3: The number of channels shows the type of receiver in a Taiwanese OBS instrument.

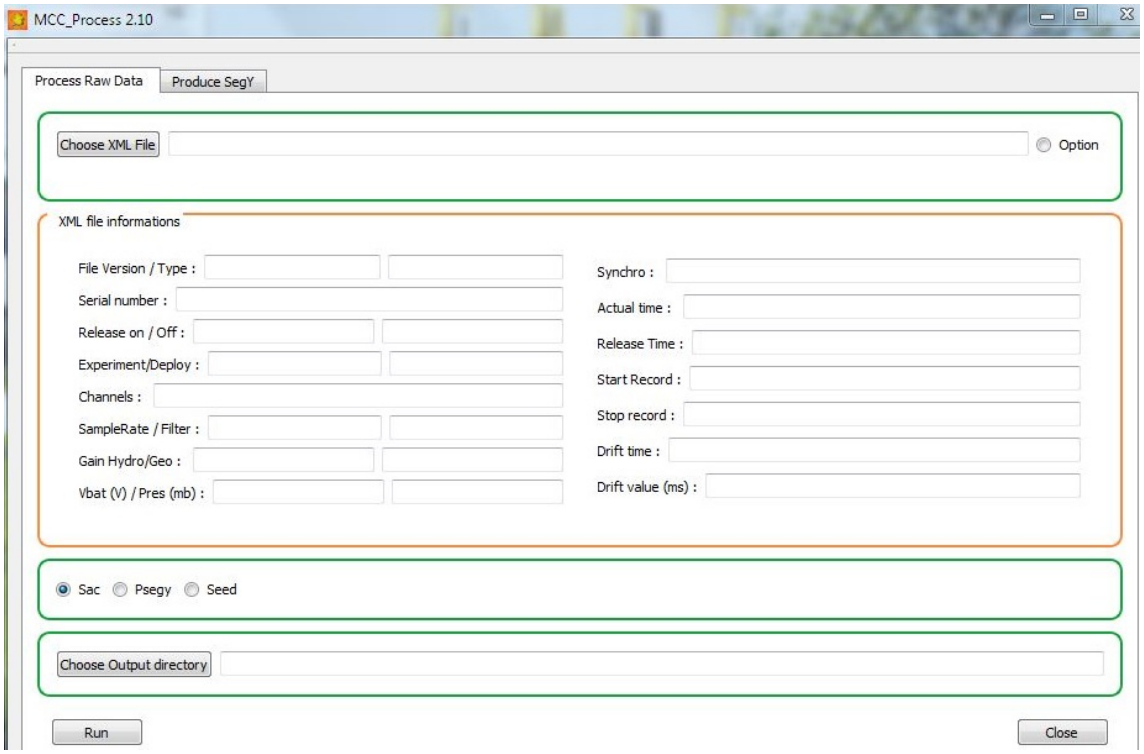


Figure 4.5: The interface of MCC-Process 2.10 software for conversion of the Taiwanese data set.

## 4.2 Acquisition and preparation of active seismic data

The active seismic data used in this investigation was acquired by 16 2D OBSs (long horizontal profile in Figure 4.1). To analyze active data, we used only the hydrophone component of OBS. The OBSs are located in an EW profile sub-parallel to the ridge axis in the easternmost part of SWIR. The length of the profile is 56 km.

| Number of channels | Type of Canadian receiver |
|---|---|
| 1 | Hydrophone |
| 2 | Vertical |
| 3 | Horizontal |
| 4 | Horizontal |

Table 4.4: The number of channels shows the type of receiver in a Canadian OBS instrument.

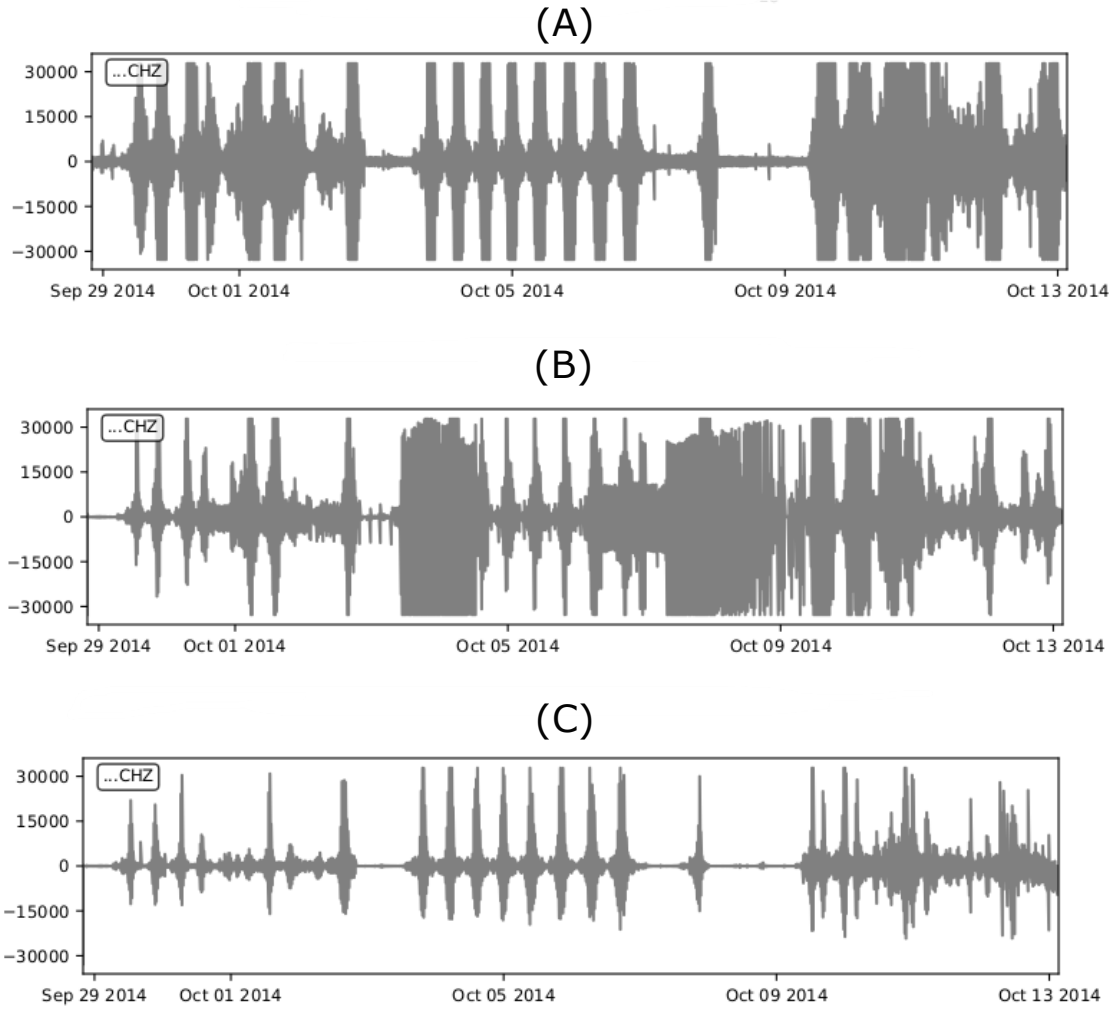


Figure 4.6: Display of SAC data from three Canadian stations for the whole time of acquisition. From top to bottom, the station numbers are C2, C5, and C19. The component of the receiver is vertical.

The seismic source included 14 guns for a total volume of 6790 in3. The average depth of the seismic source was 14 m (Leroy et al., 2015; Leroy and Cannat, 2014). 360 shots were used in this study. The shot interval between stations 4 and 15 was 150 meters, and for the rest of the stations, it was 300 meters. The inter-station distance was 2.1–7.2 km, and OBS's depths ranged between 4.2 and 4.8 km. The standard format of active data is SEGY. A relocated data set in SEGY format was handed to us from Dalhousie University. Figure 4.7 depicts the display of three OBS SEGY files.

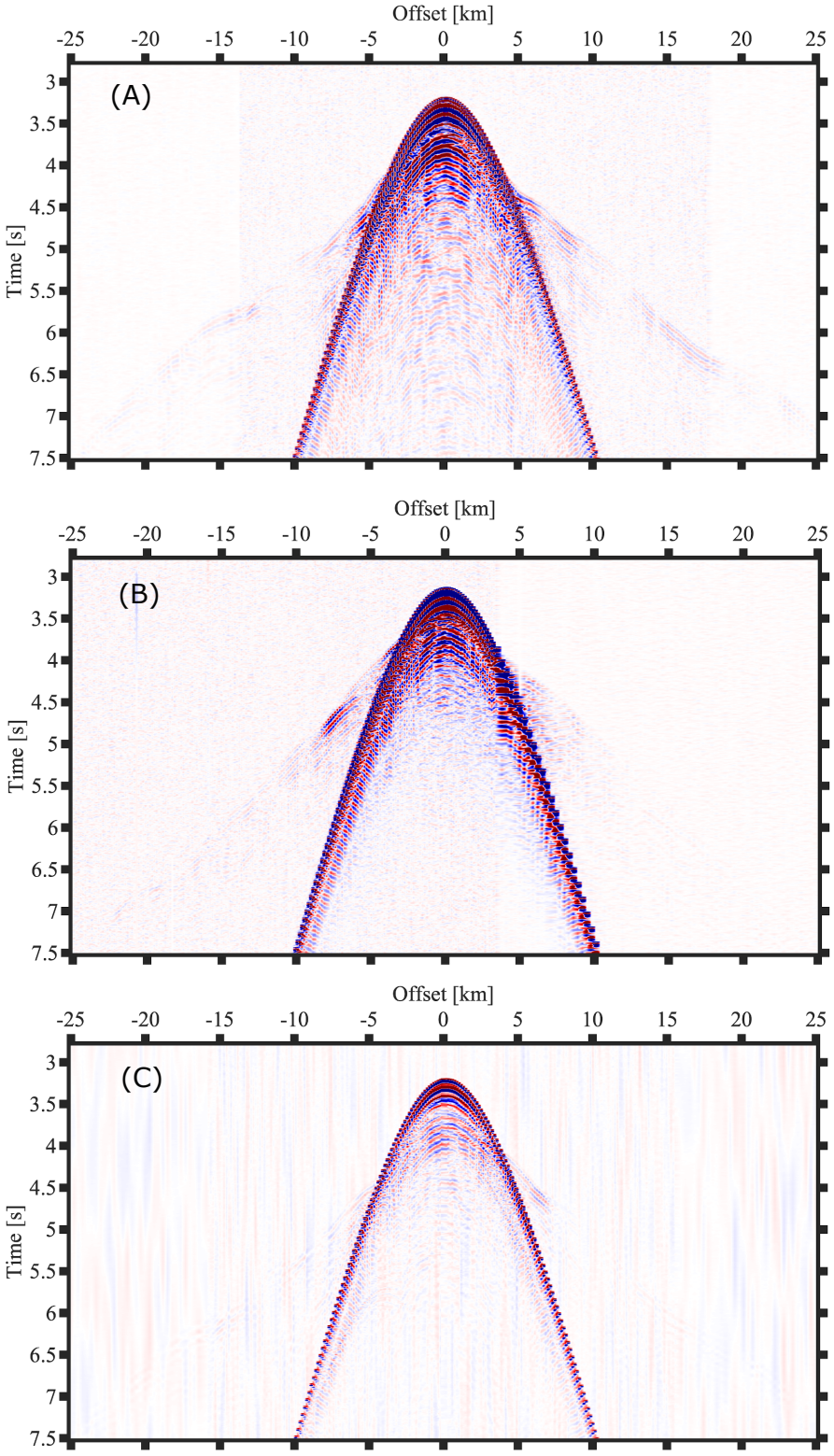


Figure 4.7: The display of OBS gathers of three stations. A) Station T1; B) Station C28; and C) Station F2. The component of the receiver is the hydrophone.

# Chapter 5

# Seismic Ambient Noise Imaging of a Quasi-Amagmatic Ultra-Slow Spreading Ridge


## Summary

This chapter focuses on the usage of ambient noise interferometry in SWIR and has been published as: Mohamadian Sarvandani, M., Kästle, E., Boschi, L., Leroy, S. and Cannat, M., 2021. Seismic Ambient Noise Imaging of a Quasi-Amagmatic Ultra-Slow Spreading Ridge. Remote Sensing, 13(14), p.2811. The published article can be found through the link: https://doi.org/10.3390/rs13142811.


## 5.1 Abstract


Passive seismic interferometry has become very popular in recent years in exploration geophysics. However, it has not been widely applied in marine exploration. The purpose of this study is to investigate the internal structure of a quasi-amagmatic portion of the Southwest Indian Ridge by interferometry and to examine the performance and reliability of interferometry in marine explorations. To reach this goal, continuous vertical component recordings from 43 ocean bottom seismometers were analyzed. The recorded signals from 200 station pairs were cross-correlated in the frequency domain. The Bessel function method was applied to extract phase–velocity dispersion curves from the zero crossings of the cross-correlations. An average of all the dispersion curves was estimated in a period band 1–10 s and inverted through a conditional neighborhood algorithm which led to the final 1D S-wave velocity model of the crust and upper mantle. The obtained S-wave velocity model is in good agreement with previous geological and geophysical studies in the region and also in similar areas. We find an average crustal thickness of 7 km with a shallow layer of low shear velocities and high Vp/Vs ratio. We infer that the uppermost 2 km are highly porous and may be strongly serpentinized.

## 5.2 Study Area and Motivation

The Southwest Indian Ridge (SWIR) is an ultra-slow spreading ridge that separates Africa and Antarctica. It reaches from the Bouvet triple junction (BTJ) in the southern Atlantic Ocean to the Rodrigues triple junction (RTJ) in the Indian Ocean (Figure 5.1A). The mean spreading rate of this ridge is about 14 mm/year (Sauter and Cannat, 2010). Our study area is located in the easternmost part of the SWIR, centered at 64°35′E and 28°S. This easternmost portion of the ridge comprises its deepest parts reaching more than 5500 m below sea level. Compared to other mid-oceanic ridges, it is relatively melt-poor (Cannat et al., 1999).

Previous surveys revealed the apparent absence of volcanic activities both at segment ends and along the ridge axis for over 100 km (Sauter et al., 2004; Carbotte et al., 2016). A large amount of mantle peridotite was detected in the axial valley (Dick et al., 2003; Sauter et al., 2004). The considerable quantity of outcrops of serpentinized peridotite on the seafloor is ascribed to exhumation in the footwall of detachment faults known as Oceanic Core Complexes (OCC) (Momoh et al., 2020). Corrugated OCCs appear in more magmatically active regions of the SWIR and can be identified by spreading-parallel corrugations. OCCs also occur in amagmatic and smooth terrains of the SWIR, which are named non-corrugated OCCs (Cannat et al., 2006; Sauter et al., 2013). Seafloor sampling in corrugated OCCs shows a variety of petrologic compositions including peridotites, gabbros, and volcanic types (Zhao et al., 2013). The dredging of the non-corrugated OCCs exhibited 90% serpentinized peridotites with a minor contribution of gabbros (Sauter et al., 2013). The exposed part of the detachment fault system related to these OCCs is divided into emergence and breakaway (Figure 5.1B).

Sampling and direct geological observations were limited to the near-surface seafloor and could not define the extension and depth distribution of serpentinization, magmatic rocks, and detachment faults. Therefore, geophysical methods were recruited to better understand the processes involved in shaping this melt-poor, ultra-slow spreading ridge. Limited off-axis geophysical data in the late 1990s indicated significant crustal thickness variations across and along the ridge axis in the eastern part of the SWIR. These significant variations suggested that the melt supply is spatially more concentrated and short-lived, in comparison to faster spreading ridges (Cannat et al., 2003). The first comprehensive off-axis data set in the easternmost part of the SWIR was collected in 2003 by bathymetric, magnetic, and gravimetric methods, covering an area of up to 250 km away from the ridge axis on both sides (Cannat et al., 2006). It was found that 37% of the surveyed seafloor showed only little or no evidence of volcanic activity. This non-volcanic seafloor is termed smooth seafloor because of its rounded topography. It has no equivalent at faster spreading ridges (Cannat et al., 2006). Four percent of the mapped region was identified as corrugated OCCs (Tucholke et al., 1998) and the remaining 59% was shown to be formed by volcanic activity (Sauter and Cannat, 2010). The melt supply appears to be focused beneath the volcanic centers. This focusing has been explained with melt originating near the base of the lithosphere and rapid extraction via dikes (Momoh et al., 2017; Smith et al., 2006; Cannat et al., 2003; Sauter et al.,

2004; Standish et al., 2008). Off-axis studies showed higher values of magnetic anomaly over volcanic seafloor areas and lower magnetization over smooth seafloor or non-volcanic regions. This weakly induced magnetization in non-volcanic areas of the seafloor is supposed to be produced by serpentinized peridotites (Sauter et al., 2008; Sauter and Cannat, 2010). A similar separation can be seen from maps of residual mantle Bouguer gravity anomaly where lower values (negative) were found for volcanic seafloor and higher values (positive) for deep sections or non-volcanic regions (Standish et al., 2008; Cannat et al., 2003).

Seismic reflection profiles near 64°E suggested reflectors dipping 45–55° down to 5 km below the seafloor beneath the emergence of the axial detachment fault. These reflectors are interpreted as tectonic damage zone in the basement (Momoh et al., 2017, 2020). Next to these damage zones, the thickness of the crust was greater than further away from it. The existence of a low Vp seismic crust of a total thickness of up to 5 km , defined as Vp < 7.5 km/s (Momoh et al., 2020), is explained by a downward gradient of serpentinization, with small magmatic intrusions. Several dipping reflectors were imaged in the hanging wall of the axial detachment fault and interpreted as small offset faults and trapped volcanic rocks emplaced in the ultramafic basement (Momoh et al., 2017). East of our study area, at 66°E, Minshull et al. (2006) report crustal thicknesses between 2.2–5.4 km (avg. 4.2).

Imaging the crustal structure is necessary to understand past and ongoing tectonic processes and provides an important prior to mantle tomographic studies. In this study, we investigate the robustness of the ambient-noise method in a marine exploration setting. The obtained subsurface shear-velocity model will be compared to previous studies and interpreted in the context of the regional tectonic evolution.

## 5.3 Ambient Noise Interferometry

Seismic ambient noise is a relatively continuous signal generated by the coupling between ocean waves and solid earth (Longuet-Higgins, 1950; Hasselmann, 1963). It is dominated by surface waves, with a period-dependent ratio of Rayleigh- to Love-wave energy (Friedrich et al., 1998). Cross-correlating and stacking continuous ambient-noise records of arbitrarily chosen station pairs yields the empirical inter-station Green's function which can be used to extract phase-velocity information (Campillo and Paul, 2003). Often, only the Rayleigh component of the surface waves is used because it is more energetic and can be measured on the vertical receiver component (Shapiro and Campillo, 2004). Rayleigh wave phase-velocity measurements are most sensitive to the subsurface Vs structure with a minor dependence on Vp and density. The resulting ambient noise models yield complementary information to more classical teleseismic earthquake tomography and active source experiments, with each of the methods being sensitive to a different frequency range and having a different ray path coverage (Boschi and Weemstra, 2015). Additionally, active source methods have become less popular due to the potentially detrimental effects on the marine fauna.

Passive seismic interferometry has been widely utilized to image the crust and

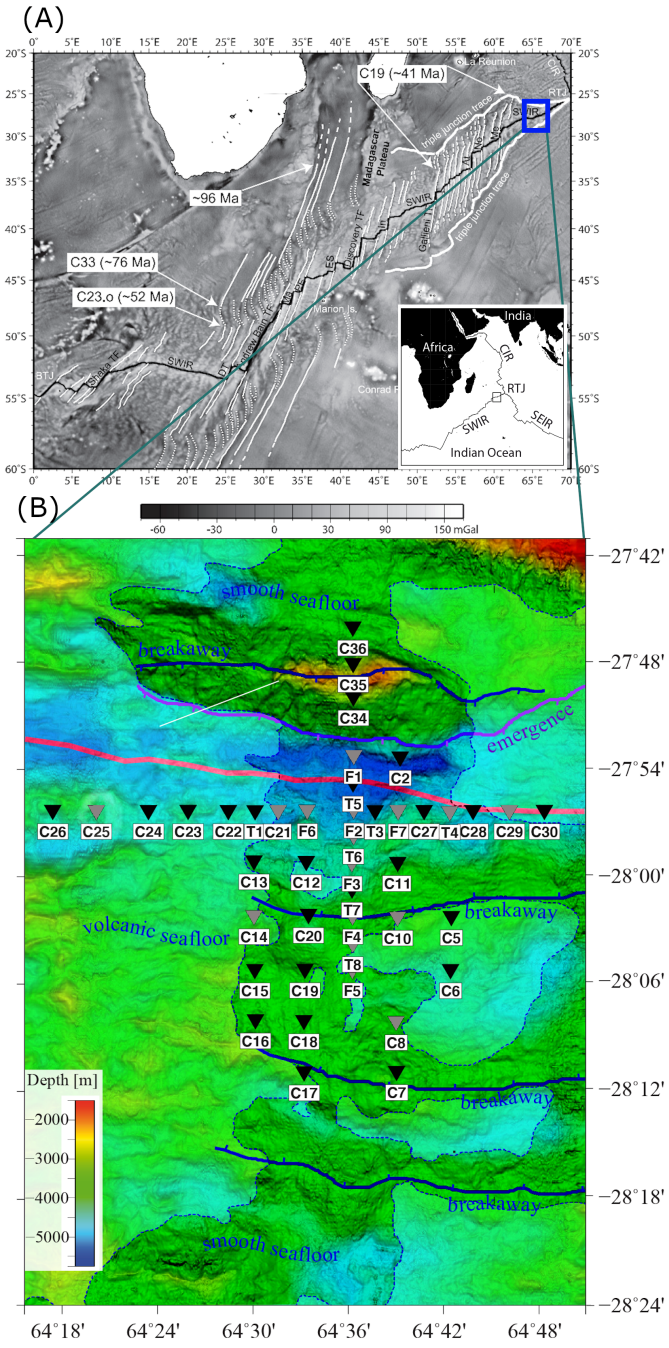


Figure 5.1: (**A**) Free-air gravity anomalies over Southwest Indian Ridge (SWIR). The thin black line shows SWIR axis. Variation of fracture zones orientation represents the variation of spreading direction with time (Chu and Gordon, 1999). The blue rectangle marks our study area. (**B**) Bathymetry map of the study area. The locations of ocean bottom seismometers are shown by reverse triangles. The final stations used for inversion are indicated by black color and the removed stations based on data analysis are shown by gray color. Most of the stations have been placed on smooth seafloor. The red thick line is the axis and the purple line is indicating the emergence of the axial detachment fault system. The breakaway of the active fault is located at the top of the northern axial valley and suggested breakaways of inactive faults are seen in the southern Antarctic plate.

upper mantle in continental areas (Lin et al., 2007; Moschetti et al., 2007; Zheng et al., 2008; Yang et al., 2007). There are significantly fewer studies in oceanic regions, mainly because of limited availability of seismic networks on the ocean

bottom and high levels of local noise, e.g., instrumental noise which is unusable as opposed to the ambient-noise signal (Harmon et al., 2007; Yao et al., 2011). In the next steps, we will explain theoretical concepts of measurement, processing, and imaging with ambient noise data. Furthermore, we illustrate how we have applied the concepts to get the final S-wave velocity model.

## 5.4 Measurement of Ambient-Noise Data

The marine seismic data used in this study were acquired by 43 Ocean Bottom Seismometers (OBS), each having three components geophones and one hydrophone. To analyze the ambient-noise signals, we used only the vertical component of the geophones (Yao et al., 2011; Bohlen et al., 2004). The data acquisition took place between 25 September and 30 October 2014 during the SISMOSMOOTH cruise (Leroy and Cannat, 2014; Leroy et al., 2015). As the instruments were from three different countries, we have labeled the stations Canadian (C), Taiwanese (T), and French (F) (Figure 5.1B). Of the 43 OBS stations used in this study, 29 were Canadian, 7 Taiwanese, and 7 French. The sampling rate was 250 Hz. Based on the furthest inter-station distances, the east-west and north-south aperture of the array was 56 km and 19 km, respectively. The spacing between the OBS stations was 2.5–5 km, and their depth ranged between 3.9 and 5.01 km. The raw records have been split into their components and corrected for clock drift and relocation errors.

## 5.5 Data Analysis

### 5.5.1 Probability Density Function (PDF)

We did a power spectral density (PSD) estimation of the recorded signals and their probability density function (PDF) at each station (McNamara and Boaz, 2006). While this analysis is expected to be dominated by ambient-noise sources, it includes also earthquakes and undesired signals, i.e., instrumental glitches, body waves or signals that do not propagate between stations pairs, that may deteriorate the ambient-noise measurements. We use this information to (1) estimate the intensity of the ambient-noise signals at different frequencies, (2) estimate the portion of undesired signals, and (3) check the overall health of the instrument.

The PSD curves were estimated in terms of decibel at each frequency via direct Fourier transform introduced in (Cooley and Tukey, 1965). PDFs were constructed at each frequency distribution bin by gathering PSDs in 1/8 octave of period intervals and 1 decibel of power intervals. We have shown 4 exemplary PDF plots in Figure 5.2. Each figure is for the vertical component of one station and during the whole time of recording. The PSD curves with higher probability distribution were interpreted as the ambient noise whereas the scattered PSD curves can be attributed to undesired signals (Agius et al., 2014). The analysis indicates that the recorded energy is low at frequencies below ~0.1 Hz. Between 0.1 and 3 Hz, the curves reach a flat level showing low amplitude variations and a high probability level. At frequencies above 3 Hz, the variance between PSD curves increases significantly, which represent likely a result of random, local noises (McNamara

and Boaz, 2006; Mordret et al., 2013). We used the PDF analysis in the junction with an inspection of the cross-correlation curves shown in the next section to limit the range of frequencies used in this study. This reduction of the frequency range speeds up the processing.

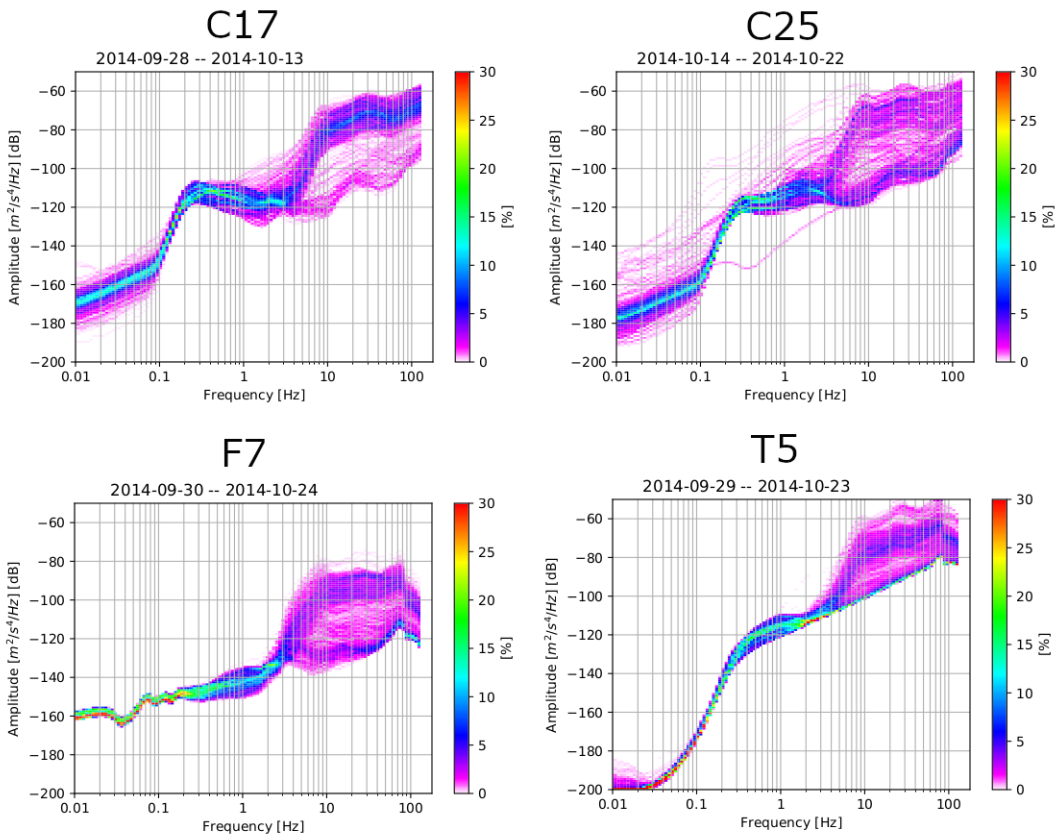


Figure 5.2: Initial analysis of noise data: every individual curve gives the power spectral density (PSD). Color bars display the probability of distribution of seismic power spectral density at different frequencies. Every plot represents the vertical component of one station (station ID at the top) during the entire recording time. Both high amplitudes and low signal variability can be observed mostly between 0.1 and 3 Hz.

### 5.5.2 Cross-Correlation

Of the 43 available stations, we made sure to only correlate station data with identical instrumentation to avoid any potential phase bias, as we did not have access to the instrument response data. This left us with 200 possible station pairs. The signals recorded at each station were cut into time windows of 10 min with an overlap of 60 percent between successive windows. More complete explanations about the effects of overlapping time windows can be found in (Seats et al., 2012). We did not explicitly remove earthquake signals which are expected to have only a minor effect on the obtained phase velocities (Ekström, 2014). However, we applied spectral whitening (Bensen et al., 2007), to equalize spectral amplitudes and down-weight the effects of earthquake signals and monochromatic sources. The whitened 10-min segments were cross-correlated between station pairs and stacked. The cross-correlation traces show forward and backward propagating signals (causal/acausal)

from opposing directions along the inter-station path, visible at positive and negative lag times in Figure 5.3. At inter-station distances greater 28 km, we did not observe any clear Rayleigh-wave signals whereas at distances below 5 km causal and acausal signals are not well-separated. This limitation is similar to the criteria of inter-station threshold recruited in the literature (see, e.g., in (Bensen et al., 2007; Mordret et al., 2013)) and resulted in 176 acceptable cross-correlations used in this study (Figure 5.3). The time-domain cross-correlations can be used to inspect the distribution of ambient-seismic-noise sources. Perfect symmetry between the cross-correlations at positive and negative lag times is an indicator of a homogeneous azimuthal noise-source distribution (Harmon et al., 2007; Yao et al., 2011). In theory, the waves moving in opposite directions should be identical between station pairs (Li et al., 2010). An asymmetric cross-correlation thus indicates a low signal-to-noise ratio.

We show 176 time-domain cross-correlations for four frequency bands 0.05–0.2 Hz, 0.2–0.4 Hz, 0.4–0.8 Hz, and 0.8–1.2 Hz in Figure 5.3 with regard to the inter-station distances on the vertical axis. We can discern the symmetry between positive and negative time lags in the frequency range of less than 0.8 Hz. The arrival of the Rayleigh wave signal cannot clearly be detected at higher frequencies (0.8–1.2 Hz). This loss means that the seismic noise sources are too weak and/or the random signals level is too high for a recording time of one month. Based on this analysis and the PDFs shown in the previous section, we limited our study to the frequency range between 0.05 and 1 Hz. This frequency range is in agreement with oceanic microseism utilized also in other seismic noise tomographic studies and typically generated by the non-linear interaction between the ocean and the solid earth (primary microseisms  0.07 Hz, secondary microseisms  0.14 Hz (Longuet-Higgins, 1950)). The amplitude differences between causal and acausal parts of the cross-correlations in Figure 5.4 are low, indicating a relatively homogeneous source distribution. This is supported by the more detailed comparison provided in Figure 5.4.

### 5.5.3 Amplitude Ratio

The amplitude ratios can be used to estimate the homogeneity of the noise-source distribution (Liu et al., 2020). The amplitude ratio is defined as the maximum amplitude at the positive lag time of the cross-correlations over the maximum amplitude at negative lag time. The rose diagram in Figure 5.5 shows amplitude ratios of all station pairs in our array. This diagram is a proxy for the azimuthal distribution of noise sources. If two microseisms propagate along the inter-station path in opposite directions and with the same amplitude, the amplitude ratio will be one. If the ambient-noise energy coming from one direction is larger, we will observe a dominant direction in the rose diagram. A comparison of Figure 5.5A–D suggests that the noise–source distribution is more uniform at relatively high (Figure 5.5D) compared to relatively low (Figure 5.5A) frequencies. However, apart from some peaks in the rose diagrams, we find no clear preferential noise–source direction. In other words, the ambient noise sources are approximately equi-distributed within the stud-

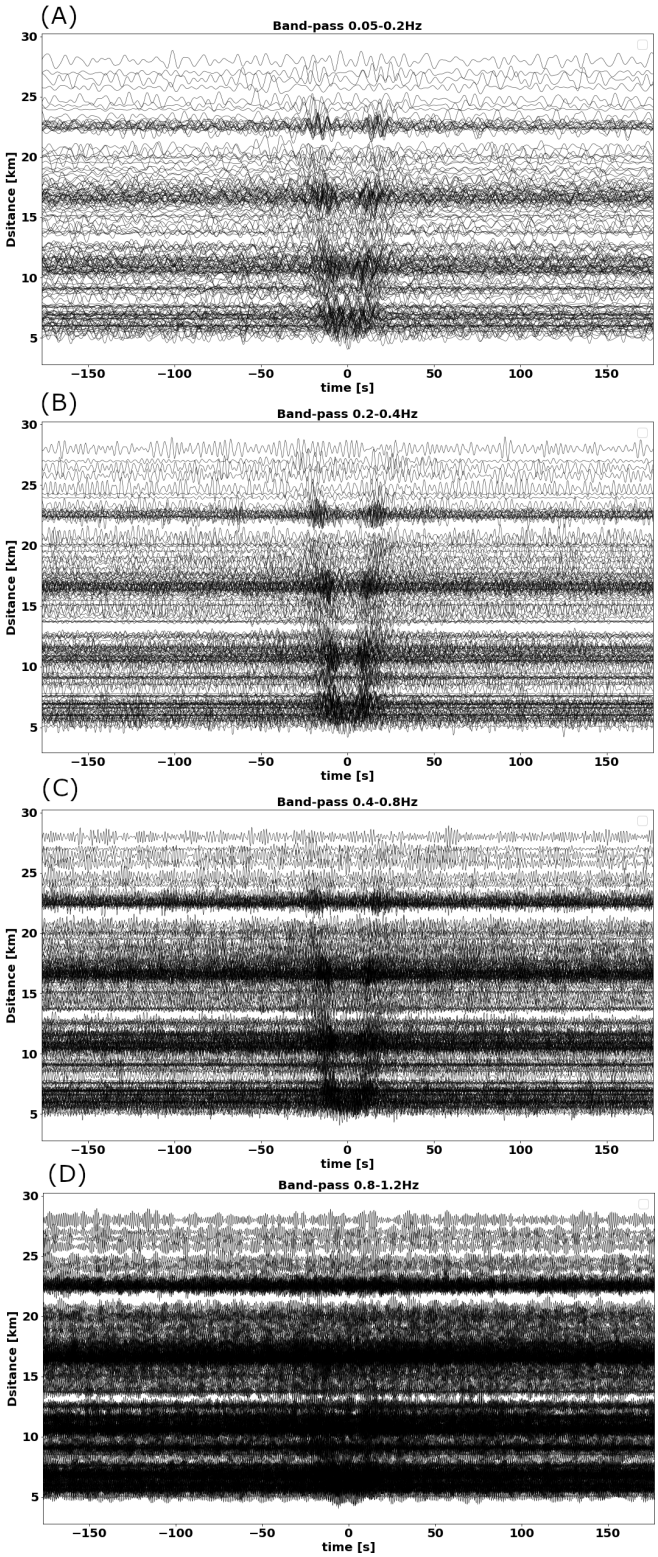


Figure 5.3: Cross-correlation in time domain for all the station pairs with inter-station distance between 5 and 28 km and for four frequency bands (**A**) 0.05–0.2 Hz, (**B**) 0.2–0.4 Hz, (**C**) 0.4–0.8 Hz, and (**D**) 0.8–1.2 Hz. The symmetry in positive and negative lags show the ambient-noise sources were homogeneously distributed. This symmetry is best observable for frequencies less than 0.8 Hz.

ied frequency range which is another endorsement for the quality of time-domain cross-correlations.

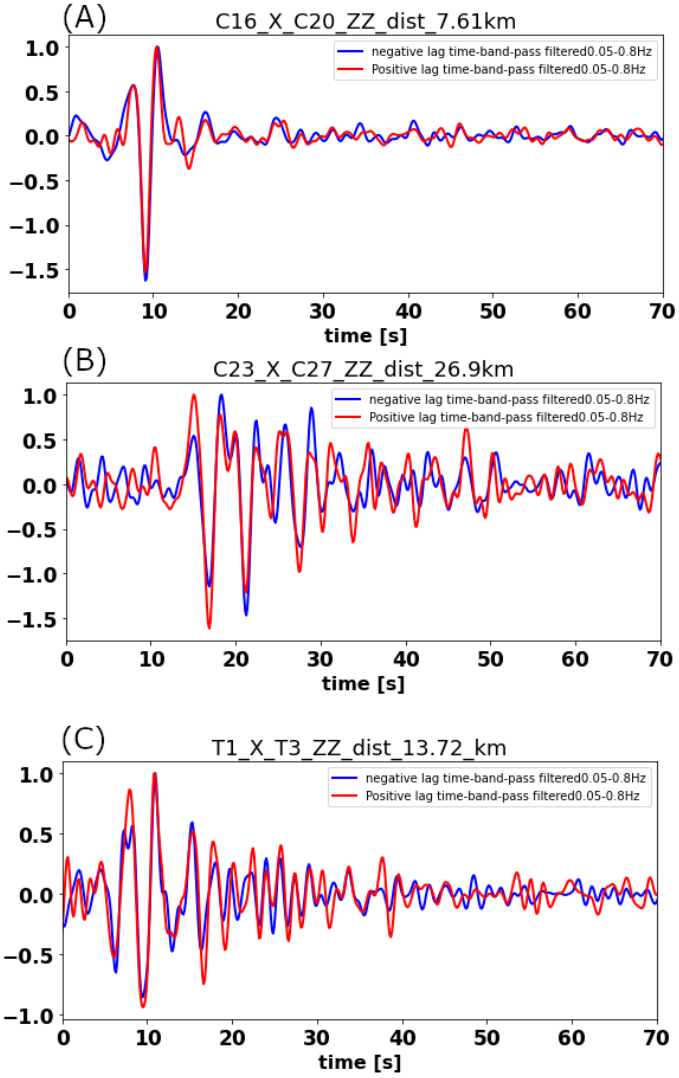


Figure 5.4: Comparison between the positive and negative lag time signals of station pairs (**A**) C16–C20, (**B**) C23–C27, and (**C**) T1–T3. The name of station pair, type of receiver (zz = vertical) and the inter-station distance in km is given at the top of every panel. Red lines show the positive lag time signal, flipped onto the negative time axis. The selected range of frequency is 0.05–0.8 Hz. The good overlap between positive and negative lag time signals confirms the symmetry in time domain cross-correlation and is taken as indication of the spatial homogeneity of source distribution.

### 5.5.4 Phase Velocity Determination

The cross-correlations can be used to obtain the empirical Green's functions and were analyzed to gain information on the subsurface structure between the receiver pairs (Boschi et al., 2012). Most authors either picked group velocities by identifying the maximum in the envelope of surface-wave packets (Shapiro et al., 2005; Stehly et al., 2006, 2009) or measured the phase velocity dispersion (Lin et al., 2008; Ekström et al., 2009). Fewer authors preferred utilizing the full waveform in their analysis (Tromp et al., 2010). In this study, we extracted phase velocities, because of the advantages in terms of accuracy, depth of investigation, and less contamination by interfering phases (Kästle et al., 2016; Boschi et al., 2012; Molinari et al., 2015).

Several methods of phase-velocity measurements have been introduced such

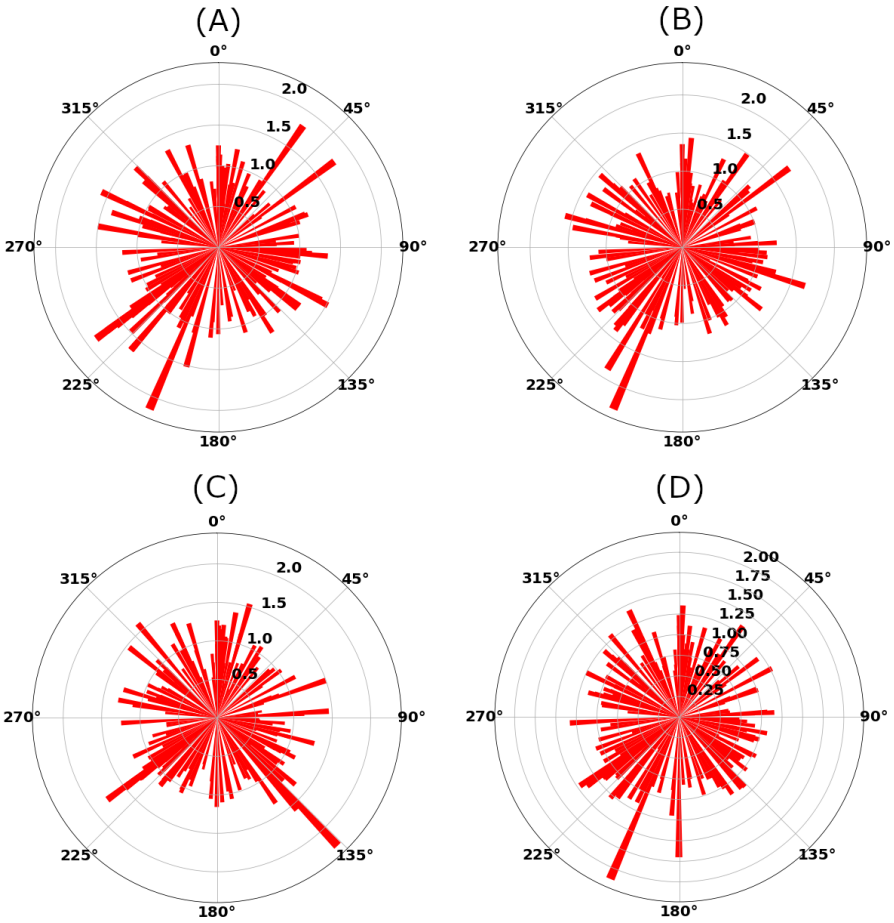


Figure 5.5: Rose diagrams of amplitude ratios for frequency bands: (**A**) 0.05–0.2 Hz, (**B**) 0.2–0.4 Hz, (**C**) 0.4–0.8 Hz, and (**D**) 0.05–0.8 Hz. The rose diagrams serve as proxy for the azimuthal distribution of noise sources.

as the image transformation technique in the time-domain (Yao et al., 2006), the Frequency-wave number (F-K) method (Lacoss et al., 1969; Capon, 1969), multiple filter analysis (Herrmann, 2013), and Bessel function methods based on the theory of (Aki, 1957) such as direct fitting in the frequency domain (Menke and Jin, 2015) or the herein applied zero-crossing fitting (Ekström et al., 2009; Ekström, 2014; Kästle et al., 2016). The intrinsic limitation of these methods is poor performance at low levels of signal-to-noise ratio. Plus, if the inter-station distance is too small, only a few zero-crossings can be picked along the frequency axis, thus degrading the resolution of this method (Menke and Jin, 2015). To mitigate these limitations, as explained above, we have only cross-correlated the station pairs distant by more than 5 km and also we checked the homogeneous distribution of sources in the data analysis (Figure 5.5D).

We used the previously computed cross-correlations and extract their zero crossings in the frequency domain (Figure 5.6). The zero crossings can be related to the phase velocity by comparison with the known zero crossings of a Bessel function (Ekström et al., 2009; Aki, 1957). We apply a smoothing filter to the cross-correlations which removes spurious zero crossings and thus stabilizes the obtained phase-velocity curves (Kästle et al., 2016). The phase-velocity picks from

the 176 station-station cross-correlations were then taken manually. The picking procedure was performed in two iterations: after picking the phase-velocities for all station pairs in the first round, we calculated an average dispersion curve based on the regression that was used to guide the manual picking in the second round. We applied several quality criteria: as explained above, we only accepted station pairs with an inter-station distance between 5 and 28 km. Because of their low signal-to-noise ratio, the French station data were not used. In addition, cross-correlations with large imaginary parts were discarded.

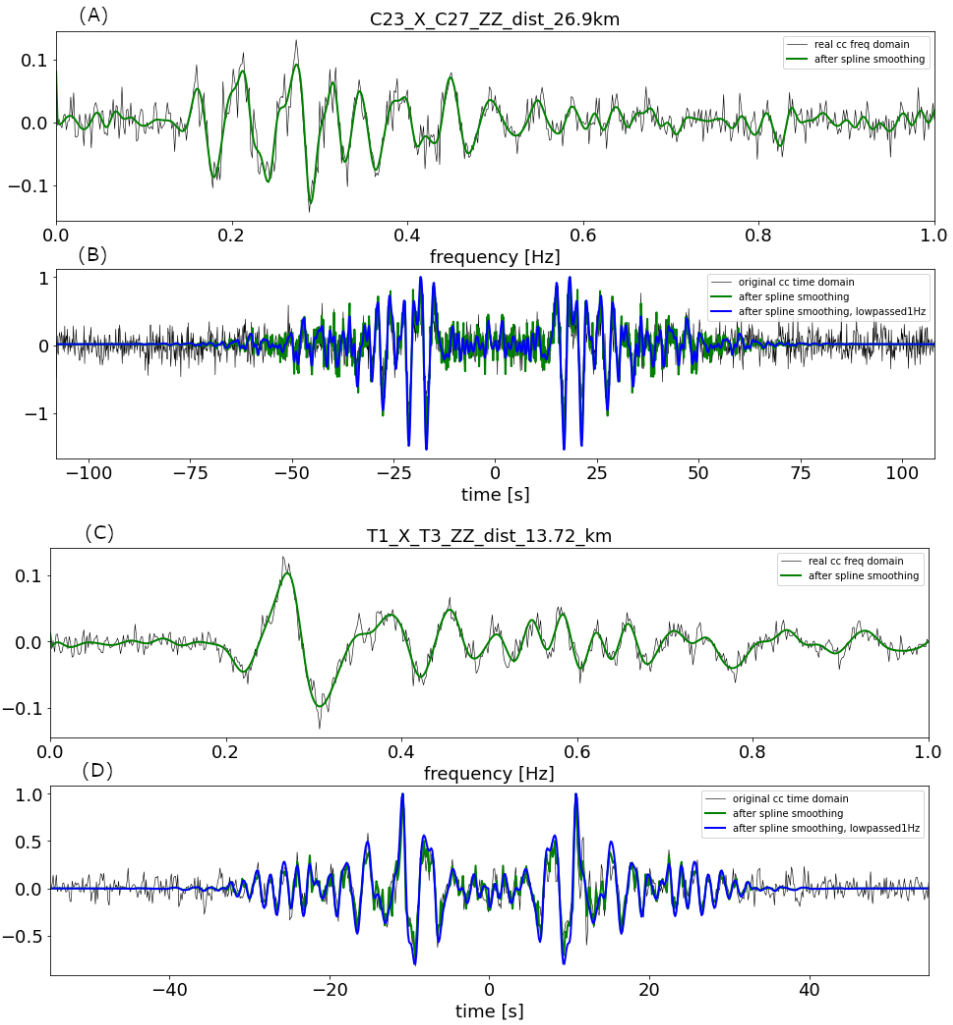


Figure 5.6: (**A**) Real part of the cross-correlation of station pair C23–C27 with an inter-station distance of 26.9 km in the frequency domain. (**B**) Cross-correlation of station pair C23–C27 in the time domain. (**C**) Real part of the cross-correlation of station pair T1–T3 with an inter station distance of 13.72 km in the frequency domain. (**D**) Cross-correlation of station pair T1–T3 in the time domain. Smoothing (green line) helps to reduce the effect of spurious zero crossings (Kästle et al., 2016). According to the data analysis, the maximum range of frequency set to 1 Hz.

## 5.6 Inversion of Phase-Velocity Dispersion Curves

We made use of the dispersive nature of Rayleigh waves to obtain a 1D depth-dependent shear-velocity profile. We used the average phase-velocity curve shown

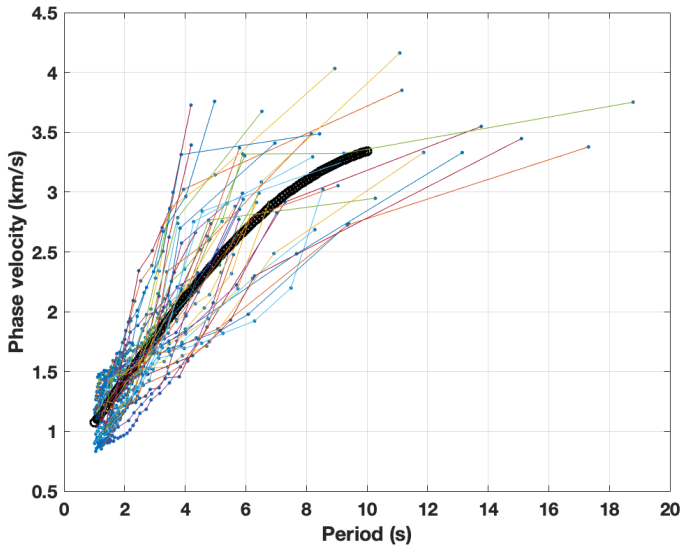


Figure 5.7: The picked phase velocity of every station pair is shown as colored lines. Blue circles are all the picked phase velocities. The thick black curve gives the average dispersion curve of all the picked data up to a maximum of 10 s.

in Figure 5.7, thus neglecting any lateral variations of the subsurface structure. The dispersion curve can be inverted with linearized methods (Herrmann, 1994; Nolet, 1981; Tarantola, 1987). However, we preferred applying a Bayesian approach because of the highly nonlinear relation between phase velocity and subsurface structure and the subsequent non-uniqueness of the problem. We used the conditional neighborhood algorithm implemented in the Dinver software (Wathelet, 2005). As in other Monte Carlo methods, we had to pre-define a range of priors for the pseudo-random sampling approach (Table 5.1). The range of statistical speculation and the role of prior information in this method are discussed in articles such as (Scales and Tenorio, 2001) and (Mosegaard and Tarantola, 1995). Compared to other Monte Carlo approaches, the conditional neighborhood algorithm is more self-adaptive when searching through the parameter space. The search starts with a pre-defined number ($n_{s0}$) of models distributed with a uniform probability in parameter space. The misfit function ($L_2$ norm) is calculated for every model and the $n_r$ models with the lowest misfits are selected for the next iterations. This is iterated $n_t$ times, and at each iteration the selected lowest-misfit models are decomposed into $n_s/n_r$ new models. The data misfit is given in relative units, normalized by the input data. In the conditional neighborhood algorithm, the dependency between parameters is taken into account at the beginning of the inversion by using a variable transformation (Wathelet, 2005).

The model is parameterized in terms of thickness, shear wave velocity (Vs), compressional wave velocity (Vp), and density ($\rho$) for each layer. Among them, Vs has the most important role and $\rho$ exercises the least influence on the dispersion curve. The Poisson's ratio, which links Vs and Vp, was allowed to vary between 0.2 and 0.5 as indicated in Table 5.1, according to the value of Poisson's ratio for geological materials (Wathelet, 2005). Vp and Vs are free parameters of the inversion. The Poisson's ratio is not a free parameter, but if a solution is generated with Vp and Vs such that the value of the Poisson's ratio is outside of the allowed

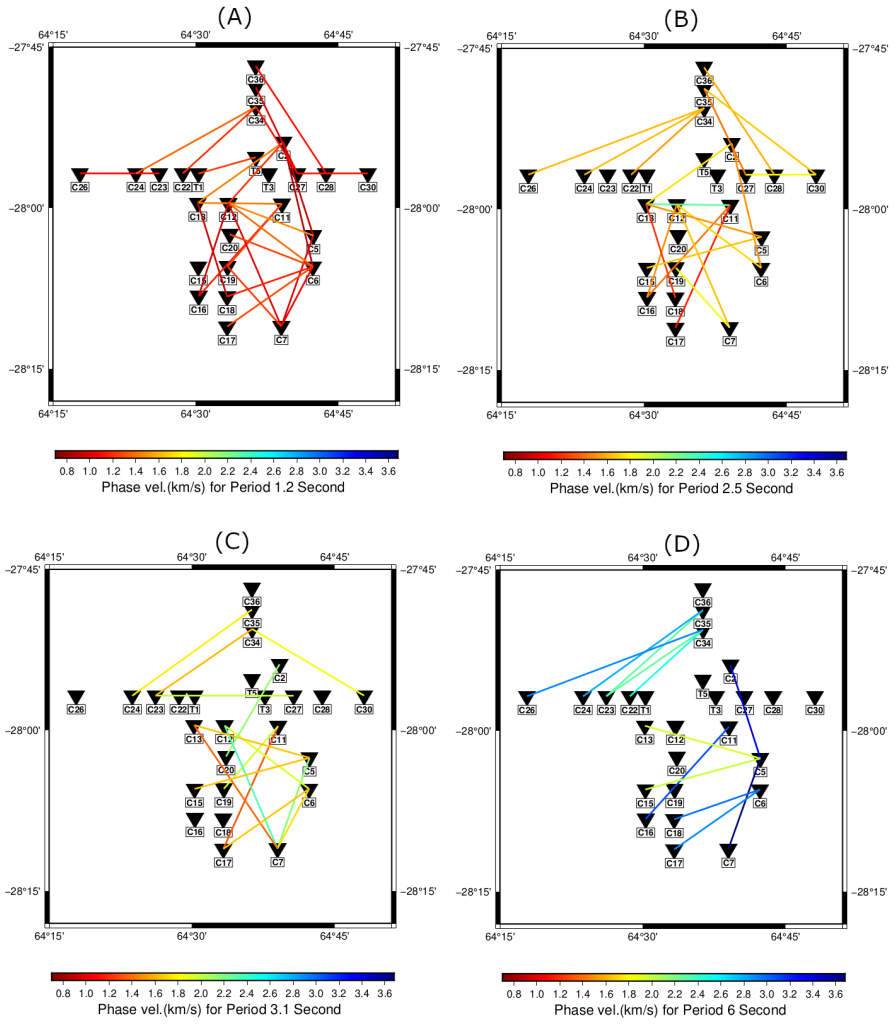


Figure 5.8: Phase velocity variations are indicated in (**A**) period 1.2 s, (**B**) period 2.1 s, (**C**) period 3.1 s, and (**D**) period 6 s. Reverse triangles indicate the location of the stations used in the final analysis. An increasing trend of the measured phase velocity from shorter to longer periods is observable.

range, that solution is discarded. We chose the following model search parameters: $n_{s0}$ = 50, $n_r$ = 50 and generated 10,000 models in total. We chose to use four layers whose prior ranges (Table 5.1) were defined based on the Preliminary Reference Earth Model (PREM) (Dziewonski and Anderson, 1981) and on several test runs in which we made sure that the search algorithm would generate a reasonably wide range of models centered around the measured data (Figure 5.9C). The obtained P-wave and S-wave velocity models are shown in Figure 5.9A,B, respectively. The black lines represent the average of the 5000 models with the lowest misfit and will be used for interpretation. The shown Vs profiles are more reliable, because of the higher sensitivity of Rayleigh waves to Vs compared to Vp.

## 5.7 Results and Discussion

We limit the discussion to the velocity models obtained from phase velocities up to a period of 10 s. This constraint allows investigating the subsurface structures down

Table 5.1: Parameterization for inversion

| Layer | $V_s$ (m/s) | Depth (m) | $V_p$ (m/s) | Poisson's ratio | density |
|---|---|---|---|---|---|
| $V_0$ | 200 to 1500 | 200 to 5000 | 300 to 3500 | 0.2 to 0.5 | 2.4 |
| $V_1$ | 1500 to 2800 | 1000 to 8000 | 2000 to 6500 | 0.2 to 0.5 | 2.6 |
| $V_2$ | 2600 to 3900 | 2000 to 12000 | 3500 to 9000 | 0.2 to 0.5 | 2.9 |
| $V_3$ | 4200 to 5500 | - | 4000 to 12000 | 0.2 to 0.5 | 3.4 |

to ~15 km. In general, we consider our average Rayleigh-wave dispersion curve to be robust. Because Rayleigh waves are mostly sensitive to Vs, we are also confident that our Vs models are reasonably well constrained. Rayleigh waves are well known to be much less sensitive to Vp than Vs (see Figure 5.10), so our inferences are Vp and the Poisson's ratio should be taken with care. We shall show, however, that the values we obtained are reasonable based on independent knowledge of those parameters. We also provide in Figure 5.9A,B a rough estimate of model uncertainty, defining as our confidence interval the range of values from three standard deviations below to three above the average. This definition of confidence is complicated near interfaces, where uncertainties in seismic velocity and interface depth are entangled with each other.

We first compare our average dispersion curve (Figure 5.9C) with results from ambient-noise tomography obtained in the south central Pacific (Figure 6 in (Harmon et al., 2007)) and in the transform fault region of East Pacific Rise (Figure 4 in (Yao et al., 2011)). These two areas were selected as two of the rare examples where ambient-noise interferometry has been used to image the oceanic lithosphere. While our study areas are different, this qualitative comparison provided us with some insights from similar tectonic settings. In the average dispersion curve in Figures 5.7 and 5.9C, we can identify an increasing trend of phase velocity up to a period of 20 s. This trend is similar to that found in the two other oceanic studies. Up to 16 s, both other regions have a phase velocity range of approximately 1.5–3.7 km/s while this range in our case is approximately 1–3.5 km/s. Lack of data in periods less than 2 s in (Harmon et al., 2007) probably account for the different minimum phase velocity.

Similar to our upper period bound of 10 s, (Yao et al., 2011) and (Harmon et al., 2007) mentioned that their phase velocity estimations for the fundamental mode of Rayleigh wave were subject to high uncertainty at periods greater than 8 s and 9 s, respectively. Nevertheless, longer recording time (200 days in (Harmon et al., 2007) and over 1 year in (Yao et al., 2011)) enabled them to benefit from ambient noise data up to periods of 16 s and 30 s. A longer recording time will usually lead to a smoother distribution of incoming ambient-noise energy and suppresses errors in the dispersion-curve measurements (Yao and Beghein, 2009).

The P-wave velocity in the crustal layer is expected to be lower than the velocity for olivine-rich gabbros, which is about 7 km/s (Miller and Christensen, 1997) which we use to approximate the the Moho depth. Therefore, we infer an approximate crustal thickness of 7.2 km from Figure 5.9A. A similar conclusion can be drawn from the S-wave velocity model in Figure 5.9B, where the maximum expected crustal S-wave velocity is approx. 3.9 km/s (Miller and Christensen, 1997). This

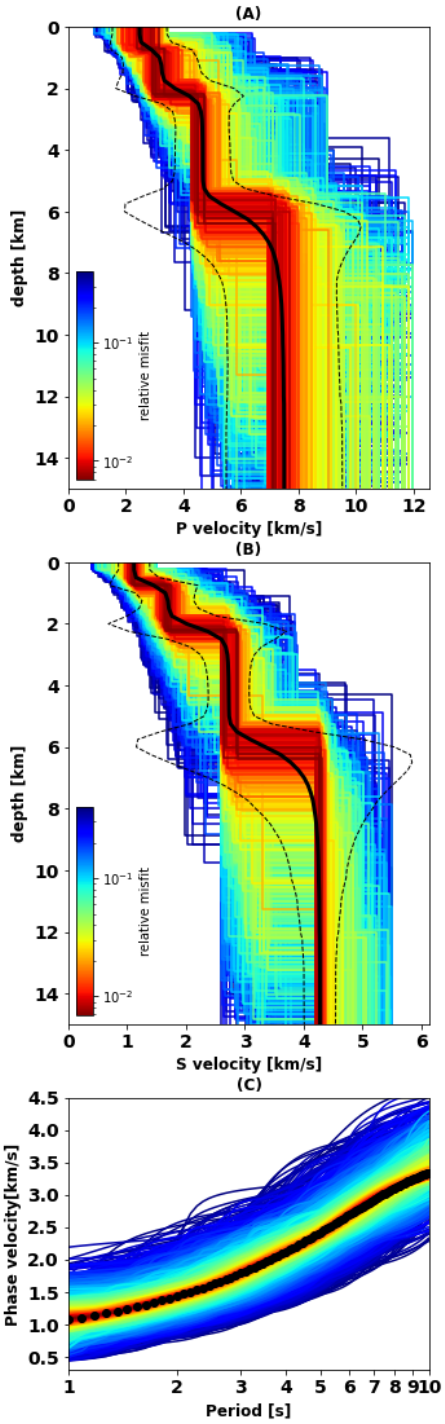


Figure 5.9: (**A**) 5000 lowest misfit P-wave velocity models, and (**B**) corresponding S-wave velocity model, with color denoting misfit value, as indicated by the color bars. The black solid lines denote the Vp and Vs averages of all shown models. Dashed lines identify our selected confidence interval, which we define as three standard deviations above and below the average, at each depth. Bulges in the dashed lines around discontinuities are inevitable artifacts of combining uncertainty in seismic velocity and discontinuity depth. (**C**) Rayleigh phase-velocity data corresponding to the models in (**A**,**B**). The black curve in panel (**C**) identifies the picked values of phase velocity.

thickness is larger than the 4.2–5 km estimated from the P-wave velocity model in (Momoh et al., 2017) in the central part of the study area. The larger estimate of crustal thickness resulting from our approach could be due to the location of

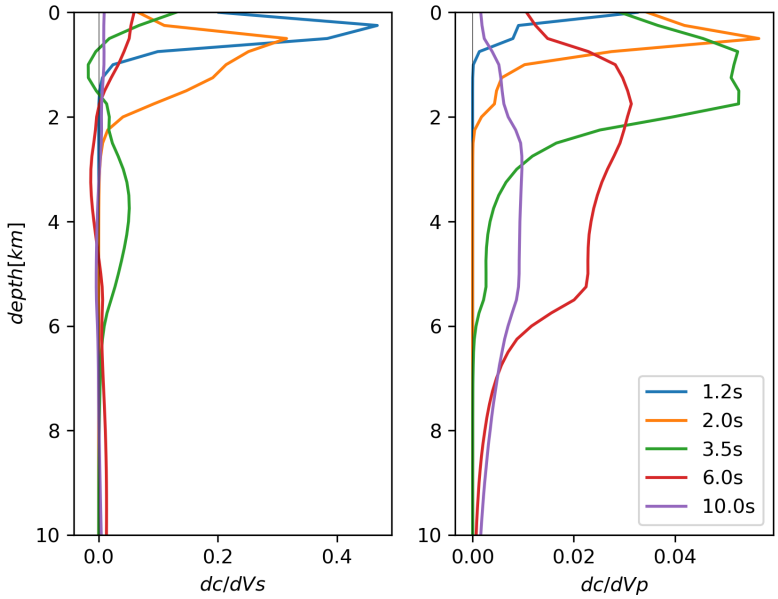


Figure 5.10: Sensitivity kernels relating Rayleigh-wave phase velocity estimates to Vs (**left**) and Vp (**right**) at depth. Note the difference in horizontal scale between the left and right panels: sensitivity of Rayleigh waves to Vp is one-order-of-magnitude smaller than their sensitivity to Vs, as expected. The reference assumed for the computation of the kernels is our final Vp, Vs profile (solid black lines in Figure 5.9A,B). Kernels were calculated via Keurfon Luu's "disba" Python package.

most used stations in the hanging wall compartment of the south facing active axial detachment fault (Figure 5.1). Both P-wave and S-wave velocity models represent almost linear and monotonic velocity to depth variations in Figure 5.9A,B.

As shown in Figure 5.9, the crustal range of S-wave velocities is approximately 1.1–3.9 km/s. It varies between 2.5 and 7 km/s for the P-wave velocity. We calculated the Vp/Vs ratio at different depths from our best Vp and Vs models (Figure 5.9). The comparison between the minimum and maximum values of S and P velocities gives a Vp/Vs ratio equal to 2.23 and 1.81, respectively (Figure 5.11). The ratio of P and S wave velocities provides an additional constraint on the the lithology (Kandilarov et al., 2008) and is sensitive to the presence of fluids (Hamada, 2004). The high ratio of Vp/Vs = 2.23 at a shallower depth of the crust is indicative of high porosity and some amount of serpentinized peridotite. The minimum ratio of 1.81 is predicting lower porosity at deeper parts and is in agreement with Vp/Vs ratio of SWIR gabbroic rocks analyzed in (Miller and Christensen, 1997). Fast variations of P-wave and S-wave velocities at depths below 6.5–7.2 km and slow changes at depths >7.2 km can be another sign of permeability and porosity regime. This regime can affect the serpentinization process in the crust and upper mantle. The variable range of Vp/Vs in the crust and considerable serpentinization can be explained by the fracturing of the crust associated with detachment faults systems (Rouméjon et al., 2015). Another evidence of the fracturing of the crust was discovered in south dipping reflectors by Momoh et al. (2017) which was interpreted as the damage zone. This zone is located within 2–2.8 km horizontally from the emergence of the active axial detachment fault system (deep regions on the map in Figure 5.1). The suggested serpentinization expressed in the velocity models

is in agreement with seafloor sampling in non-corrugated oceanic core complexes collected from smooth (non-volcanic) seafloor (Sauter et al., 2013).

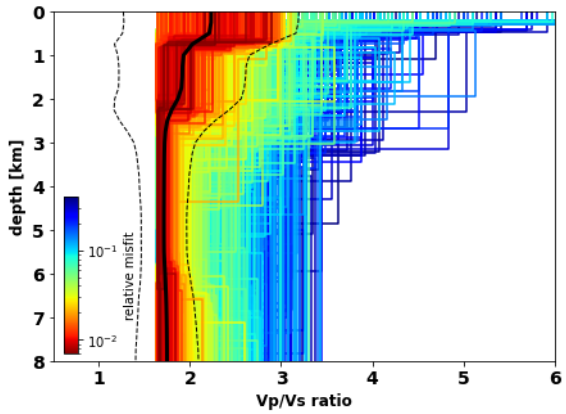


Figure 5.11: Vp/Vs ratio (thick black line), obtained from the final Vp and Vs models (black curves in Figure 5.9A,B), as a function of depth. Dashed lines identify the confidence interval, defined as in Figure 5.9. The full distribution of sampled models with the lowest misfit is shown in color.

We also compare our P-wave model with other models of ultramafic crusts. The P-wave velocity model of ultramafic crust at the Mid-Atlantic ridge at 23°N (Canales et al., 2000) is more linear and the observed velocity of the uppermost crust is higher than in our study, reaching the mantle faster. This higher range of velocity may be caused by gabbroic intrusions or fewer deformations of the exhumed, ultramafic crust in that region. The magma-poor rifted margins in Iberia-Newfoundland (Minshull, 2009) and in western Iberia (Davy et al., 2016) also demonstrated a higher range of P-wave velocity in the upper ultramafic crust. Sedimentation and older ages of these margins likely explain why we observe this higher range of velocity.

An S-wave velocity higher than 3.9–4 km/s is typical for mantle rocks and our model is therefore indicating that unserpentinized and unfractured mantle is found at depths greater than 7 km. The average shear wave velocity between the base of the crust (defined by a 4 km/s Vs threshold), and the maximum depth of our model (15 km) is 4.2 km/s which is less than the global reference value of 4.5 km/s (Kennett et al., 1995), that concerns old, off-axis oceanic lithosphere, but close to the 4.29 km/s of young oceanic lithosphere in the Pacific (Yao et al., 2011). This relatively low value suggests that pristine and unfractured uppermost mantle may in fact be found deeper than 15 km below the hanging wall seafloor. This is consistent with results from a microseismicity study that shows earthquakes down to that depth in the investigated area (Jie et al., 2020 AGU abstract and paper soon to be submitted). The absence of a seismically well-defined and distinct Moho is consistent with reflectivity studies of (Momoh et al., 2017) in our study area. Moreover, other reflectivity studies predicted that more visible and recognizable Moho should be formed at faster spreading ridges, where mafic oceanic crust emplaced on the ultra-mafic mantle (Aghaei et al., 2014; Boulahanis et al., 2020). This prediction was also confirmed by another magma-poor ultra-slow spreading ridge by (Grevemeyer et al., 2018).

## 5.8 Conclusions and Outlook

1. We analyzed and cross-correlated ambient-noise recordings from 43 OBS stations. The symmetry of the cross-correlations in the time-domain and the amplitude ratio analysis showed that the noise source distribution is very homogeneous, despite the short operation time of the recorders.

2. The phase velocities extracted from the inter-station correlation functions ranged between 1 km/s to 3.5 km/s for periods between 1 s to 10 s and was in good agreement with other oceanic studies. Outside this period range, the low signal-to-noise ratio prohibited further analysis. Joint long-time recording of ambient noise and earthquake data is proposed to cover also longer periods.

3. While the general P-wave velocity structure of our study is similar to previous works, we find a significantly thicker crust of ~7 km, averaged over the study region. At uppermost mantle depths, our results suggest an average shear velocity of around 4.2 km/s which is less than the global average. This can be explained by the younger age of the seafloor in our area.

4. Our model suggests a very low S-wave velocity of around 1–1.5 km/s at shallow depths above 1 km in junction with a high Vp/Vs ratio of approx. 2.2. We infer that this may be due to the high porosity of the shallow, water-rich uppermost layer. The Vp/Vs ratio gradually decreases to $\sim$1.8 at a depth of 2.5 km. We propose that this transition reflects the decrease in porosity and assume a higher degree of serpentinization of the crustal material at shallow depths.

5. The ambient seismic noise method can be used as a complementary technique in geophysical studies of the oceanic lithosphere. The S-wave velocity model obtained provides new constraints to evaluate the velocity structure of the crust and uppermost mantle at a melt-poor portion of the ultra-slow spreading SWIR.

# Chapter 6

# Full waveform inversion: initial results


## Summary

Imaging the P-wave velocity model with a higher resolution can be accomplished by full waveform inversion. We present the application of full waveform inversion on an OBS profile along the ridge axis. The investigation reported here is still in progress and the results are still at an initial stage. The format of this chapter is according to the draft of a scientific manuscript.


## 6.1 Abstract


Investigating the contributions of tectonic, magmatic, and other involved processes is necessary to gain a conceptual model of ultra-slow spreading ridges. Understating the velocity structure beneath the ultra-slow spreading ridges provides a window to analyze the crust and upper mantle structures, the faulting dynamics linked to the divergence, and the mechanism of seafloor accretion. The aim of this study is to explore the oceanic the crust formed in the easternmost part of the Southwest Indian Ridge (SWIR). The velocity model is created by full waveform inversion of 16 ocean bottom seismometers along the ridge axis. We proposed that the variations in the velocity with depth are connected to the changes in the degree of serpentinization. The velocity model of the profile is divided into three distinctive regions: the western zone or volcanic region, the transition, and the eastern zone with a lithospheric composition of serpentinized peridotite. A westward increase in melt supply is proposed in the seafloor accretion mode. The serpentinization and P wave velocity model suggest that the Moho is a gradual transition from hydrated to unaltered peridotite. Our results are consistent with the accretion model of detachment fault systems.


## 6.2 Introduction

The plate separation at the ultra-slow spreading ridges can be accommodated by two contrasting mechanisms of accretion. If the melt supply is high enough, the magmatic spreading is dominant and produces a thick igneous crust. In this case, the Moho is regarded as a petrological boundary separating the gabbros from the

unaltered peridotite of the upper mantle (Carlson, 2001). Plate divergence in the center of most slow and ultra-slow spreading ridges is a result of volcanic injection and moderate offset faults. Therefore, more volcanic rocks might be seen on the seafloor of axial domains (Smith and Cann, 1999). In contrast, at segment ends and segments with poor melt supply, the plate separation is mainly accommodated through detachment fault systems. In this accretion model, the Moho is a gradual transition from partially serpentinized peridotite in the lower crust to unaltered peridotite in the upper mantle (Carlson, 2001). The detachment fault systems were proposed to explain the presence of ultramafic rocks in the ultra-slow spreading ridges. They bring mantle-derived ultramafic rocks on the seafloor through the axial lithosphere (Cannat, 1993).

The mechanism or mode of spreading has a large effect on the lithology of the crust and upper mantle, the chemical interaction between the ocean and the solid earth, as well as the biology of the seafloor (Cannat et al., 2019). Exhumation of mantle-derived ultramafic rocks has consequences on the thermal evolution of the plate boundary.

Seismic velocity models can be used to distinguish between two different modes of crustal spreading in ultra-slow spreading ridges. In magmatic accretion, following the Penrose model, the crust can be split into two layers according to the seismic velocity of each layer. The upper crust, or layer 2, may be presented with a relatively low P-wave velocity (4.1-6.5 km/s) and a high vertical velocity gradient (1-2 $s^{-1}$). The lower crust has a higher range of velocity (6.5-7.0 km/s) with a reduced velocity gradient (0.1-0.2 $s^{-1}$) (Miller and Christensen, 1997). In contrast, in crustal spreading based on the detachment fault systems, the P-wave velocity of the crust increases more rapidly to 6.5-7 km/s beneath the seafloor (Canales et al., 2007, 2017). So far, two studies have imaged P-wave velocity models of the lithosphere in the easternmost parts of SWIR. The obtained models resulted from seismic tomography of OBS data (Momoh et al., 2017; Corbalán et al., 2021). However, recent studies showed interesting results, but the tomography method suffers from several limitations: 1) It is not able to provide good constraints on low-velocity zones (Vasco et al., 1995). 2) it relies on a high-frequency estimation (Tromp et al., 2005). 3) It assumes that seismic events are retrieved completely by travel times (Woodward, 1992). We considered the FWI to overcome the disadvantages of tomography. The full waveform inversion can provide higher resolution than classical tomography methods if there is a suitable strategy to do an iterative convergence to a logical solution (Virieux and Operto, 2009; Chauris, 2021). In this study, we present the FWI results of one OBS profile. Using these results, we determine the mechanism of the accretion model along the profile. Our seismic velocity model is expected to provide greater accuracy and resolution on the distribution of the inter-detachment faults, crustal thickness, degree of exhumed mantle serpentinization, lithosphere composition, and transition zone from the dominant exhumed mantle region to the volcanic crust region.

## 6.3 Theoretical background of FWI

The first configuration and formalism of FWI were created by Tarantola and his group (Tarantola, 1984; Mora et al., 1987). At first, the concentration of FWI was on the 1D velocity model. Nevertheless, the advancement of computer facilities and progress in data acquisition has extended the application of FWI to 2D models (Operto et al., 2006; Arnulf et al., 2011) and recently to 3D models (Plessix et al., 2013; Raknes et al., 2015). FWI has experienced the development from acoustic mediums to elastic and visco-elastic mediums, including the context of anisotropy and attenuation parameters (Chauris, 2021). We have used TwistPS in this study to find a two-dimensional P-wave velocity model (Shipp and Singh, 2002). The objective of FWI in marine geophysics is to find a velocity model that minimizes the least-squared difference between the amplitude and phase of observed and modeled seismic data. The least-squares misfit function is defined as follows (Chauris, 2021):

$$J(m) = \frac{1}{2} \left\| d_{cal}(m) - d_{obs} \right\|^2 \tag{6.1}$$

where m is the model and it is a function of spatial coordinates. $d_{obs}$ is the observed data. $d_{cal}$ or calculated data set denotes the solution of the wave equation and is a function of the model. The general form of the wave equation is as follows:

$$L(m) d_{cal}(s, r, t) = \delta(s - r)\Omega(t) \tag{6.2}$$

where $L$ is the wave equation operator, $\Omega$ (t) is the representative of the seismic source, and $\delta$ shows the Dirac distribution. Our strategy for convergence to a minimum of the misfit function is the local search method (Shipp and Singh, 2002). This approach determines the model iteratively through the calculation of the gradient of the misfit function (Plessix, 2006). The starting model for this strategy is usually determined based on a standard tomography model. The gradient of the misfit function is defined as the derivative of the misfit function with regard to the model parameters (Chauris, 2021). The iterative procedure of this approach is as follows (Shipp and Singh, 2002):

$$m_{n+1} = m_n - \alpha \frac{\partial J}{\partial m} \tag{6.3}$$

where n is the number of iteration, $\frac{\partial J}{\partial m}$ is the gradient of the misfit function and $\alpha$ represents a positive scalar step length. $\alpha$ is evaluated at each iteration like the method of Pica et al. (1990). In parallel with the objective of the FWI, the gradient of the misfit function indicates the direction that the misfit function is maximized (Shipp and Singh, 2002).

In order to obtain the synthetic data, we solve the elastic wave equation in the time domain. The strength of this approach is the ability to produce all the probable wave types in a model (Shipp and Singh, 2002). Only P-wave velocity is directly inverted and S-wave velocity is coupled with P-wave velocity and updated in forward modeling based on the empirical relationships. Solving the wave equation is performed by the finite-difference method with discretization on a grid. Our preferred method was introduced in Levander (1988) based on a staggered grid

with a scheme of second order in time and fourth order in space. In the finite-difference method, the time and space increment on the grid cannot be random, and the increment should satisfy the dispersion and stability conditions. If we define the space increment along the x and z axis by $\Delta x$ and $\Delta z$ and we define the time increment by $\Delta t$, the dispersion and stability conditions are written as follows respectively (Levander, 1988; Chauris, 2021):

$$\Delta x = \Delta z \leq \frac{1}{5}\frac{v_{min}}{f_{max}} \tag{6.4}$$

$$\Delta t \leq 0.606\frac{\Delta x = \Delta z}{v_{max}} \tag{6.5}$$

In the dispersion equation 6.4, the space increment $\Delta x$ or $\Delta z$ should be 5 times smaller than the minimum wavelength, defined by minimum expected velocity and maximum frequency. As long as the dispersion condition is not met in finite difference, the dispersion can be seen on the signal. Notice that for a larger value of maximum frequency, the grid increment must be smaller, and consequently, more storage and a stronger CPU and RAM memory space will be needed. The stability equation 6.5 is a function of maximum velocity. Failure to meet this condition can lead to unprofitable information (Chauris, 2021).

## 6.4 Acquisition of OBS data set

The active seismic data used in this investigation was acquired by 16 Ocean Bottom Seismometers (OBS), each having one hydrophone and three orthogonal component geophones. The data acquisition took place in 2014 during the SISMOSMOOTH cruise (Leroy et al., 2015). The OBSs are located in an EW profile sub-parallel to the ridge axis in the easternmost part of SWIR. The names of the stations were chosen by numbers from 1 to 16 (see figure 6.1) The seismic source included 14 guns for a total volume of 111.27 L. The average depth of the seismic source was 14 m (Leroy et al., 2015; Leroy and Cannat, 2014). 622 shots were used in this study. The shot interval between stations 20 and 31 was 150 meters, and for the rest of the stations, it was 300 meters. The inter-station distance was 2.1–7.2 km, and OBS's depths ranged between 4.2 and 4.8 km. The OBS data is recorded continuously on the seafloor at a sampling rate of 250 Hz.

## 6.5 Seismic data processing

The swell noise is the most dominant disturbance in the marine seismic data. This type of noise interferes in the low-frequency band of the amplitude spectrum (Dondurur, 2018). Marine seismic data can also be contaminated by high-frequency noise produced from electrical cables or heavy machines (Asghar, 2011). A smooth version of a band-pass filter with a low cut-off frequency of 3 Hz and a high cut-off frequency of 4 Hz was utilized to mitigate the effects of noise and increase the signal-to-noise ratio (SNR) (Mousa and Al-Shuhail, 2011). To meet the stability condition

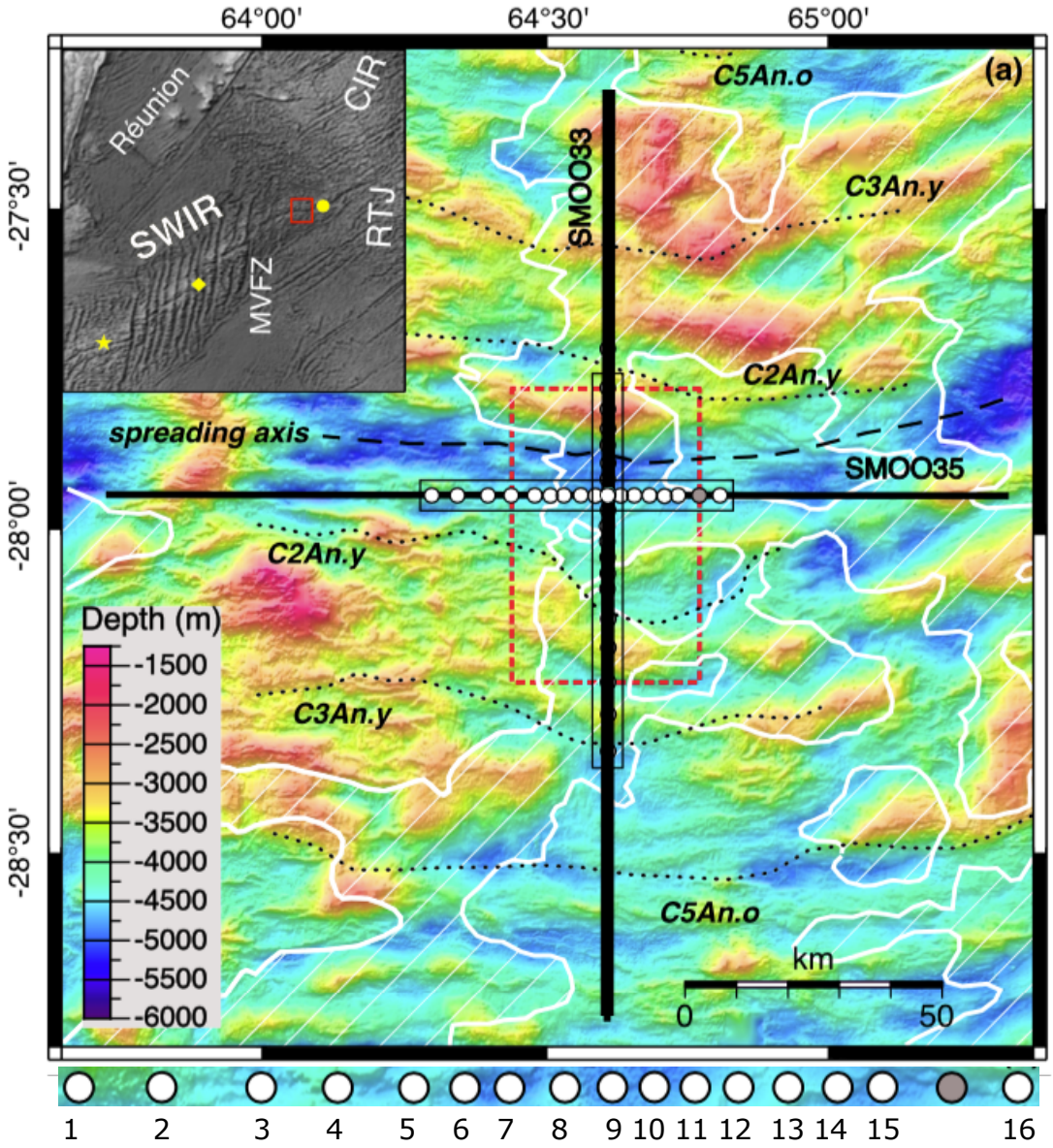


Figure 6.1: We studied the EW profile (SMOO35). The location of OBS's overlay bathymetry map is shown in this figure. The thick black lines present shot locations. The white circles are analyzed stations, and the gray circle is a station without useful data. At the bottom of the map, one can find the number of OBSs. The shot interval inside the dashed red rectangle is 150 meters and outside it is 300 meters. The spreading axis is represented by a dashed black line. Areas bounded by thick white lines and filled with oblique thin white lines are indicative of smooth non-volcanic seafloor (Corbalán et al., 2021)

.

in equation 6.5, the time sampling interval of the data set has been resampled to 2 ms (regarding maximum velocity equal to 8000 m/s and grid spacing of 30 meters). Our targeted data for inversion is the energy corresponding to the refraction events. For this reason, we have muted other parts of OBS gathers. We can see the results in Figure 6.2 before and after resampling, denoising, frequency filtering, and muting. Another step is to estimate the source wavelet. The importance of source estimation in FWI is that synthetic receiver gathers, which are compared to observed data, are created from the convolution between the estimated wavelet and the earth's impulse

response (Margrave and Lamoureux, 2019). The source is estimated based on the near offset traces of the OBS gathers (Figure 6.3).

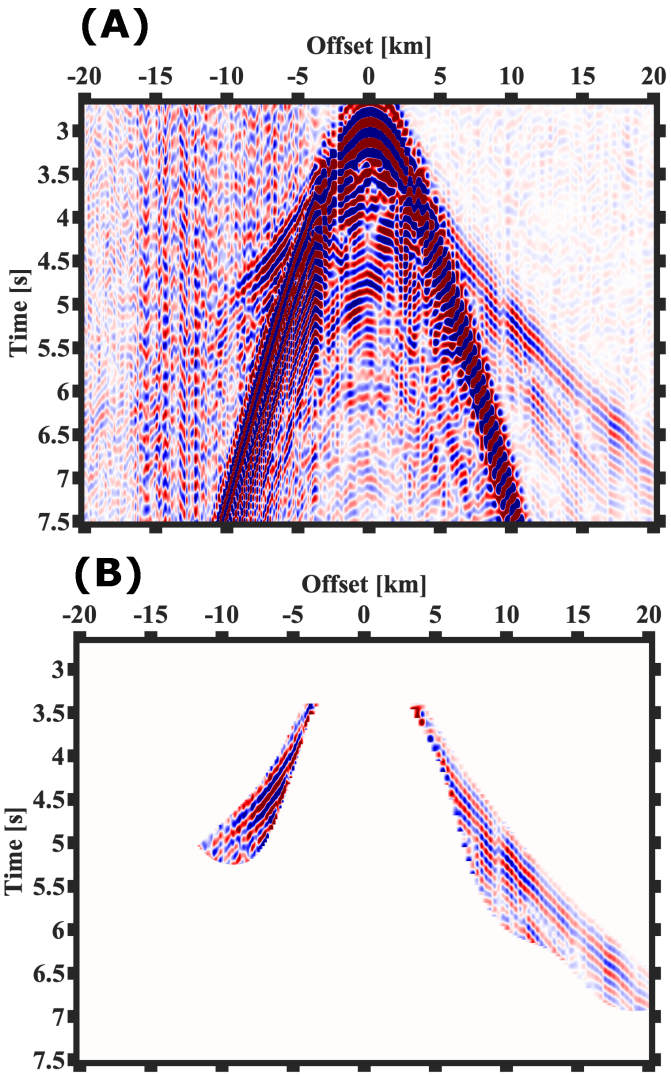


Figure 6.2: A) Prior to filtering, raw OBS gather. B) OBS gather is obtained after resampling, denoising, frequency filtering (3-4 Hz), and muting.

## 6.6 Starting model

Choosing the initial velocity model close to the true model is an important step in the FWI to avoid cycle skipping (estimated waveform in comparison with observed waveform is out of phase for more than half a cycle (see Figure C.1 and Figure C.2)) and ensure the convergence to the global minimum (Zhou, 2016). One of the ways to obtain the initial velocity model for 2D FWI is ray-based travel time tomography. This approach is defined based on first-arrival travel times. Our initial 2D P-wave velocity model (see Figure 6.4A) was obtained by Corbalán et al. (2021) using TOMO2D (Korenaga et al., 2000). The first break of arrivals on OBS data was picked manually by PASTEUP (Fujie et al., 2008). The starting model of

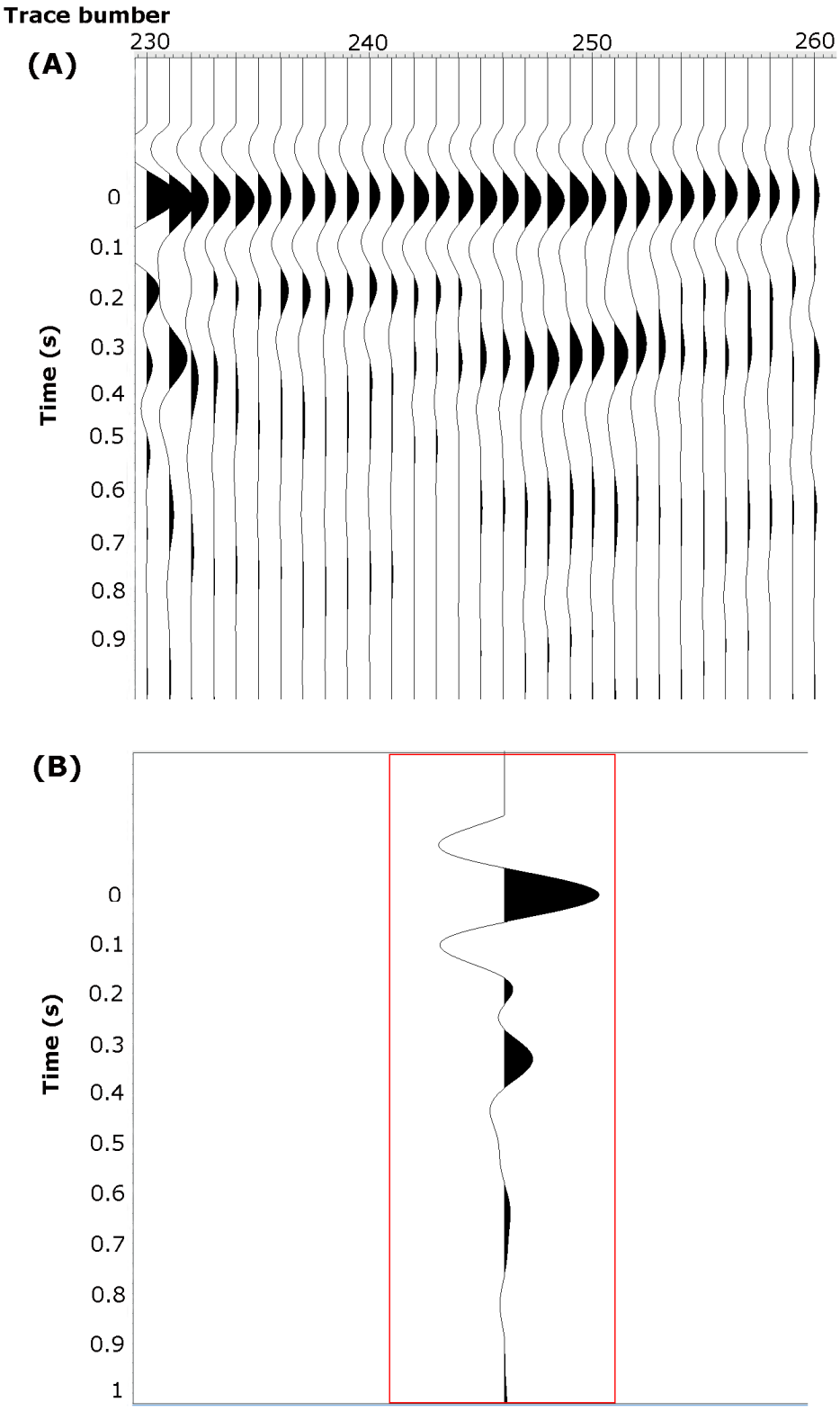


Figure 6.3: Shot signature estimation. A) Example of shot signatures extracted from the near-offset direct wave arrivals of one OBS. B) Estimated source wavelet filtered to a bandwidth 3-4 Hz.

the tomography procedure was defined based on average velocity models in other ultra-slow spreading ridges (Grevemeyer et al., 2018; Van Avendonk et al., 2017) and 1D average velocity of (Momoh et al., 2017) (Figure 16) .

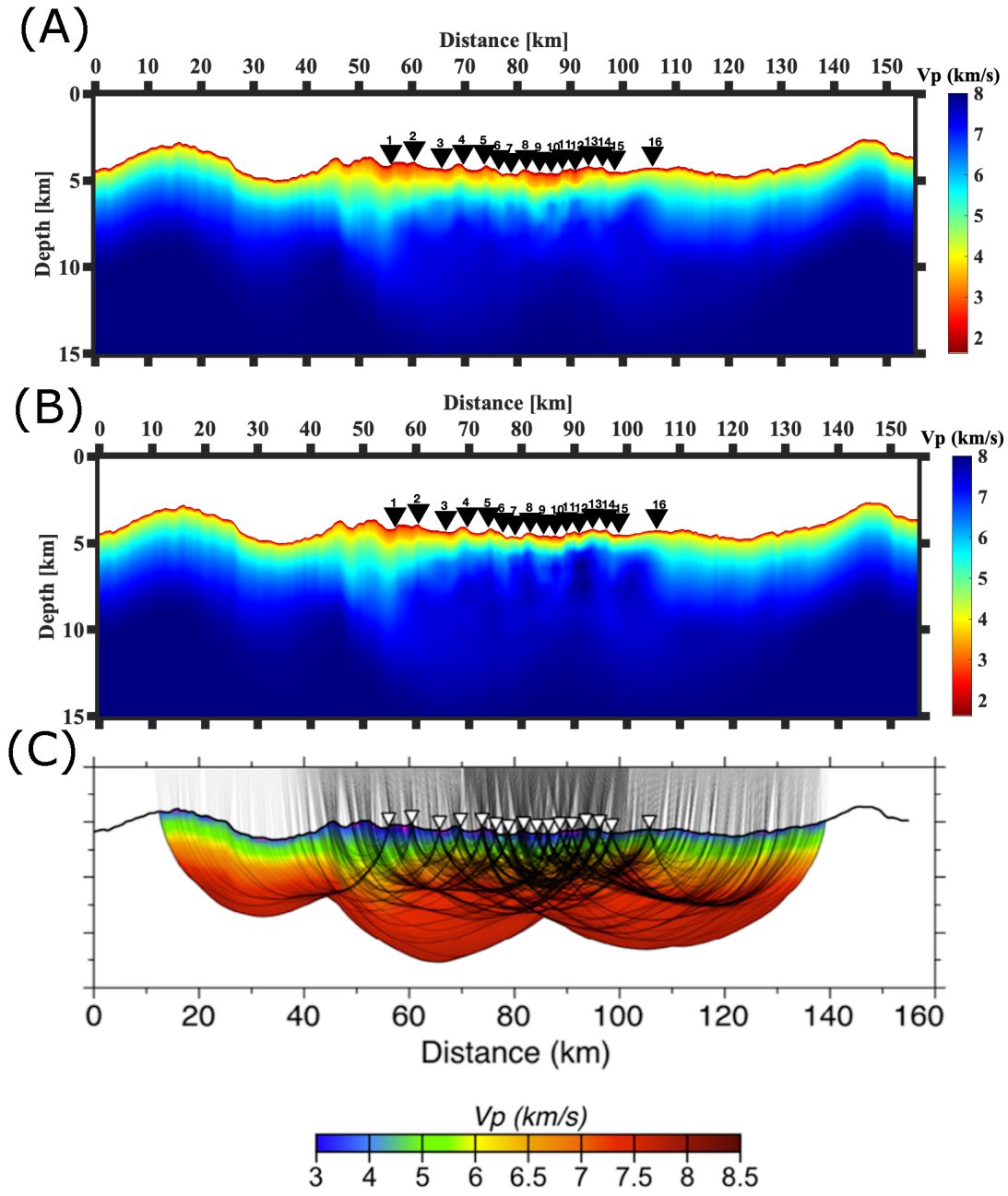


Figure 6.4: A) Initial 2D P-wave velocity model. B) P-wave velocity model obtained from FWI after 60 iterations. Inverted triangles are the station locations. C) Raypaths (black lines) of the first arrivals (Corbalán et al., 2021). White inverted triangles indicate the locations of the OBSs on the seafloor.

## 6.7 Inversion strategy

Our inversion is based on hydrophone data. Convolutional Perfectly Matched Layer (CPML) absorbing boundary condition in the manner of Martin and Komatitsch (2009) is imposed to reduce the computational burden of forward modeling and to prevent the spurious events (energy leakage) from the boundary of models into the modeled data. In total, 16 receivers and 622 traces of shots are included in the inversion. 4001 time samples were available after resampling, and we truncated

the recording time up to 8 seconds. We interpolated our initial 2D P-wave velocity model (having 155 km length and 15 km depth) to 5167×497 gird nodes with a node spacing of 30 m. Using this grid spacing and a min velocity of 1500 m/s can lead to accurate modeling for frequencies less than 9 Hz (see equation 6.4). Sources and receivers positions are adjusted to match grid nodes. We inverted our data in the frequency range of 3-4 Hz for 60 iterations. The inverted model can be found in Figure 6.4B. We applied receiver-source reciprocity due to its advantages in the calculations (Warner et al., 2013). Figure 6.5 shows that the waveform inversion was able to fit a significant part of the data.

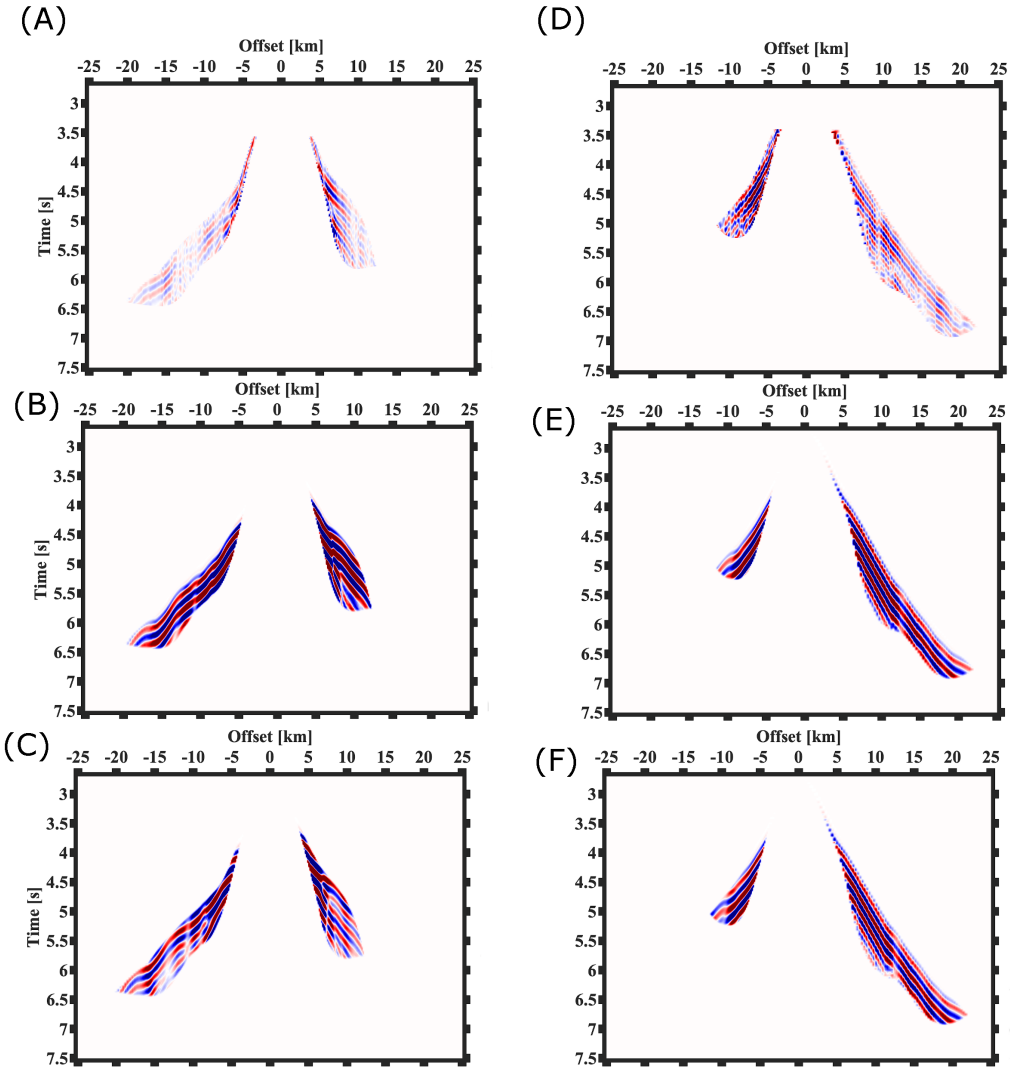


Figure 6.5: A) Observed OBS gather number 10. B) Modeled OBS gather number 10 after first iteration. C) Modeled OBS gather number 10 after 60 iterations. D) Observed OBS gather number 16. E) Modeled OBS gather number 16 after first iteration. F) Modeled OBS gather number 16 after 60 iterations

## 6.8 Serpentinization analysis

The conversion of seismic velocity to a degree of serpentinization is performed by a linear relationship described in (Carlson and Miller, 2003). The estimated degree

of serpentinization can be found in Figure 6.6B. We choose the relationship for a temperature of 300° Celsius, in agreement with oxygen isotope studies in the area. This conversion is done under the assumption that the profile is composed of serpentinized peridotite at shallower depths and unaltered peridotite at deeper parts. This assumption is supported by the following evidence. First, no well-characterized Moho was identified in the region by MCS analysis in (Momoh et al., 2017). Second, we could not observe any wide-angle Moho reflection (PmP) arrivals in our OBS data set. This absence of wide-angle Moho reflection (PmP) arrivals was consistent with other ultra-slow spreading ridges with low melt supply (Delescluse et al., 2015; Grevemeyer et al., 2018) but not with faster spreading ridges (Canales et al., 2000; Horning et al., 2016). Third, significant peridotite was sampled on the seafloor of shading area (Rouméjon and Cannat, 2014; Sauter et al., 2013) (see Figure 6.1).

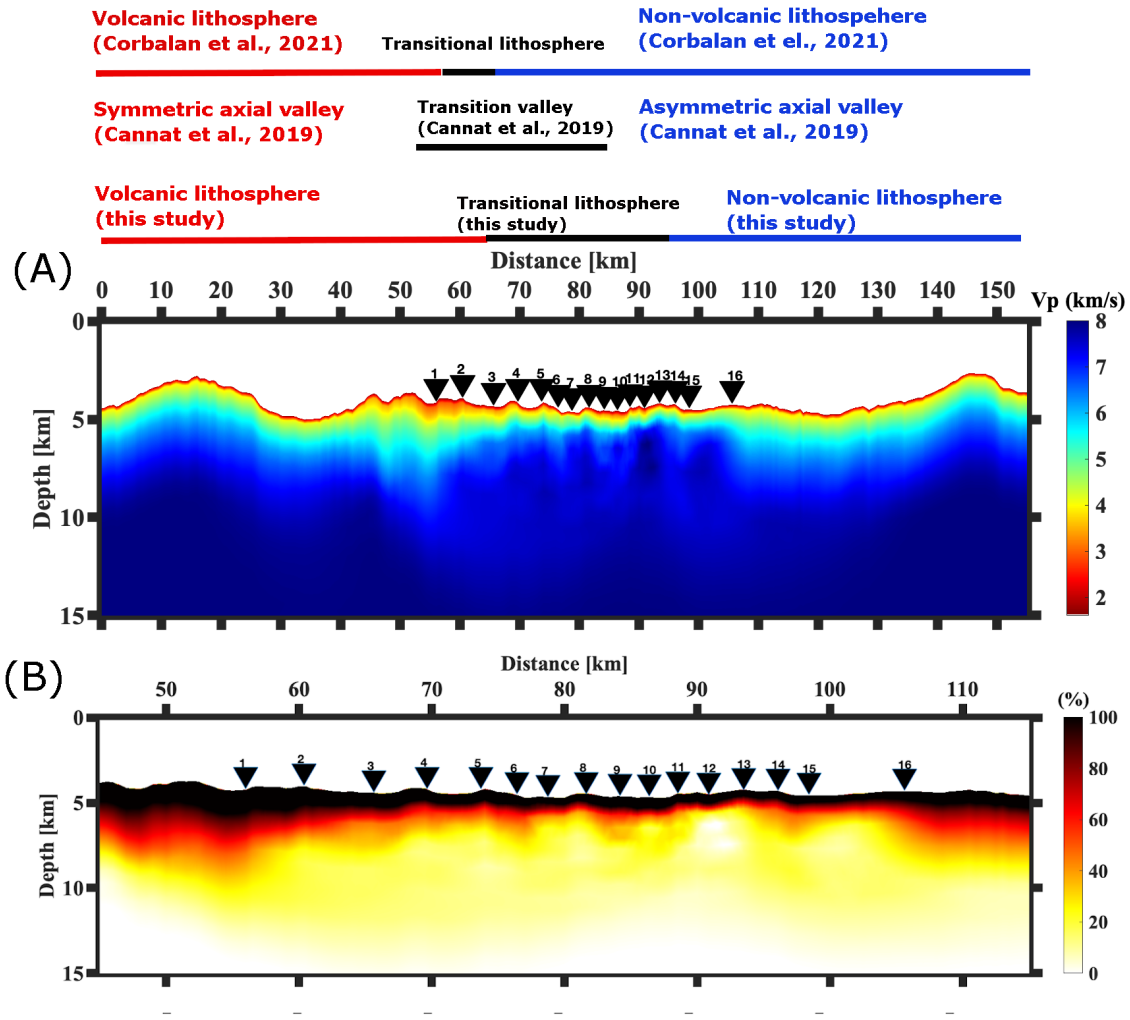


Figure 6.6: A) Determination of volcanic, non-volcanic, and transition in our study and previous research. B) Estimated degree of serpentinization. Inverted triangles are the station locations.

## 6.9 Discussion

The final P-wave velocity model of the selected profile gives insights into the subsurface structures of the SWIR. Our interpretation is limited to 10 km away from the first and last stations on both sides of the profile based on Monte Carlo and ray coverage analysis in (Corbalán et al., 2021) (see Figure 6.4C). The P-wave velocity in the crustal layer is expected to be either lower than the velocity for olivine-rich gabbros, which is about 7 km/s (Miller and Christensen, 1997) or lower than the transition between the partially serpentinized peridotite and unaltered peridotite (∼7-8 km/S) (Christensen, 2004). We use the value of 7 km/s to approximate the crustal thickness. Previous seafloor mapping across the profile expressed a transition from smooth non-volcanic seafloor with exhumed serpentinized ultramafic rocks in the eastern part to volcanic seafloor in the western part (Cannat et al., 2006). A wider transition was later proposed from an asymmetric axial valley (characteristics of non-volcanic seafloor) to a symmetric axial valley (characteristics of volcanic seafloor). The length of this transitional area was estimated to be between 20-30 km based on the analysis of four profiles perpendicular to the ridge-axis (Cannat et al., 2019) (see Figure 6.6A)).

Our P-wave velocity model suggests variations in the compositions along the profile. The velocity model is divided into three distinctive regions: The western zone (model distance <65 km), transition (65 km to 95 km model distance), and the eastern zone (model distance > 95 km). The eastern zone represents velocities of 3.5–4 km/s at a depth of 0.5 km beneath the seafloor and 7 km/s at depths of 3–4.5 km (see Figure 6.6A). The features in the eastern zone are compatible with exhumed serpentinized mantle-derived peridotite where the percentage of serpentinization decreases with depth (see Figure 6.6B right to station 13). 100% serpentinization is observed at the shallow depths of the profile, and 20% serpentinization is extended up to 3–4 km below the seafloor of the profile in the transition and the eastern zones (see Figure 6.6B). The velocities lower than 4.5 km/s at the shallow depths of these zones can possibly support the full serpentinized as well as very fractured peridotite at the shallow depths. The presence of the fully serpentinized peridotite at the top of the model of these zones is in agreement with the seafloor studies (Cannat et al., 2006; Sauter et al., 2013). We can see a quick change in serpentinization from 100% to 20% and velocities < 7 km/s at shallow depths in the central and eastern zones (Figure 6.6). This variation is gradual for serpentinization smaller than 20% and velocities > 7 km/s. This gradual decrease in serpentinization and velocities at the deeper sections of the zones suggests that the Moho could be a gradual transition from hydrated to unaltered peridotite. This suggestion is consistent with elsewhere along the SWIR (Mével, 2003; Dick et al., 2019) as well as the lack of Moho reflection in OBS and MCS data (Momoh et al., 2017). Our average thickness estimation in the transition and eastern zone is approximately 3-4 km (less than the 4.2-5 km thickness estimated in the smooth seafloor by Momoh et al. (2017)). The variable crustal thickness in the transition is derived from the dike injections and normal small faults. The dike injections could be responsible for lower values in the Bouguer anomaly that resulted in the interpretation of this area as volcanic seafloor

in (Cannat et al., 2006). In agreement with side-scan sonar investigations, our results strengthen the possibility that the lava patches are erupted directly onto the seafloor by small offset normal faults (Cannat et al., 2019; Sauter et al., 2013). Our transition is very close to ∼54-86 km obtained by Cannat et al. (2019). Momoh et al. (2020) also suggested the presence of intrusive magmatic sills to explain seismic reflectors in the transition. Another endorsement of our study was obtained by the shallow cluster of earthquakes at the depth of less than 2 km below the seafloor in the transition in Chen et al. (2021). They also concluded that the shallow cluster has a tectonic origin and this tectonic activity is triggered by a magmatic injection at the 6 to 11 km bsf in the detachment footwall (see Figure 6.7). In the transition, we can see a gradual westward change in the velocities. We can better distinguish between volcanic and non-volcanic zones and the length of the transition is bigger than the distance 59-69 km proposed by Corbalán et al. (2021).

The western zone indicates velocities of 3–4 km/s at a depth of 1 km beneath the seafloor and 7 km/s at a depth of 5–6 km. The velocity is lower than 4.5 km/s at the top of the model in the western zone, which is probably basalt. The lower level of velocity in the western zone extended up to deeper parts of the profile and could be indicative of a volcanic domain. This probability is reinforced by thicker thickness (5–6 km) and quicker change of serpentinization in the deeper parts of this zone. We think the magmatic spreading is dominant in the western zone. The deep-west cluster of earthquakes at a depth of 6-11 km was also interpreted as related to the volcanic injection in Chen et al. (2021) (see Figure 6.7). Our suggestion is also consistent with the negative gravity anomaly in Cannat et al. (2006) and determined volcanic zone (distance less than 59 km along the profile) in Corbalán et al. (2021).

To aid the discussion, we plot the average one-dimensional velocity model extracted along the profile (Figure 6.8). We compare our average velocity models with corresponding results from previous studies in different locations of SWIR. Our 1D velocity model is in general agreement with the 1D velocity model of Momoh et al. (2017) from 64°30'. Momoh et al. (2017) indicates velocity at the seafloor ranging from 2.7 to 4.5 km. Our model constrains the velocities to a wider range (1.9 - 5 km/s) at the seafloor. The range of velocity at the seafloor is also wider than the profile of Corbalán et al. (2021) (2.5 - 3.5 km/s). Nevertheless, the smooth increasing trend of velocity up to 8 km dbsf is in good agreement with Corbalán et al. (2021). However, our interpretation is similar to Momoh et al. (2017) and Corbalán et al. (2021), our model has provided deeper and more detailed information about the lithosphere structures. Minshull et al. (2006) present a narrower range of velocity at the seafloor (2.3 - 3.5 km/s) at 66°E. They show a high vertical velocity gradient of up to 6.4 - 7 km/s at 2.7 km dbsf and a low-velocity gradient of up to 6.5 - 8 km/s at depths greater than 2.7 km bsf. Our average velocity fits well with the velocity of Minshull et al. (2006). Nevertheless, different interpretations were put forward in our studies. They suggested that mafic rocks form the crustal structure and constrained Moho with seismic and gravity data. Moreover, the velocity structure of Minshull et al. (2006) is indicative of a high gradient layer 2 on top of a low gradient layer. The gradual decrease in the vertical velocity gradient at 64°30'E is consistent with a gradual decrease in pore pressure and serpentinization with

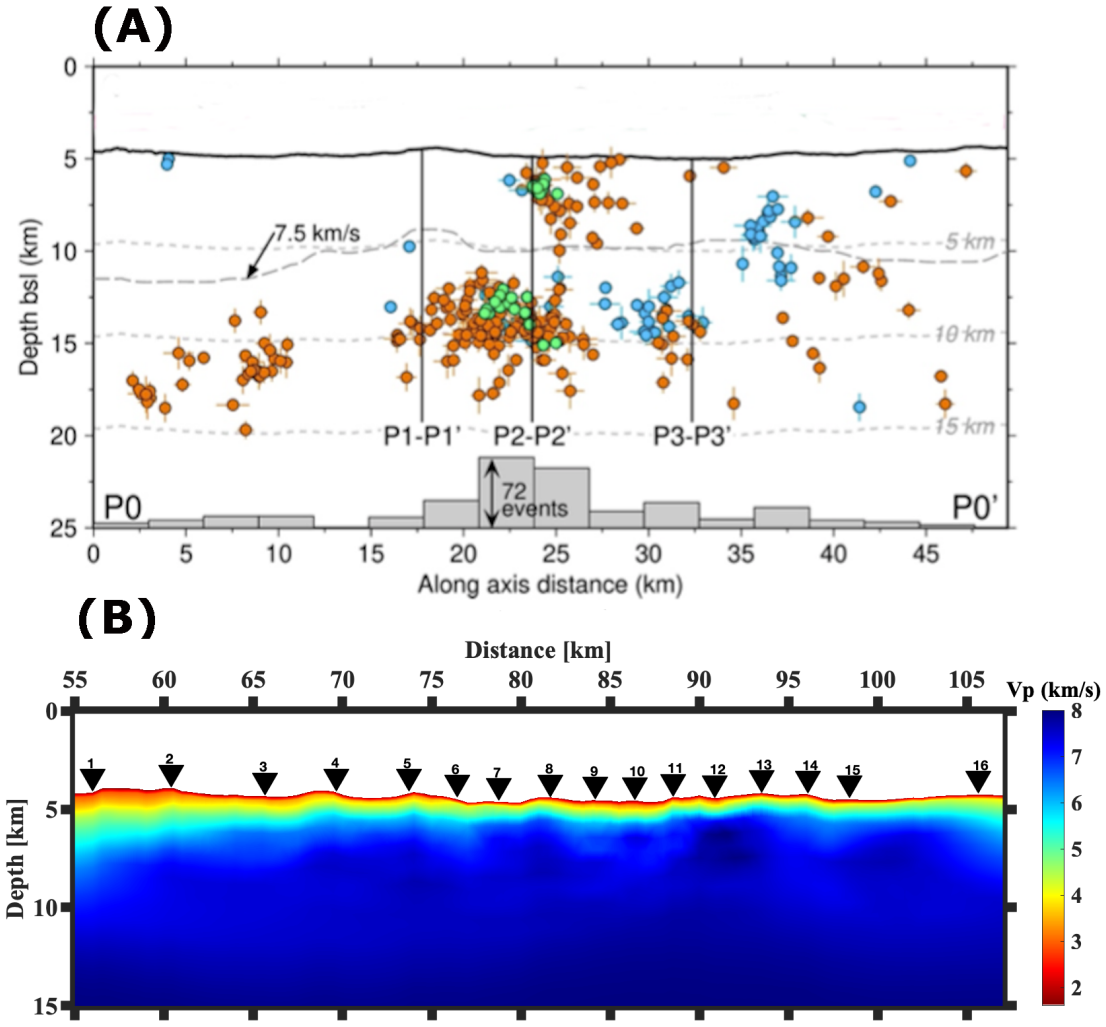


Figure 6.7: A) Histogram of earthquake depth below the seafloor along the ridge axis. The orange circles show the events of RVSMO catalogs, the blue circles are related to SMSMO catalogs, and the seismic swarms are green (Figure with partial modification from Chen et al. (2021)). The distance is defined based on the location of OBSs. B) P-wave velocity model obtained from FWI. For better comparison with the histogram of earthquakes, the model covering only the location of OBSs is shown.

depth. The average velocity in the models of Momoh et al. (2017), Corbalán et al. (2021) and Minshull et al. (2006) reaches 7-8 km/s at a depth of 4-5 km. This range of velocity in our 1D model is at a depth of 7 km and indicates a similar crustal thickness (7 km) with estimated 1D velocity models of ambient noise interferometry (see Figure 5.9).

## 6.10 Conclusion

We use 16 Ocean Bottom Seismometers (OBS) of a 155 km profile along the ridge axis in the easternmost part of the SWIR at E64°30'. Data analysis using travel time tomography has been useful for advancing our knowledge about the crustal structures in the easternmost part of the SWIR. Here, we apply FWI to wide-angle seismic refraction data to attempt to derive a high-resolution crustal-scale velocity model, the first such result in the SWIR. Our main findings are as follows:

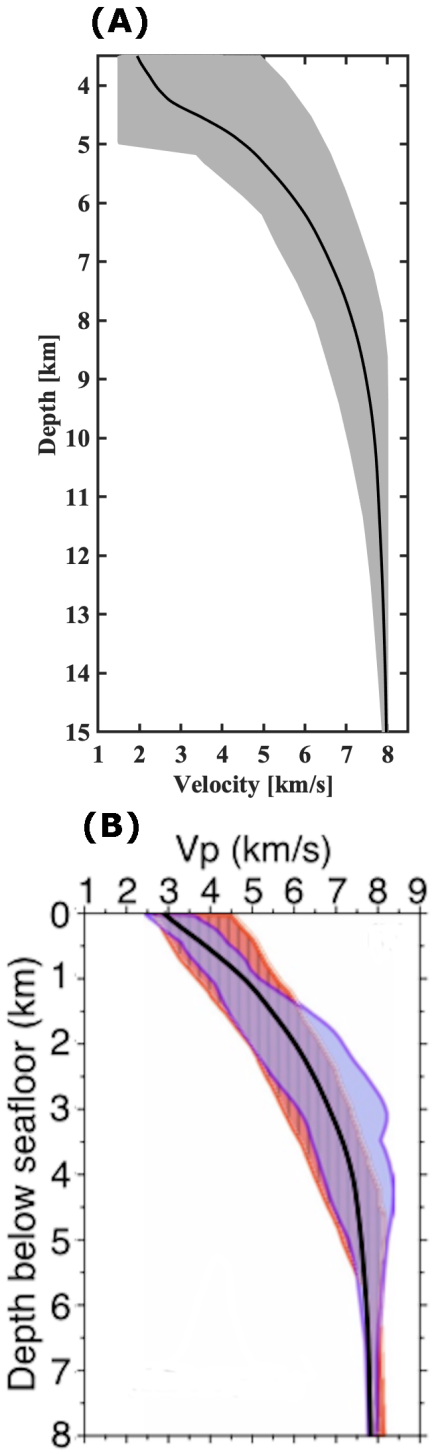


Figure 6.8: A) Average 1D velocity model along the inverted profile (black curve). 1D velocity model along the inverted profile (gray area). B) 1D velocity-depth fields (light purple areas bounded by dark purple lines and average black curve estimated in Corbalán et al. (2021). 1D velocity-depth fields (light red area) studied in Momoh et al. (2017).

In good agreement with Cannat et al. (2019) and Corbalán et al. (2021), the velocity model of the profile is divided into three distinctive regions: Western zone or volcanic region (model distance <65 km), transition (65 km to 95 km model distance), and eastern zone with a lithospheric composition of serpentinized

peridotite (model distance > 95 km). This transition is predicted to have a tectonic origin at the shallow cluster and magmatic injection at depth of 6 to 11 km bsf. The thickness of the crust is estimated to be 3-4 km in the eastern and transition zones. The average crustal thickness is expected 5-6 km in the volcanic western zone. A westward increase in melt supply is proposed in the seafloor spreading mode. Our analysis proposed a Moho consisting of a gradual transition from hydrated to unaltered peridotite in most parts of the profile. Our model has provided deeper information about the structures.

# Chapter 7

# Summary, Conclusion, and Suggestions

## 7.1 Summary and Conclusion

The apparent absence of volcanic activity both at segment ends and along the ridge axis for over 100 km (Sauter et al., 2004; Carbotte et al., 2016) as well as a large amount of mantle peridotite in the axial valley (Dick et al., 2003) demanded to discover the dominant role of tectonic setting in the easternmost Southwest Indian Ridge. The current hypothesis in the area is that the presence of detachment fault systems is responsible for forming the underlying crust and seafloor morphology. While little research has been done in the region, imaging the crustal structure was necessary to understand and recognize past and ongoing tectonic processes, the damaged zone of the system, crustal thickness, the spatial distribution and intensity of serpentinization, and the lithology. Some of our main findings are imaged in Figure 7.1.

We employed seismic refraction data and ambient noise data to image the crustal and upper mantle structures. It was the first time that FWI was used in the along-axis profile of the region. Moreover, the use of ambient noise interferometry was quite a new approach in the study of mid-ocean ridges.

The vertical components of 43 OBS were used to analyze the ambient-noise signals. The analysis of seismic refraction data was based on the hydrophone components of 16 OBS. Our main data preparation stage was the conversion of raw data into SAC format for ambient noise interferometry, while the SEG-Y format was delivered to us for the processing and modeling of refraction data. Data conversion was a very time-consuming part of my job. For each type of instrument, I had to find a way to convert them from raw to a continuous SEG-Y format and not based on a shooting table, as it is usually used. Then, I converted the data into SAC format.

In ambient noise interferometry, 176 cross-correlations in the time domain were acceptable with an inter-station distance of 5–28 km and for frequencies less than 1 Hz. Our cross-correlation results demonstrated that the continuous ambient noise signals recorded in the region included a considerable amount of coherent energy.

The phase velocities extracted from the inter-station correlation functions and regression ranged between 1 km/s and 3.5 km/s for periods between 1 s and 10 s and were in good agreement with two rare examples of the use of ambient noise interferometry in the imaging of the oceanic lithosphere (Harmon et al., 2007; Yao

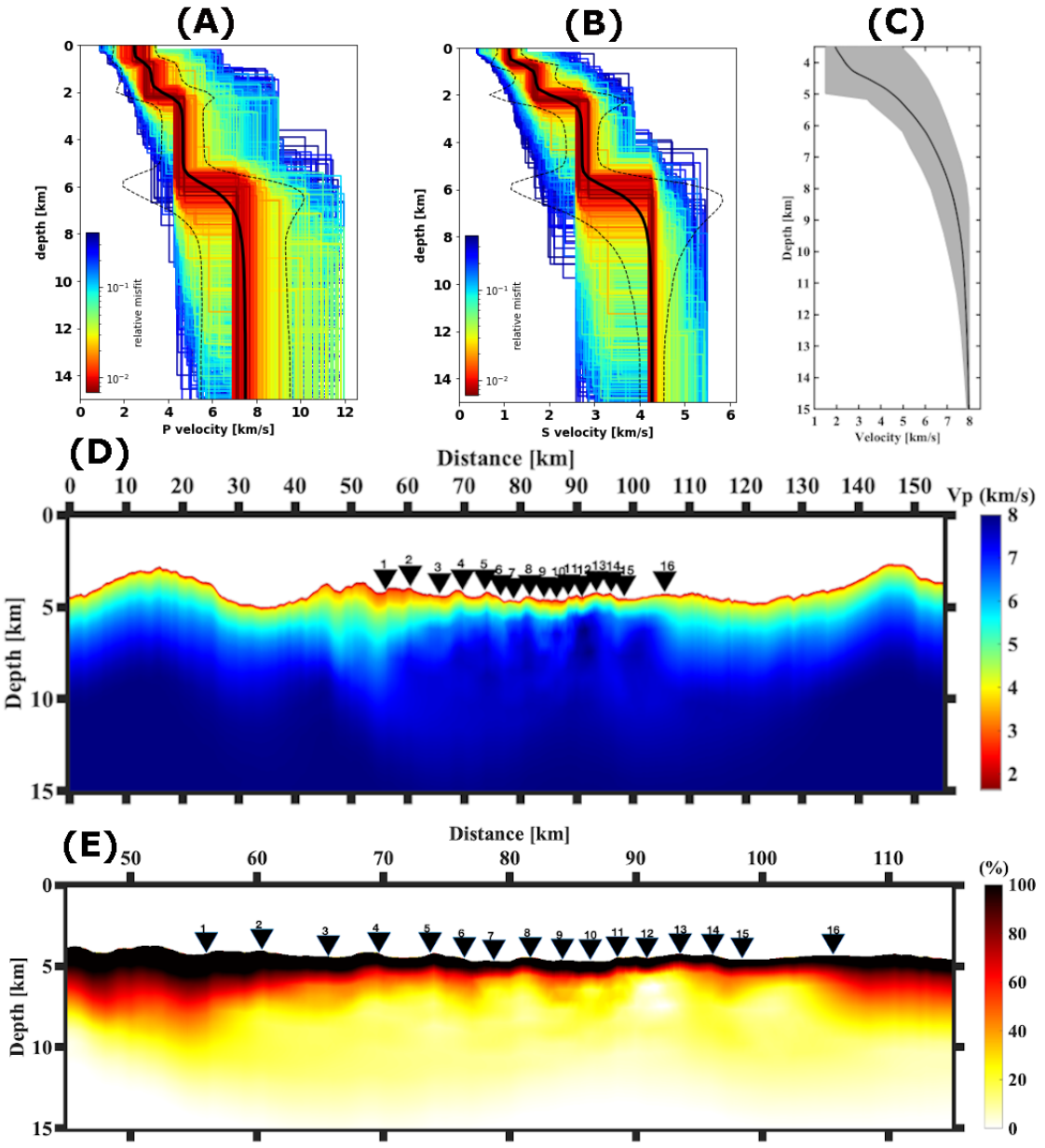


Figure 7.1: A) 1D P-wave velocity model obtained from ambient noise interferometry. B) 1D S-wave velocity model obtained from ambient noise interferometry. The black solid lines denote the Vp and Vs averages models. C) Average 1D velocity model along the inverted profile (black curve). 1D velocity model along the inverted profile (gray area). D) 2D P-wave velocity model obtained from FWI. E) Estimated degree of serpentinization.

et al., 2011). Outside this period range, the low signal-to-noise ratio prohibited further analysis.

The P and S wave velocity models obtained from ambient noise tomography indicated a crustal thickness of about 7 km. This thickness is larger than the 4.2–5 km estimated from the P-wave velocity model in (Momoh et al., 2017) in the central part of the study area.

The average shear wave velocity between the base of the crust (defined by a 4 km/s Vs threshold) and the maximum depth of our model (15 km) is 4.2 km/s, which is less than the global reference value of 4.5 km/s (Kennett et al., 1995). This

can be explained by the younger age of the seafloor in our area.

The high ratio of Vp/Vs at a shallower depth of the crust was indicative of high porosity and some amount of serpentinized peridotite. The minimum ratio predicted lower porosity at deeper parts and was in agreement with the Vp/Vs ratio of SWIR gabbroic rocks analyzed in (Miller and Christensen, 1997). Fast variations of P-wave and S-wave velocities at depths below 6.5–7.2 km and slow changes at depths >7.2 could also show the variations of the serpentinization process in the crust and upper mantle. The variable range of Vp/Vs in the crust and considerable serpentinization were explained by the fracturing of the crust associated with detachment fault systems and were compatible with the geological heterogeneous model (Mével, 2003; Rouméjon et al., 2015). These findings of serpentinization and fractures are in agreement with (Corbalán et al., 2021).

Our P-wave velocity model obtained from FWI suggests considerable variations in the upper lithospheric compositions along the axis-parallel profile. A transition is expected at a model distance of ∼65-95 km from the predominantly volcanic domain in the western zone to variable serpentinized peridotite in the eastern zone. A westward increase in melt supply is proposed in the seafloor accretion mode.

We could not observe any wide-angle Moho reflected arrivals (PmP) in our OBS data set. The lack of PmP arrivals is compatible with other ultra-slow spreading ridges (Grevemeyer et al., 2018). Our OBS data associated with MCS data (Cannat et al., 2006; Sauter et al., 2013; Momoh et al., 2017) indicated that a continuous basaltic top layer is absent. We can see a quick change in serpentinization from 100% to 20% and velocities < 7 km/s at shallow depths in the transition and eastern zone. This variation is gradual for serpentinization smaller than 20% and velocities > 7 km/s. The gradual decrease in serpentinization and P-wave velocities at the deeper sections also suggests that the Moho is a gradual transition from hydrated to unaltered peridotite in most parts of the profile.

The velocities lower than 4.5 km/s in the transition and eastern zone can possibly support the full serpentinized peridotite at shallow depths. The presence of the fully serpentinized peridotite at the top of the model of these zones is in agreement with the seafloor studies (Cannat et al., 2006; Sauter et al., 2013).

In the transition and eastern zones, we estimate an average thickness of 3–4 km (less than the 4.2–5 km thickness estimated by (Momoh et al., 2017) in the smooth seafloor). The variable crustal thickness in the transition could be derived from the dike injections and normal small faults. The dike injections could be responsible for lower values in the Bouguer anomaly (Cannat et al., 2006). In agreement with side-scan sonar investigations, our results strengthen the possibility that the lava patches are erupted directly onto the seafloor by small offset normal faults (Cannat et al., 2019; Sauter et al., 2013). Our transition is very close to ∼54-86 km obtained by (Cannat et al., 2019). Momoh et al. (2020) also suggested the intrusive magmatic sills to explain the presence of seismic reflectors in the transition. Further support for our interpretation was provided by a shallow cluster of earthquakes at a depth of less than 2 km below the seafloor in the transition domain (Chen et al., 2021).

The deep-west cluster of earthquakes at a depth of 6-11 km confirms the volcanic injection in the western zone (Chen et al., 2021). The volcanic spreading in the

western zone is also consistent with the negative gravity anomaly (Cannat et al., 2019).

The average crustal thickness is expected to be 5-6 km in the volcanic western zone of the P-wave velocity model. This thickness is nearly close to the estimated thickness (4 - 5.3 km) by Corbalán et al. (2021) in the western zone.

The average 1D P-wave velocity model of this study is in compliance with the smoothing trend of 1D models in (Momoh et al., 2017; Corbalán et al., 2021; Minshull et al., 2006). Having said that, the range of velocity at the seafloor is wider (2.5 - 3.5 km/s) in our model. The average velocity in the models of Momoh et al. (2017); Corbalán et al. (2021) and Minshull et al. (2006) reaches 7-8 km/s at a depth of 4-5 km. This range of velocity in our 1D model is at a depth of 7 km and indicates a similar crustal thickness (7 km) with estimated 1D velocity models of ambient noise interferometry (Mohamadian Sarvandani et al., 2021).

Overall, the study reported here could be used as a reference for other ultra-slow spreading ridges with low melt supply and also divergent margins such as the magma-poor oceanic-continent transition zone.

## 7.2 Challenges and Suggestions

Ambient-noise interferometry requires in principle that noise sources be uniformly distributed in space, a condition that is not always strictly met in practical situations. As a result, some uncertainty is to be expected. It is proposed to validate the phase velocity with information from earthquakes (Kästle et al., 2016).

Inversion of passive seismic data still suffers from non-uniqueness since we use only the fundamental mode of dispersion curve. To avoid this non-uniqueness and increase the accuracy of the inversion, other modes could be taken into account (Wang et al., 2019).

In passive seismic tomography, we have used depth inversions independently in 1D modeling beneath each geographical location. Recently, (Zhang et al., 2018) demonstrated that these depth inversions are spatially correlated. Therefore, a 3D Monte Carlo method with 3D parameterization is proposed to take into account these correlations (Zhang et al., 2018).

The seismic method still suffers from considerable limitations for determining the serpentinization (Rouméjon and Cannat, 2014): 1. It is not easy to approximate the extent of serpentinization since the seismic velocities of gabbro, basalt, and dolerites are close to the velocity of partially serpentinized peridotites (Miller and Christensen, 1997). 2. The resolution of seismic velocity models is sometimes not enough, and moderate serpentinization can have the same seismic properties as complete serpentinization. 3. Low seismic velocities in the upper crust do not correspond to fully serpentinized peridotites, implying that fracturing reduces velocity (Behn and Kelemen, 2003). Further constraints are suggested to mitigate these limitations.

While one of our objectives was to determine the damage zone of the region, the location of our stations did not allow us to achieve this. Full waveform inversion of OBS data for profiles across the ridge axis will help us in this context.

The derived P-wave velocity model from FWI can be used as a background velocity model for reverse time migration (Prieux et al., 2013).

Even though we have meticulously calculated the OBS gathers in FWI through the finite-difference method, there exists no perfect method of computing OBS gathers accurately for the elastic wave equation and with covering high and low frequencies (Cao and Greenhalgh, 1992).

Applying FWI to real-world data remains difficult. These challenges could be connected to the lack of data in the low-frequency range, source determination, poor refraction for long-offsets, inaccuracy of the selected wave equation, and decoupling between parameters (Messud et al., 2021).

We utilized wide-angle refraction to directly target crustal structures. Nevertheless, one of the main disadvantages of this data is its low structural resolution (Hübscher and Gohl, 2013).

A longer passive seafloor seismic experiment, leaving the OBS for a longer period of time, would yield better results for both seismicity and ambient noise tomography.

## Conclusion générale

L'absence apparente d'activité volcanique à la fois aux extrémités des segments et le long de l'axe de la dorsale sur plus de 100 km (Sauter et al., 2004; Carbotte et al., 2016) ainsi qu'une grande quantité de péridotite mantellique dans la vallée axiale (Dick et al., 2003) ont permis de proposer un style d'accrétion à tectonique dominante pour la partie la plus orientale de la dorsale Sud Ouest Indienne. L'hypothèse actuelle dans cette région est que la présence de systèmes de failles de détachement est responsable de la formation de la croûte sous-jacente et de la morphologie du plancher océanique. Bien qu'un nombre croissant de recherches aient été effectuées dans la région, l'imagerie de la structure crustale était nécessaire pour comprendre et reconnaître les processus tectoniques passés et en cours, la zone endommagée du système, l'épaisseur de la croûte, la distribution spatiale et l'intensité de la serpentinisation, et la lithologie.

Nous avons utilisé des données de réfraction sismique et des données de bruit ambiant pour imager les structures de la croûte et du manteau supérieur. C'est la première fois que la FWI a été utilisée dans la région sur un profil parallèle à l'axe. De plus, l'utilisation de l'interférométrie à bruit ambiant était une approche assez nouvelle dans l'étude des dorsales médio-océaniques.

Les composantes verticales de 43 OBS ont été utilisées pour analyser les signaux de bruit ambiant. L'analyse des données de sismique réfraction était basée sur les composantes hydrophones de 16 OBS. La principale étape de préparation des données a été la conversion des données brutes au format SAC pour l'interférométrie à bruit ambiant, tandis que le format SEG-Y est utilisé pour le traitement et la modélisation des données de réfraction. La conversion des données était une partie très chronophage de mon travail. Pour chaque type d'instrument, j'ai dû trouver un moyen de convertir les données du format brut au format SEG-Y continu et non

basé sur une table de tir, comme c'est habituellement le cas en sismique grand-angle. Puis j'ai transformé les données en format SAC.

En interférométrie dans le bruit ambiant, 176 corrélations croisées dans le domaine temporel étaient acceptables avec une distance inter-stations de 5-28 km et pour des fréquences inférieures à 1Hz. Nos résultats de cross-correlation ont démontré que les signaux de bruit ambiant continu enregistrés dans la région comprenaient une quantité considérable d'énergie cohérente.

Les vitesses de phase extraites des fonctions de corrélation inter-stations et régression se situaient entre 1 km/s et 3,5 km/s pour des périodes comprises entre 1 s et 10 s et étaient en bon accord avec deux rares exemples d'utilisation de l'interférométrie du bruit ambiant dans l'imagerie de la lithosphère océanique (Harmon et al., 2007; Yao et al., 2011). En dehors de cette plage de périodes, le faible rapport signal/bruit a interdit toute analyse supplémentaire.

Les modèles de vitesse des ondes P et S obtenus par tomographie du bruit ambiant ont indiqué une épaisseur crustale d'environ 7 km. Cette épaisseur est plus importante que les 4.2-5 km estimés à partir du modèle de vitesse des ondes P dans (Momoh et al., 2017) dans la partie centrale de la zone d'étude. Cette plus grande épaisseur crustale pourrait être due à l'emplacement de la plupart des stations utilisées dans le compartiment du mur de la faille de détachement axial active orientée vers le sud.

La vitesse moyenne des ondes de cisaillement entre la base de la croûte (définie par un seuil Vs de 4 km/s) et la profondeur maximale de notre modèle (15 km) est de 4.2 km/s, ce qui est inférieur à la valeur de référence globale de 4.5 km/s (Kennett et al., 1995). Cela peut s'expliquer par l'âge plus jeune du plancher océanique dans notre région.

Le rapport élevé de Vp/Vs à une profondeur moindre de la croûte indique une porosité élevée et une certaine quantité de péridotite serpentinisée. Le rapport minimum prédisait une porosité plus faible dans les parties plus profondes et était en accord avec le rapport Vp/Vs des roches gabbroïques SWIR analysées dans (Miller and Christensen, 1997). Les variations rapides des vitesses des ondes P et S à des profondeurs inférieures à 6,5-7,2 km et les changements lents à des profondeurs supérieures à 7,2 pourraient également montrer les variations du processus de serpentinisation dans la croûte et le manteau supérieur. La gamme variable de Vp/Vs dans la croûte et la serpentinisation considérable ont été expliquées par la fracturation de la croûte associée aux systèmes de failles de détachement et était compatible avec le modèle géologique hétérogène (Mével, 2003; Rouméjon et al., 2015). Ces résultats de serpentinisation et de fractures sont en accord avec les travaux de modélisation des ondes P de (Corbalán et al., 2021).

Notre modèle de vitesse des ondes P obtenu à partir de FWI suggère des variations considérables dans les compositions de la lithosphère supérieure le long du profil parallèle à l'axe. Une transition est attendue à une distance de modèle de $\sim$65-95 km entre un domaine à prédominance volcanique dans la zone occidentale et celui composé de péridotite serpentinisée dans la zone orientale. Une augmentation vers l'ouest de l'approvisionnement en matière fondue est proposée dans le mode d'accrétion du plancher océanique.

Nous n'avons pas pu observer d'arrivées réfléchies par le Moho grand angle (PmP) dans notre ensemble de données OBS. L'absence d'arrivées PmP est compatible avec d'autres dorsales océaniques ultra-lentes (Grevemeyer et al., 2018). Nos données OBS associées aux données MCS et de bathymétrie (Cannat et al., 2006; Sauter et al., 2013; Momoh et al., 2017) permettent de suggérer qu'une couche supérieure basaltique continue soit absente. Nous pouvons voir un changement rapide de la serpentinisation de 100% à 20% et des vitesses < 7 km/s à faible profondeur dans la zone de transition et dans la zone orientale. Cette variation est graduelle pour une serpentinisation inférieure à 20% et des vitesses > 7 km/s. La diminution graduelle de la serpentinisation et des vitesses des ondes P dans les sections plus profondes suggère également que le Moho est une transition graduelle de la péridotite hydratée à la péridotite non altérée dans la plupart des parties du profil.

Les vitesses inférieures à 4,5 km/s dans la zone de transition et la zone orientale peuvent éventuellement soutenir la présence de péridotite entièrement serpentinisée à faible profondeur. La présence de péridotite entièrement serpentinisée au sommet du modèle de ces zones est en accord avec les études du plancher océanique (Cannat et al., 2006; Sauter et al., 2013).

Dans les zones de transition et orientale, nous estimons une épaisseur moyenne de 3-4 km (inférieure à l'épaisseur de 4,2-5 km estimée par (Momoh et al., 2017) dans le plancher océanique lisse). L'épaisseur variable de la croûte dans la transition pourrait être dérivée des injections de dikes et des petites failles normales. Les injections de dikes pourraient être responsables des valeurs plus faibles de l'anomalie de Bouguer (Cannat et al., 2006). En accord avec les investigations par sonar latéral, nos résultats renforcent la possibilité que les zones de lave soient éjectées directement sur le plancher océanique par de petites failles normales décalées (Cannat et al., 2019; Sauter et al., 2013). Notre domaine de transition ∼54-86 km est très proche de celui obtenu par (Cannat et al., 2019). Momoh et al. (2020) ont également suggéré des sills magmatiques intrusifs pour expliquer les réflecteurs sismiques dans la transition. Un autre appui de notre étude est constitué par la présence d'un essaim de séismes peu profonds à une profondeur de moins de 2 km sous le plancher océanique dans la transition (Chen et al., 2021).

L'essaim de tremblements de terre à une profondeur de 6-11 km dans la zone ouest confirme l'injection volcanique dans cette zone ouest (Chen et al., 2021). L'accrétion océanique magmatique dans la zone occidentale est également cohérente avec l'anomalie gravimétrique négative (Cannat et al., 2019).

L'épaisseur moyenne de la croûte devrait être de 5-6 km dans la zone occidentale volcanique du modèle de vitesse d'onde P. Cette épaisseur est presque proche de l'épaisseur estimée (4 - 5,3 km) par Corbalán et al. (2021) dans la zone occidentale.

La moyenne du modèle 1D de vitesse des ondes P de cette étude est conforme à la tendance au lissage des modèles 1D dans (Momoh et al., 2017; Corbalán et al., 2021; Minshull et al., 2006). Cela dit, la gamme de vitesse au niveau du plancher océanique est plus large (2,5 - 3,5 km/s) dans notre modèle. La vitesse moyenne dans les modèles de Momoh et al. (2017); Corbalán et al. (2021) et Minshull et al. (2006) atteint 7-8 km/s à une profondeur de 4-5 km. Cette gamme de vitesse

dans notre modèle 1D est à une profondeur de 7 km et indique l'épaisseur crustale similaire (7 km) avec les modèles de vitesse 1D estimés de l'interférométrie de bruit ambiant (Mohamadian Sarvandani et al., 2021).

Dans l'ensemble, l'étude décrite ici pourra être utilisée comme référence pour d'autres dorsales océaniques ultra-lentes avec un faible apport en magma et également pour des marges divergentes telles que la zone de transition océan-continent pauvre en magma.

# Appendices

# Appendix A

# Additional explanation of chapter 2

## A.1 Basic concepts: waves, source, and receiver

In general, we have two kinds of seismic methods in terms of their sources: passive and active. All the seismic methods work upon the principle that waves travel through the subsurface and the returned wave can be processed regarding the properties of the subsurface (Hübscher and Gohl, 2013). In principle, we need four main elements to observe seismic waves (Mari, 2021):

1. Source distribution: The duty of the source is to produce the deformation in the medium.
2. Physical medium or geological formations defined by mechanical parameters Vs, Vp, density, and quality factor.
3. An elastic deformation in the medium produced by the source.
4. Receiver distribution: It must be able to record the deformation in the medium. This record is carried out either by variations in displacement, velocity, or acceleration (geophones, accelerometers) or through the measurement of pressure variations (hydrophone).

The details of the waves, sources, and receivers will be explained in the following.

### A.1.1 Waves

In the active seismic method, the emitted wave is a P-wave, or sound wave, and is generated by humans. What is very important is that we must know the emitted and recorded waves in active or passive seismic acquisition. In an active seismic survey, when the emitted P-waves enter the Earth, in addition to transmission and reflection to the receiver, they are converted into S waves (Hendrick, 2006; OGP, 2011). To have a better perception of how P-waves are converted into S-waves, see Figure A.1B. In passive seismic, the source (such as an earthquake) radiates S waves and P waves in all directions (Figure A.2). In both active and seismic surveys, the interaction of body waves with the surface of the earth produces surface waves (Figure A.2C). Therefore, typically, what we receive as a result of ground motions in the receivers are body waves (P and S waves) and surface waves (Rayleigh waves and Love waves). Based on how these waves move the ground, we can record these waves in the components of the receivers. Based on our target, we use the P-wave, S-wave, or surface wave in the processing or imaging of data. For example, in

P-wave or S-wave tomography or in P-wave or S-wave migration, we may pick only one component of the receiver. This selection of P-wave or S-wave is the same for passive and active data. In the next part, we will explain these waves in more detail.

Seismic waves are not only divided into body and surface waves but also classified into short and long periods. When the wave arrives, the surface of the ground rises to the maximum amplitude. After that, it starts falling to its initial level, or flatness. This rise and fall of the ground are quicker for short-period waves (e.g., 1 second) and slower for long-period waves (e.g., 1 minute). These short and long-period waves are also called high-frequency and low-frequency waves, respectively, by geophysicists.

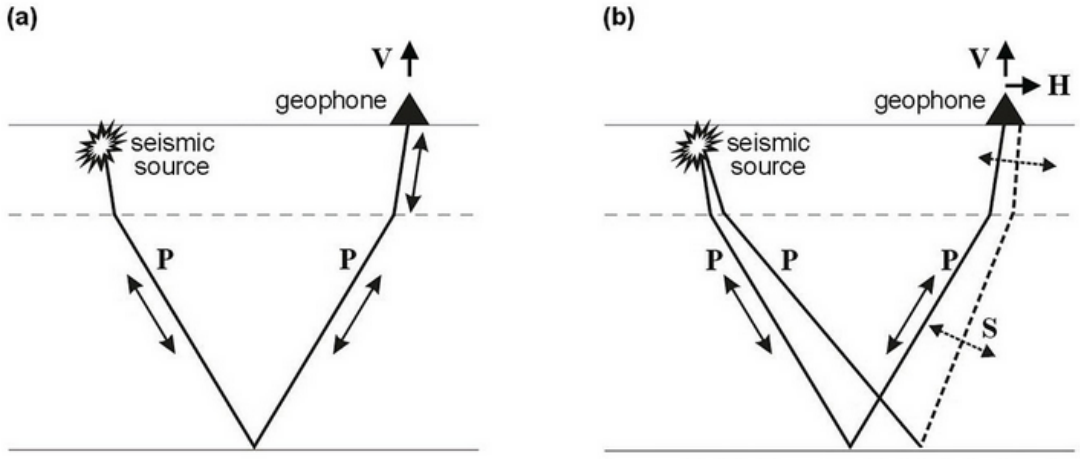


Figure A.1: A) The P-wave is received directly at the vertical component of the geophone. B) The P-wave is divided into P-wave and S-wave components, with the P-wave being recorded by the vertical components and the S-wave being recorded by the horizontal components (Hendrick, 2006).

#### A.1.1.1 Body waves: P and S waves

Body waves propagate through the interior structures of the Earth. The first kind of body wave is the P-wave or primary wave. This is the fastest kind of seismic wave and, consequently, the first to arrive at a seismic station (receiver). In P-waves, the vibration of the rock is in the direction of wave propagation or travel (Schuck and Lange, 2007) (see Figure A.1, Figure A.2B and Figure A.3). P-waves are compressive and travel upward through the body of the earth. So, the P-wave mostly affects the vertical movement of the ground and is recorded by the vertical component of the receiver (Hendrick, 2006). The P-wave can move through solid rock and fluids like water or the liquid layers of the earth. P-waves are also known as compressional waves. The second type of body wave is the S-wave or secondary wave. The particle motion generated by the S-wave is perpendicular to the direction of propagation (Schuck and Lange, 2007) (see Figure A.1, Figure A.2A and Figure A.3). When S-waves arrive at the earth's surface, they mainly move the ground horizontally and can be recorded by the horizontal components of the receiver (Hendrick, 2006). However, a less energetic S-wave can be detected on the vertical component of the receiver. An S-wave travels at a slower rate than a P-wave and can only pass through solid rock (Kumar et al., 2021). It should be noticed that in

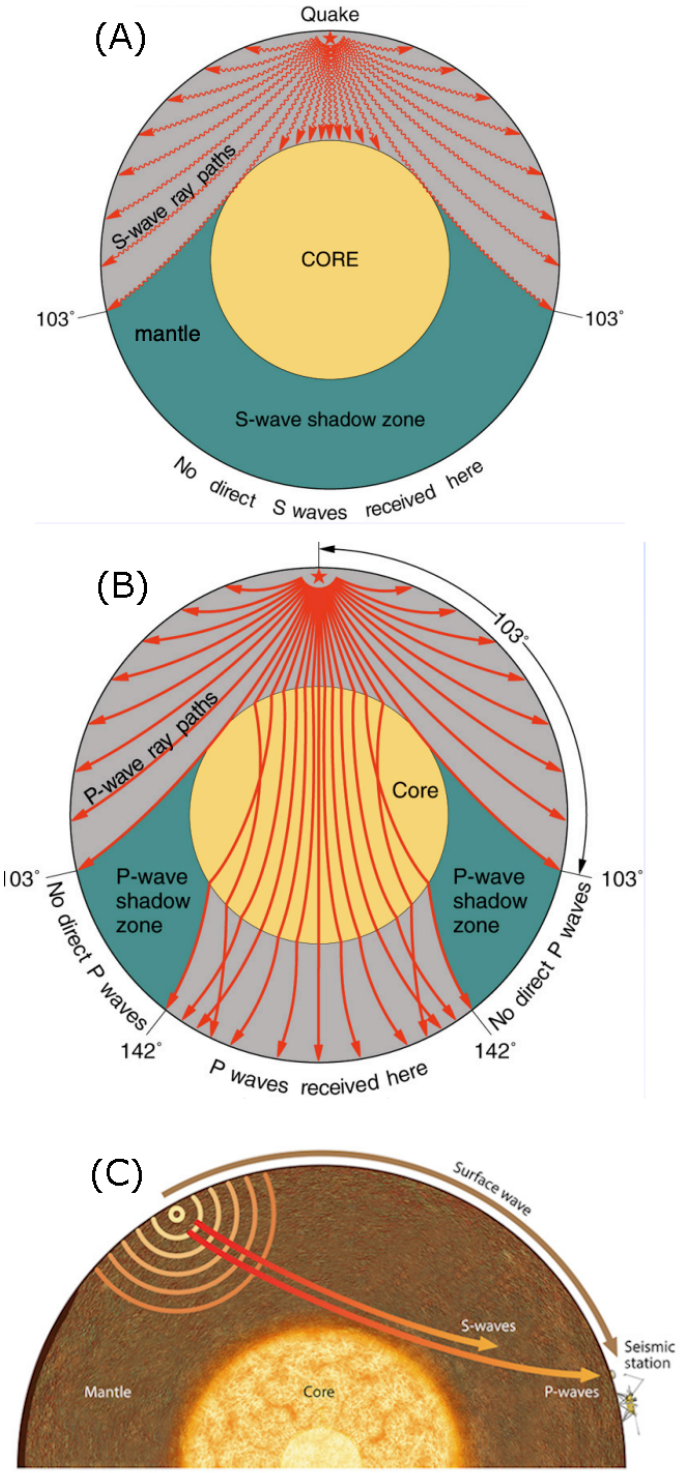


Figure A.2: A) The propagation of S-waves beneath the Earth caused by earthquakes. The particle motion is perpendicular to the direction of propagation. B) Propagation of a P-wave caused by an earthquake beneath the Earth. The particle motion is in parallel with the direction of propagation. C) Propagation of surface waves on the earth's surface and body waves (P and S waves) beneath the Earth (Plummer, 2004; Ducros, 2018). The direction of particles motion has been ignored in C.

Figure A.3, we are showing the movement of P-wave and S-wave in a layer but not on the surface of the Earth. When a P-wave and an S-wave arrive at the surface, the ground motion is mostly vertical and horizontal accordingly (see Figure A.1).

#### A.1.1.2 Surface waves: Love waves and Rayleigh waves

Surface waves propagate only at the interface between two different mediums, such as the interface between the surface of the Earth and the atmosphere. They arrive at the receivers after the P and S waves and are confined to the near-surface layers of the Earth. Traveling only through the crust, surface waves usually have larger amplitudes and longer wavelengths than body waves (Kumar et al., 2021). However, they move more slowly than body waves, they are often the most destructive type of seismic wave (Leiber, 2003). The two most common types of surface waves are Rayleigh waves and Love waves. Love waves are the fastest surface waves and move the ground from side to side in a horizontal plane perpendicular to the direction that the waves are traveling (see Figure A.3). That's why they are observable in the horizontal components of receivers. Rayleigh waves roll along the ground just like a wave rolls across a lake or ocean (see Figure A.3). These waves are generated by the interaction of P and S waves at the surface of the earth. They move the ground up and down, and side-to-side. Therefore, the motion of these waves can be recorded by the vertical and horizontal components of receivers.

### A.1.2 Sources and receivers

In passive seismic, the sources are earthquakes and ambient noise. The source of ambient noise seems to be generated by coupling between the ocean wave energy and solid earth (Longuet-Higgins, 1950; Hasselmann, 1963; Hillers et al., 2012; Gualtieri et al., 2013). In land active seismic, the source is normally an explosion, and in marine seismic, air guns are mostly used as the main source. The air gun generates a high-amplitude signal by sending high-pressure air into the water. The energy emitted by the air gun is primarily vertically downward (Landrø and Amundsen, 2010). The pressurized or compressed air of the air gun is supplied by an air compressor during the shooting. The main disadvantage of the air gun is the bubble pulse produced by the expansion-collapse cycle of the air bubble. The typical solution for suppressing bubble noise is to use several air guns with different volumes as well as clustering of air guns in an array (Dondurur, 2018). The air gun array consists of some strings (sub-arrays) Each string can contain individual air guns or clusters of air guns The volume of the air gun array is calculated by the summation of the volumes of each gun (typically 49.2–131.6 liter) (Landrø and Amundsen, 2010).

Ocean bottom seismometers (OBS) are receivers in marine seismic that contain 3 components of seismometers and a hydrophone to record long-offset seismic data. Some of the energy from the waves comes back to the recording receivers. The receivers measure the strength of the energy and the travel time of this energy between the earth's layers and the location of the receivers. However, the words "amplitude" and "energy" are often used interchangeably in recorded data in the receivers; energy is proportional to the square of the amplitude. The measured data, using the seismic processing methods, is converted into an image of the subsurface of the earth in the region (OGP, 2011).

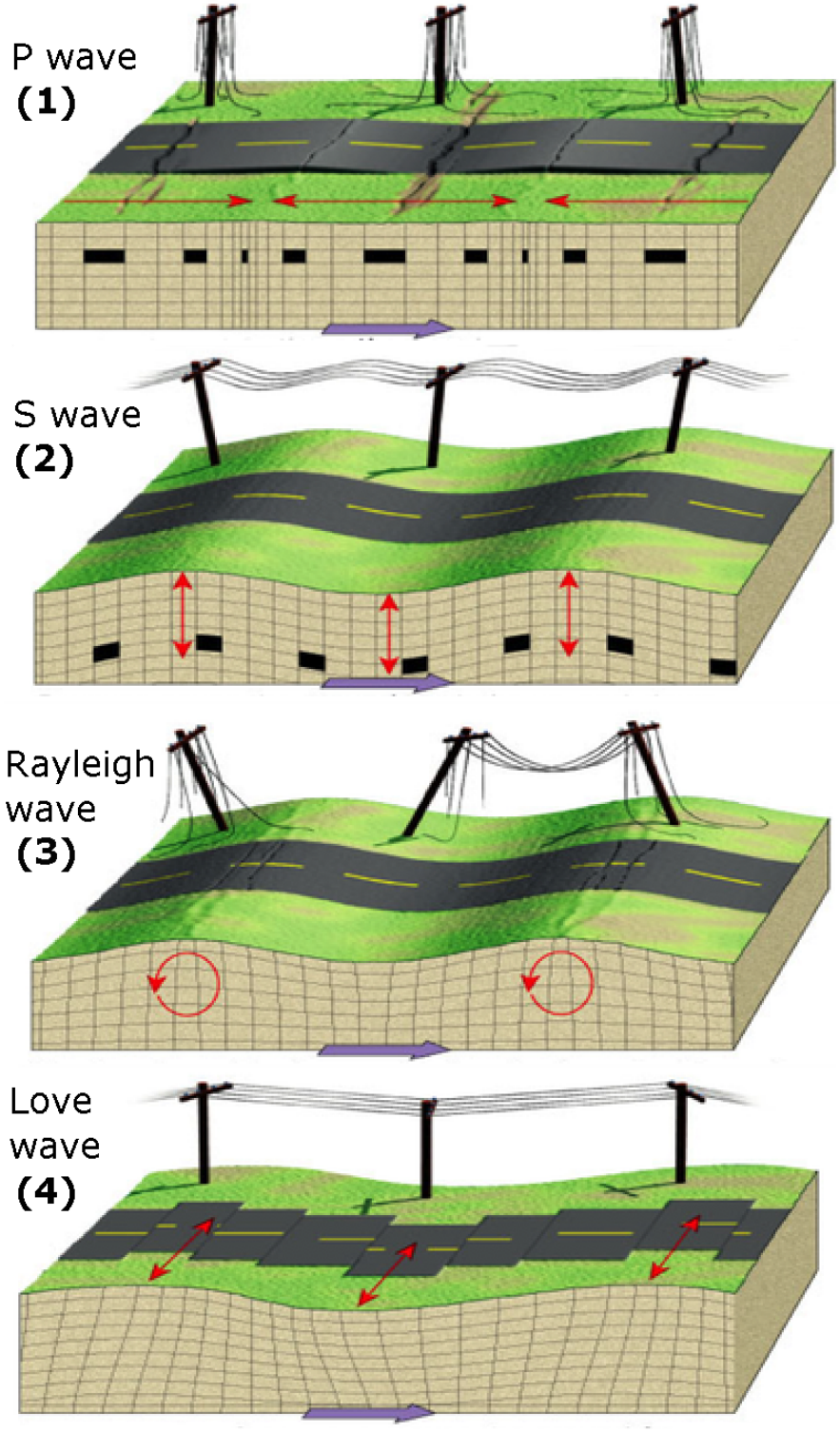


Figure A.3: Top to bottom: 1. Motion of particles (red arrow) parallel with the direction of P-wave propagation in a layer. 2. Motion of particles in a layer perpendicular to the direction of wave propagation3. horizontal and vertical motion of Rayleigh waves near the Earth's surface. 4. Horizontal motion of the love wave near the Earth's surface (Craven, 2011).

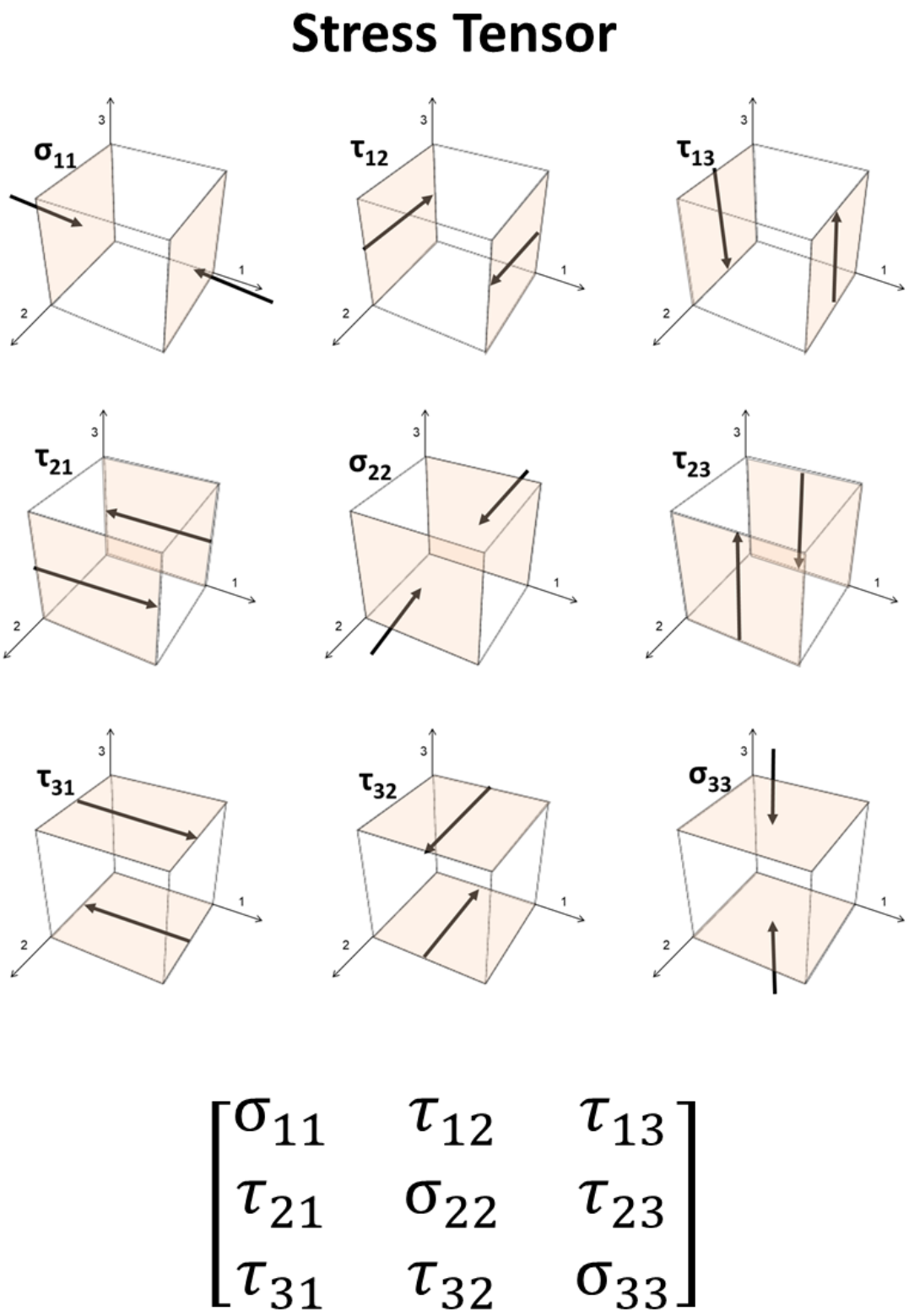


Figure A.4: Stress is specified as the force per unit area. The normal stress is shown by $\sigma$ and it is perpendicular to the surface of the object. The shear stress is parallel to the object's surface and is denoted by $\tau$ in the Figure. The stresses in different directions are presented in the stress tensor. In $\tau_{ij}$ or $\sigma_{ij}$, i is indicative of the plane and j is representative of the stress direction (Thierney, 2019).

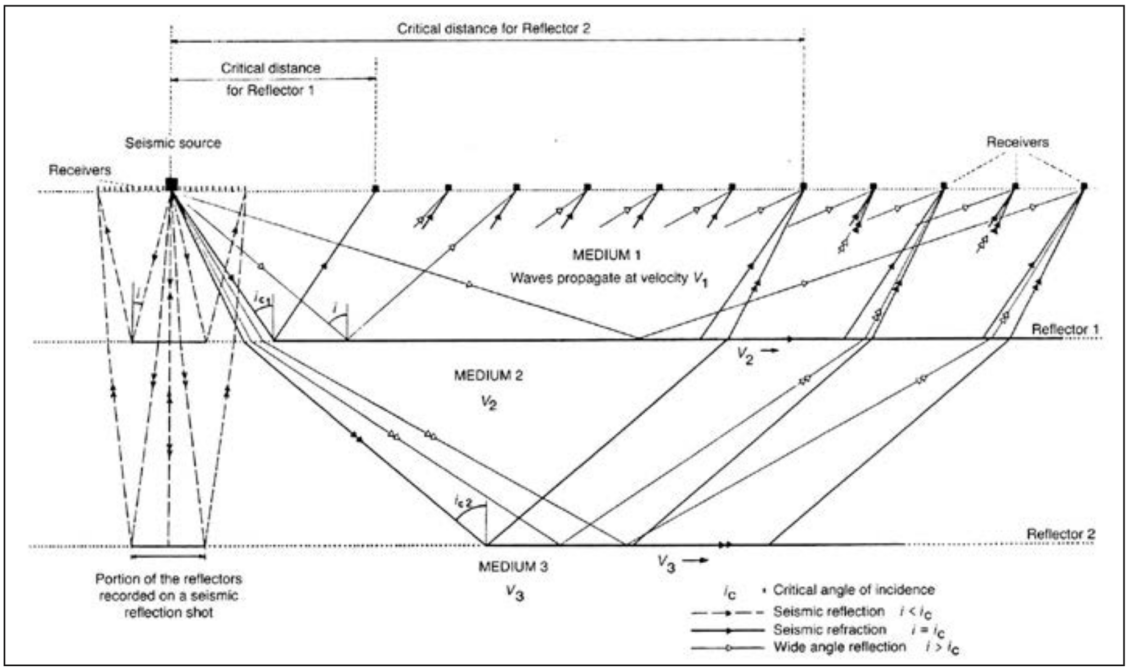


Figure A.5: Three types of seismic surveys At distances smaller than the critical distance reflected waves can be recorded. At distances equal to critical distance and greater than critical distances, refracted and wide-angle reflected waves will be captured by receivers (Mari, 2021).

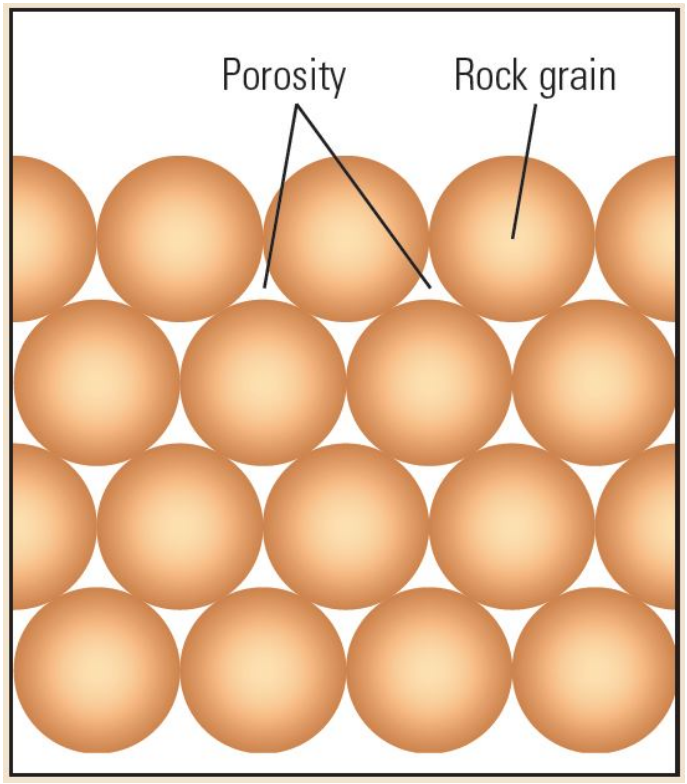


Figure A.6: The void space in rocks is porosity (Smithson, 2015).

# Appendix B

# Additional explanation of chapter 3

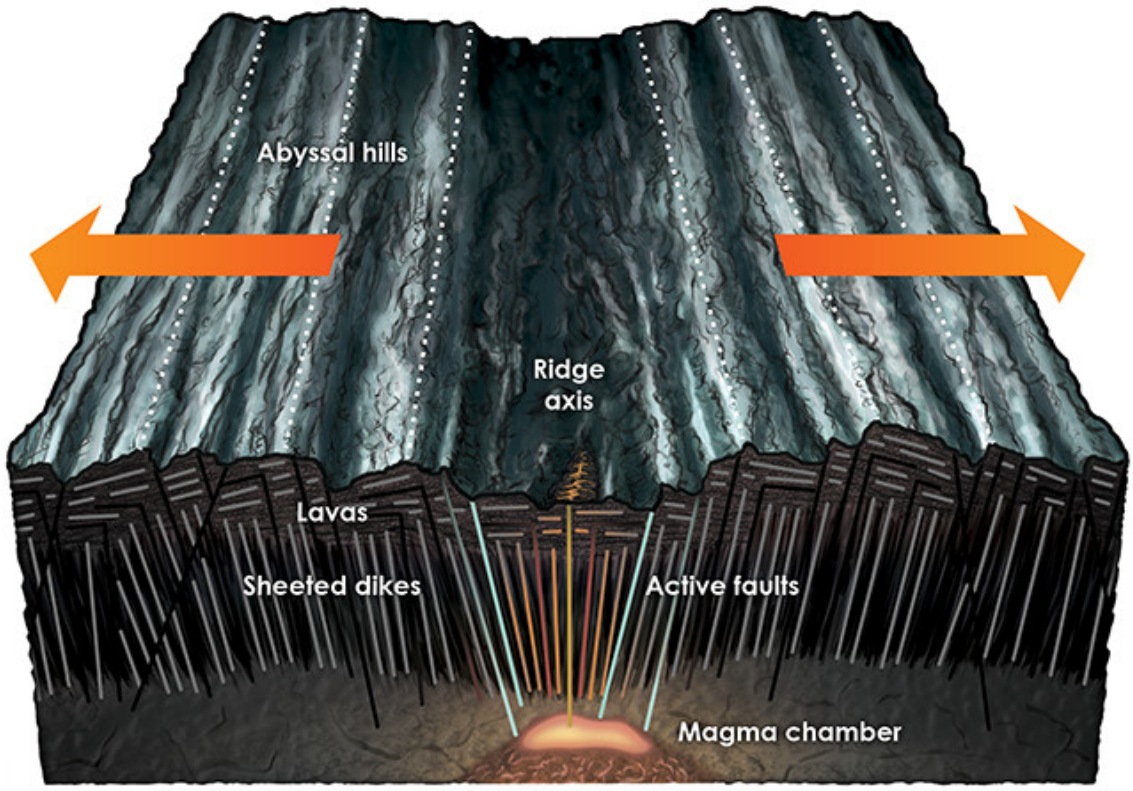


Figure B.1: Symmetric abyssal hills are created when small-offset faults beak on both sides of the ridge axis (Rosen, 2015).

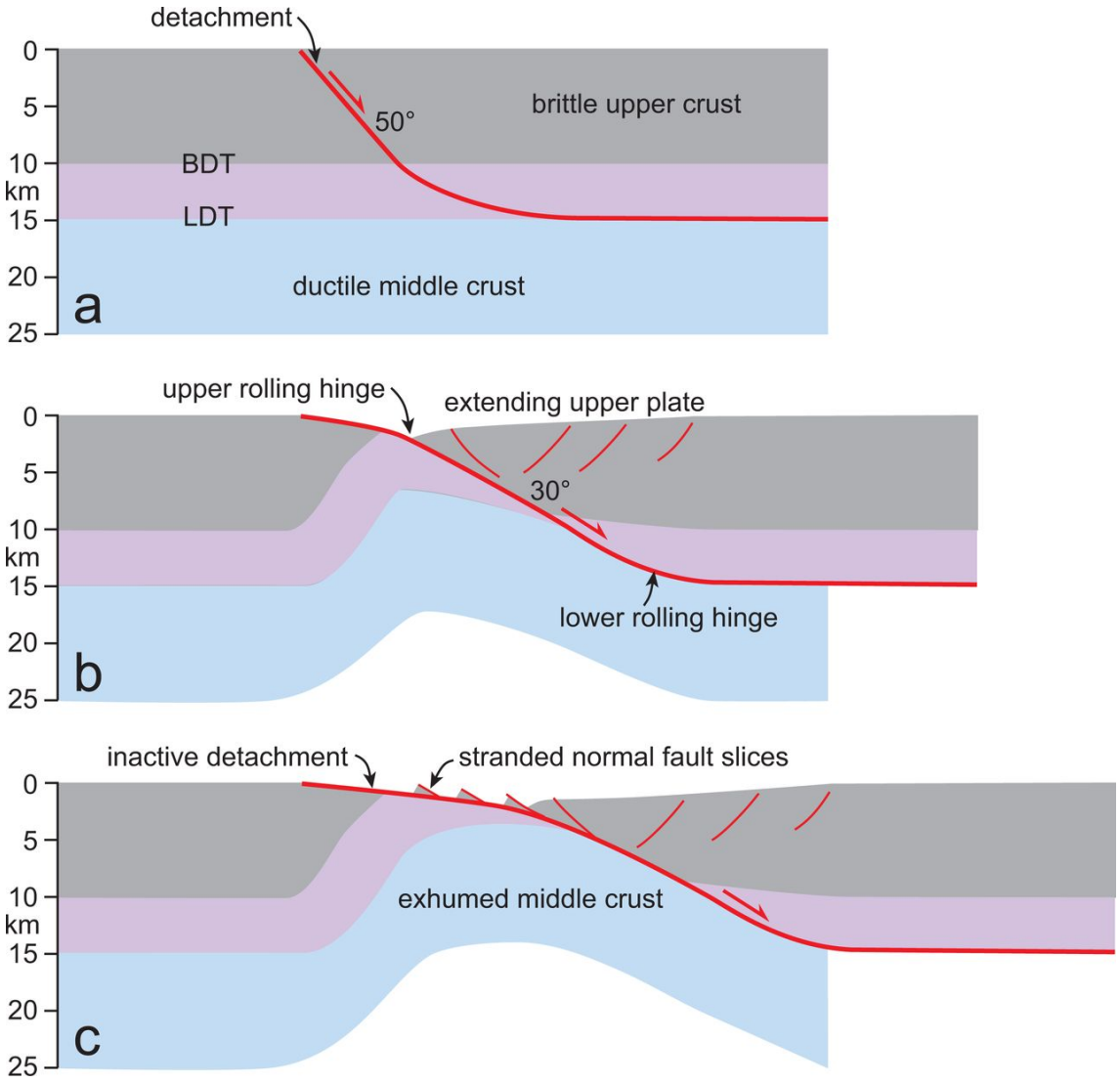


Figure B.2: Setting of a detachment fault system when the magma is poor or the M value is less than 0.5. A) Detachment fault system activation at 50° dip. B) Decrease in dip to 30° by horizontal moving of the upper plate. C) Detachment fault rolling in a horizontal direction (Platt et al., 2015).

# Appendix C

# Additional explanation of chapter 6

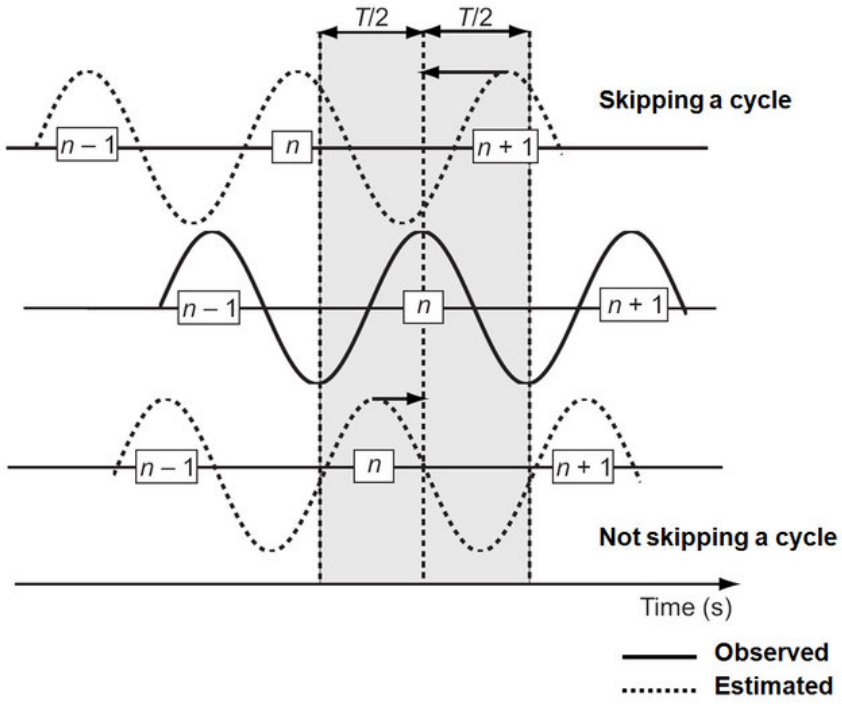


Figure C.1: A schematic diagram presents the cycle-skipping concept in FWI. The period of the observed seismogram is T. The upper estimated seismogram with a time delay of > T/2 causes cycle-skipping (the n+1th cycle of estimated data will match the nth cycle of observed data). There is no cycle-skipping for the upper estimated seismogram with a time delay of < T/2 (Roy, 2013)

.

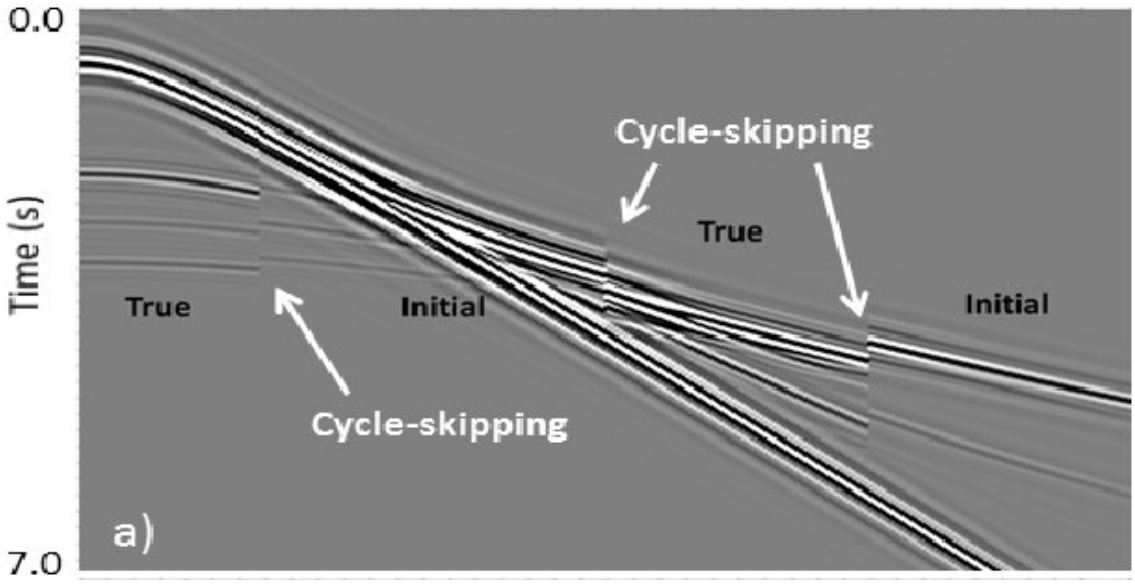


Figure C.2: The presence of cycle skipping when the initial model is far from the true model (Ramos-Martínez et al., 2018).

# Bibliography


Aghaei, O., Nedimović, M. R., Carton, H., Carbotte, S. M., Canales, J. P., and Mutter, J. C. (2014). Crustal thickness and moho character of the fast-spreading east pacific rise from 9° 42′ n to 9° 57′ n from poststack-migrated 3-d mcs data. *Geochemistry, Geophysics, Geosystems*, 15(3):634–657.

Agius, M. R., D'Amico, S., Galea, P., and Panzera, F. (2014). Performance evaluation of wied dalam (wdd) seismic station in malta. *Journal of The Malta Chamber of Scientists*.

Aki, K. (1957). Space and time spectra of stationary stochastic waves, with special reference to microtremors. *Bulletin of the Earthquake Research Institute*, 35(3):415–456.

Aki, K. and Richards, P. G. (2002). Quantitative seismology, sausalito.

Albers, E., Bach, W., Pérez-Gussinyé, M., McCammon, C., and Frederichs, T. (2021). Serpentinization-driven h2 production from continental break-up to mid-ocean ridge spreading: Unexpected high rates at the west iberia margin. front. *Earth Sci*, 9:673063.

Allan Jones, B. C. and Picton, P. (2020). Signal processing: First-order filters.

Alterman, Z. and Karal Jr, F. (1968). Propagation of elastic waves in layered media by finite difference methods. *Bulletin of the Seismological Society of America*, 58(1):367–398.

Arnulf, A., Harding, A., Singh, S., Kent, G., and Crawford, W. (2012). Fine-scale velocity structure of upper oceanic crust from full waveform inversion of downward continued seismic reflection data at the lucky strike volcano, mid-atlantic ridge. *Geophysical Research Letters*, 39(8).

Arnulf, A., Singh, S., Harding, A., Kent, G., and Crawford, W. (2011). Strong seismic heterogeneity in layer 2a near hydrothermal vents at the mid-atlantic ridge. *Geophysical Research Letters*, 38(13).

Asghar, A. (2011). Processing and interpretation of multichannel seismic data from isfjorden, svalbard. Master's thesis, The University of Bergen.

Aumento, F. and Loubat, H. (1971). The mid-atlantic ridge near 45 n. xvi. serpentinized ultramafic intrusions. *Canadian Journal of Earth Sciences*, 8(6):631–663.

Bach, W., Banerjee, N. R., Dick, H. J., and Baker, E. T. (2002). Discovery of ancient and active hydrothermal systems along the ultra-slow spreading southwest indian ridge 10°–16° e. *Geochemistry, Geophysics, Geosystems*, 3(7):1–14.

Bakulin, A. and Calvert, R. (2004). Virtual source: new method for imaging and 4d below complex overburden. In *SEG Technical Program Expanded Abstracts 2004*, pages 2477–2480. Society of Exploration Geophysicists.

Behn, M. D. and Kelemen, P. B. (2003). Relationship between seismic p-wave velocity and the composition of anhydrous igneous and meta-igneous rocks. *Geochemistry, Geophysics, Geosystems*, 4(5).

Bensen, G., Ritzwoller, M., Barmin, M., Levshin, A., Lin, F., Moschetti, M., Shapiro, N., and Yang, Y. (2007). Processing seismic ambient noise data to obtain reliable broad-band surface wave dispersion measurements. *Geophysical Journal International*, 169(3):1239–1260.

Billette, F. and Brandsberg-Dahl, S. (2005). The 2004 bp velocity benchmark. In *67th EAGE Conference & Exhibition*, pages cp–1. EAGE Publications BV.

Bishop, T., Bube, K., Cutler, R., Langan, R., Love, P., Resnick, J., Shuey, R., Spindler, D., and Wyld, H. (1985). Tomographic determination of velocity and depth in laterally varying media: Geophysics. *Q)() 3_023*.

Bohlen, T., Kugler, S., Klein, G., and Theilen, F. (2004). 1.5 d inversion of lateral variation of scholte-wave dispersion. *Geophysics*, 69(2):330–344.

Boore, D. M. (1972). Finite difference methods for seismic wave propagation in heterogeneous materials. *Methods in computational physics*, 11:1–37.

Bormann, P., Engdahl, B., and Kind, R. (2012). Seismic wave propagation and earth models. In *New manual of seismological observatory practice 2 (NMSOP2)*, pages 1–105. Deutsches GeoForschungsZentrum GFZ.

Boschi, L. and Weemstra, C. (2015). Stationary-phase integrals in the cross correlation of ambient noise. *Reviews of Geophysics*, 53(2):411–451.

Boschi, L., Weemstra, C., Verbeke, J., Ekström, G., Zunino, A., and Giardini, D. (2012). On measuring surface wave phase velocity from station–station cross-correlation of ambient signal. *Geophysical Journal International*, 192(1):346–358.

Bouchon, M., Campillo, M., and Gaffet, S. (1989). A boundary integral equation-discrete wavenumber representation method to study wave propagation in multi-layered media having irregular interfaces. *Geophysics*, 54(9):1134–1140.

Boulahanis, B., Carbotte, S. M., Huybers, P. J., Nedimović, M. R., Aghaei, O., Canales, J. P., and Langmuir, C. H. (2020). Do sea level variations influence mid-ocean ridge magma supply? a test using crustal thickness and bathymetry data from the east pacific rise. *Earth and Planetary Science Letters*, 535:116121.

Britannica, T. (2020). Editors of encyclopaedia. *Argon. Encyclopedia Britannica*.

Brossier, R., Virieux, J., and Operto, S. (2008). Parsimonious finite-volume frequency-domain method for 2-dp–sv-wave modelling. *Geophysical Journal International*, 175(2):541–559.

Brown, J. R. and Karson, J. A. (1988). Variations in axial processes on the mid-atlantic ridge: The median valley of the mark area. *Marine geophysical researches*, 10(1):109–138.

Buck, W. R. (1988). Flexural rotation of normal faults. *Tectonics*, 7(5):959–973.

Buck, W. R., Lavier, L. L., and Poliakov, A. N. (2005). Modes of faulting at mid-ocean ridges. *Nature*, 434(7034):719.

Bücker, C., Jenisch, U., Lutter, S., Matz-Lück, N., Messner, J., Petersen, S., Rüpke, L. H., Schwarz-Schampera, U., Wallmann, K., Berndt, C., et al. (2014). World ocean review 2015: Living with the oceans 3. marine resources-opportunities and risks.

Bussat, S. and Kugler, S. (2011). Offshore ambient-noise surface-wave tomography above 0.1 hz and its applications. *The Leading Edge*, 30(5):514–524.

Campillo, M. and Paul, A. (2003). Long-range correlations in the diffuse seismic coda. *Science*, 299(5606):547–549.

Canales, J. P., Collins, J. A., Escartín, J., and Detrick, R. S. (2000). Seismic structure across the rift valley of the mid-atlantic ridge at 23 20′(mark area): Implications for crustal accretion processes at slow spreading ridges. *Journal of Geophysical Research: Solid Earth*, 105(B12):28411–28425.

Canales, J. P., Dunn, R. A., Arai, R., and Sohn, R. A. (2017). Seismic imaging of magma sills beneath an ultramafic-hosted hydrothermal system. *Geology*, 45(5):451–454.

Canales, J. P., Sohn, R. A., and Demartin, B. J. (2007). Crustal structure of the trans-atlantic geotraverse (tag) segment (mid-atlantic ridge, 26° 10′ n): Implications for the nature of hydrothermal circulation and detachment faulting at slow spreading ridges. *Geochemistry, Geophysics, Geosystems*, 8(8).

Cannat, M. (1993). Emplacement of mantle rocks in the seafloor at mid-ocean ridges. *Journal of Geophysical Research: Solid Earth*, 98(B3):4163–4172.

Cannat, M., Fontaine, F., and Escartin, J. (2010). Serpentinization and associated hydrogen and methane fluxes at slow spreading ridges.

Cannat, M., Mevel, C., Maia, M., Deplus, C., Durand, C., Gente, P., Agrinier, P., Belarouchi, A., Dubuisson, G., Humler, E., et al. (1995). Thin crust, ultramafic exposures, and rugged faulting patterns at the mid-atlantic ridge (22–24 n). *Geology*, 23(1):49–52.

Cannat, M., Rommevaux-Jestin, C., and Fujimoto, H. (2003). Melt supply variations to a magma-poor ultra-slow spreading ridge (southwest indian ridge 61° to 69° e). *Geochemistry, Geophysics, Geosystems*, 4(8).

Cannat, M., Rommevaux-Jestin, C., Sauter, D., Deplus, C., and Mendel, V. (1999). Formation of the axial relief at the very slow spreading southwest indian ridge (49 to 69 e). *Journal of Geophysical Research: Solid Earth*, 104(B10):22825–22843.

Cannat, M., Sauter, D., Bezos, A., Meyzen, C., Humler, E., and Le Rigoleur, M. (2008). Spreading rate, spreading obliquity, and melt supply at the ultraslow spreading southwest indian ridge. *Geochemistry, Geophysics, Geosystems*, 9(4).

Cannat, M., Sauter, D., Lavier, L., Bickert, M., Momoh, E., and Leroy, S. (2019). On spreading modes and magma supply at slow and ultraslow mid-ocean ridges. *Earth and Planetary Science Letters*, 519:223–233.

Cannat, M., Sauter, D., Mendel, V., Ruellan, E., Okino, K., Escartin, J., Combier, V., and Baala, M. (2006). Modes of seafloor generation at a melt-poor ultraslow-spreading ridge. *Geology*, 34(7):605–608.

Cao, S. and Greenhalgh, S. (1992). Finite-difference simulation of p—sv-wave propagation: a displacement-potential approach. *Geophysical Journal International*, 109(3):525–535.

Capon, J. (1969). High-resolution frequency-wavenumber spectrum analysis. *Proceedings of the IEEE*, 57(8):1408–1418.

Carbotte, S. M., Smith, D. K., Cannat, M., and Klein, E. M. (2016). Tectonic and magmatic segmentation of the global ocean ridge system: a synthesis of observations. *Geological Society, London, Special Publications*, 420(1):249–295.

Carlson, R. (2001). The abundance of ultramafic rocks in atlantic ocean crust. *Geophysical Journal International*, 144(1):37–48.

Carlson, R. L. and Miller, D. J. (2003). Mantle wedge water contents estimated from seismic velocities in partially serpentinized peridotites. *Geophysical Research Letters*, 30(5).

Cawood, P. A., Kroner, A., and Pisarevsky, S. (2006). Precambrian plate tectonics: criteria and evidence. *GSA today*, 16(7):4.

Chapman, C. et al. (1985). Ray theory and its extensions: Wkbj and maslov seismograms. *Journal of Geophysics*, 58(1):27–43.

Charlou, J.-L. and Donval, J.-P. (1993). Hydrothermal methane venting between 12° n and 26° n along the mid-atlantic ridge. *Journal of Geophysical Research: Solid Earth*, 98(B6):9625–9642.

Charlou, J. L., Fouquet, Y., Bougault, H., Donval, J. P., Etoubleau, J., Jean-Baptiste, P., Dapoigny, A., Appriou, P., and Rona, P. A. (1998). Intense ch4 plumes generated by serpentinization of ultramafic rocks at the intersection of the 15 20′ n fracture zone and the mid-atlantic ridge. *Geochimica et Cosmochimica Acta*, 62(13):2323–2333.

Chauris, H. (2021). Full waveform inversion. In *Seismic imaging: a practical approach*, pages 123–146. EDP Sciences.

Chen, J., Crawford, W., and Cannat, M. (2021). Microseismicity and lithosphere thickness at a nearly amagmatic mid-ocean ridge.

Christensen, N. I. (2004). Serpentinites, peridotites, and seismology. *International Geology Review*, 46(9):795–816.

Chu, D. and Gordon, R. G. (1999). Evidence for motion between nubia and somalia along the southwest indian ridge. *Nature*, 398(6722):64.

Ciazela, J., Koepke, J., Dick, H. J., and Muszynski, A. (2015). Mantle rock exposures at oceanic core complexes along mid-ocean ridges. *Geologos 21 (2015)*.

Claerbout, J. F. (1968). Synthesis of a layered medium from its acoustic transmission response. *Geophysics*, 33(2):264–269.

Cohen, J. and Stockwell, J. (2003). Seismic unix release 37: a free package for seismic research and processing. *Center for Wave Phenomena, Colorado School of Mines*.

Conley, M. M. and Dunn, R. A. (2011). Seismic shear wave structure of the uppermost mantle beneath the mohns ridge. *Geochemistry, Geophysics, Geosystems*, 12(10).

Cooley, J. W. and Tukey, J. W. (1965). An algorithm for the machine calculation of complex fourier series. *Mathematics of computation*, 19(90):297–301.

Corbalán, A., Nedimović, M., Louden, K., Cannat, M., Grevemeyer, I., Watremez, L., and Leroy, S. (2021). Seismic velocity structure along and across the ultraslow-spreading southwest indian ridge at 64° 30′ e showcases flipping detachment faults. *Journal of Geophysical Research: Solid Earth*, 126(10):e2021JB022177.

Craven (2011). Christchurch earthquakes.

Danecek, P. and Seriani, G. (2008). An efficient parallel chebyshev pseudo-spectral method for large scale 3d seismic forward modelling. In *70th EAGE Conference and Exhibition incorporating SPE EUROPEC 2008*, pages cp–40. European Association of Geoscientists & Engineers.

Davy, R., Minshull, T., Bayrakci, G., Bull, J., Klaeschen, D., Papenberg, C., Reston, T. J., Sawyer, D., and Zelt, C. (2016). Continental hyperextension, mantle exhumation, and thin oceanic crust at the continent-ocean transition, west iberia: New insights from wide-angle seismic. *Journal of Geophysical Research: Solid Earth*, 121(5):3177–3199.

de Ridder, S. (2011). Ambient seismic noise tomography at valhall. In *SEG Technical Program Expanded Abstracts 2011*, pages 1597–1601. Society of Exploration Geophysicists.

Delescluse, M., Funck, T., Dehler, S. A., Louden, K. E., and Watremez, L. (2015). The oceanic crustal structure at the extinct, slow to ultraslow labrador sea spreading center. *Journal of Geophysical Research: Solid Earth*, 120(7):5249–5272.

DeMets, C., Gordon, R. G., Argus, D. F., and Stein, S. (1994). Effect of recent revisions to the geomagnetic reversal time scale on estimates of current plate motions. *Geophysical research letters*, 21(20):2191–2194.

Derode, A., Larose, E., Tanter, M., De Rosny, J., Tourin, A., Campillo, M., and Fink, M. (2003). Recovering the green's function from field-field correlations in an open scattering medium (l). *The Journal of the Acoustical Society of America*, 113(6):2973–2976.

Dewey, J. F. and Bird, J. M. (1970). Mountain belts and the new global tectonics. *Journal of geophysical Research*, 75(14):2625–2647.

Dick, H. (1989). Abyssal peridotites, very slow spreading ridges and ocean ridge magmatism. *Geological Society, London, Special Publications*, 42(1):71–105.

Dick, H., Thompson, G., and Bryan, W. (1981). Low-angle faulting and steady-state emplacement of plutonic rocks at ridge-transform intersections. *Eos Trans. AGU*, 62(17):406.

Dick, H. J., Lin, J., and Schouten, H. (2003). An ultraslow-spreading class of ocean ridge. *Nature*, 426(6965):405.

Dick, H. J., Macleod, C. J., Blum, P., Abe, N., Blackman, D. K., Bowles, J. A., Cheadle, M., Cho, K., Ciazela, J., Deans, J., et al. (2019). Dynamic accretion beneath a slow-spreading ridge segment: Iodp hole 1473a and the atlantis bank oceanic core complex. *Journal of Geophysical Research: Solid Earth*, 124(12):12631–12659.

Dick, H. J., Tivey, M. A., and Tucholke, B. E. (2008). Plutonic foundation of a slow-spreading ridge segment: Oceanic core complex at kane megamullion, 23 30′ n, 45 20′ w. *Geochemistry, Geophysics, Geosystems*, 9(5).

Dietz, R. S. (1963). Alpine serpentines as oceanic rind fragments. *Geological Society of America Bulletin*, 74(7):947–952.

Dondurur, D. (2018). *Acquisition and processing of marine seismic data*. Elsevier.

Draganov, D. and Ruigrok, E. (2014). Passive seismic interferometry for subsurface imaging. *Encyclopedia of Earthquake Engineering*, pages 1–13.

Ducros, D. (2018). Different types of seismic wave.

Dziewonski, A. M. and Anderson, D. L. (1981). Preliminary reference earth model. *Physics of the earth and planetary interiors*, 25(4):297–356.

Earle, S. (2019). Physical geology.

Edwards, M., Kurras, G., Tolstoy, M., Bohnenstiehl, D. R., Coakley, B. J., and Cochran, J. R. (2001). Evidence of recent volcanic activity on the ultraslow-spreading gakkel ridge. *Nature*, 409(6822):808–812.

Ekström, G. (2014). Love and rayleigh phase-velocity maps, 5–40 s, of the western and central usa from usarray data. *Earth and Planetary Science Letters*, 402:42–49.

Ekström, G., Abers, G. A., and Webb, S. C. (2009). Determination of surface-wave phase velocities across usarray from noise and aki's spectral formulation. *Geophysical Research Letters*, 36(18).

Engel, C. G. and Fisher, R. L. (1975). Granitic to ultramafic rock complexes of the indian ocean ridge system, western indian ocean. *Geological Society of America Bulletin*, 86(11):1553–1578.

Freudenreich, Y. and Singh, S. (2000). Full waveform inversion for seismic data-frequency versus time domain. In *62nd EAGE Conference & Exhibition*, pages cp–28. European Association of Geoscientists & Engineers.

Friedrich, A., Krueger, F., and Klinge, K. (1998). Ocean-generated microseismic noise located with the gräfenberg array. *Journal of Seismology*, 2(1):47–64.

Früh-Green, G. L., Kelley, D. S., Bernasconi, S. M., Karson, J. A., Ludwig, K. A., Butterfield, D. A., Boschi, C., and Proskurowski, G. (2003). 30,000 years of hydrothermal activity at the lost city vent field. *Science*, 301(5632):495–498.

Fujie, G., Kasahara, J., Murase, K., Mochizuki, K., and Kaneda, Y. (2008). Interactive analysis tools for the wide-angle seismic data for crustal structure study (technical report). *Exploration Geophysics*, 39(1):26–33.

Garcés, M. and Gee, J. S. (2007). Paleomagnetic evidence of large footwall rotations associated with low-angle faults at the mid-atlantic ridge. *Geology*, 35(3):279–282.

Georgen, J. E., Lin, J., and Dick, H. J. (2001). Evidence from gravity anomalies for interactions of the marion and bouvet hotspots with the southwest indian ridge: Effects of transform offsets. *Earth and Planetary Science Letters*, 187(3-4):283–300.

GEOS (2006). seismic data processing.

Geosci (2017). P-wave and s-wave velocities in common rocks. https://gpg.geosci.xyz/content/physical_properties/seismic_velocity_duplicate.html#factors-impacting-the-seismic-velocity.

Goldstein, P., Dodge, D., Firpo, M., Minner, L., Lee, W., Kanamori, H., Jennings, P., and Kisslinger, C. (2003). Sac2000: Signal processing and analysis tools for seismologists and engineers. *The IASPEI International Handbook of Earthquake and Engineering Seismology*, 81:1613–1620.

Goldstein, P. and Snoke, A. (2005). Sac availability for the iris community. dms electronic newsletter 7 (1).

Gordon, J., Gillespie, D., Potter, J., Frantzis, A., Simmonds, M. P., Swift, R., and Thompson, D. (2003). A review of the effects of seismic surveys on marine mammals. *Marine Technology Society Journal*, 37(4):16–34.

Gouedard, P., Stehly, L., Brenguier, F., Campillo, M., De Verdière, Y. C., Larose, E., Margerin, L., Roux, P., Sánchez-Sesma, F. J., Shapiro, N., et al. (2008). Cross-correlation of random fields: mathematical approach and applications. *Geophysical prospecting*, 56(3):375–393.

Grevemeyer, I., Hayman, N. W., Peirce, C., Schwardt, M., Van Avendonk, H. J., Dannowski, A., and Papenberg, C. (2018). Episodic magmatism and serpentinized mantle exhumation at an ultraslow-spreading centre. *Nature Geoscience*, 11(6):444–448.

Grindlay, N. R., Madsen, J. A., Rommevaux-Jestin, C., and Sclater, J. (1998). A different pattern of ridge segmentation and mantle bouguer gravity anomalies along the ultra-slow spreading southwest indian ridge (15° 30′ e to 25° e). *Earth and Planetary Science Letters*, 161(1-4):243–253.

Gualtieri, L., Stutzmann, E., Capdeville, Y., Ardhuin, F., Schimmel, M., Mangeney, A., and Morelli, A. (2013). Modelling secondary microseismic noise by normal mode summation. *Geophysical Journal International*, 193(3):1732–1745.

Hamada, G. (2004). Reservoir fluids identification using vp/vs ratio? *Oil & Gas Science and Technology*, 59(6):649–654.

Haney, M. M., Mikesell, T. D., van Wijk, K., and Nakahara, H. (2012). Extension of the spatial autocorrelation (spac) method to mixed-component correlations of surface waves. *Geophysical Journal International*, 191(1):189–206.

Hanssen, P. (2011). Passive seismic methods for hydrocarbon exploration. In *Third EAGE Passive Seismic Workshop-Actively Passive 2011*.

Harmon, N., Forsyth, D., and Webb, S. (2007). Using ambient seismic noise to determine short-period phase velocities and shallow shear velocities in young oceanic lithosphere. *Bulletin of the Seismological Society of America*, 97(6):2009–2023.

Hasselmann, K. (1963). A statistical analysis of the generation of microseisms. *Reviews of Geophysics*, 1(2):177–210.

Hendrick, N. (2006). Converted-wave seismology for coal exploration. *CSEG Recorder*, 27:31.

Herrmann, R. (1994). Computer program in seismology, vol iv. *St Louis University*.

Herrmann, R. B. (2013). Computer programs in seismology: An evolving tool for instruction and research. *Seismological Research Letters*, 84(6):1081–1088.

Hess, H. (1965). Mid-oceanic ridges and tectonics of the sea-floor. *Submarine Geology and Geophysics, edited by: Whittard, WF and Bradshaw*.

Hess, H., Engel, A., James, H., and Leonard, B. (1962). History of ocean basins.

Hillers, G., Graham, N., Campillo, M., Kedar, S., Landès, M., and Shapiro, N. (2012). Global oceanic microseism sources as seen by seismic arrays and predicted by wave action models. *Geochemistry, Geophysics, Geosystems*, 13(1).

Horning, G., Canales, J., Carbotte, S., Han, S., Carton, H., Nedimović, M., and Van Keken, P. (2016). A 2-d tomographic model of the juan de fuca plate from accretion at axial seamount to subduction at the cascadia margin from an active source ocean bottom seismometer survey. *Journal of Geophysical Research: Solid Earth*, 121(8):5859–5879.

Hübscher, C. and Gohl, K. (2013). Reflection/refraction seismology. *Encyclopedia of Marine Geosciences*, pages 1–15.

IRIS (2021). 3-component seismogram records seismic-wave motion, how do we capture the motion of an earthquake?

Kahraman, S. (2019). *The effect of water saturation on the P-wave velocity of sedimentary rocks*. Universitätsbibliothek der RWTH Aachen.

Kandilarov, A., Mjelde, R., Okino, K., and Murai, Y. (2008). Crustal structure of the ultra-slow spreading knipovich ridge, north atlantic, along a presumed amagmatic portion of oceanic crustal formation. *Marine Geophysical Researches*, 29(2):109–134.

Kao, H., Behr, Y., Currie, C. A., Hyndman, R., Townend, J., Lin, F.-C., Ritzwoller, M. H., Shan, S.-J., and He, J. (2013). Ambient seismic noise tomography of canada and adjacent regions: Part i. crustal structures. *Journal of Geophysical Research: Solid Earth*, 118(11):5865–5887.

Karson, J. (1990). Seafloor spreading on the mid-atlantic ridge: Implications for the structure of ophiolites and oceanic lithosphere produced in slow-spreading environments. In *Troodos 1987. Symposium*, pages 547–555.

Kästle, E. D., Soomro, R., Weemstra, C., Boschi, L., and Meier, T. (2016). Two-receiver measurements of phase velocity: cross-validation of ambient-noise and earthquake-based observations. *Geophysical Journal International*, 207(3):1493–1512.

Kay, R., Hubbard, N. J., and Gast, P. W. (1970). Chemical characteristics and origin of oceanic ridge volcanic rocks1. *Journal of Geophysical Research*, 75(8):1585–1613.

Kelley, D. S., Karson, J. A., Blackman, D. K., FruÈh-Green, G. L., Butterfield, D. A., Lilley, M. D., Olson, E. J., Schrenk, M. O., Roe, K. K., Lebon, G. T., et al. (2001). An off-axis hydrothermal vent field near the mid-atlantic ridge at 30 n. *Nature*, 412(6843):145–149.

Kelly, K. R., Ward, R. W., Treitel, S., and Alford, R. M. (1976). Synthetic seismograms: A finite-difference approach. *Geophysics*, 41(1):2–27.

Kennett, B. (1983). Seismic wave propagation in stratified media, cambridge univ. *Pres., Cambridge*.

Kennett, B. L., Engdahl, E., and Buland, R. (1995). Constraints on seismic velocities in the earth from traveltimes. *Geophysical Journal International*, 122(1):108–124.

Klem-Musatov, K., Aizenberg, A., et al. (1985). Seismic modelling by methods of the theory of edge waves. *Journal of Geophysics*, 57(1):90–105.

Kohnen, H. (1974). The temperature dependence of seismic waves in ice. *Journal of Glaciology*, 13(67):144–147.

Konter, S. (2021). Introseis shearer, chapter 8, surface waves and normal modes.

Korenaga, J., Holbrook, W., Kent, G., Kelemen, P., Detrick, R., Larsen, H.-C., Hopper, J., and Dahl-Jensen, T. (2000). Crustal structure of the southeast greenland margin from joint refraction and reflection seismic tomography. *Journal of Geophysical Research: Solid Earth*, 105(B9):21591–21614.

Kumar, N., Hazarika, D., and Sain, K. (2021). Earthquakes: Basics of seismology and computational techniques. In *Basics of Computational Geophysics*, pages 47–80. Elsevier.

Lacoss, R. T., Kelly, E. J., and Toksöz, M. N. (1969). Estimation of seismic noise structure using arrays. *Geophysics*, 34(1):21–38.

Lan, H. and Zhang, Z. (2011). Comparative study of the free-surface boundary condition in two-dimensional finite-difference elastic wave field simulation. *Journal of Geophysics and Engineering*, 8(2):275.

Landrø, M. and Amundsen, L. (2010). Marine seismic sources part i. *Geo ExPro*, 7(1):32–34.

Lavier, L. L., Roger Buck, W., and Poliakov, A. N. (1999). Self-consistent rolling-hinge model for the evolution of large-offset low-angle normal faults. *Geology*, 27(12):1127–1130.

Leiber, C.-O. (2003). *Assessment of safety and risk with a microscopic model of detonation*. Elsevier.

Leroy, S. and Cannat, M. (2014). Md 199/sismo-smooth cruise, marion dufresne r/v.

Leroy, S., Cannat, M., Momoh, E. I., Singh, S. C., Watremez, L., Sauter, D., Autin, J., Louden, K. E., Nedimovic, M. R., Daniel, R., et al. (2015). Seismic structure of an amagmatic section of the ultra-slow spreading south west indian ridge: the 2014 sismosmooth cruise. *AGUFM*, 2015:V21A–3027.

Levander, A. R. (1988). Fourth-order finite-difference p-sv seismograms. *Geophysics*, 53(11):1425–1436.

Li, H., Bernardi, F., and Michelini, A. (2010). Surface wave dispersion measurements from ambient seismic noise analysis in italy. *Geophysical Journal International*, 180(3):1242–1252.

Lin, F.-C., Moschetti, M. P., and Ritzwoller, M. H. (2008). Surface wave tomography of the western united states from ambient seismic noise: Rayleigh and love wave phase velocity maps. *Geophysical Journal International*, 173(1):281–298.

Lin, F.-C., Ritzwoller, M. H., Townend, J., Bannister, S., and Savage, M. K. (2007). Ambient noise rayleigh wave tomography of new zealand. *Geophysical Journal International*, 170(2):649–666.

Liu, C., Aslam, K., and Langston, C. A. (2020). Directionality of ambient noise in the mississippi embayment. *Geophysical Journal International*, 223(2):1100–1117.

Lizarralde, D., Gaherty, J. B., Collins, J. A., Hirth, G., and Kim, S. D. (2004). Spreading-rate dependence of melt extraction at mid-ocean ridges from mantle seismic refraction data. *Nature*, 432(7018):744.

Lobkis, O. I. and Weaver, R. L. (2001). On the emergence of the green's function in the correlations of a diffuse field. *The Journal of the Acoustical Society of America*, 110(6):3011–3017.

Longuet-Higgins, M. S. (1950). A theory of the origin of microseisms. *Philosophical Transactions of the Royal Society of London. Series A, Mathematical and Physical Sciences*, 243(857):1–35.

Louboutin, M., Witte, P., Lange, M., Kukreja, N., Luporini, F., Gorman, G., and Herrmann, F. J. (2018). Full-waveform inversion, part 2: Adjoint modeling. *The Leading Edge*, 37(1):69–72.

Madariaga, R. (1976). Dynamics of an expanding circular fault. *Bulletin of the Seismological Society of America*, 66(3):639–666.

Marfurt, K. J. (1984). Accuracy of finite-difference and finite-element modeling of the scalar and elastic wave equations. *Geophysics*, 49(5):533–549.

Margrave, G. F. and Lamoureux, M. P. (2019). *Numerical methods of exploration seismology: With algorithms in MATLAB®*. Cambridge University Press.

Mari, J.-L. (2021). Wave propagation. In *Seismic imaging: a practical approach*, pages 17–34. EDP Sciences.

Martin, R. and Komatitsch, D. (2009). An unsplit convolutional perfectly matched layer technique improved at grazing incidence for the viscoelastic wave equation. *Geophysical Journal International*, 179(1):333–344.

MASON, R. (1985). Ophiolites. *Geology Today*, 1(5):136–140.

McNamara, D. E. and Boaz, R. (2006). *Seismic noise analysis system using power spectral density probability density functions: A stand-alone software package*. Citeseer.

Mendel, V., Sauter, D., Parson, L., and Vanney, J.-R. (1997). Segmentation and morphotectonic variations along a super slow-spreading center: the southwest indian ridge (57 e-70 e). *Marine Geophysical Researches*, 19(6):505–533.

Menke, W. (2018). *Geophysical data analysis: Discrete inverse theory*. Academic press.

Menke, W. and Jin, G. (2015). Waveform fitting of cross spectra to determine phase velocity using aki's formula. *Bulletin of the Seismological Society of America*, 105(3):1619–1627.

Messud, J., Carotti, D., Hermant, O., Sedova, A., and Lambaré, G. (2021). Optimal transport full-waveform inversion: from theory to industrial applications with examples from the sultanate of oman. *First Break*, 39(12):45–53.

Mével, C. (2003). Serpentinization of abyssal peridotites at mid-ocean ridges. *Comptes Rendus Geoscience*, 335(10-11):825–852.

Miller, D. J. and Christensen, N. I. (1997). Seismic velocities of lower crustal and upper mantle rocks from the slow-spreading mid-atlantic ridge, south of the kane transform zone (mark). In *PROCEEDINGS-OCEAN DRILLING PROGRAM SCIENTIFIC RESULTS*, pages 437–456. NATIONAL SCIENCE FOUNDATION.

Min, D.-J., Shin, C., Pratt, R. G., and Yoo, H. S. (2003). Weighted-averaging finite-element method for 2d elastic wave equations in the frequency domain. *Bulletin of the Seismological Society of America*, 93(2):904–921.

Minshull, T., Muller, M., and White, R. (2006). Crustal structure of the southwest indian ridge at 66 e: Seismic constraints. *Geophysical Journal International*, 166(1):135–147.

Minshull, T. A. (2009). Geophysical characterisation of the ocean–continent transition at magma-poor rifted margins. *Comptes Rendus Geoscience*, 341(5):382–393.

Mohamadian Sarvandani, M., Kästle, E., Boschi, L., Leroy, S., and Cannat, M. (2021). Seismic ambient noise imaging of a quasi-amagmatic ultra-slow spreading ridge. *Remote Sensing*, 13(14):2811.

Molinari, I., Verbeke, J., Boschi, L., Kissling, E., and Morelli, A. (2015). Italian and alpine three-dimensional crustal structure imaged by ambient-noise surface-wave dispersion. *Geochemistry, Geophysics, Geosystems*, 16(12):4405–4421.

Momoh, E., Cannat, M., and Leroy, S. (2020). Internal structure of the oceanic lithosphere at a melt-starved ultraslow-spreading mid-ocean ridge: Insights from 2-d seismic data. *Geochemistry, Geophysics, Geosystems*, 21(2):e2019GC008540.

Momoh, E., Cannat, M., Watremez, L., Leroy, S., and Singh, S. C. (2017). Quasi-3-d seismic reflection imaging and wide-angle velocity structure of nearly amagmatic oceanic lithosphere at the ultraslow-spreading southwest indian ridge. *Journal of Geophysical Research: Solid Earth*, 122(12):9511–9533.

Momoh, E. I. (2018). *Insights on the Nature of the Geophysical Crust at a Nearly Amagmatic Section of the Ultra-Slow-Spreading Southwest Indian Ridge (64okayE)*. PhD thesis, Institut de Physique du Globe de Paris.

Montési, L. G. and Behn, M. D. (2007). Mantle flow and melting underneath oblique and ultraslow mid-ocean ridges. *Geophysical Research Letters*, 34(24).

Mora, P., Bernabini, M., Carrion, P., Jacovetti, G., Rocca, F., Treitel, S., and Worthington, M. (1987). Elastic wavefield inversion for low and high wavenumbers of the p-and s-wave velocities, a possible solution. *Deconvolution and inversion: Blackwell Scientific Publications, Inc*, pages 321–337.

Mordret, A., Landès, M., Shapiro, N., Singh, S., Roux, P., and Barkved, O. (2013). Near-surface study at the valhall oil field from ambient noise surface wave tomography. *Geophysical Journal International*, 193(3):1627–1643.

Moschetti, M., Ritzwoller, M., and Shapiro, N. (2007). Surface wave tomography of the western united states from ambient seismic noise: Rayleigh wave group velocity maps. *Geochemistry, Geophysics, Geosystems*, 8(8).

Mosegaard, K. and Tarantola, A. (1995). Monte carlo sampling of solutions to inverse problems. *Journal of Geophysical Research: Solid Earth*, 100(B7):12431–12447.

Mousa, W. A. and Al-Shuhail, A. A. (2011). Processing of seismic reflection data using matlab™. *Synthesis Lectures on Signal Processing*, 5(1):1–97.

Naranjo, D., Parisi, L., Jousset, P., Weemstra, C., and Jónsson, S. (2021). Determining obs clock drift using ambient seismic noise. In *EGU General Assembly Conference Abstracts*, pages EGU21–13999.

Nicolson, H., Curtis, A., Baptie, B., and Galetti, E. (2012). Seismic interferometry and ambient noise tomography in the british isles. *Proceedings of the Geologists' Association*, 123(1):74–86.

Nolet, G. (1981). Linearized inversion of (teleseismic) data. In *The solution of the inverse problem in geophysical interpretation*, pages 9–37. Springer.

OGP, I. (2011). An overview of marine seismic operations. *International Association of Oil and Gas Producers*, 448.

Olive, J.-A., Behn, M. D., and Tucholke, B. E. (2010). The structure of oceanic core complexes controlled by the depth distribution of magma emplacement. *Nature Geoscience*, 3(7):491.

Operto, S., Gholami, Y., Prieux, V., Ribodetti, A., Brossier, R., Metivier, L., and Virieux, J. (2013). A guided tour of multiparameter full-waveform inversion with multicomponent data: From theory to practice. *The leading edge*, 32(9):1040–1054.

Operto, S., Virieux, J., Dessa, J.-X., and Pascal, G. (2006). Crustal seismic imaging from multifold ocean bottom seismometer data by frequency domain full waveform tomography: Application to the eastern nankai trough. *Journal of Geophysical Research: Solid Earth*, 111(B9).

Palin, R. M. and Santosh, M. (2021). Plate tectonics: What, where, why, and when? *Gondwana Research*, 100:3–24.

Pica, A., Diet, J., and Tarantola, A. (1990). Nonlinear inversion of seismic reflection data in a laterally invariant medium. *Geophysics*, 55(3):284–292.

Platt, J. P., Behr, W. M., and Cooper, F. J. (2015). Metamorphic core complexes: windows into the mechanics and rheology of the crust. *Journal of the Geological Society*, 172(1):9–27.

Plessix, R., Milcik, P., Rynja, H., Stopin, A., Matson, K., and Abri, S. (2013). Multiparameter full-waveform inversion: Marine and land examples. *The Leading Edge*, 32(9):1030–1038.

Plessix, R.-E. (2006). A review of the adjoint-state method for computing the gradient of a functional with geophysical applications. *Geophysical Journal International*, 167(2):495–503.

Plummer, C. C. (2004). *Physical Geology & the Environment*. McGraw-Hill Ryerson.

Popov, M. M. (1982). A new method of computation of wave fields using gaussian beams. *Wave motion*, 4(1):85–97.

Pressling, N., Morris, A., John, B. E., and MacLeod, C. J. (2012). The internal structure of an oceanic core complex: An integrated analysis of oriented borehole imagery from iodp hole u1309d (atlantis massif). *Geochemistry, Geophysics, Geosystems*, 13(9).

Prieto, G., Lawrence, J., and Beroza, G. (2009). Anelastic earth structure from the coherency of the ambient seismic field. *Journal of Geophysical Research: Solid Earth*, 114(B7).

Prieux, V., Brossier, R., Operto, S., and Virieux, J. (2013). Multiparameter full waveform inversion of multicomponent ocean-bottom-cable data from the valhall field. part 2: imaging compressive-wave and shear-wave velocities. *Geophysical Journal International*, 194(3):1665–1681.

Purdy, G. and Detrick, R. S. (1986). Crustal structure of the mid-atlantic ridge at 23° n from seismic refraction studies. *Journal of Geophysical Research: Solid Earth*, 91(B3):3739–3762.

Püthe, C. and Gerya, T. (2014). Dependence of mid-ocean ridge morphology on spreading rate in numerical 3-d models. *Gondwana Research*, 25(1):270–283.

Raknes, E. B., Arntsen, B., and Weibull, W. (2015). Three-dimensional elastic full waveform inversion using seismic data from the sleipner area. *Geophysical Journal International*, 202(3):1877–1894.

Raknes, E. B. and Arntsen, B. r. (2017). Challenges and solutions for performing 3d time-domain elastic full-waveform inversion. *The leading edge*, 36(1):88–93.

Rakovan, J. (2009). Word to the wise: felsic & mafic. *Rocks & Minerals*, 84(6):559–560.

Ramos-Martínez, J., Qiu, L., Kirkebø, J., Valenciano, A., and Yang, Y. (2018). Long-wavelength fwi updates beyond cycle skipping. In *SEG Technical Program Expanded Abstracts 2018*, pages 1168–1172. Society of Exploration Geophysicists.

Reinen, L. A., Weeks, J. D., and Tullis, T. E. (1994). The frictional behavior of lizardite and antigorite serpentinites: Experiments, constitutive models, and implications for natural faults. *Pure and Applied Geophysics*, 143(1):317–358.

Rickett, J. and Claerbout, J. (1999). Acoustic daylight imaging via spectral factorization: Helioseismology and reservoir monitoring. *The leading edge*, 18(8):957–960.

Rosen, J. (2015). Reading the ridges: Are climate and the seafloor connected?, https://www.earthmagazine.org/article/reading-ridges-are-climate-and-seafloor-connected.

Rouméjon, S. and Cannat, M. (2014). Serpentinization of mantle-derived peridotites at mid-ocean ridges: Mesh texture development in the context of tectonic exhumation. *Geochemistry, Geophysics, Geosystems*, 15(6):2354–2379.

Rouméjon, S., Cannat, M., Agrinier, P., Godard, M., and Andreani, M. (2015). Serpentinization and fluid pathways in tectonically exhumed peridotites from the southwest indian ridge (62–65 e). *Journal of Petrology*, 56(4):703–734.

Roy, S. (2013). *Near-surface characterization via seismic surface-wave inversion*. PhD thesis.

Sajeva, A., Aleardi, M., Stucchi, E., Bienati, N., and Mazzotti, A. (2016). Estimation of acoustic macro models using a genetic full-waveform inversion: Applications to the marmousi model. *Geophysics*, 81(4):R173–R184.

Salah, M. K., Alqudah, M., Abd El-Aal, A. K., and Barnes, C. (2018). Effects of porosity and composition on seismic wave velocities and elastic moduli of lower cretaceous rocks, central lebanon. *Acta Geophysica*, 66(5):867–894.

Sauter, D. and Cannat, M. (2010). The ultraslow spreading southwest indian ridge. *Diversity of Hydrothermal Systems on Slow Spreading Ocean Ridges*, 88:153–173.

Sauter, D., Cannat, M., and Mendel, V. (2008). Magnetization of 0–26.5 ma seafloor at the ultraslow spreading southwest indian ridge, 61–67 e. *Geochemistry, Geophysics, Geosystems*, 9(4).

Sauter, D., Cannat, M., Rouméjon, S., Andreani, M., Birot, D., Bronner, A., Brunelli, D., Carlut, J., Delacour, A., Guyader, V., et al. (2013). Continuous exhumation of mantle-derived rocks at the southwest indian ridge for 11 million years. *Nature Geoscience*, 6(4):314.

Sauter, D., Carton, H., Mendel, V., Munschy, M., Rommevaux-Jestin, C., Schott, J.-J., and Whitechurch, H. (2004). Ridge segmentation and the magnetic structure of the southwest indian ridge (at 50 30′ e, 55 30′ e and 66 20′ e): Implications for

magmatic processes at ultraslow-spreading centers. *Geochemistry, Geophysics, Geosystems*, 5(5).

Saygin, E. and Kennett, B. (2012). Crustal structure of australia from ambient seismic noise tomography. *Journal of Geophysical Research: Solid Earth*, 117(B1).

Scales, J. A. and Tenorio, L. (2001). Prior information and uncertainty in inverse problems. *Geophysics*, 66(2):389–397.

Schmid, F. (2017). *Magmatic versus amagmatic-a study of local seismicity and lithospheric structure at two contrasting Southwest Indian Ridge segments*. PhD thesis, Staats-und Universitätbibliothek Bremen.

Schouten, H., Smith, D. K., Cann, J. R., and Escartín, J. (2010). Tectonic versus magmatic extension in the presence of core complexes at slow-spreading ridges from a visualization of faulted seafloor topography. *Geology*, 38(7):615–618.

Schuck, A. and Lange, G. (2007). Seismic methods. In *Environmental Geology*, pages 337–402. Springer.

Schuster, G. T. (2001). Theory of daylight/interferometric imaging-tutorial. In *63rd EAGE Conference & Exhibition*.

Seats, K. J., Lawrence, J. F., and Prieto, G. A. (2012). Improved ambient noise correlation functions using welch′ s method. *Geophysical Journal International*, 188(2):513–523.

Seyler, M., Cannat, M., and Mével, C. (2003). Evidence for major-element heterogeneity in the mantle source of abyssal peridotites from the southwest indian ridge (52° to 68° e). *Geochemistry, Geophysics, Geosystems*, 4(2).

Shapiro, N. M. and Campillo, M. (2004). Emergence of broadband rayleigh waves from correlations of the ambient seismic noise. *Geophysical Research Letters*, 31(7).

Shapiro, N. M., Campillo, M., Stehly, L., and Ritzwoller, M. H. (2005). High-resolution surface-wave tomography from ambient seismic noise. *Science*, 307(5715):1615–1618.

Sheriff, R. E. and Geldart, L. P. (1995). *Exploration seismology*. Cambridge university press.

Shipp, R. M. and Singh, S. C. (2002). Two-dimensional full wavefield inversion of wide-aperture marine seismic streamer data. *Geophysical Journal International*, 151(2):325–344.

Shock, E. and Holland, M. E. (2004). Geochemical energy sources that support the subsurface biosphere. In *The Subseafloor Biosphere at Mid-Ocean Ridges, 2004*, pages 153–165. Blackwell Publishing Ltd.

Shoja, S., Abolhassani, S., and Amini, N. (2018). A comparison between time-domain and frequency-domain full waveform inversion. In *80th EAGE Conference*

*and Exhibition 2018*, volume 2018, pages 1–3. European Association of Geoscientists & Engineers.

Sirgue, L. and Pratt, R. G. (2004). Efficient waveform inversion and imaging: A strategy for selecting temporal frequencies. *Geophysics*, 69(1):231–248.

Slideplayer (2019). chapter9, plate tectonics,https://slideplayer.com/slide/10510190/.

Smith, D. K. and Cann, J. R. (1999). Constructing the upper crust of the mid-atlantic ridge: A reinterpretation based on the puna ridge, kilauea volcano. *Journal of Geophysical Research: Solid Earth*, 104(B11):25379–25399.

Smith, D. K., Cann, J. R., and Escartín, J. (2006). Widespread active detachment faulting and core complex formation near 13 n on the mid-atlantic ridge. *Nature*, 442(7101):440.

Smith, D. K., Escartín, J., Schouten, H., and Cann, J. R. (2008). Fault rotation and core complex formation: Significant processes in seafloor formation at slow-spreading mid-ocean ridges (mid-atlantic ridge, 13–15 n). *Geochemistry, Geophysics, Geosystems*, 9(3).

Smithson, T. (2015). The defining series: Measuring porosity downhole. https://www.slb.com/resource-library/oilfield-review/defining-series/defining-porosity.

Snieder, R. (2004). Extracting the green's function from the correlation of coda waves: A derivation based on stationary phase. *Physical Review E*, 69(4):046610.

Snow, J. E. and Edmonds, H. N. (2007). Ultraslow-spreading ridges rapid paradigm changes. *Oceanography*, 20(1):90–101.

Sohn, R. A., Willis, C., Humphris, S., Shank, T. M., Singh, H., Edmonds, H. N., Kunz, C., Hedman, U., Helmke, E., Jakuba, M., et al. (2008). Explosive volcanism on the ultraslow-spreading gakkel ridge, arctic ocean. *Nature*, 453(7199):1236–1238.

Standish, J. J., Dick, H. J., Michael, P. J., Melson, W. G., and O'Hearn, T. (2008). Morb generation beneath the ultraslow spreading southwest indian ridge (9–25 e): Major element chemistry and the importance of process versus source. *Geochemistry, Geophysics, Geosystems*, 9(5).

Stehly, L., Campillo, M., and Shapiro, N. (2006). A study of the seismic noise from its long-range correlation properties. *Journal of Geophysical Research: Solid Earth*, 111(B10).

Stehly, L., Fry, B., Campillo, M., Shapiro, N., Guilbert, J., Boschi, L., and Giardini, D. (2009). Tomography of the alpine region from observations of seismic ambient noise. *Geophysical Journal International*, 178(1):338–350.

Stewart, P. (2006). Interferometric imaging of ocean bottom noise. In *SEG Technical Program Expanded Abstracts 2006*, pages 1555–1559. Society of Exploration Geophysicists.

Tarantola, A. (1984). Inversion of seismic reflection data in the acoustic approximation: Geophysics.

Tarantola, A. (1987). Inversion of travel times and seismic waveforms. In *Seismic tomography*, pages 135–157. Springer.

Thierney, S. (2019). Moment tensors – a practical guide , https://mxrap.com/moment-tensors-a-practical-guide/.

Tromp, J., Luo, Y., Hanasoge, S., and Peter, D. (2010). Noise cross-correlation sensitivity kernels. *Geophysical Journal International*, 183(2):791–819.

Tromp, J., Tape, C., and Liu, Q. (2005). Seismic tomography, adjoint methods, time reversal and banana-doughnut kernels. *Geophysical Journal International*, 160(1):195–216.

Tucholke, B. E., Behn, M. D., Buck, W. R., and Lin, J. (2008). Role of melt supply in oceanic detachment faulting and formation of megamullions. *Geology*, 36(6):455–458.

Tucholke, B. E., Lin, J., and Kleinrock, M. C. (1998). Megamullions and mullion structure defining oceanic metamorphic core complexes on the mid-atlantic ridge. *Journal of Geophysical Research: Solid Earth*, 103(B5):9857–9866.

Van Avendonk, H. J., Hayman, N. W., Harding, J. L., Grevemeyer, I., Peirce, C., and Dannowski, A. (2017). Seismic structure and segmentation of the axial valley of the m id-c ayman s preading c enter. *Geochemistry, Geophysics, Geosystems*, 18(6):2149–2161.

Vasco, D. W., Peterson Jr, J. E., and Majer, E. L. (1995). Beyond ray tomography: Wavepaths and fresnel volumes. *Geophysics*, 60(6):1790–1804.

Virieux, J. (1984). Sh-wave propagation in heterogeneous media: Velocity-stress finite-difference method. *Geophysics*, 49(11):1933–1942.

Virieux, J. (1986). P-sv wave propagation in heterogeneous media: Velocity-stress finite-difference method. *Geophysics*, 51(4):889–901.

Virieux, J. and Operto, S. (2009). An overview of full-waveform inversion in exploration geophysics. *Geophysics*, 74(6):WCC1–WCC26.

Wang, J., Wu, G., and Chen, X. (2019). Frequency-bessel transform method for effective imaging of higher-mode rayleigh dispersion curves from ambient seismic noise data. *Journal of Geophysical Research: Solid Earth*, 124(4):3708–3723.

Wapenaar, K. (2004). Retrieving the elastodynamic green's function of an arbitrary inhomogeneous medium by cross correlation. *Physical review letters*, 93(25):254301.

Wapenaar, K., Draganov, D., Snieder, R., Campman, X., and Verdel, A. (2010). Tutorial on seismic interferometry: Part 1—basic principles and applications. *Geophysics*, 75(5):75A195–75A209.

Warner, M., Ratcliffe, A., Nangoo, T., Morgan, J., Umpleby, A., Shah, N., Vinje, V., Štekl, I., Guasch, L., Win, C., et al. (2013). Anisotropic 3d full-waveform inversion. *Geophysics*, 78(2):R59–R80.

Wathelet, M. (2005). Array recordings of ambient vibrations: surface-wave inversion. *PhD Diss., Liége University*, 161.

White, R. S., McKenzie, D., and O'Nions, R. K. (1992). Oceanic crustal thickness from seismic measurements and rare earth element inversions. *Journal of Geophysical Research: Solid Earth*, 97(B13):19683–19715.

Whitmarsh, R., Manatschal, G., and Minshull, T. (2001). Evolution of magma-poor continental margins from rifting to seafloor spreading. *Nature*, 413(6852):150–154.

Woodward, M. (1992). Wave-equation tomography: Geophysics.

Wu, R.-S. (2003). Wave propagation, scattering and imaging using dual-domain one-way and one-return propagators. *Pure and Applied Geophysics*, 160(3):509–539.

Xia, J., Miller, R. D., Park, C. B., and Tian, G. (2003). Inversion of high frequency surface waves with fundamental and higher modes. *Journal of Applied Geophysics*, 52(1):45–57.

Yang, Y., Ritzwoller, M. H., Levshin, A. L., and Shapiro, N. M. (2007). Ambient noise rayleigh wave tomography across europe. *Geophysical Journal International*, 168(1):259–274.

Yao, H. and Beghein, C. (2009). Rd van derhilst (2009). *Surface wave array tomography in SE Tibet from ambient seismic noise and two-station analysis–II. Crustal and upper-mantle structure, Geophys. J. Int*, 173(1):205–219.

Yao, H., Gouedard, P., Collins, J. A., McGuire, J. J., and van der Hilst, R. D. (2011). Structure of young east pacific rise lithosphere from ambient noise correlation analysis of fundamental-and higher-mode scholte-rayleigh waves. *Comptes Rendus Geoscience*, 343(8-9):571–583.

Yao, H., van Der Hilst, R. D., and De Hoop, M. V. (2006). Surface-wave array tomography in se tibet from ambient seismic noise and two-station analysis—i. phase velocity maps. *Geophysical Journal International*, 166(2):732–744.

Yilmaz, Ö. (2001). *Seismic data analysis: Processing, inversion, and interpretation of seismic data*. Society of exploration geophysicists.

Zhang, X., Curtis, A., Galetti, E., and De Ridder, S. (2018). 3-d monte carlo surface wave tomography. *Geophysical Journal International*, 215(3):1644–1658.

Zhao, M., Qiu, X., Li, J., Sauter, D., Ruan, A., Chen, J., Cannat, M., Singh, S., Zhang, J., Wu, Z., et al. (2013). Three-dimensional seismic structure of the dragon flag oceanic core complex at the ultraslow spreading southwest indian ridge (49° 39′ e). *Geochemistry, Geophysics, Geosystems*, 14(10):4544–4563.

Zheng, S., Sun, X., Song, X., Yang, Y., and Ritzwoller, M. H. (2008). Surface wave tomography of china from ambient seismic noise correlation. *Geochemistry, Geophysics, Geosystems*, 9(5).

Zhou, W. (2016). *Velocity model building by full waveform inversion of early arrivals & reflections and case study with gas cloud effect*. PhD thesis, Université Grenoble Alpes.

Zulfakriza, Z., Saygin, E., Cummins, P., Widiyantoro, S., Nugraha, A. D., Lühr, B.-G., and Bodin, T. (2014). Upper crustal structure of central java, indonesia, from transdimensional seismic ambient noise tomography. *Geophysical Journal International*, 197(1):630–635.